Université de Neuchâtel
Institut de Microtechnique

Hybrid Optics for Space Applications

Thèse

Présentée à la Faculté des Sciences
pour obtenir le titre de docteur ès sciences
par

Reinhard H. Czichy

Neuchâtel, Mars 1992

IMPRIMATUR POUR LA THÈSE

Hybrid Optics for Space Applications

de Monsieur Reinhard H. Czichy

UNIVERSITÉ DE NEUCHÂTEL

FACULTÉ DES SCIENCES

La Faculté des sciences de l'Université de Neuchâtel sur le rapport des membres du jury,

MM. les professeurs R. Dändliker, N. de Rooij, H. Buczek et K. Biedermann (Stockholm)

autorise l'impression de la présente thèse.

Neuchâtel, le 6 octobre 1992

Le doyen:

A. Robert

Table of Contents

Chapter 1
Introduction 1

Chapter 2
Objectives 4

Chapter 3
Theoretical Aspects of Hybrid Optics 8
3.1 Introduction 8
3.2 Diffraction and Dispersion 8
3.3 Diffractive Optical Elements 16
3.3.1 General 16
3.3.2 Definitions and Special Features 16
3.3.3 DOE Classification 20
3.3.4 Diffraction Efficiency and Phase Quantization 33
3.3.5 Considerations on DOE Signal-to-Noise Ratio 36
3.3.6 DOE Dispersion Properties 40
3.3.7 DOE Modelling Methods 44
3.3.7.1 Overview 44
3.3.7.2 The High Refractive Index Model 47
3.3.7.3 DOE Models in Optical Design Programs 51
3.4 Hybrid Optics 54
3.4.1 General 54
3.4.2 Chromatic Aberrations 54
3.4.2.1 Hybrid Achromats 55
3.4.2.2 Hybrid Apochromats 60
3.4.3 Monochromatic Aberrations and Glass Selection 63

Chapter 4
Design Examples for Hybrid Optical Elements 65
4.1 General Design Approach 65
4.2 Diffractive Structure Quantization 66
4.3 Tolerancing Considerations 70
4.4 Design Examples 74
4.4.1 General 74
4.4.2 Hybrid Achromat 1:1.8 74
4.4.3 Hybrid Achromat for Medium Infrared 83

4.4.4 Microlens Array for Matrix Detector Devices 88
4.4.5 Optical System for Tracking Sensor/Receiver Combinations . 92

Chapter 5
Requirements for Optics for Space Applications 97
5.1 General 97
5.2 Lifetime and Reliability 98
5.3 Reproducibility of Manufacturing Processes 99
5.4 Environmental Loads 100
5.4.1 Thermal Environment 100
5.4.2 Mechanical Loads 101
5.4.3 Radiation Loads 102
5.4.3.1 General 102
5.4.3.2 UV Radiation 103
5.4.3.3 Highly Energetic Radiation 104
5.4.4 Vacuum Conditions 108
5.4.5 Atomic Oxygen 109
5.4.6 Micrometeorites 110

Chapter 6
Manufacturing of Hybrid Optical Elements 111
6.1 Review of Hybrid Optics Manufacturing Technologies 111
6.1.1 General 111
6.1.2 Methods of DOE Pattern Generation and Transfer 111
6.1.3 Material Selection and Processing 117
6.1.4 Ion Beam Etching 123
6.1.4.1 Process Description 123
6.1.4.2 Process Thermal Control 130
6.1.4.3 Etch Rates of Optical Materials 140
6.2 Description of Hybrid Optics Manufacturing Process 143
6.2.1 General 143
6.2.2 DOE Manufacturing Process 143
6.2.3 Assembly of DOE and Lens 156

Chapter 7
Hybrid Optical Element Performance Verification 165
7.1 Description of Verification Approach 165
7.2 Test Methods and Equipment 166
7.2.1 General Description 166
7.2.2 Special Test Equipment 170

7.2.2.1 Twyman-Green Interferometer 170
7.2.2.2 Hartmann Test Setup 173
7.2.2.3 Diffraction Efficiency/Pattern Test Equipment 182
7.2.2.4 Focal Length Test Setup 186
7.3 Verification Results 189
7.3.1 General Test Results 189
7.3.2 Diffraction Efficiency/Pattern 194
7.3.3 Focal Length 202
7.3.4 Chromatic Aberrations 208
7.3.5 Wavefront Quality 212
7.4 Technological Evaluation 214

Chapter 8
The Technical Potential of Hybrid Optics 217

Chapter 9
Application of Hybrid Optics in Space 220

Chapter 10
Summary and Conclusions 222

Acknowledgements 226

References 228

Chapter 1

INTRODUCTION

Basic elements for the design of optical systems have been, for a long time, only lenses and mirrors - refractive and reflective elements -, preferably of spherical shape. The progress made in the field of modern optical science and technology over the last two decades has added a further type of component, the diffractive element.

Diffractive elements have been in principle known for a long time: the first diffraction gratings were made by the American astronomer D.Rittenhouse (1785) and in Europe J.Fraunhofer (1821) manufactured gratings which he used for his studies on the solar spectrum. H.A.Rowland refined significantly the manufacturing techniques and fabricated high quality reflection gratings on plano and on concave substrates (1882). These first diffractive elements were mainly used in scientific instrumentation, astronomical spectrographs for instance.
The discovery of the principles of holography in 1948 (D. Gabor) initiated a new series of developments in the field of diffractive elements which were essentially supported by the invention of the laser about twelve years later. A further important step was made by the application of modern computer tools for the mathematical generation of holograms in 1966 (B.Brown, A.Lohmann). The first elements generated in this way still suffered from problems caused by photographic reduction processes and the relatively low diffraction efficiencies, but very soon the transfer of photolithographic production technology developed in the semiconductor industry for LSI/VLSI circuit production provided the necessary means for technological refinements.

Diffractive optical elements (DOE's) which can be designed today using these new technologies can be called with good reason computer generated optical elements (CGOE's): the processes of CGOE design and tooling are governed by the use of computers and their associated output devices, the subsequent manufacturing is to a large extent reduced to the transfer of a computer generated pattern onto a substrate. CGOE's provide a unique design flexibility since they are not restricted to rotationally symmetric surface shapes and certain minimum dimensions and geometries: they can be

tailored to application specific configurations in order to provide optimum performance.

The combination of this type of optical element with conventional optics shall be called "Hybrid Optics". Hybrid optics seem to offer very interesting new possibilities for optical system/instrument design for a number of reasons. Some of them - e.g. the miniaturization potential, the compactness, the attractiveness for UV/IR applications - make this technology in particular interesting for applications in space. This was the prime motivation to initiate a research project in the field of hybrid optics resulting in this dissertation.

Due to the fact that no comprehensive overview exists in the literature covering both the field of hybrid/diffractive optics design and the related manufacturing technologies, it was decided to include these aspects in the dissertation, in order to provide a good basis for follow-on activities. Therefore, this report presents in some areas more technical details than are absolutely necessary for a scientific study.

The dissertation is structured as follows: Chapter 2 recalls the objectives of this research project and presents the theses being addressed in this work. The work programme is outlined in this chapter and the different resources that were available to support the execution of this work are also listed.
Chapter 3 presents a proposal for the classification of diffractive optical elements and discusses some aspects of the theory of hybrid optics, including a definition of basic design methods.
A number of design examples for hybrid optical elements and design concepts for more complex optoelectronic systems involving hybrid optics are given in chapter 4.
In chapter 5 an overview of the basic design constraints for space optics is presented. This list of constraints served as a guideline for the identification/definition of space qualifiable manufacturing technologies to be used for the production of hybrid optics.
Chapter 6 provides a review these technologies and presents an outline of the process actually used to fabricate one of the design examples described in chapter 4.
The hybrid element resulting from this fabrication was characterized in terms of its optical performance. The test methods used and the results obtained are presented in chapter 7.

Based upon these results and exploratory investigations carried out in several areas of space optics design, the technical potential of hybrid optics was assessed and is presented in chapter 8.
A list of possible applications for hybrid optics in space is provided in chapter 9.
Chapter 10 summarizes the results of this research project highlighting the major achievements reached with regard to the original objectives. Finally, future development perspectives are identified and discussed.

Chapter 2

OBJECTIVES

It was the aim of the work presented here to investigate and to demonstrate the potential of hybrid optics for space applications and to establish a basis for follow-on activities. Since hybrid optics is a new field in optical technology, this work had to include:

- an exploration of basic design methods for hybrid optics and an investigation of their applicability by means of dedicated design studies,

- a review and identification of manufacturing technologies for hybrid optics (materials and processes) suitable for production of space qualifiable hardware, and their validation by test sample manufacturing,

- an experimental verification of the test sample optical performance and a comparison of the results with the theoretical predictions.

The result of the technological investigations was used to establish the basis for an assessment of the potential of hybrid optics for use in space and an identification of possible areas of application.

In particular, the work was guided by the following theses:

1. *Hybrid optical elements can be described by a special model which* makes it possible to treat the elements with the same mathematical tools as conventional optics, e.g. the rules of Gaussian optics apply, conventional lens design programmes can be used for optimization without any modification.

2. Hybrid optical elements can be manufactured using processes which are derived from VLSI production and which are well characterized in terms of process parameters, reproducibility and overall quality.

3. The manufacturing technologies for hybrid optical elements are independent of the effective shape of the element, any arbitrary shape can be produced with almost the same precision.

4. The flexibility provided by hybrid optics with respect to the possible surface shapes provides additional degrees of freedom for optical system optimization, which can lead to novel system design approaches.

5. The application of hybrid optics improves optical system reliability due to reduction of element numbers and interfaces.

6. Use of hybrid optics in complex optical/optoelectronic systems can lead to significant mass saving and reduction of dimensions.

The study logic which was followed in treating these theses is illustrated in figure 2-1. The work programme for this project consisted of the three major groups of activities which are already indicated above: theoretical studies, sample manufacturing, and activities concerning experimental performance verification.

The theoretical studies comprised the establishment of a new classification scheme for diffractive optical elements, an investigation of various design methods for hybrid optics including a test of three commercial lens design programmes. Based upon the results, one programme was selected for detailed design studies. A separate software package was developed for mask calculation and transformation of the design results into manufacturing data files. Various hybrid optical elements and systems were designed in order to test the design approach and to demonstrate its validity. A review of the special requirements for space optics was used to prepare for the definition of a space qualifiable manufacturing technology for hybrid optics.

It was the aim of the sample manufacturing to fabricate one of the hybrid elements designed within the theoretical study phase and to develop and characterize the manufacturing processes involved in such a way that reproducible manufacturing becomes possible. Part of this work was also the characterization of process parameters for various optical glasses and the development of suitable assembly and mounting techniques for the hybrid element.

In order to be able to compare the results of the manufacturing activities with the theoretical predictions and to prove the validity of the design approach chosen, a detailed performance verification programme was carried out. For this purpose several special test methods have been developed and associated test equipment was built. The most significant performance

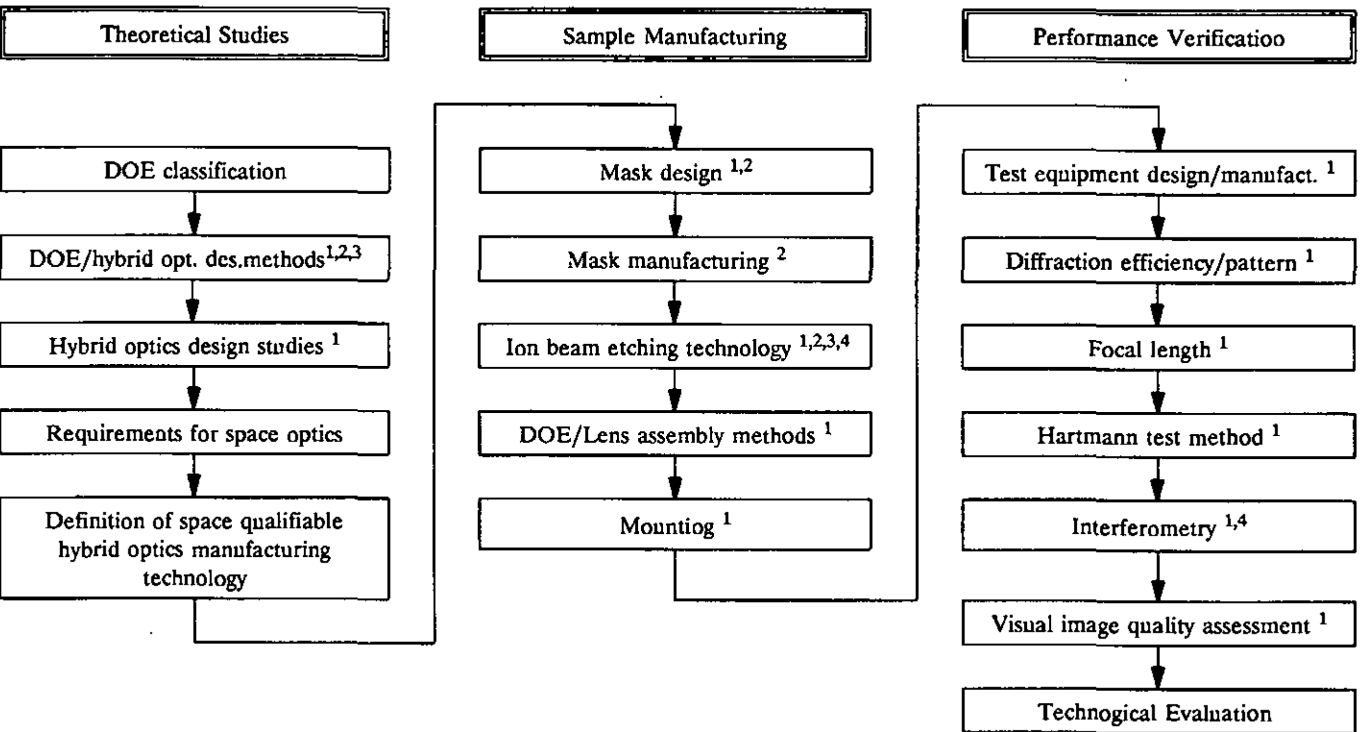

Fig. 2-1 Work programme for the research project on hybrid optics for space applications (Resources used: ESA (1), CSEM (2), IMT (3), Industry (4))

characteristics of the hybrid elements were measured and have been compared with the theoretical predictions. This verification work entailed the necessity of becoming familiar with a number of other technological disciplines outside the normal confines of optical engineering. An evaluation of the manufacturing technologies used for sample fabrication with respect to the requirements for space optics was also included in this part of the work programme.

For the execution of certain tasks of this programme it was possible to make use of various technological resources (see also figure 2-1): optical design programmes were available for evaluation at the Institut de Microtechnique (IMT, Université de Neuchâtel, Switzerland), at the Centre Suisse d'Electronique et de Microtechnique (CSEM, Neuchâtel) and at ESA-ESTEC (Noordwijk, The Netherlands). At ESA-ESTEC, the computer facilities were used for the development of software for generation of manufacturing data files. The finalization of mask design with a dedicated CAD system and the mask manufacturing was performed with the support of CSEM. The manufacturing of DOE's and the process characterization was possible using the facilities of CSEM and IMT. Centering/cementing methods for hybrid elements and the associated tools were developed at ESA-ESTEC. The development of test equipment and the execution of the optical performance verification programme also took place in the ESA-ESTEC laboratories.In addition, various industrial companies supported the work at several stages, for instance in delivering reference spheres for interferometric tests or elements for process characterization.

Only the availability of these resources and the good cooperation within the project made it possible to cover the wide range of scientific and technological disciplines outlined above, within a reasonable time schedule. The material presented in the following chapters clearly shows that the cross-fertilization between existing and new fields of technology along with the efficient combination of resources can easily lead to the development of the new field of hybrid optics. The future potential for this new optical technology, both for space and ground based applications, is both clear and promising.

Chapter 3

THEORETICAL ASPECTS OF HYBRID OPTICS

3.1 Introduction

The aim of the following discussion is to present a clear statement of the physical principles underlying the behaviour of hybrid optics, in order to convey a conceptual understanding of their operation.

A classification scheme for diffractive optical elements (DOE's) in terms of physical type and technological characteristics will be presented which shall contribute to the clarification of some definitions used very often in the literature. Finally, basic methods for hybrid optics design will be reviewed and some aspects of hybrid optics aberration correction will be explained using first and third order theory.

3.2 Diffraction and Dispersion

Optics deals in its widest sense with the interaction of high frequency electromagnetic waves with matter. Well established methods exist to control this interaction by means of optical components like lenses or mirrors, the design of which is based on the basic rules of refraction, reflection and diffraction. The type of optical component which shall be discussed here - Hybrid Optics - makes use of a purposeful combination of two effects, namely diffraction and dispersion, which is quite novel. For the better understanding of this approach and the consequences resulting from it, the theory of diffraction and dispersion shall be briefly recalled here.

An electromagnetic wave is described by its

- amplitude
- frequency
- direction of propagation
- orientation of the oscillation relative to a known axis of a reference system
- variation of all above mentioned factors with time

A spherical monochromatic wave emanating from a point source has an electric field E which is described by

$$E(r,t) = A(r) \cdot e^{i(kr-\omega t)} \tag{1}$$

where A is the amplitude of the wave, r the distance to the source and

$$k = \frac{2\pi}{\lambda} \tag{2}$$

$$\omega = \frac{2\pi}{\nu} \tag{3}$$

with k being the wave vector, ω the angular frequency, λ the wavelength and ν the frequency of the light wave. Since the amplitude of the wave A(r) depends, in isotropic non-absorbing media, only on the source distance r, it follows:

$$A(r) = \frac{A_0}{r} \tag{4}$$

with A_0 representing the unit amplitude. Equation (1) reduces then to

$$E(r,t) = \frac{1}{r} \cdot A_0 \cdot e^{i(kr-\omega t)} \tag{5}$$

Since most of the optical phenomena can be described as being stationary, the time dependence in equation (5) can be suppressed and the equation simplifies therefore to

$$E(r) = \frac{1}{r} \cdot A_0 \cdot e^{ikr} \tag{6}$$

The irradiance of light on a detector is consequently given by

$$I(r) = \frac{1}{T} \cdot \int_0^T Re^2 \, [E(r)] \, dt = \frac{1}{r^2} \cdot A_0^2 \tag{7}$$

Re is the real part of the complex number in (6), T is the time interval for integration. This equation is known as the photometric distance law.

For larger source distances spherical waves convert to plane waves, because the radius of curvature approaches infinity. Such plane waves can be described for the monochromatic case by the electric field vector $\bar{E}$

$$\bar{E} = \bar{E}_0 \cdot e^{i(\bar{k}\bar{r} - \omega t + \varphi_0)} \tag{8}$$

The wave vector $\bar{k}$ points in the propagation direction of the wave. $\bar{r}$ is a position vector defining the observation point and E_0 is the vectorial amplitude, which describes the polarization status of the wave. φ_0 is the phase delay at the zero coordinate point.
Assuming that the plane wave is polarized in the y direction and propagates in the z-direction, (8) can be written as

$$E_y = A_{0y} \cdot e^{i(kz - \omega t + \varphi_0)} \tag{9}$$

If electromagnetic waves interact with matter they experience changes of their initially defined characteristics. The basic effects of material-light interaction are:

- absorption
- change of wavelength
- change of polarization status
- change of propagation direction

All effects can be stationary as well as time dependent. It is clear that these effects are manifest not in isolation but in combination.

In order to explain satisfactorily the basics of diffractive/hybrid optics it is necessary to discuss now in more detail the change of propagation direction of electromagnetic waves in matter.

Following the definition of Sommerfeld (see [3.1], p.156), the change of propagation direction of an electromagnetic wave shall be defined as diffraction, if it cannot be explained by reflection or refraction effects. Directional changes due to diffraction are caused by the interaction of a wave with a screen, an aperture or a periodic structure like a grating for instance. The theory of diffraction is well established, it was formulated first by Kirchhoff (see [3.2], [3.3]) and later on refined by Sommerfeld as rigorous diffraction theory (see [3.1], p.156 ff.). It shall not be repeated here, however some of the results shall be recalled in the following.

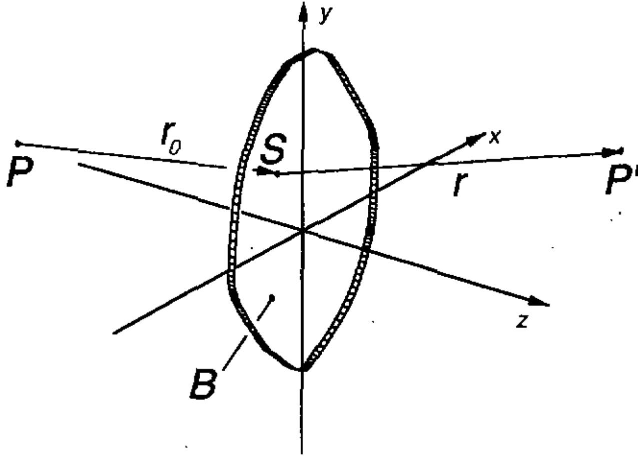

Fig. 3.2-1 Diffraction at screen aperture

A spherical light wave with an electric field described by equation (6) emanating from point P shall illuminate a non transparent screen with an aperture B, as shown in figure 3.2-1. The amplitude distribution U at the observation point P', which is proportional to the value of the electric field strength E, is then described by

$$U(P') = c \cdot \iint u_0(x,y) \cdot u(S) \cdot \frac{e^{-ikr}}{r} dx\,dy \tag{10}$$

Where u(S) is the amplitude of the lightwave at point S and c is a distance scaling factor. The term $u_0(x,y)$ represents the complex amplitude transparency of the screen, which is

$$u_0(x,y) = \begin{cases} 0 & \textit{outside } B \\ u_t(x,y) \cdot e^{-i\varphi(x,y)} & \textit{within } B \end{cases} \tag{11}$$

This function can be used for description of diffraction effects on two-dimensional structures in general.

Equation (11) consists of two terms, an amplitude and a phase term:

$$u_t(x,y) = T(x,y) \qquad (12)$$

$$\varphi(x,y) = k \cdot d(x,y) \cdot (n(x,y) - 1) \qquad (13)$$

T(x,y) describes the transparency of the aperture B, d(x,y) the thickness and n(x,y) the refractive index distribution. If amplitude and phase terms are constant within B, diffraction is caused only at the boundary of B, which is the case for any conventional optical system. If the amplitude and/or the phase term is a function of x,y within B, a diffraction effect is induced by this structure. The diffractive structure described by these terms need not be a geometrical structure but could for instance be a transmission pattern or a refractive index pattern, not having any surface profile. Off course, the aperture border causes an additional diffraction effect.

However, the description in x and y is only an approximation since a diffractive structure is not confined to an infinitely thin surface layer. For a general solution of this problem one has to extend the diffraction theory therefore to three-dimensional structures. This was first done by von Laue [3.4], Bragg [3.5] 1912 and later in the year 1930 by Born [3.6], in describing the diffraction of electrons in crystal structures. For the description of diffraction gratings, holograms, integrated optics etc. this theory was extended later-on to the diffraction of light by transparent objects by Burckhardt (1966 [3.7]), Wolf (1969 [3.8]), Kogelnik (1969 [3.9]) and Evans (1970 [3.10]). Magnusson and Gaylord ([3.11], [3.12]) compared the results of several theoretical approaches used for description of diffractive structures concerning single-wave, two-wave and multiwave diffraction analysis. Criteria were given for classification of diffractive structures to be treated as "thin" and "thick", respectively. These criteria shall be recalled here briefly, since they are important for the classification of DOE's.

According to Magnusson and Gaylord, "the distinction between "thin" and "thick" gratings may be described in terms of the factor Q' given by

$$Q' = \frac{2\pi \cdot \lambda \cdot d}{n_0 \cdot L^2 \cdot \cos\vartheta} \qquad (14)$$

where λ is the free-space wavelength of the incident plane wave, d is the thickness of the grating, n_0 is the average refractive index, L is the grating

period, and ϑ is the angle of incidence inside the medium" [3.12]. Following the results of these analyses, a grating can be treated as being "thin" if the Q' factor is $Q' \ll 1$ and "thick" if $Q' \gg 1$. The discussion of diffraction efficiencies in section 3.3.4 will make reference to these definitions.

It was initially implied, that the electromagnetic wave illuminating the aperture shall be monochromatic. In case of a polychromatic source, amplitude and phase terms (equations 12,13) become wavelength dependent. The wavelength dependence of the refractive index, the dispersion, is the second effect which is used for the design of hybrid optics and some basics shall be recalled therefore.

The wave vector k is with the angular frequency ω related via two material constants, the permeability μ and the dielectric constant ϵ:

$$k = \sqrt{\epsilon \cdot \mu} \cdot \omega \qquad (15)$$

The dimension of $\sqrt{\epsilon \mu}$ is a reciprocal velocity, the phase velocity of light within a medium. One can write therefore

$$k = \frac{1}{v} \cdot \omega \qquad (16)$$

with v being the phase velocity. For the case of vacuum, the phase velocity is:

$$v_{vac} = c = \frac{1}{\sqrt{\epsilon_0 \cdot \mu_0}} \qquad (17)$$

with ϵ_0 being the dielectric constant of vacuum and μ_0 the permeability for vacuum. The relation between the phase velocity v within a medium and the phase velocity c in vacuum shall be called refractive index n :

$$n = \frac{c}{v} = \frac{c \cdot k}{\omega} = \frac{\sqrt{\epsilon \cdot \mu}}{\sqrt{\epsilon_0 \cdot \mu_0}} \qquad (18)$$

The dependence of the refractive index on wavelength results from the following considerations (for details, see Sommerfeld [3.1], p.75 ff.):
Describing the optical field within an isotropic isolator as non-stationary (in contrast to what was assumed to derive equation (6)), one has to introduce

a polarization vector. This results in three differential equations for $\overline{H}$, $\overline{E}$ and $\overline{P}$, with $\overline{H}$ being the magnetic field vector and $\overline{P}$ the polarization vector. By the elimination of $\overline{P}$ and $\overline{H}$ one can derive a single fourth-order differential equation for $\overline{E}$:

$$\left(\frac{\partial^2}{\partial t^2}+\omega_0^2\right)\cdot\left(\frac{1}{c^2}\ddot{\overline{E}}-\Delta\overline{E}\right)+\frac{\mu_0\cdot N\cdot e^2}{m}\cdot\ddot{\overline{E}}=0 \tag{19}$$

N is the number of electrons per volume unit, m is the electron mass and e is its charge. ω_0 is the electron eigenfrequency, which corresponds to a wavelength in the far UV.
Restricting the case to a plane, linearly polarized wave of angular frequency ω, a wave vector k propagating into +z-direction, and assuming for the solution a formulation of the type

$$E_z = A_z \cdot e^{i(kx-\omega t)} \tag{20}$$

one can derive an expression for the wavevector in the form

$$k^2 = \frac{\omega^2}{c^2}\cdot\left[1+\frac{\mu_0\cdot c^2\cdot N\cdot e^2/m}{\omega_0^2-\omega^2}\right] \tag{21}$$

Substituting k with the expression $k = \omega n/c$ (18) one gains an equation for the refractive index

$$n^2 = 1+\frac{\frac{N\cdot e^2}{m\cdot\epsilon_0}}{\omega_0^2-\omega^2} \tag{22}$$

The dispersion, the frequency dependence of the refractive index, is clearly shown in the denominator of the equation: since $\omega < \omega_0$ within the entire visible spectrum, the denominator stays always positive and the refractive index is getting smaller with decreasing frequency and larger with increasing frequency of light.

In contrast to the diffraction effect, dispersion does not depend on any macroscopic structure, but is purely dependent on material constants. Both, diffraction and dispersion, generate in optical elements the same phenomenon, namely a deviation from the straight propagation direction, which can be described as an angular dispersion $d\varphi/d\lambda$. However, it depends

on the type of optical element whether the angular dispersion can be described as diffraction or as a material dispersion effect (see also figure 3.2-2): If the surface is not structured at all, or has a structure with a spatial frequency $\nu_s \ll 1/\lambda$, the observed angular dispersion is due to material dispersion and is described by

$$\frac{d\varphi}{d\lambda} = \frac{d\varphi}{dn} \cdot \frac{dn}{d\lambda} \tag{23}$$

If the spatial frequency on the surface is high with $\nu_s > 1/\lambda$, the angular dispersion is caused by a diffraction effect with basically different laws:

$$\frac{d\varphi}{d\lambda} = \frac{m}{b \cdot \cos\varphi} \tag{24}$$

with $b = 1/\nu_s$ and m as diffractive order.

Refractive elements

Diffractive elements

$+\varphi$

$+\varphi$

$-\varphi$

Spatial frequency ν_s

Low: $\lambda \ll \nu_s$

High: $\lambda \leq \nu_s$

Fig. 3.2-2 Dispersion and diffraction

In the first case, the angular dispersion depends on a material constant and the material dispersion, in the second case it depends largely on the spatial frequency of the structure. These basic phenomena will be used for the design of diffractive optics and - in their combination - in particular for hybrid optics design, which is described in more detail in section 3.4.

3.3 Diffractive Optical Elements

3.3.1 General

A hybrid optical element consists of two components, a conventional optical element such as a lens, and a diffractive optical element (DOE). The special properties of hybrid elements as they will be discussed within the following chapters are determined predominantly by the properties of the DOE component. It seems therefore important to deal with this type of element in more detail providing some basic definitions and highlighting special DOE features.
Since the term "DOE" describes a large variety of elements an attempt at a physical and technological classification was made which is presented in the following.

3.3.2 Definitions and Special Features

The term "Diffractive Optical Element (DOE)" shall describe a type of optical element which is predominantly effective due to diffraction in zero and/or higher order. The diffraction properties of DOE's are defined by the complex amplitude transparency function (as was shown in section 3.2). This class of optical elements comprises a large variety of different types:

- **Holograms**
  Elements for storage/reconstruction of phase and amplitude information of a wavefront
  Subgroups are:
  - Detour phase holograms
  - Modified off-axis reference beam holograms
  - Interferogram type holograms
  - Computer generated holograms

- **Holographic optical elements (HOE)**
  Elements for imaging application, fabrication based on holographic recording techniques
  Subgroups are:
  - Interferometrically recorded HOE's
  - Computer generated HOE's

- **Binary optical elements (BOE)**
  Elements for imaging applications fabricated by digitization of an analog defined shape
  Subgroups are:
  - Single level elements
  - Multiple level elements

- **Kinoforms**
  Elements influencing only the phase of an incident wavefront
  Subgroups are:
  - Kinoforms recorded by analog techniques
  - Digitized kinoforms (see binary optical elements)

- **Corrector plates and phase plates**
  Elements without refractive power used for wavefront shaping
  Subgroups are:
  - Analog or digitized pupil corrector plates
  - Phase matching plates

- **Filters**
  Elements without refractive power but with strong wavelength dependent reflectivity
  Subgroups are:
  - Beam combiner
  - Filter/isolator

- **Hybrid optics**
  Combination of diffractive optical elements with conventional optics in close contact
  Subgroups are:
  - Holographic hybrid optics
  - Kinoform hybrid optics

The majority of these elements are computer generated, which means that they are designed using computer aided design tools and fabricated by transfer of the design data onto the substrate without human intervention. This intensive use of computer design tools, combined with computer controlled output devices for "master fabrication" justifies the introduction of the term "Computer Generated Optical Element" (CGOE) for this type of component. Although all CGOE's are not necessarily DOE's, the majority

tend to be. The diffractive optical elements used for hybrid optics design are CGOE's without exception.

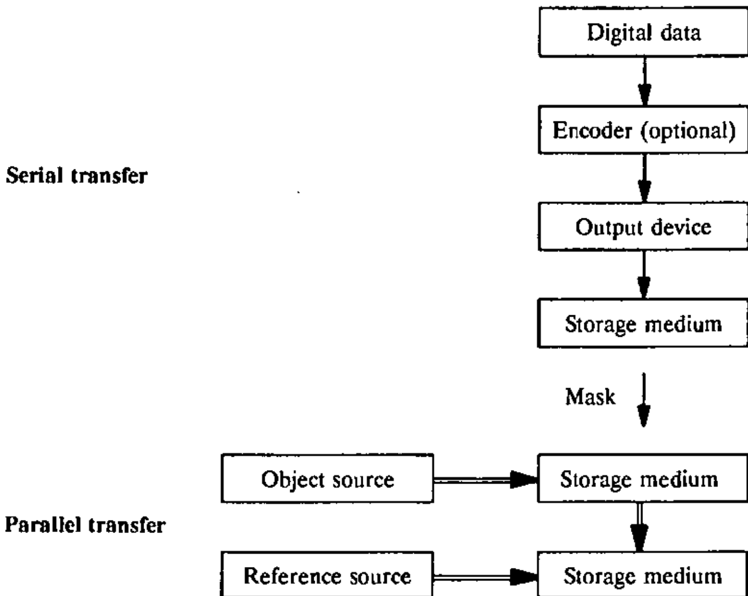

Fig. 3.3.2-1 Typical DOE production sequence

Figure 3.3.2-1 shows a typical production sequence of a CGOE. The design of the element is made with a computer and the results are provided as a data file. Depending on the type of element, the data are either encoded by certain algorithms before transferring it to an output device, or directly sent to an output device without encoding. The output device writes the data in the form of a pattern onto a carrier material which can be used later-on for copying the data onto other carriers, e.g. photoplate, chromium mask or film. Up to now the data flow was organized as serial or pointwise transfer with the possibility to manipulate the data and to introduce local corrections for instance.
The next steps are characterized by parallel channel data transfer: the pattern is copied onto the final substrate either by a contact copying process or by imaging. Depending on the type of CGOE/DOE produced, this step can be repeated several times - in case of multilevel binary elements - or it can be performed by a holographic process recording the mask information

together with a reference wave on the final substrate. The special features of CGOE's/DOE's which are important for hybrid optics design are:

- **Special dispersion properties**
  Since DOE's have quite different dispersion properties compared to glass they can be used efficiently to achieve a good chromatic correction, also with exotic materials. This aspect will be treated in detail in section 3.4.

- **Transmission properties**
  The effective structure of DOE's is quite thin compared with conventional lenses, since it makes use of a "surface" effect. Therefore, the optical element can be made considerably thinner than a lens of the same refractive power. This is an advantage for optics to be designed for the IR or the UV region, where in conventional optics a significant loss is due to bulk material absorption. An example for the achievable performance improvements is given in section 4.4.

- **High design flexibility**
  Due to the methods used for generation and transfer of the effective structure onto the substrate, the optics designer is not restricted to the use of rotationally symmetric surface shapes only [3.93]:
  CGOE production methods give the designer complete freedom in definition of surface shapes since the form can be generated to extremely high accuracies by computer controlled output devices. It is also possible to design combinations of several different functions/elements in one single CGOE substrate. A simple example is a lens array, more complex ones will be described in chapter 4.

- **High miniaturization potential**
  CGOE technology allows for extreme miniaturization of optical elements, thus opening applications areas which could not be covered by conventional optics technology: on-chip integration of optical elements with receivers or transmitters, highly compact spatial detector arrays are some examples, which are of high potential, in particular for aerospace applications.

- **Good technological heritage and compatibility**
  CGOE's are fabricated by making use of processes which are well characterized in semiconductor manufacturing. A sound technological

basis exists therefore which is indispensable for the efficient evolutionary development of optics specific manufacturing technologies. The materials used both for semiconductor and optics fabrication are to a large extent compatible, which enables efficient use to be made of existing installations and proven technologies. Examples of such production processes will be given in chapter 6.

3.3.3 DOE Classification

As shown above, the term "Diffractive Optical Element" describes a broad variety of elements for various applications, which can be quite different with respect to their physical type and their technological characteristics, as related to manufacturing methods, materials, etc.. An attempt shall be made therefore to establish a general classification for DOE's. This classification will group the **physical types** of DOE's on one side with certain **technological characteristics** on the other. Reference shall be made to the element types already mentioned in section 3.3.2 and their respective areas of application.

In this context, the term "physical type" shall signify the principal physical characteristics of the DOE resulting from the optical concept of the element as such. The "technological characteristics" cover the aspects of the transfer of the optical design data into the real DOE.

DOE Physical Types

The physical types can be derived from the complex amplitude transparency function (11) introduced in section 3.2. This function has two terms, an amplitude and a phase term. The DOE specific diffraction properties are caused by spatial variation of these terms across the element. Two basic physical types are therefore the amplitude and the phase DOE's.

For amplitude elements, the function T(x,y) of equation (12) represents the spatial variation of a material property, the transparency T. For phase elements (see eq. 13), the spatial phase function can be determined by two components, the spatial variation of structure thickness d(x,y) and the spatial variation of the refractive index n(x,y). The first component describes a macroscopic property, namely the structure depth d, the second describes again a variation of a material property, the refractive index n. Phase

elements can be generated therefore in two principle ways, namely by variation of optical material properties and by formation of a surface structure. This aspect will be taken up during the discussion of the technological classification criteria. Both element types can be designed as transmissive or reflective elements.

The structure of a DOE which is described by the complex amplitude transparency function (11), shall be called the "effective structure". This term encompasses both the surface structure of the phase elements, and the refractive index/transmission patterns, which are buried in the material of the phase and amplitude elements respectively.
The phenotype of the DOE effective structure is another classification criterion for the physical types: a structure can be characterized by its periodicity, its symmetry, its shape, and its amplitude. The term amplitude

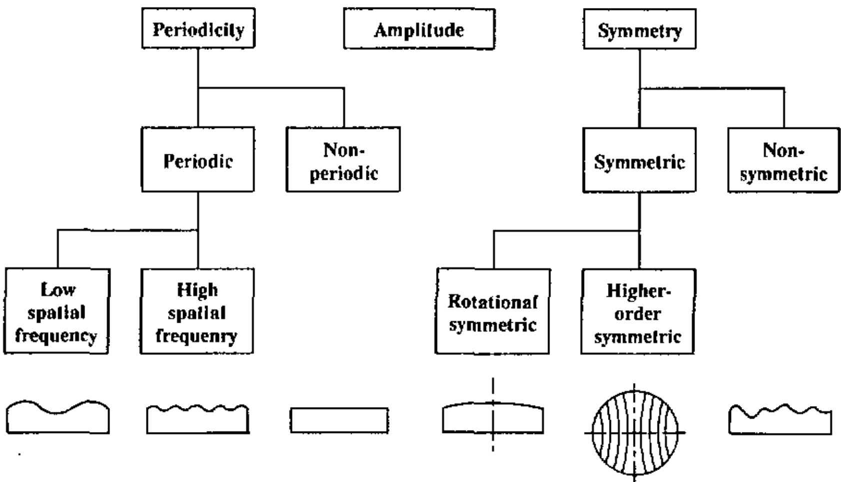

Fig. 3.3.3-1 DOE effective structure phenotypes

refers in this case to variations in terms of optical density or optical thickness n·d. Figure 3.3.3.-1 gives an illustration of existing phenotypes. The shapes of the structures discussed here can be in principle either analog or binary. The spatial variation of the above mentioned properties is not confined to a layer with infinitely small thickness but to real physical dimensions. This

leads to a third classification criterion which was already mentioned in section 3.2, namely the "thin" and the "thick" structure.

Summarising, the following **physical types** of DOE's have been identified:

- Amplitude/phase elements
- Transmissive/reflective elements
- Effective structure phenotypes
  - Periodic/non-periodic structure
  - Low/high spatial frequency structure
  - Symmetric/non-symmetric structure
  - Rotational/higher order symmetric
- Thin/thick elements

<u>DOE Technological Characteristics</u>

The technological characteristics are the second organizing principle for the classification. These characteristics can be broken down in the following aspects:

- Effective structure design
- Manufacturing technology
- Material technology

The first aspect deals with the methods used to transfer the DOE optical design into a real physical element. A large number of possibilities exist for an effective structure design and it must be decided with respect to the performance requirements, its application, and the production quantities involved, which design type is to be chosen.

The basic **effective structure design** types are:

- Analog/digitized structures
- Surface/buried structures
- Film/bulk substrate structures

Examples are shown in figure 3.3.3-2 a to c. These effective structure design types shall now be discussed in more detail:

Analog/digitized structures

An example for an analog structured DOE is a hologram recorded on a photoplate: the information is stored in form of interference fringes which show analog, namely sinusoidal, transparency characteristics.
If the hologram interference pattern is processed with a non-linear limiter function giving 0 or 1 output only, a digital structure can be created which has a rectangular shaped transparency function, transparent and non-transparent lines. Such digitized structures, in terms of amplitude as well as in phase, can be produced with different quantization levels by using appropriate limiter functions. The number of quantization levels determines the diffraction efficiency of the DOE (see section 3.3.4). A further possibility for structure design is coding of the DOE data prior to or during recording: the holographic recording technique is a simple example for a DOE with physically coded data: a wavefront is recorded on a photoplate in terms of

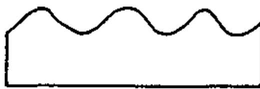

Analog structure a. Digitized structure

Buried structure b. Surface structure

Film substrate on carrier c. Bulk substrate

Fig. 3.3.3-2 DOE effective structure design types

phase and amplitude (object wave) by means of interference with another wave (reference wave) and can be reconstructed only by using the same reference. This type of physical coding can be performed in a large number of ways, depending on recording geometries, wavefront types etc., e.g. Fresnel holograms, Fourier transform holograms, image holograms and lensless Fourier transform holograms. For the generation of CGOE's mathematical coding methods are used. Examples are the methods of Brown and Lohmann [3.13], Lee [3.14], Buczek and Teijido [3.15], Burch [3.16]. Detailed descriptions are given in the referenced literature.

A phaseplate is an example for an uncoded DOE: the phase delay is directly represented by the element effective structure. However, it is often processed with a limiter function, to allow efficient coverage of phase multiples.

Surface/buried structures

As indicated when discussing the complex amplitude transparency function, there are in principle two ways of information storage, one makes use of material constant variation, the other uses a surface profile variation. This corresponds to the above mentioned classification criterion concerning surface and buried structures: a surface structure is any structure with a depth profile, a buried structure is a structure represented by optical material constant variations, e.g. refractive index profiles (see figure 3.3.3-2 b).

Film substrate/bulk substrate

An important aspect for effective structure design is the question whether the information can be stored in a thin film layer on top of a carrier plate (film substrate), or whether the information can be embedded into a self-supporting bulk substrate, as shown in figure 3.3.3-2 c. This question concerns the manufacturing processes to be used and is independent of the previously discussed criterion (surface/buried structure).
An example for a bulk substrate embedded effective structure design is an element fabricated by ion exchange in glass. An example for film substrate embedded information storage is a photoresist recorded phase DOE which is deposited on a glass plate carrier.

This leads to the next classification criterion which was mentioned above, the **manufacturing technology** used for DOE fabrication.
In the discussion of DOE special features (section 3.3.2), a typical DOE manufacturing process was outlined. It consists of two main steps, pattern generation and pattern recording including substrate processing. The following will concentrate on the last step.
The recording of DOE design data on the DOE substrate can be performed by direct writing or machining, mask processes, interferometric recording, or replication.
In direct writing the DOE pattern is written by an appropriate output device directly on the DOE substrate. For lower spatial frequencies the pattern can also be impregnated by a machining process.
In mask processes the pattern is recorded on a mask and the mask pattern is then transferred onto the final DOE substrate, via contact copying or projection for instance. Subsequent substrate processing transfers the pattern into the substrate. If this mask process is repeated several times, multilevel DOE's can be fabricated (see [3.86], [3.94], [3.95], [3.96], [3.97]).
For interferometric recording an object and reference wave are superposed on a photosensitive DOE substrate. The object wave usually carries the DOE pattern information which is imposed onto it by an auxiliary CGOE [3.18], as shown also in figure 3.3.2-1.

The fourth recording method, replication, consists of two major steps: the fabrication of a surface relief structure by one of the two initially mentioned methods (direct writing or mask processes), and the embossing of this relief into the DOE substrate by plastic deformation or a heat supported process [3.19].

Most of these recording methods require subsequent substrate processing to develop and preserve the effective structure in the substrate. The processing methods depend on the substrate type and shall be briefly outlined as follows:

- Photosensitive DOE substrates
  Photographic process, consisting for instance of
  - Exposure
  - Development
  - Fixation
  - Bleaching

- Non-photosensitive DOE substrates
  - Deposition of photosensitive layer
  - Direct recording or mask copying
  - Photographic processing of intermediate layer (see above)
  - Processing of substrate via openings in residual layer by:
    - Etching
    - Deposition
    - Epitaxy
    - Ion exchange
    - Ion implantation

The photographic methods used for processing of photosensitive DOE substrates depend strongly on the type of photosensitive material used. Biedermann has given a detailed overview of the materials and processes used for DOE recording [3.20]. Further examples are also given in the literature (e.g.[3.14], [3.21], [3.22]), therefore this type of processing will not be discussed here in any further detail.

The fabrication of DOE's on non-photosensitive substrates requires more complicated techniques making use of intermediate steps involving photo-sensitization, except for the method of direct machining.
Figure 3.3.3-3 shows the principal processing steps. A layer of photosensitive material is deposited on the carrier material and the DOE pattern is copied onto the photosensitive layer via exposure through a mask. The development of the photosensitive material leaves behind a template for the next processing step, namely the impregnation of the effective structure into the DOE substrate. The methods for impregnation are:

- Etching methods
  - Wet etching (isotropic, anisotropic) [3.27]
  - Dry etching (reactive ion beam etching, ion beam etching, ion milling, plasma etching) [3.17]
- Material deposition
  - Galvanic processes [3.19]
  - Epitaxy
  - High vacuum deposition (thermal evaporation, sputtering, etc) [3.28]
- Ion exchange ([3.29], [3.30], [3.89])
- Ion implantation

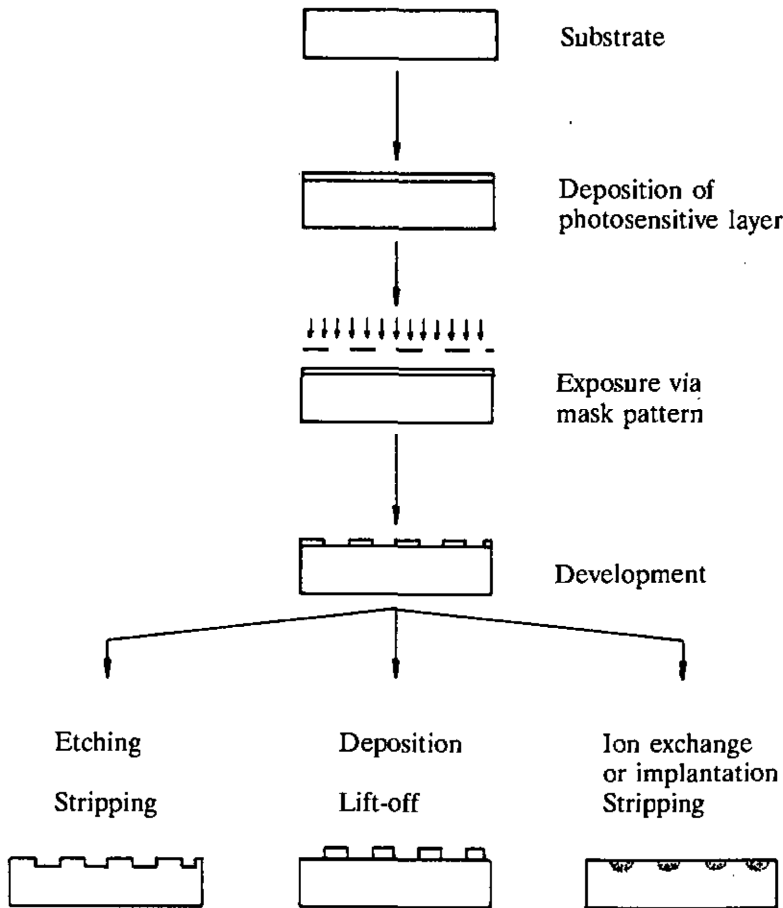

Fig. 3.3.3-3 DOE fabrication process for non-photosensitive substrates

After pattern impregnation the residual layer of photosensitive material is removed and the DOE effective structure remains on the carrier. If a DOE with multiple levels is produced, the surface is again coated with photosensitive material and the process is repeated as often as necessary to achieve the required number of quantization levels.
The process technology for DOE production on non-photosensitive substrates will be discussed in more detail in chapter 6.

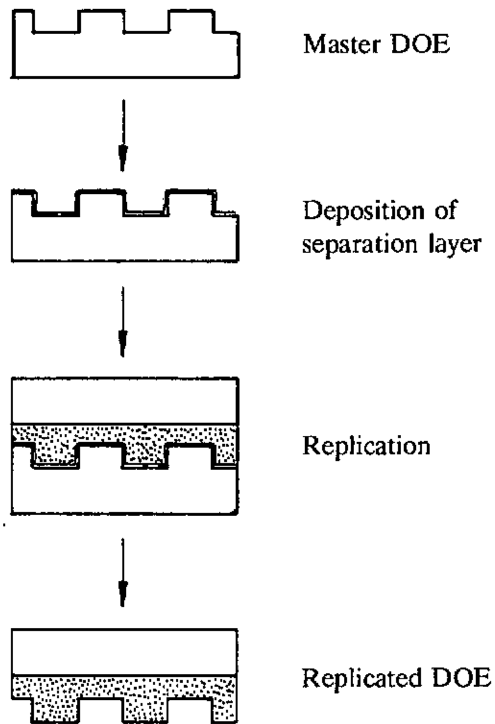

Fig. 3.3.3-4 DOE fabrication by replication

The replication method for DOE production is treated here separately, since it is a combined process. The first step results in a surface structure type master DOE (see above), the second makes use of this master for replication on a different substrate. Figure 3.3.3-4 illustrates this method.
Replication techniques are candidate technologies for high quantity DOE production. From various studies it seems possible to achieve high optical quality with replicated DOE's.

The third of the DOE technological characteristics concerns the **material technology** used. Again, the DOE substrate material can consist of photosensitive or non-photosensitive materials, both of organic or inorganic nature.

Table 3.3.3-1 gives an overview of the materials used for DOE's and provides corresponding literature references.

Table 3.3.3-2 summarizes the classification criteria identified, showing physical types on one side and technological characteristics on the other.

Table 3.3.3-3 correlates the identified physical DOE types with the possible technological characteristics and identifies examples of the sort of DOE's which are fabricated in the corresponding technologies. The "thick reflective amplitude" element, which is mentioned in the table refers to Lippmann's method for colour photography [3.98].The different phenotypes are not explicitly identified since DOE's, and in particular CGOE's, can be manufactured in any effective structural shape.

Material type	Sensitivity	
	Photosensitive	Non-Photosensitive
Organic	▪ Gelatin with silver halides ([3.14], [3.20], [3.26]) ▪ Dichromated gelatin (DCG) ([3.21], [3.31], [3.32], [3.33]) ▪ Methylene blue sensitized DCG ([3.24], [3.25]) ▪ Polyvinyl alcohol (PVA) [3.23] ▪ Polymethylmethacrylate (PMMA) [3.34] ▪ Photoresist ([3.34], [3.35], [3.40]) ▪ Photopolymer ([3.22], [3.36], [3.37], [3.38]) ▪ Thermoplastics[1]([3.19], [3.34], [3.35]) ▪ Photochromes[1]([3.19], [3.34], [3.35])	▪ Polymers [3.19,3.34,3.35]
Inorganic	▪ Photochromes[1]([3.19], [3.34], [3.35]) ▪ Electrooptical materials ([3.19], [3.34], [3.35]) - Lithium niobate - Lithium tantalate - KDP	▪ Optical Glasses [3.29,3.87,3.88] ▪ Dielectrics/Semiconductors [3.17,3.27,3.39, 3.41] - Fused silica - Zerodur - ULE - Titanium oxide - Magnesium oxide - Sapphire - Silicon - Germanium - Silicon nitride - Gallium arsenide - Diamond ▪ Metals [3.27] - Gold - Aluminium - Beryllium - Copper - Titanium

Table 3.3.3-1 DOE materials

[1] This material can also be used for erasable DOE's

Classifying Parameter	Category	Sub-Category
Physical Types	Amplitude	▪ Transmissive - Thin - Thick ▪ Various phenotypes
	Phase	▪ Transmissive ▪ Reflective - Thin - Thick ▪ Various phenotypes
Technological Characteristics	Effective Structure Design	▪ Analog ▪ Digitized ▪ Surface structure ▪ Buried structure ▪ Layer substrate ▪ Bulk substrate
	Manufacturing Technologies	▪ Pattern transfer - Direct writing - Mask processes - Interferometric recording - Replication ▪ Substrate processing - Photographic process - Etching - Deposition - Deformation - Ion exchange - Ion implantation - Epitaxy
	Material Technology	▪ Organic materials - Photosensitive materials - Non-photosensitive materials ▪ Inorganic materials - Photosensitive materials - Non-photosensitive materials

Table 3.3.3-2 DOE classification summary

Technological Characteristics	Physical types						
	Amplitude			Phase			
	Transmissive		Refl.	Transmissive		Reflective	
	Thin	Thick	Thick	Thin	Thick	Thin	Thick
Effective Structure Design							
Analog	x	x	x	x	x		
Digitized	x	x		x	x	x	x
Surface structure				x	x	x	x
Buried structure	x	x	x	x	x		
Film substrate	x	x	x	x	x	x	x
Bulk substrate				x	x		
Manufacturing Technologies *Pattern Transfer*							
Direct writing	x	x		x	x	x	x
Mask processes	x	x			x	x	x
Interference recording	x	x	x	x	x		
Replication						x	x
Substrate Processing							
Photographic process	x	x	x	x	x		
Etching				x	x		x
Deposition				x	x		x
Deformation				x	x		
Ion exchange				x	x		
Ion implantation				x	x		
Epitaxy							x
Material Technology *Organic Materials*							
Photosensitive	x	x	x	x	x		
Non-photosensitive				x	x	x	x
Inorganic Materials							
Photosensitive	x	x	x	x	x		
Non-photosensitive				x	x	x	x

Table 3.3.3-3 DOE types and technological characteristics

3.3.4 Diffraction Efficiency and Phase Quantization

The diffraction efficiency η of a DOE shall be defined as the ratio between the flux I_1 in Watt in the working diffractive order - usually the first order - and the total flux in the illuminating beam I_0 as measured directly behind the element (reflection losses are eliminated due to this approach):

$$\eta = \frac{I_1}{I_0} \tag{25}$$

It is calculated theoretically by integration of the complex amplitudes of the illuminating wave and the diffracted first order wave taking into account the complex amplitude transparency function of the DOE (for more details, see [3.35], [3.41], [3.42]). It is clear that the efficiency depends strongly on the physical type of the DOE and its effective structure design.
Table 3.3.4-1 shows examples for diffraction efficiencies of various physical DOE types and two types of effective structures, an analog and a binary structure with two levels.

	Max. efficiency (%)							
	Physical DOE types							
Effective structure design type	Phase				Amplitude			
	Thin		Thick		Thin		Thick	
Reflective (R) or transmissive (T)	R	T	R	T	R	T	R	T
Analog	33.9	33.9	100.0	100.0	6.5	6.5	7.2	3.7
Binary (2 level)	40.5	40.5	85.0	40.0	10.0			

Table 3.3.4-1 Examples for DOE diffraction efficiencies ([3.35], [3.41], [3.42])

As shown in the table, the highest efficiency figures are achieved with thick phase grating and analog effective structures. The continuous profile shapes of analog structures can be approximated also by binary structures with multilevel phase quantization, as shown in figure 3.3.4-1a to e. Figure (a) shows a plano convex lens, which served as a starting point for the quantization. The optical path length of the lens is treated with a limiter function f(z) (figure b), which is described by equation (26).

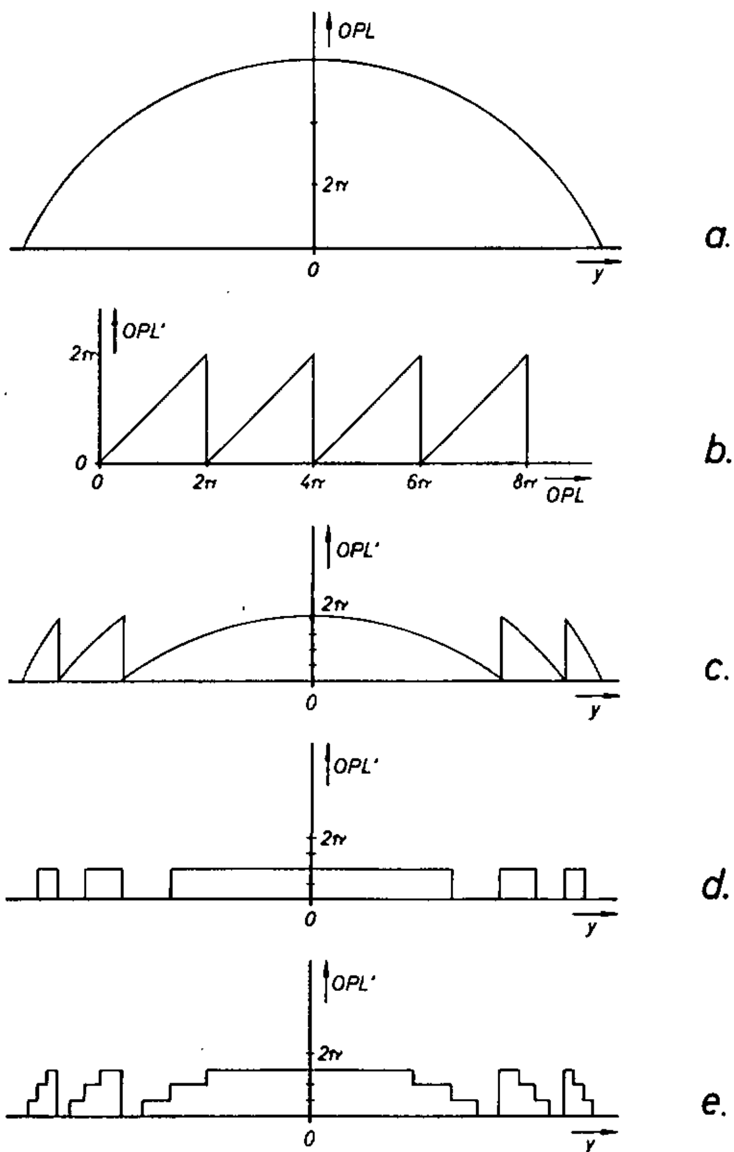

Fig. 3.3.4-1 Approximation of analog structures by multilevel phase quantization

$$f(z) = z \quad \textit{for } 0 \textit{ to } n \cdot 2\pi, \textit{ with } n = 1,\ldots,\infty \tag{26}$$

This results in a Fresnel lens type of DOE having an analog structure (figure 3.3.4-1c). This structure can be quantized and figure (d) shows the result of a two level quantization. Figure (e) shows a better approximation of the analog shape of (c) with four quantization levels.

The diffraction efficiency of a multilevel binary structure for the first order is given by (see [3.41]):

$$\eta = \left[\frac{N}{\pi} \cdot \sin\left(\frac{\pi}{N}\right)\right]^2 \tag{27}$$

with N being the number of quantization levels. The equation is based upon scalar approximation and is therefore valid only for Q'-factors smaller than 1 (see section 3.2).

A multilevel binary DOE is usually manufactured using binary masks, and the number of quantization levels N generated with m masks is

$$N = 2^m \tag{28}$$

Figure 3.3.4-2 shows theoretical efficiencies of binary phase elements as a function of the number of quantization levels.

The quantization error made due to the stepwise approximation induces a phase error in the diffracted wave, which limits the achievable optical performance in terms of wavefront accuracy. The quantization error of the phase is $\pm\pi/N$. The effective phase error induced due to that is, according to the definition of phase noise as used in electronics (see [3.43]):

$$\varphi_{neff} = \frac{2\pi}{\sqrt{12} \cdot N} \tag{29}$$

The resulting rms phase error is:

$$\varphi_{rms} = \frac{\pi}{\sqrt{3} \cdot N} \tag{30}$$

Figure 3.3.4-3 shows the rms phase error as a function of the number of DOE quantization levels. This means that an element with an rms wavefront

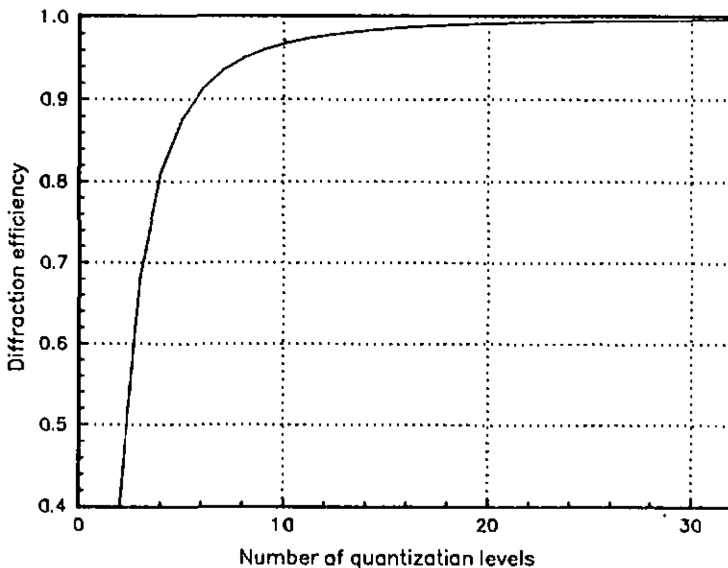

Fig. 3.3.4-2 Theoretical efficiencies of binary phase elements as a function of the number of quantization levels

error of $\lambda/50$ requires at least 14 quantization levels. Manufacturing errors are not included in these figures, they will be discussed in chapter 6.

3.3.5 Considerations on DOE Signal-to-Noise Ratio

The first diffracted order in DOE's is usually superimposed with a background signal which is due to higher order diffraction and straylight caused by edge scatter or surface defects. This unwanted light shall be considered as noise. Consequently, the signal-to-noise ratio (SNR) for DOE's shall be defined by the ratio of the intensity in the first - or any other - working diffractive order to the intensity of the background signal within the same solid angle.

These considerations have some importance for the design of optoelectronic devices such as tracking sensors, which make use of photoelectric detectors with spatial resolution (e.g. CCD array, 4-quadrant detector). A light spot with a certain diameter is located on the detector and its position is determined by centroiding algorithms.

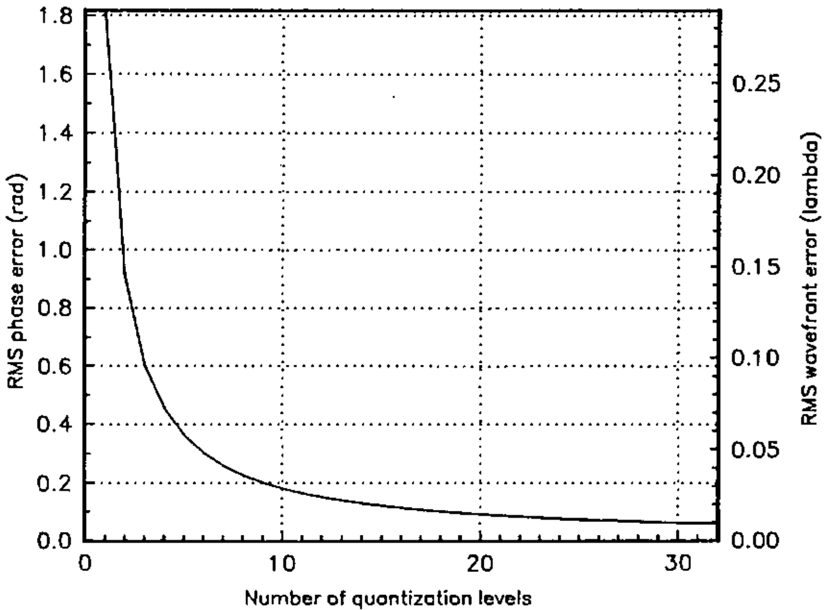

Fig. 3.3.4-3 DOE phase and wavefront errors vs. number of quantization levels

The accuracy achievable is limited, in addition to other factors, by the background light level on the surrounding pixels.

Since the SNR depends on various design/technology related factors, only some special cases shall be discussed which show quantitatively the achievable SNR performance of multilevel quantized DOE's.

Figure 3.3.5-1 shows a DOE which is illuminated by a collimated wave. The total flux incident on the DOE is I_0 [W]. The element is designed such that the light from the first diffracted order is focused at a distance f onto a detector with an area A. The flux incident at the focus shall be I_s [W]. The diffraction efficiency is, according to the definition in the previous chapter, $\eta = I_s/I_0$. The relation I_0-I_s = I_n represents the light flux due to the higher orders and from randomly scattered light.

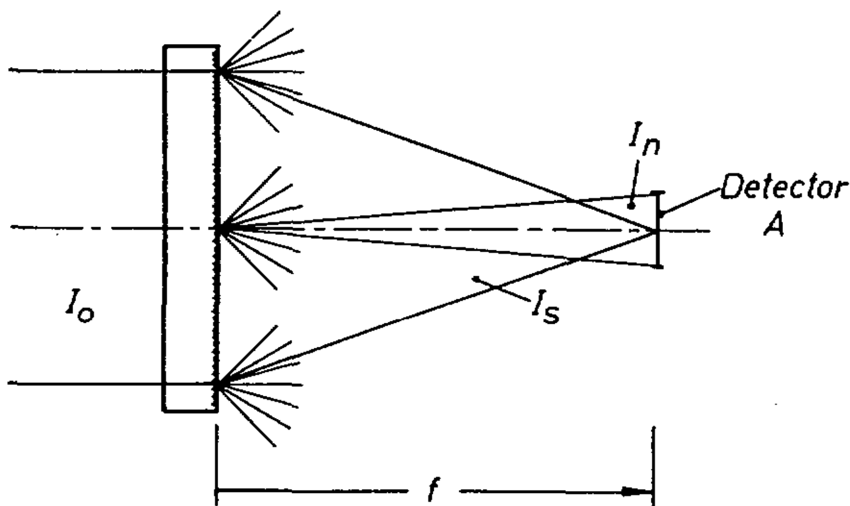

Fig. 3.3.5-1 Definition of DOE signal-to-noise ratio (SNR)

Three cases shall be now discussed:

1. I_n is concentrated on the detector area A.

2. The number of quantization levels approaches infinity, and I_n is negligible as compared to the noise caused by surface imperfections.

3. I_n has a uniform distribution within the hemisphere.

The first case is certainly the worst case in terms of signal to noise ratio:

$$\frac{S}{N} = 10 \cdot \log\left(\frac{I_s}{I_n}\right) \ [dB] \tag{31}$$

The second case sets a limit for the best achievable performance: if the number of quantization levels approaches infinity, the intensity in the higher orders becomes negligible compared to the scattered light due to polishing imperfections. A highly polished, coated optical surface can be assumed to have a total integrated scatter (TIS) of approximately $1 .. 5 \cdot 10^{-5}$ [3.44]. With the worse figure and assuming that the scattered light is uniformly distributed over the hemisphere, the SNR for a detector subtending a solid angle of 1 steradian is:

$$\frac{S}{N} = 10 \cdot \log\left(\frac{2\pi \cdot I_s}{I_n}\right) = 10 \cdot \log\left(\frac{2\pi \cdot 0.99995}{0.00005}\right) = 50.99\ [dB] \qquad (32)$$

The third case assumes also uniform noise signal distribution and gives an intermediate value between the above mentioned limits. The S/N ratio must again be understood per steradian detector area and is:

$$\frac{S}{N} = 10 \cdot \log\left(\frac{2\pi \cdot I_s}{I_n}\right)\ [dB] \qquad (33)$$

Figure 3.3.5-2 shows for different quantization levels the total flux in the first order versus the flux in the other orders and gives the corresponding SNR according to equation (33). If the DOE acts as a Lambertian scatterer, the effective solid angle for the flux received reduces to π instead of 2π, which diminishes the maximum achievable SNR to 47.98 dB.

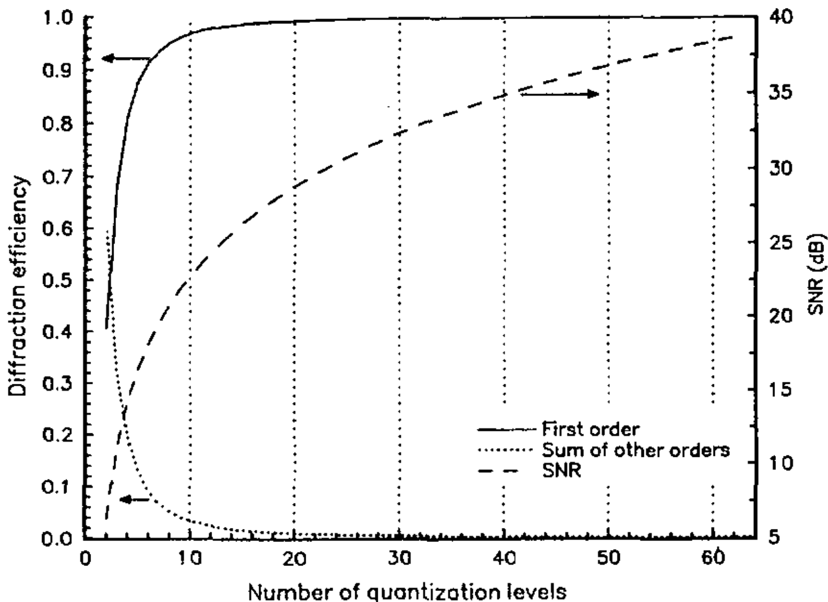

Fig. 3.3.5-2 Diffraction efficiency and SNR of multilevel binary DOE's

3.3.6 DOE Dispersion Properties

As already shown is section 3.2, the optical performance of refractive optics and DOE's have fundamentally different wavelength dependencies: for refractive optics it depends on the material dispersion which is in general not linear with wavelength, whereas the performance of a DOE is linearly dependent on the wavelength via the effective structure spatial frequency. Katyl published in 1972 three papers dealing with the compensation of hologram dispersion properties and the use of these elements with broadband light ([3.90], [3.91], [3.92]).

For obvious reasons it is desirable to have for DOE's a definition of their wavelength performance which is comparable to that of conventional optical components, i.e. a type of "effective material dispersion".

In 1977, Kleinhans and Sweatt have published independently an equivalent definition for DOE's ([3.45], [3.46]). Stone et al., Buralli et al. and other authors have used this definition later on for the design of holographic optical element-lens combinations (for details, see [3.47], [3.48], [3.49]).

Since the definition of DOE dispersion property plays a major role in the optics design approaches presented later, it shall be recalled here in more detail.

The dispersion of optical materials is usually defined by the Abbe number:

$$\nu_d = \frac{n_d - 1}{n_F - n_C} \tag{34}$$

with n_d, n_F, n_C being the refractive indices at the wavelengths λ_d, λ_F and λ_C. The refractive power F_{Ref} of a thin lens at wavelength λ is

$$F_{Ref}(\lambda) = \frac{1}{f_{Ref}(\lambda)} = (n_\lambda - 1) \cdot \frac{r_2 - r_1}{r_1 \cdot r_2} = (n_\lambda - 1) \cdot c_{Ref} \tag{35}$$

The wavelength dependence of the power is given by the first term, the basic power by the second, with r_1, r_2 being the radii of curvature of the lens surfaces.

For a DOE equation (35) can be expressed by

$$F_{Dif}(\lambda) = \frac{1}{f_{Dif}(\lambda)} = \lambda \cdot c'_{Dif} \cdot m = \lambda \cdot c_{Dif} \tag{36}$$

with m the spatial frequency of the DOE, which determines the power, and c_{Dif} a constant. Again, the first term describes the wavelength dependence, the second the power. In analogy to (35), equation (36) can be rewritten as

$$F_{Dif}(\lambda) = \frac{1}{f_{Dif}(\lambda)} = (n_{\lambda eff}-1) \cdot c_{Dif} \tag{37}$$

Since the refractive power of a DOE's is linearly wavelength dependent, it is

$$F_{Dif}(\lambda_1) = \frac{\lambda_1}{\lambda_0} \cdot F_{Dif}(\lambda_0) \tag{38}$$

Replacing λ_0, λ_1 by the wavelengths used for the definition of the Abbe number gives

$$F_{Dif}(\lambda_d) = (n_{deff}-1) \cdot c_{Dif} \tag{39}$$

$$F_{Dif}(\lambda_C) = (n_{Ceff}-1) \cdot c_{Dif} \tag{40}$$

$$F_{Dif}(\lambda_F) = (n_{Feff}-1) \cdot c_{Dif} \tag{41}$$

Now, with

$$F_{Dif}(\lambda_F) = \frac{\lambda_F}{\lambda_d} \cdot F_{Dif}(\lambda_d) \tag{42}$$

and

$$F_{Dif}(\lambda_C) = \frac{\lambda_C}{\lambda_d} \cdot F_{Dif}(\lambda_d) \tag{43}$$

and using (39) to (41) one can define an effective Abbe number for DOE's, which is equivalent to (34):

$$\nu_{deff} = \frac{n_{deff}-1}{n_{Feff}-n_{Ceff}} = \frac{\lambda_d}{\lambda_F-\lambda_C} = -3.453405 \tag{44}$$

Other effective Abbe numbers can be calculated accordingly. Table 3.3.6-1 shows the wavelengths used for the calculations, the mostly used Abbe numbers are given in table 3.3.6-2.

Wavelength [nm]	Spectral line
365.0146	i
404.6561	h
435.8343	g
479.9914	F'
486.1327	F
546.0740	e
587.5618	d
632.8	
643.8469	C'
656.2725	C
706.5188	r
852.1101	s
1013.98	t

Table 3.3.6-1 Spectral lines and their wavelengths

$\nu_{d\ eff}$	- 3.453405
$\nu_{e\ eff}$	- 3.332655

Table 3.3.6-2 Effective Abbe numbers of DOE's

With respect to their effective Abbe numbers, DOE's appear to perform like strong flint glasses, however with linear slope and the opposite sign.

The effective refractive index is defined as linear dependent of the corresponding wavelength and can be expressed as

$$n_{eff}(\lambda) = a \cdot \lambda \tag{45}$$

with a being a constant (>1), which is the same for all λ used for the effective Abbe number definition. In the ν_d/n_d diagram DOE's can be represented therefore by a line parallel to the n_d-axis at $\nu_{d\ eff.}$ = - 3.452405.
With the same formalism one can also define the effective relative partial dispersions $P_{x,y\ eff}$ and $P'_{x,y\ eff}$:

$$P_{x,yeff} = \frac{n_{xeff}-n_{yeff}}{n_{Feff}-n_{Ceff}} = \frac{\lambda_x-\lambda_y}{\lambda_F-\lambda_C} \tag{46}$$

$$P'_{x,yeff} = \frac{n_{xeff}-n_{yeff}}{n_{F'eff}-n_{C'eff}} = \frac{\lambda_x-\lambda_y}{\lambda_{F'}-\lambda_{C'}} \tag{47}$$

Table 3.3.6-3 shows numeric values for DOE effective relative partial dispersions.

$P_{x,yeff}$	Effective relative partial dispersion
$P_{h,g}$	0.1832504
$P_{e,d}$	0.2438453
$P_{d,C}$	0.4038484
$P_{i,h}$	0.2329937
$P'_{i,h}$	0.2419296
$P'_{h,g}$	0.1902786
$P'_{g,F'}$	0.2694880
$P'_{g,e}$	0.6727860
$P'_{F',c}$	0.4032980
$P'_{e,d}$	0.2531974
$P'_{e,C'}$	0.5967019
$P'_{C',r}$	0.3824827

$\lambda_{F'} - \lambda_{C'}$	- 163.8555
$\lambda_F - \lambda_C$	- 170.1398

Table 3.3.6-3 Effective relative partial dispersions of DOE's

3.3.7 DOE Modelling Methods

3.3.7.1 Overview

The previous sections gave an overview about the special optical properties of DOE's. It shall now be described how these properties can be mathematically represented in the optical design computations. The model used for those computations has to describe the physical properties of the optical element in a way that allows for calculation of various types of aberrations and their computer controlled minimization, or their balancing, within the optical system.

DOE's can be described for these purposes in three different approaches: as three-dimensional objects when taking into account the thickness of the effective structure, as two-dimensional thin objects, or with a special phenomenologically oriented model.

The treatment of the DOE as three-dimensional object provides a complete description of the interaction of the light wave with the element by diffraction theory. The complex amplitude transparency defined by eq. (11) is extended then for the three-dimensional case. Basic publications on methods for describing thick dielectric gratings were made by Kogelnik 1965 [3.50], 1967 [3.51] and 1969 [3.9]. He described the diffraction effects for two coupled waves and considered also the case of absorbing elements. Later, in 1970, Chang and George extended this theory to four waves [3.52]. In 1967 Saccocio published a diffraction model which was based on dynamic X-ray scattering theory and its application to holographic gratings [3.53]. A quite different approach was taken by Alferness 1975/76 ([3.54], [3.55], [3.56]): he adopted the method of finite elements ([3.57], [3.58]) for the solution of the diffraction problem in thick gratings. The thick grating is subdivided into a large number of thin gratings which can be described by a two-dimensional complex amplitude transparency function. One incoming wave is diffracted into n outgoing waves which represent the input to the following thin grating. The method provides results which are in excellent agreement with the rigorous diffracti on theory and other comparable theoretical models (see also [3.48], [3.59], [3.11]). Burkhardt published in 1966 a volume grating analysis by rigorous diffraction analysis for the case of a plane wave and a sinusoidal modulated dielectric medium [3.7]. Burckhardt's approach was extended by Kaspar 1973 [3.60] to cover also complex dielectric constants and non-sinusoidal modulation. The coupled wave analysis of Kogelnik and

its later extensions were refined to a general multiwave theory by Magnusson and Gaylord in 1977 [3.61]. It was demonstrated [3.11] that this theory gives valid results for all values of the thickness parameter Q' (see section 3.2).
In 1982 Stone and George published a paper describing the diffraction grating as a three-dimensional pattern of infinitesimal scattering particles [3.62], a representation of the silver halide crystals in photographic emulsions. Comparisons with other theories were published by the same authors in 1985 [3.48] and by Stone in 1986 [3.59]. This phased-scatterer-analysis was found to provide a good approximation of other, more comprehensive theories. It is in particular useful due to the physical insight it provides into volume scattering and diffraction processes. Further refinements were made later-on of the rigorous coupled-wave analysis by Moharam and Gaylord ([3.63], [3.64], [3.65]).
It can be stated that many of these theories lead to the same results, depending on the number of waves retained in the computation for a given Q' factor. Stone [3.59], Magnusson and Gaylord [3.66] and Alferness [3.67] provided some comparative analyses of different theories which prove their validity and equivalence in most of the cases.
The treatment of DOE's as three-dimensional objects provides following results:

- Diffraction efficiency for different orders of diffraction
- Image location as a function of diffraction order
- Image quality

The second modelling method initially mentioned, treats the DOE as a two-dimensional object, a thin grating. Its imaging properties are modeled by tracing rays and computing their diffraction at discrete local gratings, which represent the complex amplitude transparency function of the element. A first publication describing ray tracing through diffractive elements was made by Latta 1971 [3.68]. He extended this method to multiple hologram configurations and analyzed basic two- and three-element systems [3.69]. The raytracing algorithm was complemented by an optimization routine which allowed for minimization of various types of operands. Welford published in 1975 vector raytracing equations for DOE's of arbitrary shape [3.70]. These equations have been the basis for the development of advanced DOE design programs which can cope also with most complicated element configurations (e.g. [3.71], [3.18], [3.72]).

The representation of DOE's in two-dimensional models provides the following information:

- Image location as a function of diffractive order
- Image quality

It is common to all of the above described theoretical models, that solutions are found by solving - directly or indirectly - the Kirchhoff-Sommerfeld equation for a given complex amplitude transparency function representing the diffractive element.

A completely different approach was proposed by Sweatt 1977 ([3.45], [3.73]): the DOE model he proposed is at first sight phenomenologically oriented and describes the diffractive element as a lens with very special properties (very high refractive index, infinitely small thickness). The results obtained from this model converge for high indices very well to the results obtained by application of the rigorous diffraction theory. As with the two-dimensional model, it provides as a result the image location as a function of the diffractive order and a description of the image quality. Of course, like the two dimensional model, it does not allow for computation of diffraction efficiencies. However, the High Refractive Index (HRI) model has some attractive features concerning the representation of a DOE with standard lens design software. It shall be described therefore in more detail in the following paragraph.

In summary, one can identify the following methods for modelling DOE's and their optical properties:

- Three-dimensional DOE models
  - Rigorous diffraction theory
  - Coupled wave theory
    - Two-, four-, etc. wave model
    - General multiwave theory
  - Phased scatterer analysis
  - Thin grating decomposition model

- Two-dimensional DOE models
  - Grating diffraction

- High Refractive Index (HRI) model

3.3.7.2 The High Refractive Index Model

A diffractive element inserted into a light beam causes a deviation of the beam from the straight path due to its effective structure, as shown in section 3.2. The deviation caused by a grating is

$$\sin\alpha' - \sin\alpha = \frac{m \cdot \lambda}{b} \qquad m = 0, \pm 1, \pm 2, \ldots \tag{48}$$

with α being the ray incidence angle onto the grating, α' the angle of the diffracted ray, λ the wavelength, b the grating period and m the diffractive order, as shown in figure 3.3.7.2-1. For a given wavelength the deviation angle is only dependent on the grating period.

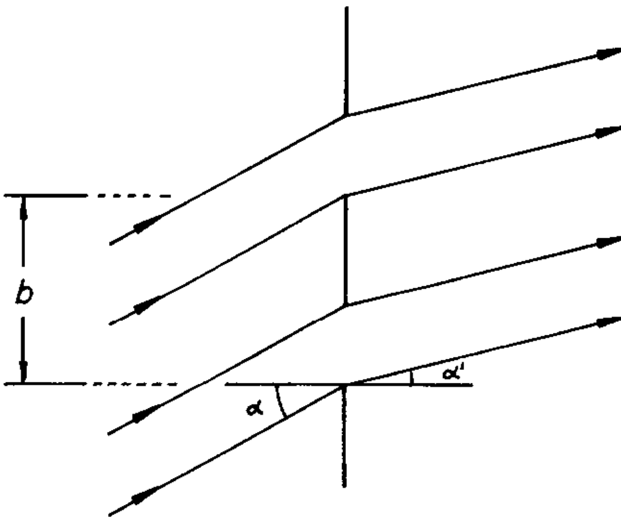

Fig. 3.3.7.2-1 Grating diffraction

This dependence can also be simulated by an infinitely thin optical component with very high refractive index. Figure 3.3.7.2-2 shows such a component. The angles α and α' represent the angles between the rays and the local normals onto a virtual plane inside the element, the angles δ and δ' are the local slope angles at the ray intersection points measured wrt. the virtual plane. The component is immersed in air and shall have a refractive

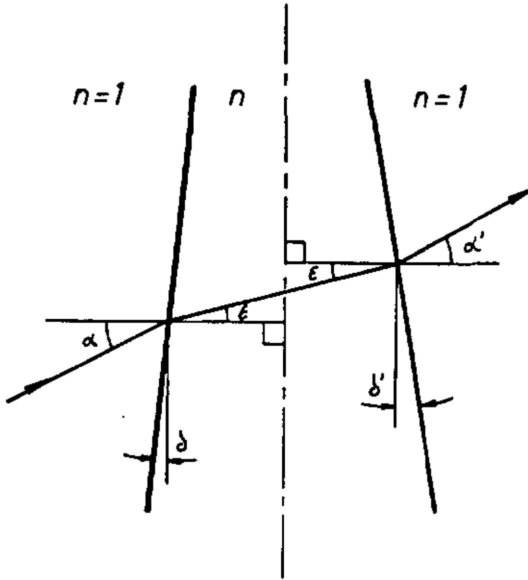

Fig. 3.3.7.2-2 Refractive component for explanation of the HRI model

index n. With these definitions, the refraction of the rays is then described by:

$$\sin(\alpha+\delta) = n\cdot\sin(\epsilon+\delta) \tag{49}$$

$$n\cdot\sin(\epsilon-\delta') = \sin(\alpha'-\delta') \tag{50}$$

Equation (49) shows that for large n the direction of the refracted ray inside the component is independent of the incidence angle, $\sin(\epsilon+\delta)$ approaches zero and the ray is therefore always refracted in the surface normal direction.

Due to the infinitely small element thickness t, the surface intersection points for incoming and outgoing rays coincide and no lateral displacement (as visible in the figure) exist.

Using the equations:

$$\sin(\alpha+\delta) = \sin\alpha\cdot\cos\delta + \cos\alpha\cdot\sin\delta \tag{51}$$

$$\sin(\alpha'-\delta') = \sin\alpha'\cdot\cos\delta' - \cos\alpha'\cdot\sin\delta' \tag{52}$$

and the following approximations for small angles δ, δ' and ϵ

$\delta \to 0$, therefore $\cos\delta \to 1$, $\sin\delta \to \delta$

$\delta' \to 0$, therefore $\cos\delta' \to 1$, $\sin\delta' \to \delta'$

$\epsilon+\delta$, $\epsilon-\delta' \to 0$, therefore $\sin\epsilon = \epsilon$

it follows:

$$n\cdot(\epsilon+\delta) = \sin\alpha + \delta\cdot\cos\alpha \tag{53}$$

$$n\cdot(\epsilon-\delta') = \sin\alpha' - \delta'\cdot\cos\alpha' \tag{54}$$

Solving (54) for ϵ and replacing ϵ by this expression in (53) leads to

$$\delta\cdot(n-\cos\alpha) + \delta'(n-\cos\alpha') = \sin\alpha - \sin\alpha' \tag{55}$$

For large values of n and small α and α' one can replace n-cosα and n-cosα' by n-1 and rewrite (55) as

$$\delta\cdot(n-1) + \delta'\cdot(n-1) = \sin\alpha - \sin\alpha' \tag{56}$$

$$(n-1)\cdot(\delta+\delta') = \sin\alpha - \sin\alpha' \tag{57}$$

$\delta + \delta'$ is the wedge angle of the component or also a local slope, which is for small angles

$$\delta+\delta' = \gamma = \frac{dt}{ds} \tag{58}$$

with dt being the local thickness and ds a local height. This leads to the following equation:

$$(n-1)\frac{dt}{ds} = \sin\alpha - \sin\alpha' \tag{59}$$

This expression is comparable to equation (48), taking into account that (sinα-sinα') is equivalent to (sinα'-sinα), since m can take positive and negative values. For large n it therefore becomes

$$(n-1)\frac{ds}{dt} = m\frac{\lambda}{s} \tag{60}$$

$$\frac{ds}{dt} = \frac{m \cdot \lambda}{s \cdot (n-1)} \tag{61}$$

The spatial frequency of the grating is represented in this formalism by the local slope of the element surface.

The dispersion properties of DOE's and the approach for their modelling which was shown in the previous sections can also be implemented in the HRI model. According to section 3.3.6, the effective Abbe numbers for DOE's can be calculated by

$$\nu_{xeff} = \frac{\lambda_x}{\lambda_F - \lambda_C} = \frac{n_{xeff} - 1}{n_{Feff} - n_{Ceff}} \tag{62}$$

High refractive indices are obtained by multiplying all wavelengths in equation (62) with the same large factor a

$$a \cdot \lambda_x = n_{xeff} - 1 \tag{63}$$

$$a \cdot \lambda_F = n_{Feff} \tag{64}$$

$$a \cdot \lambda_C = n_{Ceff} \tag{65}$$

with $a > 10^5$ for λ in μm to get sufficiently high indices. With this approach, the Abbe numbers remain unchanged and the dispersion properties of DOE's are implemented in the HRI model.

In terms of this model, a DOE is described primarily by its surface shape, which defines the local grating constant, and by its optical thickness or pathlength. The transformation of this information into a diffracting structure requires quantization of the optical pathlength for definition of the DOE fringe pattern. This will be described in more detail in chapter 4.

The High Refractive Index model was first published by Sweatt 1977/79 ([3.45], [3.73]) for modelization of holographic optical elements. He simulated in this way off-axis holographic elements and compared the results with computations based on rigorous diffraction theory. Only minor differences existed in the results for refractive indices around 100, for indices larger than 1000 no differences were found between both methods. However, it is clear that this model does not allow for predicting the efficiency of a particular DOE design.

Within this project the HRI model is used for the design of hybrid optics. It is in particular interesting for this application, since it makes use of the same design parameters like conventional optical components, namely radii, thicknesses, refractive indices, Abbe numbers. The DOE and the conventional components of the hybrid can be designed therefore using the same programme code. Thus, it is possible to benefit from the optimization routines of existing optical design software. Furthermore, both components can be optimized simultaneously without modification of the optimization routines.

3.3.7.3 DOE Models in Optical Design Programs

Within this study several optical design programs have been reviewed in order to investigate their potential for DOE and hybrid optics design. Three programs have been tested in more detail:

- ACCOS V (Version Nov.'89) by Scientific Calculations Inc, Fishers NY, USA
- SYNOPSYS (Version 6.7.1) by Optical Systems Design Inc, Medford MA, USA
- SUPER OSLO (Version 1.3) by Sinclair Optics Inc, Fairport NY, USA

All descriptions and observations presented in the following make reference to the above mentioned program versions unless stated otherwise. All three programs offer some standard DOE design features:

ACCOS V
In ACCOS V DOE's can be modeled as two-dimensional structures. Diffraction efficiencies cannot be calculated. The following object types can be defined:

- Circular, radial, linear gratings
- Fresnel surfaces
- Holographic gratings by superposition of two wavefronts, one of which can be aspheric and described by a 10th order polynomial in x,y

SYNOPSYS
The program can model DOE's as two- and as three-dimensional structures. For three-dimensional structures the efficiencies can be calculated based upon Kogelnik's method. The following objects can be defined:

- Two-dimensional
  - Linear gratings
  - Fresnel lenses

- Three-dimensional
  Holographic optical elements with aberration definition in form of a 5th order polynomial in x,y

SUPER OSLO
As a baseline, DOE's are handled in the program as two-dimensional structures. Hence, diffraction efficiency cannot be calculated. The standard object types are:

- Linear gratings
- Holographic optical elements, generated by two spherical waves

In addition, the program offers a "user definable surface". This surface is an interface which can be used for implementation of dedicated routines for DOE modelling, for instance.

All three programs were also tested with the HRI model, in order to identify their compatibility with the model and the efficiency of their optimization algorithms for this special case, which requires computations with very small and very large numbers. The following observations were made during these tests:

ACCOS V with HRI model
A macro command was used to generate the refractive indices from the set of design wavelengths: the wavelength set was multiplied by a predefinable large factor and the results were written into the index file for the particular element. The high refractive indices were definable without numeric problems and the corresponding Abbe numbers were correctly calculated. The optimization routines worked efficiently with a wide range of operand types and variables. The range of operands used comprised first order data and Seidel/fifth order aberrations, as well as all types of ray aberrations. The variables used were, besides the basic lens parameters, also aspheric deformation coefficients for rotationally symmetric surfaces and polynomial coefficients for non-rotationally symmetric polynomial surfaces. Some more details are reported in chapter 4.

SYNOPSYS with HRI model
The high indices were definable and the Abbe number was correctly calculated, however, the negative sign was not displayed: the sign of the Abbe value is obviously suppressed for display. The optimization routines were working in principal with a wide range of operands and variables, however, the program encountered numerical problems during optimization of higher order aspherics in connection with high indices and crashed quite often. It was also found, that lens data with refractive indices larger than 99 can only be stored in the working library and not in the general library.

SUPER OSLO with HRI model
The program allowed definition of high refractive indices and displayed the correct Abbe numbers. The optimization routines worked with any type of variable, however, the range of usable operands seemed to be quite restricted in connection with the high refractive indices: optimization runs with first order, Seidel and fifth order operands worked satisfactory, ray dependent operands caused the optimization to stop very soon in an unrecoverable status when total internal reflection was encountered.

Since ACCOS V offered the best performance for this particular application (HRI model), it was decided to use this programme for the other design studies to be performed within this research project.

3.4 Hybrid Optics

3.4.1 General

A hybrid optical element shall be defined as the combination of diffractive optical elements (DOE's) with conventional, reflective or refractive elements, in close contact, resulting in a single optical element. As such, hybrid optics can be considered as a special type of diffractive optics. The shape of the individual components forming the hybrid is the result of an overall correction approach taking into account the particular properties of the constituents (see section 3.3), with the aim to achieve optimum imaging performance. As it will be shown later, the design approach for hybrid optics is from this point of view absolutely equivalent to the design of conventional optics.

With respect to this definition, a grating monochromator for instance, consisting of collimator mirror, plane grating and camera mirror should not be considered as a hybrid optical system, since its elements serve well defined separated functions without interrelations in view of optical aberration correction. However, a grating monochromator with a curved surface grating in 4-f-configuration combining imaging performance with spectral dispersion in one element can be considered as a hybrid optical system.

Based upon the description of the special DOE properties presented in section 3.3, the approach for aberration correction of hybrid optics shall be explained in the following paragraphs on three basic types of optics, namely achromats, apochromats, and systems corrected for monochromatic aberrations only.

3.4.2 Chromatic Aberrations

The refractive index of optical materials is a function of the wavelength (see section 3.2). This causes in refractive optical elements a variation of the first order properties and the imaging aberrations with wavelength. The

wavelength dependent parts of the imaging aberrations are called chromatic aberrations. Optical elements which are corrected for chromatic aberrations are called in general "achromatic". Depending on the overall aberration correction status one distinguishes between different types of achromatic systems, and two of them, the achromat and the apochromat, shall be discussed in the following.

3.4.2.1 Hybrid Achromats

An achromat is an optical system which is achromatic for two wavelengths and at the same time optimally corrected for spherical aberrations for a third, medium wavelength [3.74, p.145]. In addition, achromats usually comply with the sine condition [3.75, p.167] and fulfil therefore the criterion for isoplanatism.

The chromatic effects which have to be corrected, are in most cases longitudinal (or axial) chromatic aberration and transversal (or lateral) chromatic aberration.
Longitudinal chromatic aberrations are manifest along the optical axis and are due to variation of focal length and magnification with wavelength. The chromatic variation of the spherical aberration is one type of longitudinal chromatic aberration (spherochromatism [3.76, p.75] or Gauss-Error [3.74, p.143]). Lateral chromatic aberrations are observed in the field, caused by chromatic aberrations of the chief ray [3.77, p.202ff].

Chromatic aberration correction means in case of an achromat that two wavelength rays of the same zone shall intersect the optical axis at the same point as a paraxial ray of a third, intermediate wavelength. If in addition paraxial rays of the same two outer wavelengths intersect the optical axis at the same point as the zonal rays, the system is called Gauss achromat [3.78, p.82]. To fulfil these conditions achromats consist always of at least two elements which are cemented or which are assembled with an air gap. As it will be shown later, the elements must not necessarily consist of different materials.

The principles of the hybrid optics achromatization approach shall be demonstrated in the following for the paraxial case, assuming thin lenses.

The conditions for correction of longitudinal chromatic aberrations are in this case [3.74, p.142]:

$$\frac{1}{f} = \frac{1}{f_1} + \eta_2 \frac{1}{f_2} \tag{66}$$

and

$$0 = \frac{1}{\nu_1 \cdot f_1} + \eta_2 \frac{1}{\nu_2 \cdot f_2} \tag{67}$$

with

$$\eta_2 = 1 - \frac{e_1}{f_1} \tag{68}$$

f is the overall focal length of the element, f_1, f_2 are the focal lengths of the components, ν_1, ν_2 the Abbe numbers and e_1 is the distance of the principal points of the components. Equation (66) defines the focus on axis to be the same for two wavelength, equation (67) is the condition for constant scale.

The combination of both conditions results in equations for the focal lengths of the individual elements

$$f_1 = +f \frac{\eta_2 \frac{\nu_1}{\nu_2} - 1}{\eta_2 \frac{\nu_1}{\nu_2}} \tag{69}$$

$$f_2 = -f \cdot \eta_2 \cdot (\eta_2 \frac{\nu_1}{\nu_2} - 1) \tag{70}$$

This means that the chromatic correction depends for thin lenses in the paraxial case only on the ratio of the Abbe numbers of the components and the distance of the principal planes.
The following two cases shall now be discussed: first, both elements consist of the same material, i.e. $\nu_1 = \nu_2$, and, second, the elements consist of different materials and are in close contact, either cemented or integrated on the same substrate, i.e. $e_1 = 0$.

$\nu_1 = \nu_2$

For this case equation (69) can be rewritten as

$$f_1 = +f\,\frac{\eta_2 - 1}{\eta_2} = +f\,\frac{e_1}{f_1 - e_1} \tag{71}$$

Equation (70) reduces to

$$f_2 = -\eta_2 \cdot f \cdot (\eta_2 - 1) = -f \cdot \left(\frac{e_1}{f_1} - \frac{e_1^2}{f_1^2}\right) \tag{72}$$

Substituting in (71) the expression for η_2 from (68), a quadratic equation results with the solutions

$$f_{1_{1/2}} = \frac{e_1}{2} \pm \sqrt{-\frac{e_1^2}{4} + f \cdot e_1} \tag{73}$$

Relevant solutions exist in general only for $e_1 \neq 0$, for positive focal lengths if $e_1/f \geq 4$ and for any value of e_1/f for negative overall focal lengths.

This means that it is possible to design an achromatic optical system using the same material for both elements, however, with the disadvantage of a large system length for a positive overall focal length. One example for such single-glass achromat is the Schupmann lens [3.76, p.90]. Another rather famous system of this type is the Huygens eyepiece [3.75, p.202ff]: it is corrected for transversal chromatic aberrations and complies with the scaling condition according to equation (67). Both conditions are fulfilled for $e_1 = (f_1 + f_2)/2$.

The individual elements of such a system can be also DOE's. Achromats of this type have been discussed in the literature in different configurations, mainly with holographically recorded elements ([3.69], [3.48], [3.79], [3.40], [3.80], [3.81]). However, these types of systems shall not be considered as hybrid optical systems, since only diffractive components are involved.

$e_1 = 0$

This case covers all systems with close contact components, e.g. cemented elements, integrated elements, and is considered as the typical configuration of a hybrid optical system. In this case equations (69) and (70) become

$$f_1 = +f\,\frac{\frac{\nu_1}{\nu_2}-1}{\frac{\nu_1}{\nu_2}} \tag{74}$$

and

$$f_2 = -f\cdot\left(\frac{\nu_1}{\nu_2}-1\right) \tag{75}$$

As shown already above, no solution exists in this case for $\nu_1 = \nu_2$. Figure 3.4.2.1.-1 shows the refractive power distribution $F = 1/f$ of the individual components for $f = 1$ as a function of ν_1/ν_2.

If one of the components is a DOE with the effective Abbe number given in section 3.3.2, and the other component a normal optical glass, the ratio ν_1/ν_2 becomes negative. With

$$-\left(\frac{\nu_1}{\nu_2}\right) = \nu' \tag{76}$$

$$-\left(\frac{\nu_2}{\nu_1}\right) = \frac{1}{\nu'} \tag{77}$$

equations (74) and (75) change to

$$f_1 = +f\cdot\left(1+\frac{1}{\nu'}\right) \tag{78}$$

$$f_2 = +f\cdot(1+\nu') \tag{79}$$

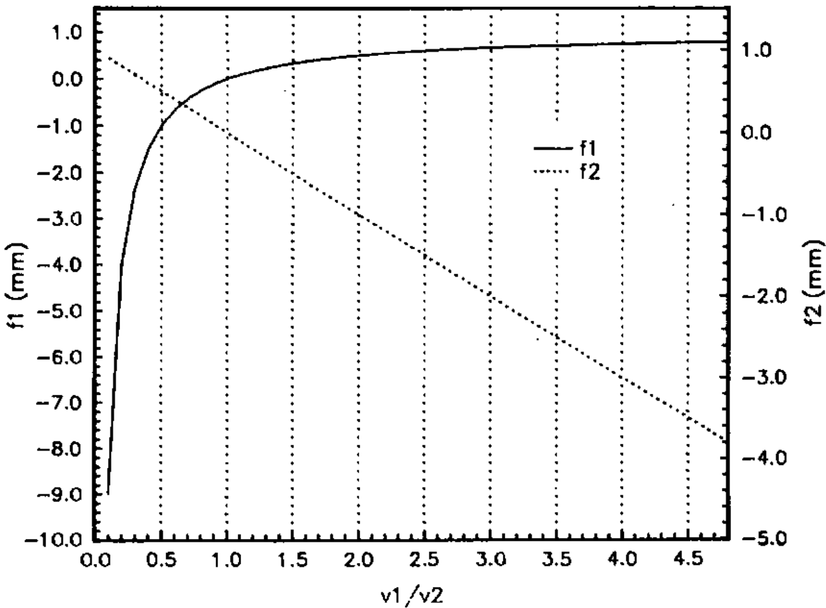

Fig. 3.4.2.1-1 Refractive power distribution in conventional achromats

For a hybrid achromat consisting of two elements of which one is a DOE and the other a normal optical glass, both components have a focal length with the same sign as the overall focal length. This means that both components have f-numbers lower than the resulting hybrid element, which is an advantage over conventional achromats in which one component has always a higher f-number than the resulting system.

Figure 3.4.2.1-2 shows the refractive power of the individual components in dependence of v_1/v_2 for $f = 1$.

The considerations presented above show by which simple means it is possible to achieve an achromatization of a hybrid optical system, making use of the definition of an effective Abbe number, as explained in section 3.3.2. However, hybrid achromats - as any other conventional achromats - suffer from secondary spectrum.

In the next paragraph an attempt shall be made to extend the formalism to the design of hybrid apochromats.

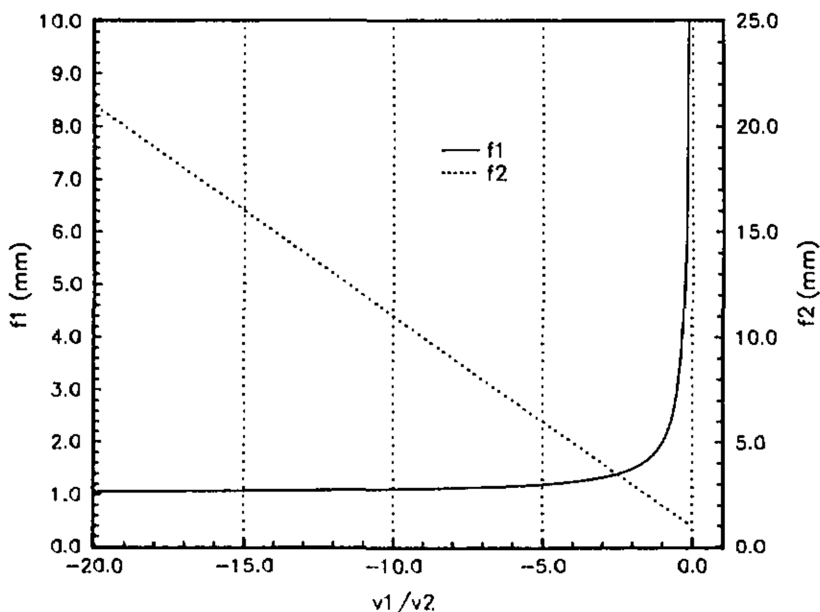

Fig. 3.4.2.1-2 Refractive power distribution in hybrid achromats

3.4.2.2 Hybrid Apochromats

An apochromat is a lens system which is achromatic for three wavelengths, i.e. the paraxial rays for three wavelengths intersect the optical axis at the same point. The sine condition shall be fulfilled for two wavelengths and it shall be isoplanatic for the same wavelength [3.82, p.248]. If, additionally, the spherical aberrations are fully corrected for two wavelengths - hence, the condition for aplanatism is fulfilled - the system is called Abbe-achromatic, according to Berek [3.78, p.82]. For apochromats, the secondary spectrum is strongly reduced compared to achromats.

Apochromats usually consist of more than two components, but using suitable glass types it is also possible to design apochromats with only two components. In terms of chromatic correction, such a two component apochromat has to comply with the conditions of equation (66) and (67), in

addition it has to fulfil the condition for achromatism for the third wavelength [3.75, p.170]:

$$\frac{P_{1x,y}}{\nu_1 \cdot f_1} + \eta_2^2 \frac{P_{2x,y}}{\nu_2 \cdot f_2} = 0 \tag{80}$$

$P_{1\,x,y}$ and $P_{2\,x,y}$ are the partial dispersions for the wavelength pairs x and y. From this equation and equation (67) follows, that the partial dispersions of both glasses used must be equal in order to achieve full paraxial correction for three colours.

In reality this can be only approximately fulfilled by few pairs of optical glasses involving types with anomalous partial dispersion (e.g. LaF, KzFS or KzF types). More details on glass selection for two component apochromats are published in ([3.75], [3.83], [3.84], [3.85]). However, the above mentioned conditions can certainly not be fulfilled by a two component hybrid (DOE and optical glass), consequently, it is not possible to design hybrid apochromats with two elements. An apochromatic hybrid must consist always of at least three components. It shall satisfy the following conditions:

$$\frac{1}{f} = \frac{1}{f_1} + \eta_2 \frac{1}{f_2} + \eta_3 \frac{1}{f_3} \tag{81}$$

$$0 = \frac{1}{\nu_1 \cdot f_1} + \eta_2^2 \frac{1}{\nu_2 \cdot f_2} + \eta_3^2 \frac{1}{\nu_3 \cdot f_3} \tag{82}$$

$$0 = \frac{P_{1x,y}}{\nu_1 \cdot f_1} + \eta_2^2 \frac{P_{2x,y}}{\nu_2 \cdot f_2} + \eta_3^2 \frac{P_{3x,y}}{\nu_3 \cdot f_3} \tag{83}$$

with

$$\eta_2 = 1 - \frac{e_1}{f_1} \tag{84}$$

$$\eta_3 = 1 - \frac{e_2}{f_2} \tag{85}$$

Solving these equations leads to following expressions which give the focal length of the individual elements (for simplification the P indices x,y have been omitted):

$$\frac{1}{f_1} = \frac{1}{f} \cdot \frac{\nu_1 \cdot (P_3 - P_2)}{A} \tag{86}$$

$$\frac{1}{f_2} = \frac{1}{f} \cdot \frac{\nu_2 \cdot (P_1 - P_3)}{\eta_2^2 \cdot A} \tag{87}$$

$$\frac{1}{f_3} = \frac{1}{f} \cdot \frac{\nu_3 \cdot (P_2 - P_1)}{\eta_3^2 \cdot A} \tag{88}$$

with

$$A = \nu_1 \cdot (P_3 - P_2) + \frac{1}{\eta_2} \nu_2 \cdot (P_1 - P_3) + \frac{1}{\eta_3} \nu_3 \cdot (P_2 - P_1) \tag{89}$$

Introducing the refractive power F = 1/f, the ratios of the individual element powers are:

$$\frac{F_2}{F_1} = \frac{\nu_2}{\nu_1} \cdot \frac{P_1 - P_3}{P_3 - P_2} \cdot \frac{1}{\eta_2^2} \tag{90}$$

$$\frac{F_3}{F_1} = \frac{\nu_3}{\nu_1} \cdot \frac{P_2 - P_1}{P_3 - P_2} \cdot \frac{1}{\eta_3^2} \tag{91}$$

If the apochromat consists of cemented elements, η_2 and η_3 are 1 (e_1 = 0). The above equations simplify accordingly.

Due to the number of different variables it is not possible to present parametric curves for the properties of the individual elements as it was done in case of the achromat. However, the following discussion shall give an idea about the refractive power distribution in apochromats consisting of two glass elements and one DOE. Table 3.4.2.2-1 shows the parameter ranges which are taken into account (see also section 3.3).

	DOE	Glass
Abbe number ν_d	-3.45	20 to 95
Partial Dispersion $P_{g,F}$	-0.29	0.52 to 0.64

Table 3.4.2.2-1 Parameter ranges for hybrid apochromats.

The refractive power ratios resulting from the above parameter ranges are shown below in table 3.4.2.2-2. No solution exists if elements 1 and 3 are DOE's.

Element			F_2/F_1	F_3/F_1
1	2	3		
DOE	Glass	Glass	negative, if $P_3 > P_2$ positive, if $P_3 < P_2$	negative, if $P_3 > P_2$ positive, if $P_3 < P_2$
Glass	DOE	Glass	negative, if $P_1 > P_3$ positive, if $P_1 < P_3$	negative
Glass	Glass	DOE	negative	negative, if $P_2 < P_1$ positive, if $P_2 > P_1$

Table 3.4.2.2-2 Refractive power ratios for hybrid apochromats.

3.4.3 Monochromatic Aberrations and Glass Selection

The monochromatic aberration of hybrid optical elements can be described in the HRI model with the same formalisms as used for any other conventional system, e.g. Seidel aberrations (third order), fifth order aberrations, ray aberrations.

The optical aberration theories shall not be discussed here in any detail, instead some results of the simulation of Seidel aberrations on thin hybrid achromats shall be presented: the achromats were designed with a selection of 19 different optical materials together with a DOE. They were corrected for an object at infinity, with the glass in front and the DOE on the image side. Only spherical surfaces were used and the wavelengths for the computations were 587.56 nm, 486.13 nm, 656.27 nm, 435.84 nm and 706.52 nm. In order to normalize the aberration coefficients, the focal length and f-number were set to 1 and the field angle to 45°. Third order lateral and

axial chromatic aberrations were eliminated, and the monochromatic aberrations have been analyzed. As an example, the results for the spherical aberration (SA3), Petzval sum (PTZ3) and coma (CMA3) as a function of the first element refractive index are shown in figure 3.4.3-1.

As expected from theory the spherical aberrations show a strong dependence on the refractive index and for the highest indices always remain slightly negative. Coma has also a strong refractive index dependence and changes its sign at about n = 1.55. The Petzval sum depends linearly on the first surface curvature.

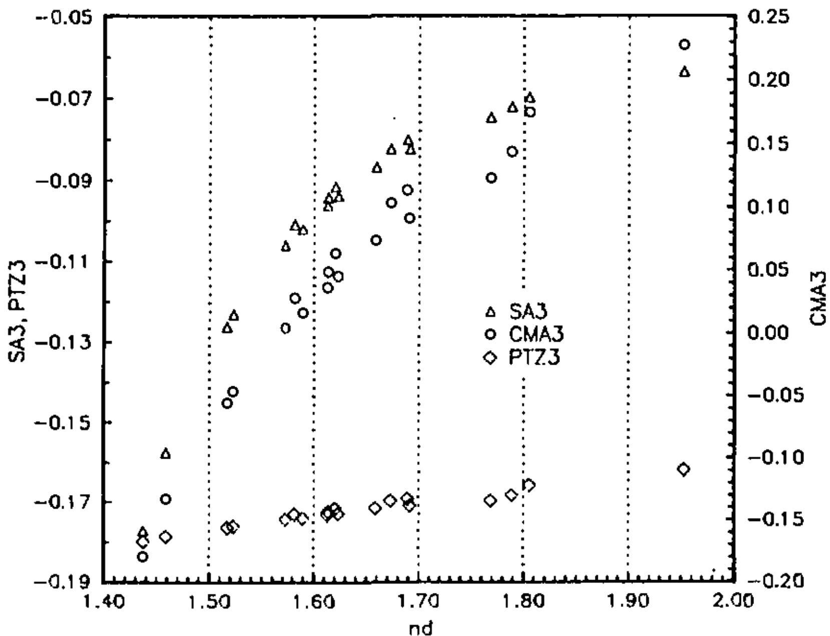

Fig. 3.4.3-1 Selected Seidel aberrations for thin hybrid achromats as a function of the glass refractive index

These results show that the monochromatic aberrations of hybrid achromats represented with the HRI model can be computed with the same aberration models as used for conventional optics, and that comparable results are obtained.

Chapter 4

DESIGN EXAMPLES FOR HYBRID OPTICAL ELEMENTS

4.1 General Design Approach

The design of hybrid optics as described here was performed in the following steps: a first thin lens predesign was be made based upon the considerations concerning chromatic correction discussed in section 3.4.2. This included the preliminary selection of glass types adequate for the desired chromatic correction and the calculation of the corresponding refractive powers of the DOE and the conventional lens.

This predesign was input to the ACCOS V lens design program making use of the High Refractive Index model as described in section 3.3.7.2. The refractive indices for the DOE were defined by multiplying the design wavelengths, expressed in μm, by 10^5. This resulted, for the visible wavelength range, in indices between 4500 and 8000, which is sufficient to get a good agreement with diffraction theory (see chapter 3.3.7.2).
Both components, the conventional lens and the DOE, were defined as infinitely thin plane plates, the lens refractive powers were specified as operands with target values resulting from the predesign calculations, and one surface radius of curvature was defined as variable. The correct surface radii of curvature, for the individual elements, were usually calculated within one optimization cycle. The resulting components were then put together to form a hybrid lens, with the desired focal length and fully corrected third-order chromatic aberrations.

In the next step the thickness of the refractive element was increased to a manufacturable value, keeping power and chromatic aberrations constant with both surface radii of curvature as variables. This was usually performed within few optimization cycles.

Having achieved a reasonable thickness the lens then represented a good starting point for correction of ray aberrations. For this purpose a set of operands was defined which consists basically of ray aberrations for several colours and the desired lens power. The radius of curvature of the refractive element and the radius of curvature and the aspheric coefficients of the DOE usually served as variables. With appropriate control of the

optimization by tuning weighting factors and adaptation of variable orders, optimum results were obtained after relatively few optimization cycles.

As a result, the diffractive component of the hybrid lens was represented by a thin film structure on one of the lens surfaces. This film defined the properties of the DOE via its refractive index n and the local thickness, given by centre thickness t_0 plus surface profile height t(x,y). To transform this element into a grating type structure, the optical path length was calculated at each point of the surface, which is

$$OPL(x,y) = n \cdot (t_0 + t(x,y)) \tag{92}$$

According to (13) the phase is calculated by

$$\varphi(x,y) = \frac{2\pi}{\lambda} OPL(x,y) \tag{93}$$

Subtraction of multiples of 2π phase values and connection of points with the same multiple values results in lines of equal optical thickness and leads to a Fresnel lens type structure as illustrated by figure 3.3.4-1c. A binary structure is then generated by quantization of the analog function in $N = 2^m$ levels.

As a result of this quantization a set of m masks for the manufacturing of the element can be generated. The quantization approach and the mask design is described in more detail in the following chapter.

4.2 Diffractive Structure Quantization

A computer program for quantization of rotationally symmetric phase profiles and mask data generation was developed within this project, in order to transform the DOE design data into a set of masks for production of the DOE component of the hybrid lens. For a better understanding of the program function the quantization approach is illustrated in figure 4.2-1a to d. Figure (a) shows the original OPL profile of the DOE. This profile was processed with a non-linear limiter function which subtracts multiples of 2π from the OPL (see also section 3.3.3). The y-values corresponding to multiples of 2π were computed by the program from f(x,y) by an iteration algorithm with adaptive step width, the accuracy of which can be predefined. These y-values define the basic ring pattern of the DOE.

In the next step the OPL profile within the basic ring pattern was quantized. In the example shown an 8-level quantization is performed with 3 masks. For quantization, the phase profile was divided into 8 ($=2^3$) equal OPL steps and the corresponding y-positions were calculated using a similar algorithm as used for the basic ring pattern computation. As before, the accuracy could be predefined. The program was also set up to detect the OPL slope direction.

The result of this operation was a table for the diffractive structure step coordinates.

A sorting algorithm transformed these data into mask specific ring coordinates. The resulting masks are shown in figure 4.2-1b to d. The specification of the rings could be adapted to the data format requirements of the output device. The input and output parameters of the program are shown in table 4.2-1. The masks shown here are designed for DOE fabrication by a material removal technique, etching for instance: the diffractive structure is etched into the substrate material, open areas in the mask pattern define the substrate areas which are etched during the corresponding processing steps. The geometrical depths d for the individual quantization steps depend on the material used for the fabrication of the DOE and are calculated according to

$$d = \frac{\lambda}{(n-1)} \tag{94}$$

with λ being the design wavelength and n the material refractive index. For the above mentioned example of a three mask design the following step depths result:

$$Mask\ 1{:}\ \ d_1 = 4\,\frac{\lambda}{8\cdot(n-1)} \tag{95}$$

$$Mask\ 2{:}\ \ d_2 = 2\,\frac{\lambda}{8\cdot(n-1)} \tag{96}$$

$$Mask\ 3{:}\ \ d_3 = 1\,\frac{\lambda}{8\cdot(n-1)} \tag{97}$$

Further details on the mask processing and associated technologies are given in section 6.2.

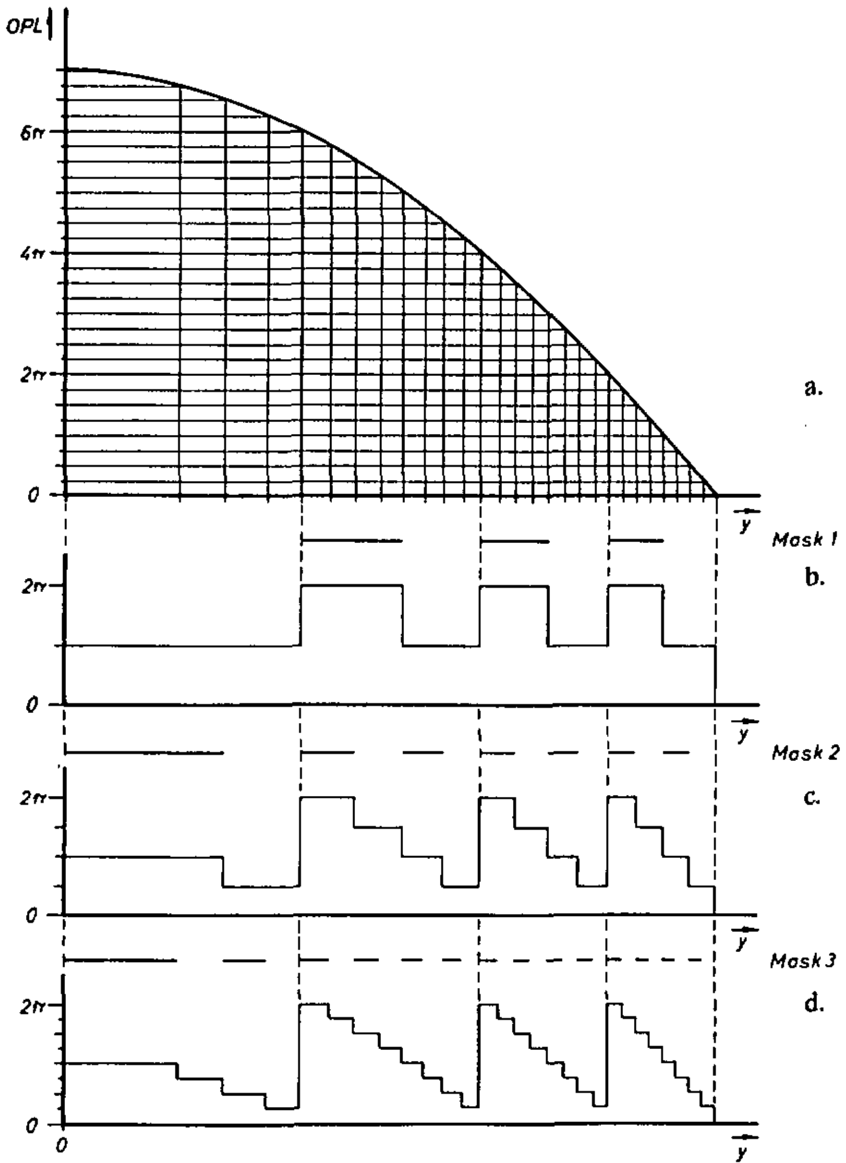

Fig. 4.2-1 Optical path length quantization with three masks

Data input	▪ DOE Definition - Radius of curvature - Conic constant - Aspheric deformation coefficients - Refractive index for DOE design - Design wavelength - DOE free diameter - Centre thickness ▪ Operational Parameters - Number of masks - Phase multiplier - Elementary sampling increment - Accuracy
Data output	▪ Option 1 - Step coordinates - Optical path length data per step ▪ Option 2 - Maximum/minimum OPL - Mask data per mask · Maximum/minimum spatial frequency · Minimum structure size · Ring definition in width and centre pitch ▪ Option 3 - As option 2, but with ring definition in terms of edge position and width ▪ Option 4 - Definition of phase profile

Table 4.2-1 DOE quantization program, data input and output

4.3 Tolerancing Considerations

For transfer of the optical design data into real hardware manufacturing tolerances have to be defined, which represent the acceptable manufacturing errors. For the case of hybrid optics one has to consider manufacturing errors for both types of elements, the diffractive element and the lens element:

- Lens element errors
  - Form
  - Dimensions
  - Centering
  - Striae
  - Birefringence
  - Surface/bulk defects

- Diffractive element errors
  - Step depth
  - Step width
  - Mask alignment
  - Surface/bulk defects

Figure 4.3-1 illustrates different error types on a hybrid singlet as an example. The error definition, in principle, follows DIN 3140 [4.1], however DOE specific errors are quoted differently. Step width/step depth should be included in the DOE specification, whereas the alignment of the effective structure is specified on the drawing. For specification of the DOE centering reference shall be made to section 6.2.3.

Form, dimension, centering and mask alignment tolerances can be determined by simulation with the optical design program, used for the hybrid design process. The influence of each error type on the overall performance can be determined and an acceptable value can be derived from the results. An example for this approach will be given later in section 4.4.2.

The effects of errors in step width and depth cannot be simulated in the same way, because the high refractive index model used for the design does not support simulation of diffraction efficiency. Another model was therefore used for these error types.

Fig. 4.3-1 Example for the definition of manufacturing error types for a hybrid singlet

Hasman [3.41] simulated depth errors on the quantization steps by

$$\eta_1 = \left| \frac{1}{2\pi} \cdot \left(e^{-i\frac{2\pi}{N}} - 1 \right) \cdot \left[\frac{1 - e^{(-i \cdot 2\pi \cdot \delta_d)}}{1 - e^{(-i \frac{2\pi}{N} \delta_d)}} \right] \right|^2 \qquad (98)$$

where η_1 is the diffraction efficiency in the first order, N the number of quantization levels and δ_d the depth error. Figure 4.3-2 shows the results of

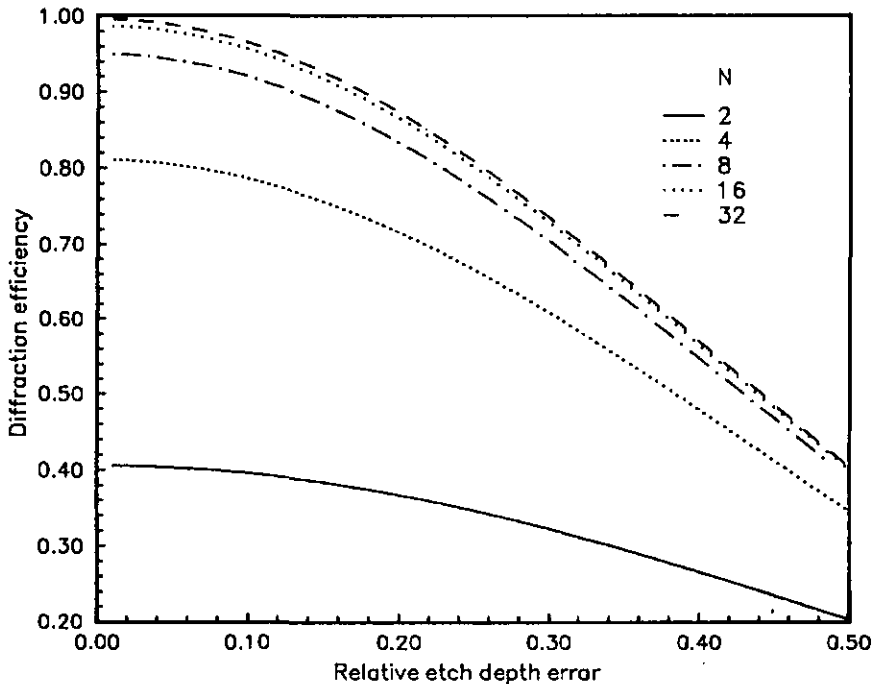

Fig. 4.3-2 DOE diffraction efficiency and quantization errors

the calculation. According to that, depth errors of up to 5% for an eight level process results in an efficiency loss of circa 0.7%, which is tolerable in general.

However, the calculation assumes equal errors for all masks, which is not very likely. A simulation was made therefore with another existing program [4.2] allocating certain mask specific errors. Designs of up to 8 quantization levels were simulated. The results are given in table 4.3-1. The efficiency losses calculated are generally lower for unequal distributions assuming maximum percentage as for equal distributions. It is clear that a 10% error at the first mask has a much larger effect than a 10% error at the third mask, due to the absolute etch depths allocated to the masks.
These results show that errors of up to 15% on one of the masks and 10% on others have effects on the overall diffraction efficiency which are tolerable for most of the applications.

The other error type mentioned above is an error in lateral mask dimensions, respectively an alignment error between individual masks, leading to a variation in grating width. Hasman [3.41] and Farn [4.3] published simulation results on this error. The effects of this error type depend on the f-number of the DOE which defines the minimum feature size. For an f/1 element fabricated with a 3 mask process (eight levels) an 0.2 μm misalignment leads to an effective loss of 0.5%, an f/3 element of the same type exhibits a loss of circa 2%. This error type is therefore considered to be the most critical.

	Phase errors [%] per mask			Efficiency [%]
Three Masks	Mask 1	Mask 2	Mask 3	
Ideal	0	0	0	94.96
One error	±10	0	0	92.64
	0	±10	0	94.38
	0	0	±10	94.82
Two errors	±10	±10	0	92.07
	±10	0	±10	92.50
	0	±10	±10	94.23
Three errors	±10	±10	±10	91.93
	±5	±5	±5	94.20
	±15	±15	±15	88.24
Two Masks	Mask 1	Mask 2		
Ideal	0	0		81.06
One error	±10	±10		79.07
	0	0		80.56
Two errors	±10	±10		78.59
One Mask	Mask 1			
Ideal	0			40.53
One Error	±10			39.54

Table 4.3-1 Tolerancing with mask dependent errors

4.4 Design Examples

4.4.1 General

In the following some examples for hybrid optical elements are presented, which were designed with the ACCOS V design programs using the High Refractive Index Model. The first example is an achromat for the visible range, f-number 1:1.8, which is diffraction limited. This element was later-on manufactured and characterized in terms of optical performance. The second example is a diffraction limited achromat for medium infrared with an f-number of 1:1.4 using silicon.

The next two examples shall demonstrate the potential that hybrid optics offers for advanced sensor design, namely an advanced matrix detector with hybrid microlens array and an integrated tracking sensor/receiver combination making use of hybrid optics.

4.4.2 Hybrid Achromat 1:1.8

A hybrid achromat shall serve as a first design example. The design goals for the element were:

F-number	1:1.8
Focal length	20.7 mm
Wavelength range	ca. 550 nm to 650 nm
Field angle	0.2°
Wavefront error	better than $\lambda/10$ p-v (λ = 633 nm)

It was planned to manufacture this element as a sample and to verify its optical performance experimentally. To facilitate the manufacturing process it was decided to restrict the design solutions to the case of plano-convex elements. This implied a compromise on the correctable aberrations, the sine condition cannot be fulfilled.

Based upon the basic consideration on correction potential and glass selection (see section 3.4), the glass LaFN21 from Schott was selected for the design. This glass combines a high refractive index with favourable manufacturing properties and is also available in a radiation stabilized version, which was one of the preconditions for space applications.

In a first step a starting system was created based upon the consideration on achromatization presented in chapter 3. The design wavelengths used are shown in table 4.4.2-1.

	λ_1	λ_2	λ_3	λ_4	λ_5
Wavelength [nm]	632.81	587.5718	643.8569	546.0740	656.2825

Table 4.4.2-1 Design wavelengths for hybrid achromat for the visible

The Abbe numbers for these wavelengths are:

LaFN21: ν_1 = (1.78484 - 1) / (1.788309 - 1.784097) = 186.334283

DOE: $\nu_{2\,\mathrm{eff.}}$ = 63280 / (58757.18 - 64385.69) = - 11.24276229

For the calculation of the DOE effective Abbe number the dispersion was calculated by multiplication of the wavelength set in nm by 10^2. The numerator is reduced by 1, however, due to the large number this results in an error of < 0.01%, which is not relevant for the calculations.

The focal lengths for the individual elements result from the paraxial chromatic correction conditions for close contact elements derived in section 3.4.2.1 (equations (74) and (75)). For a focal length of f=20.7 mm and the above given Abbe numbers the individual focal lengths were calculated to be:

$$f_1 = +f\,\frac{\dfrac{\nu_1}{\nu_{2eff.}}-1}{\dfrac{\nu_1}{\nu_{2eff.}}} = +21.9489\,mm \tag{99}$$

$$f_2 = -f\cdot\left(\frac{\nu_1}{\nu_{2eff.}}-1\right) = +363.7758\,mm \tag{100}$$

These values were taken as targets to create the corresponding thin elements, namely a plano-convex lens and a DOE, with the optical design program. Table 4.4.2-2 shows the thin lens data and the corresponding third-order aberrations. As a result of the refractive power apportionment the third-order longitudinal and lateral chromatic aberrations are both zero.

```
THIN HYBRID ACHROMAT

BASIC LENS DATA

SURF         RD                TH           MEDIUM               RN        DF
  0      0.00000000  8.52364294E+19     AIR

  1      0.00000000      0.00000000     AIR

  2     17.22636524      0.00000000     SCHOTT LAF21     1.784840    0.069
  3      0.00000000      0.00010000     DOE             **********  -9.446
  4 -2.30197319E+07     20.69994119     AIR

  5      0.00000000      0.00000000     AIR


REFRACTIVE INDICES

SURF       N1          N2          N3          N4          N5        ABBE
  2    1.784840    1.788309    1.784097    1.792269    1.783304  186.334255
  3 ****************************************************************** -11.242762

SOLVES

SURF    TYPE    PARAMETER       VALUE        SLV DATUM
  4      PY        TH        20.699941       0.000000

 REF OBJ HT                          REF AP HT   OBJ SURF   REF SURF   IMG SURF
-0.507068E+18 (    0.3408 DG)        5.75000        0          1          5

      EFL          BF        F/NBR        LENGTH         GIH
    20.6999      20.6999      1.80        0.0001        0.1231

WAVL NBR           1          2          3          4          5
WAVELENGTH      0.63280    0.58756    0.64385    0.54607    0.65627
SPECTRAL WT      1.0000     1.0000     1.0000     1.0000     1.0000


>MAB3 ALL

MONOCHROMATIC ABERRATIONS AT WAVL 1

SURF          SA3          CMA3          AST3          DIS3          PTZ3
  1        0.000000      0.000000      0.000000      0.000000      0.000000

  2       -0.052683     -0.002817     -0.000017     -0.000001     -0.000030
  3        0.032451     -0.002211      0.000017      0.000000      0.000000
  4       -0.123244      0.007918     -0.000057      0.000001      0.000000

TOTALS    -0.258255      0.005203     -0.000102      0.000000     -0.000054

>FCHY ALL

1ST ORDER CH ABS IN YZ PLANE

SURF          PAC           PLC           SAC           SLC
  1        0.000000      0.000000      0.000000      0.000000

  2       -0.004529     -0.000081     -0.003731     -0.000066
  3       -0.137536      0.003123     -0.110613      0.002512
  4        0.142065     -0.003042      0.114182     -0.002445

TOTALS     0.000000      0.000000     -0.000584      0.000000
```

Table 4.4.2-2 Thin lens model for hybrid achromat (Third-order aberrations: MAB3 monochromatic aberrations, PAC axial or longitudinal chromatic aberrations, PLC lateral chromatic aberrations)

In a next step the lens thickness was increased slowly to a value reasonable for manufacturing purposes, keeping the paraxial aberrations to zero.

For the final optimization a set of ray aberrations (monochromatic and chromatic) was defined, which had to be minimized. The variables used for the optimization were: two radii of curvature, the thickness (within limits) and a set of coefficients for definition of a rotational symmetric asphere on the DOE surface. This asphere, which has the optical axis (z-axis) as their axis of revolution is defined by:

$$z = \frac{\frac{1}{r}\cdot p^2}{1+\sqrt{1-(cc+1)\cdot\frac{1}{r}\cdot p^2}} + d\cdot p^4 + e\cdot p^6 + f\cdot p^8 + g\cdot p^{10} \qquad (101)$$

$$with \quad p^2 = x^2 + y^2$$

The coefficients describing the asphere are the conic constant cc and the higher order deformation coefficients d, e, f and g, r is the radius of the vertex curvature. The focal length of the element was kept as a constraint with a lower weight assigned to it. For the optimization run, diverging results were accepted for a limited number of iterations.

The final result of the optimization is shown in table 4.4.2-3. The optical performance of the lens provides sufficient margins for tooling and manufacturing tolerances (see aberration data).

To be able to make use for the DOE manufacturing as far as possible of existing tools, it was decided to split the hybrid element into a plane plate with the DOE and a plano-convex lens and to assemble the components by cementing. With reference to the design guidelines for space optics outlined in chapter 5, it is clear that this method is not acceptable for space hardware. However, it is adequate for purposes of this research project.

With the actual melt data of the glass, the indices of the optical cement selected for assembly (Norland NOA 61) and the radius of the test glass used for the lens manufacturing, the lens design was fine tuned by adaptation of the material thicknesses.

The manufacturing data file for the lens is shown in table 4.4.2-4, the final optical performance data are presented in figure 4.4.2-1.

```
ACHROMATIC HYBRID F=20.7MM, 1/1.8

BASIC LENS DATA

SURF        RD                 TH          MEDIUM              RN          DF
  0      0.00000000   8.52364294E+19      AIR

  1      0.00000000       0.00000000      AIR

  2     17.67679741       4.00000000      SCHOTT LAF21     1.784840    0.069
  3      0.00000000       0.00010000      DOE           ***********   -9.446
  4 -1.45922338E+07      18.64209479      AIR

  5      0.00000000       0.00000000      AIR


REFRACTIVE INDICES

SURF        N1          N2          N3          N4          N5        ABBE
  2    1.784840    1.788309    1.784097    1.792269    1.783304  186.334255
  3 *********************************************************** -11.242762

CC AND ASPHERIC DATA

SURF      CC            AD            AE            AF            AG
  4  -1.30441E+12  3.12124E-10 -3.70935E-13  3.07313E-16 -2.09011E-18


 REF OBJ HT                        REF AP HT  OBJ SURF  REF SURF  IMG SURF
-0.507068E+18 (   0.3408 DG)      5.75000       0          1         5

      EFL          BF        F/NBR        LENGTH        GIH
    20.7020     18.6421      1.80        4.0001       0.1232

WAVL NBR            1           2           3           4           5
WAVELENGTH      0.63280     0.58756     0.64385     0.54607     0.65627

>SPHAB

YFAN  -  WAVELENGTH 1

   FRC        LAY         LAX          OPD          WAVES        OSC
  0.000     0.000000    0.000000    0.0000000 (   0.000)    0.0000000
  0.100     0.000001    0.000001    0.0000000 (   0.000)    0.0001714
  0.200     0.000003    0.000003    0.0000000 (   0.000)    0.0006844
  0.300     0.000004    0.000004    0.0000000 (   0.000)    0.0015358
  0.400     0.000002    0.000002    0.0000000 (   0.000)    0.0027202
  0.500     0.000000    0.000000    0.0000000 (   0.000)    0.0042300
  0.600    -0.000001   -0.000001    0.0000000 (   0.000)    0.0060554
  0.700    -0.000004   -0.000004    0.0000000 (   0.000)    0.0081840
  0.800    -0.000001   -0.000001    0.0000000 (   0.000)    0.0106013
  0.900     0.000004    0.000004    0.0000000 (   0.000)    0.0132900
  1.000     0.000000    0.000000    0.0000000 (   0.000)    0.0162299

>COL
CHROM AXIAL COL: 1,2,3,4,5
   0.000    0.000    0.000    0.02732    0.02732
   0.000    0.000    0.000   -0.00910   -0.00910
   0.000    0.000    0.000    0.03431    0.03431
   0.000    0.000    0.000   -0.02029   -0.02029
CHROM LATERAL COL: 1,2,3,4,5
    0.123155
    0.000053
   -0.000014
    0.000096
   -0.000029
```

Table 4.4.2-3 Lens data of optimized hybrid achromat for the visible (SPHAB spherical/wavefront aberrations for 632.8 nm, COL chromatic aberrations)

```
ACHROMATIC NYBRID F=20.7 MM, 1:1.8
(MANUFACTURING DATA WITN MELT INDICES)

BASIC LENS DATA

SURF         RD               TH           MEDIUM                RN         DF
  0      0.00000000   8.52364294E+19    AIR

  1      0.00000000       0.00000000    AIR

  2     17.67800000       1.98700000    MELT   LAF21     1.784966    0.069
  3      0.00000000       0.01000000    NOA61              1.559820    0.749
  4      0.00000000       2.00000000    MELT   LAF21     1.784966    0.069
  5      0.00000000       0.00010000    DOE              ***********  -9.446
  6 -1.45922338E+07      18.64119438    AIR

  7      0.00000000       0.00000000    AIR

REFRACTIVE INDICES

SURF       N1         N2          N3          N4          N5         ABBE
  2    1.784966   1.788439    1.784223    1.792401    1.783428 186.190705
  3    1.559820   1.562306    1.559289    1.565155    1.558723 185.555187
  4    1.784966   1.788439    1.784223    1.792401    1.783428 186.190705
  5 ******************************************************** -11.242762

CC AND ASPHERIC DATA

SURF      CC            AD            AE            AF            AG
  6  -1.30441E+12  3.12124E-10 -3.70935E-13  3.07313E-16 -2.09011E-18

CLEAR APERTURES AND OBSTRUCTIONS ( CA ON )

SURF          TYPE          CAY          CAX
  1          CIRCLE        5.7500
  2          CIRCLE        5.8000
  3          CIRCLE        5.8000
  4          CIRCLE        5.8000
  5          CIRCLE        5.8000
  6          CIRCLE        5.8000

SOLVES

SURF   TYPE   PARAMETER      VALUE       SLV DATUM
  6     PY       TH        18.641194     0.000000

 REF OBJ HT                        REF AP HT  OBJ SURF  REF SURF  IMG SURF
-0.148781E+19 (    1.0000 DG)      5.75000       0          1         7

      EFL          BF        F/NBR       LENGTH       GIH
    20.7002     18.6412      1.80        3.9971      0.3613

WAVL NBR            1          2          3          4          5
WAVELENGTH       0.63280    0.58756    0.64385    0.54607    0.65627
SPECTRAL WT       1.0000     1.0000     1.0000     1.0000     1.0000

NO APERTURE STOP

LENS UNITS ARE MM

EVALUATION MODE IS FOCAL

CONTROL WAVELENGTH IS 1

PRIMARY CHROMATIC WAVELENGTHS ARE 2 - 3

SECONDARY CHROMATIC WAVELENGTHS ARE 2 - 1
```

Table 4.4.2-4 Manufacturing data for hybrid achromat (1:1.8)

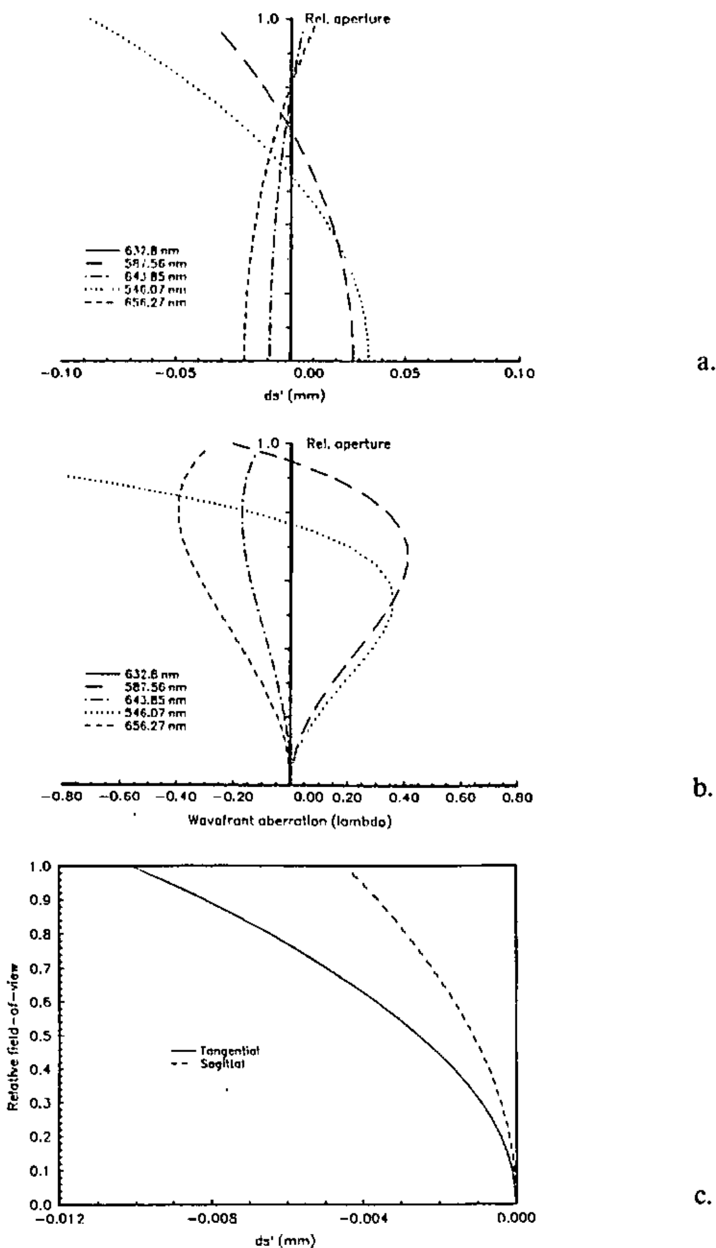

Fig. 4.4.2-1 Optical performance of hybrid achromat (1:1.8) for the visible (spherical aberrations (a), wavefront aberrations (b), field curvatures (c))

Figure 4.4.2-1a shows the spherical aberrations of the achromat (longitudinal aberrations) for the five design wavelengths. The lens is perfectly corrected for the central control wavelength of 632.8 nm, the spherical aberrations are zero over the entire aperture. The aberration curves for the other wavelengths intersect pairwise the ideal focus position for relative aperture heights between 0.55 to 0.8. Therefore, the design goal for the chromatic aberration correction was achieved over the design wavelength range. Figure 4.4.2-1b shows the spherical aberration curves in terms of optical path difference (in fractions of λ). Again, the lens is perfect for the control wavelength. Figure 4.4.2-1c shows the field curvatures for the sagittal and tangential field. The field curvatures were kept below 1 µm for a field of 0.3°. These data show that all initially stated design goals have been met and that still sufficient margins exist for tolerancing.

To define manufacturing tolerances for the elements a sensitivity analysis was made by varying each of the relevant parameters by a defined amount and observing the resulting change of optical quality. Based upon the sensitivities found a set of tolerances was defined for the hybrid which gives a margin of 0.02λ p-v with respect to the initially stated wavefront error requirement of 0.1λ p-v. Figure 4.4.2-2 shows the manufacturing drawing for the final element with tolerances quoted in DIN 3140 nomenclature. One remark has to be made on the centering definition for the DOE with respect to the lens: the definitions of DIN 3140 apply only for spherical surfaces and its methodology for describing the centering status is not adequate for the present case. The centering of the DOE with respect to the lens is therefore defined here in terms of tilt and lateral decentration (see also section 6.2.3).

As a result of the optical design the diffractive element forming part of the hybrid lens was defined as a thin film with aspherically deformed surface. The optical path length (OPL) represented by this thin film was converted by the quantization program described in section 4.2 into an eight level binary element (3 masks). Three data sets were generated each of which defined a ring grating.
The OPL step computation accuracy was set to $1 \cdot 10^{-4}\lambda$.

Table 4.4.2-5 shows the most important data of the ring gratings. The smallest details were in the order of 3 µm, which was well manageable with the technologies available. The mask design which includes, besides the grating, other features for technological verification and alignment is described in more detail within section 6.2.

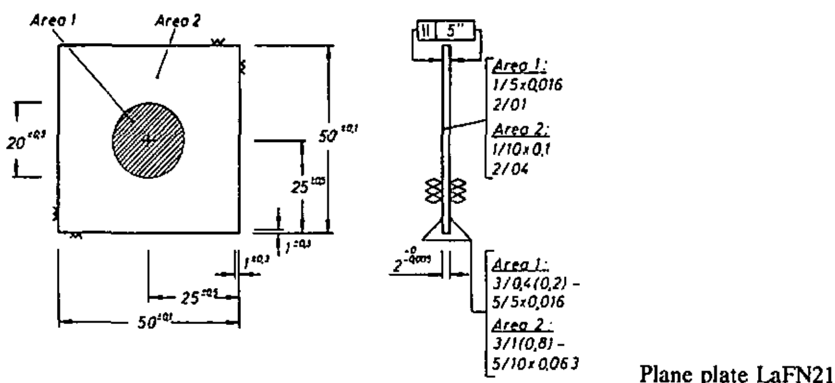

Plane plate LaFN21

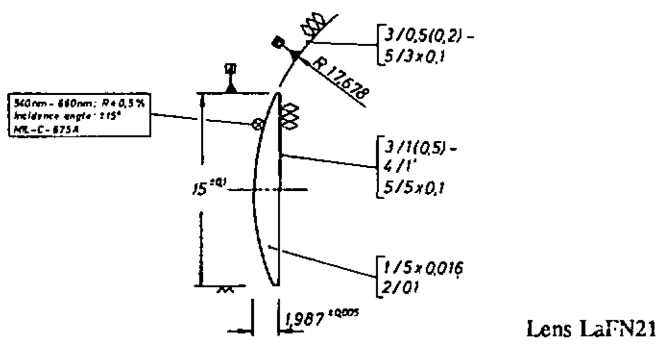

Lens LaFN21

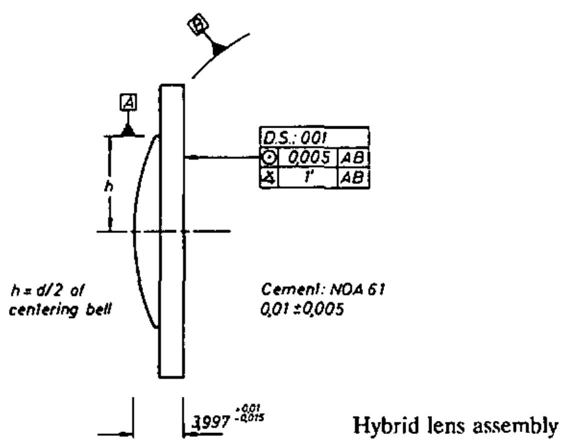

Hybrid lens assembly

Fig. 4.4.2-2 Manufacturing drawings for hybrid achromat (1:1.8)

Mask 1	
OPL step height Etch depth (LaFN21) Spatial frequency Maximum Minimum Smallest feature size	0.5 [λ] 0.403 [μm] 18.403 [lp/mm] 2.233 [lp/mm] 27.170 [μm]
Mask 2	
OPL step height Etch depth (LaFN21) Spatial frequency Maximum Minimum Smallest feature size	0.25 [λ] 0.202 [μm] 36.808 [lp/mm] 3.823 [lp/mm] 13.584 [μm]
Mask 3	
OPL Step height Etch depth (LaFN21) Spatial frequency Maximum Minimum Smallest feature size	0.125 [λ] 0.101 [μm] 73.627 [lp/mm] 6.879 [lp/mm] 6.791 [μm]

Table 4.4.2-5 Mask data for the manufacturing of the hybrid achromat for the visible range (1:1.8, λ = 632.8 nm)

4.4.3 Hybrid Achromat for Medium Infrared

As a further example a hybrid achromat for the medium infrared (MIR) was designed. The design target data were:

F-number	1:1.4
Focal length	100 mm
Wavelength range	3 μm to 5 μm
Field angle	1°
Wavefront error	better than $\lambda/10$ p-v (λ = 4 μm)

The material used for the design was silicon. The design approach was the same as outlined in the previous section. The design wavelengths are shown in table 4.4.3-1.

	λ_1	λ_2	λ_3	λ_4	λ_5
Wavelength [μm]	4	3.5	4.5	3	5

Table 4.4.3-1 Design wavelengths for the hybrid achromat for the medium infrared (MIR)

The Abbe number for silicon and the effective Abbe number for the DOE were computed to be:

Silicon: $\nu_1 = 532.948$
DOE: $\nu_2 = -4$

and the focal lengths of the individual thin elements for the paraxial case were:

$$f_1 = 100.7505 \text{ mm}$$
$$f_2 = 13423.71 \text{ mm}$$

The element data were used as the starting system for the final optimization. The same operands were used as described in the previous section, but the variable-set was different: the radii of curvatures of all three surfaces were defined as variables, the thickness of the silicon element, and the first and the DOE surface were used for aspherization with conic constants and 11 polynomial coefficients defining the aspherization with a polynomial in x,y:

$$z = \frac{\frac{1}{r}\cdot p^2}{1+\sqrt{1-(cc+1)\cdot\frac{1}{r}\cdot p^2}} + \sum_{i=2}^{21} d_i \cdot p^{i-1} \quad with \quad p^2 = x^2 + y^2 \qquad (102)$$

The optimization converged relatively soon and gave the result shown in table 4.4.3-2. Figure 4.4.3-1 shows the spherical aberrations (a) and the field curvatures (b). The element is chromatically corrected for two wavelengths and has a spherical aberration of less than $\lambda/40$ p-v. The field curvature for sagittal and tangential field is less than 50 μm for field of 1°. All initially stated design goals are fulfilled by this design result.
Table 4.4.3-3 shows a comparison between a conventional achromat for MIR consisting of a silicon and a germanium element and the hybrid achromat, both with the same focal length and f-number. Assuming the same optical

```
HYBRID ACHROMAT 1:1.4, 100MM

BASIC LENS DATA

SURF         CV              RD              TH          MEDIUM
  DF
  0     0.00000000      0.00000000  1.00000000E+20     AIR

  1     0.00000000      0.00000000      0.00000000     AIR

  2     0.00408193    244.98194618      8.00000000     MATL    SILICN

  3     0.00000000  3.90639645E+12      0.00200000     DOE

  4     0.00000000 -5.32207165E+08     97.94137617     AIR

  5     0.00000000      0.00000000      0.00000000     AIR


REFRACTIVE INDICES

SURF       N1         N2         N3         N4         N5         ABBE
  2    3.425487   3.428160   3.423609   3.432297   3.422204 532.948249
  3 ******************************************************   -4.000000

CC AND ASPHERIC DATA

SURF       CC            AD            AE            AF            AG
  2   -5.53806E+00  0.00000E+00  0.00000E+00  0.00000E+00  0.00000E+00
  4    2.19902E+12  0.00000E+00  0.00000E+00  0.00000E+00  0.00000E+00

ASPHERIC POLYNOMIAL DATA AT SUR   2 ( EVALUATION OPTION 2 )

D0001 =  2.000000000E+20
D0003 =  1.058197430E-07
D0005 =  1.167346202E-10
D0007 = -9.836033928E-15
D0009 = -4.689637987E-18
D0011 = -9.427683358E-24
D0013 = -8.371705326E-29
D0015 =  2.095848563E-30
D0017 =  1.545128607E-30
D0019 = -2.311352698E-32
D0021 =  8.025041784E-36

ASPHERIC POLYNOMIAL DATA AT SUR   4 ( EVALUATION OPTION 2 )

D0001 =  2.000000000E+20
D0003 =  1.415472909E-13
D0005 = -2.853800877E-16
D0007 =  2.148837384E-23
D0009 =  4.757010496E-23
D0011 = -6.283727063E-25
D0013 = -1.505334632E-27
D0015 =  9.329101315E-31
D0017 = -2.489105642E-35
D0019 =  4.388423124E-38

CLEAR APERTURES AND OBSTRUCTIONS ( CA UN )

SURF          TYPE          CAY          CAX
  2          CIRCLE       35.7000

 REF OBJ HT                          REF AP HT  OBJ SURF  REF SURF  IMG SURF
-0.174551E+19 (    1.0000 DG)         35.70000      0         2         5

      EFL           BF         F/NBR        LENGTH        GIH
   100.2596       97.9414      1.40        8.0020       1.7500

WAVL NBR           1           2           3           4           5
WAVELENGTH      4.00000     3.50000     4.50000     3.00000     5.00000
SPECTRAL WT      1.0000      1.0000      1.0000      1.0000      1.0000
```

Table 4.4.3-2 Design data of hybrid achromat for the medium infrared

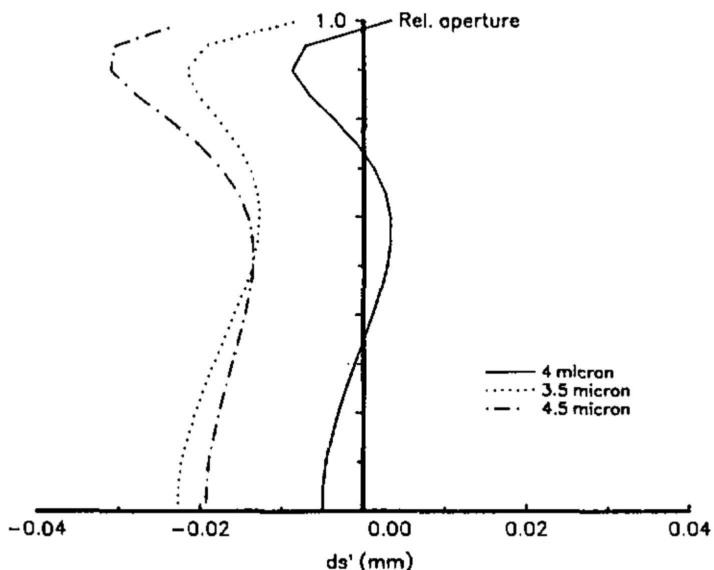

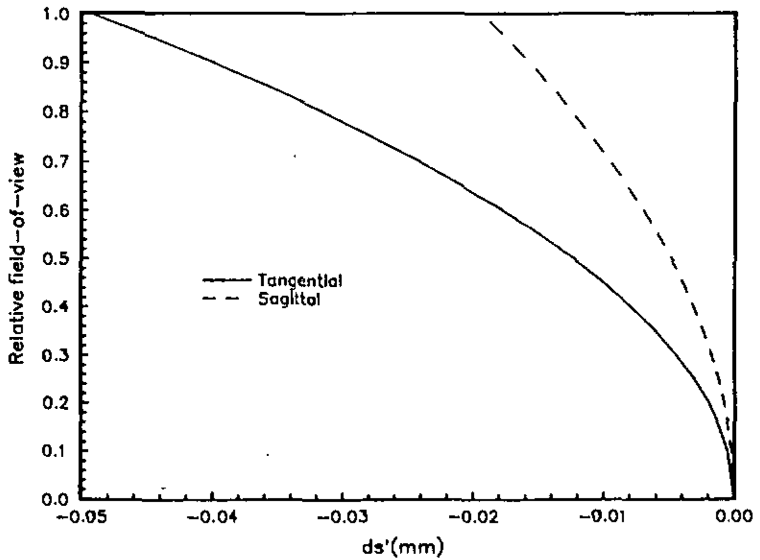

Fig. 4.4.3-1 Optical performance of hybrid achromat for the medium infrared (spherical aberration (a), field curvatures (b))

performance, the hybrid is superior to the conventional system in terms of complexity, transmission, mass and thermal properties. The thermal compensation of systems consisting of germanium and silicon is very difficult due to the different linear thermal expansion coefficients in connection with the difference in the refractive index temperature coefficients. This problem does not exist for a hybrid achromat, which makes it very attractive for such systems. One other interesting aspect is the increased transmission of the hybrid compared to the conventional silicon and germanium system. The hybrid consists of only one silicon element, which can be made in general thinner than the conventional elements due to different power distribution: a hybrid consists of two positive powers, while a conventional achromat requires a positive and a negative power. This leads for the conventional systems to higher f-numbers for each component, which results also in larger material thicknesses for the same overall focal length. Based on this analysis and taking into account the good optical performance figures which were presented one can state that hybrid achromats have a very good potential also in this wavelength range.

<table>
<tr><th>Feature</th><th colspan="2">Conventional achromat</th><th colspan="2">Hybrid achromat</th></tr>
<tr><td>Number of elements</td><td colspan="2">2</td><td colspan="2">1</td></tr>
<tr><td>Materials</td><td colspan="2">Silicon
Germanium</td><td colspan="2">Silicon</td></tr>
<tr><td>Thermal expansion coefficient</td><td colspan="2">Si 2.3×10^{-6}/K
Ge 6.1×10^{-6}/K</td><td colspan="2">Si 2.3×10^{-6}/K</td></tr>
<tr><td>Temperature coefficient of refractive index</td><td colspan="2">Si 1.6×10^{-4}/K
Ge 3.9×10^{-4}/K</td><td colspan="2">Si 1.6×10^{-4}/K</td></tr>
<tr><td rowspan="2">Transmission</td><td>10 mm Si
8 mm Ge
4 AR coatings</td><td>0.95
0.91
0.92</td><td>8 mm Si
DOE, 16 levels
2 AR coatings</td><td>0.96
0.99
0.96</td></tr>
<tr><td>Total</td><td>0.795</td><td>Total</td><td>0.912</td></tr>
<tr><td>Mass of optical elements</td><td colspan="2">ca. 290 g</td><td colspan="2">ca. 80 g</td></tr>
</table>

Table 4.4.3-3 *Comparison between conventional* and hybrid achromat for medium infrared (f=100 mm, 1:1.4)

4.4.4 Microlens Array for Matrix Detector Devices

The following example may serve for illustration of the design potential of CGOE's and hybrid optics for advanced optoelectronic sensor design.

The optical system which shall be described here is part of a smart sensor device which can be used as a wide field sensor for various applications in space: it can serve as star sensor or as a sensor for acquisition of mobile passive or active targets (e.g. in laser communication, rendezvous-docking). The configuration of the sensor is shown in figure 4.4.4-1. The sensor consists of a special matrix detector array including on-chip electronics, which is assembled in a ceramic package, and which also includes a hybrid optical system mounted in front of the detector array.

The optical system consists of an array of DOE lenslets with front apertures, a channel separator and a front lens. Figure 4.4.4-2 shows the optical paths for two lenslets and the associated detectors. In the design example presented here the sensor uses a 9 x 9 lens array with 9 x 9 detector matrices having 16 x 16 pixels each with a pixel size of 23 μm square. The lenslets have a focal length of 4 mm which results in a field-of-view of ±2.63° per subarray. With an f-number of 1:2.7 and a spacing between the lenses of 0.4 mm, this leads to a spacing of 1.532 mm between two adjacent sub-arrays. This space is used for the drive/readout electronics of the individual subarrays and allows for subarray specific commandable integration times. In addition, data processing logic can be assigned to each subarray, for spurious event discrimination for instance. Each subarray and its preprocessing logic is driven by an on-chip controller, which represents the command interface with the external user and also handles the output data stream.

The curvature of the front lens is dimensioned such that it acts - within the subsection to be considered - like a deflecting prism for the individual DOE beam paths. The deflection angle depends on the DOE position with respect to the lens optical axis, thus providing a large overall field-of-view. For the example given here it is 47° x 47°. A channel separator plate protects the individual detector subarrays from unwanted radiation. However, the lens induces strong astigmatism due to its decentration with respect to the outer channels. This can be compensated within the DOE matrix by individual correction of each imaging channel, which consists of front lens subsection, aperture and DOE. All lenses - except the central one - will get a non-rotationally symmetric effective structure shape, which compensates for

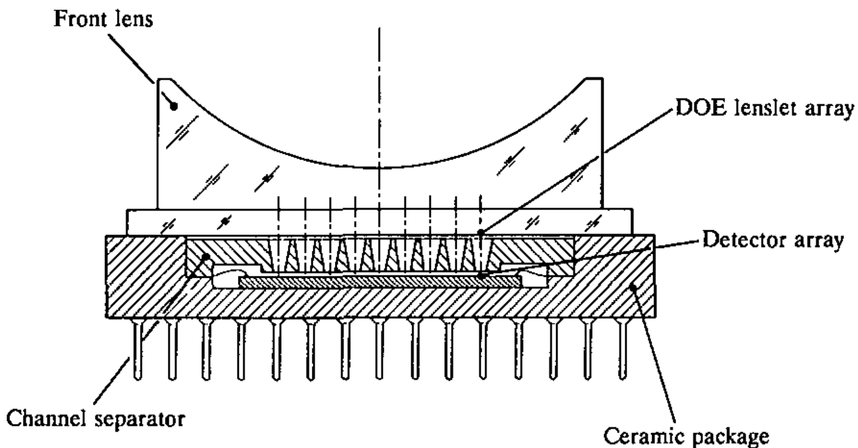

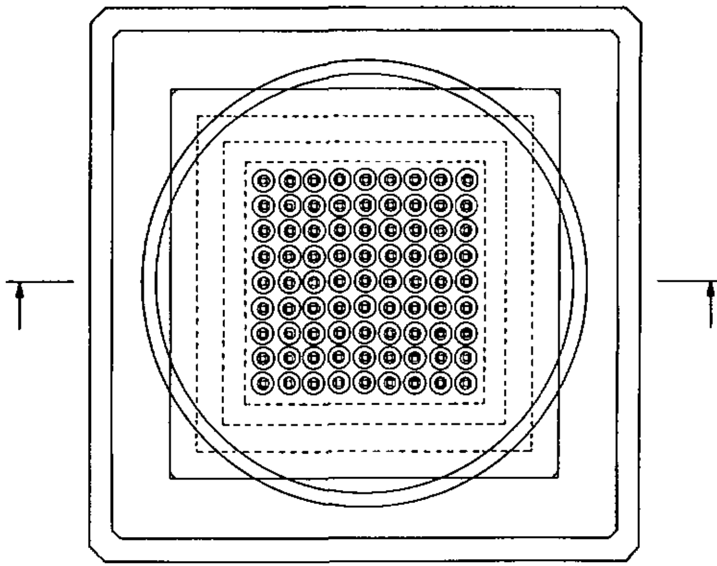

Fig. 4.4.4-1 Miniaturized optronic device with microlens array

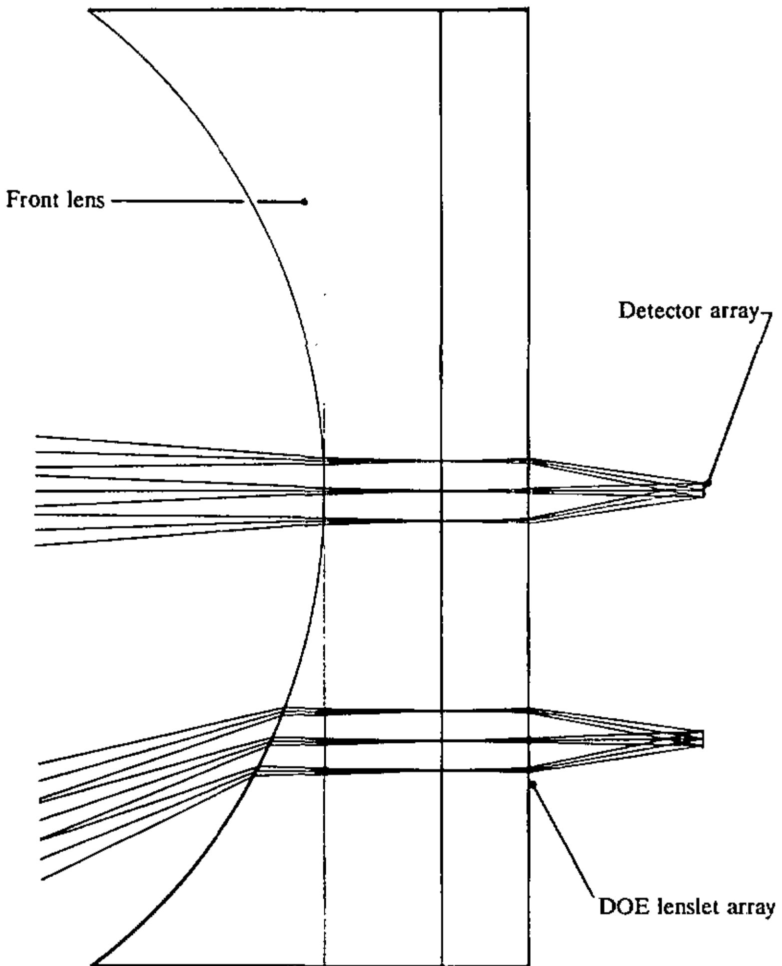

Fig. 4.4.4-2 Optical system schematic of miniaturized optronic device with microlens array

the aberration introduced by the front lens. Due to the fact that the DOE's are computer generated and fabricated by mask processes (CGOE), the complexity of the lens array resulting from the optimization process do not represent a problem for manufacturing. This design flexibility is one of the unique features of hybrid optics: it allows for fabrication of systems which

were not manufacturable with the traditional well established optical production technologies. The characteristic data of the sensor are summarized in table 4.4.4-1.

As an alternative to the refractive front lens it is also possible to use a second DOE array to provide the field of view. This would offer further degrees of freedom to the designer, since the individual elements can be tailored to very different FOV requirements and be perfectly corrected for a number of aberrations.

Optical system	
f-number	1:2.7
Focal length	4 mm
Aperture diameter	1.5 mm
Spectral bandwidth	50 nm, ca. 800 - 850 nm
Detector array	
Subarray	
Size	16 x 16 pixel, 23 μm x 23 μm (each) 0.368 mm x 0.368 mm (overall)
FOV	± 2.63° (Pixel FOV 0.328°)
Number of subarrays	9 x 9
Total FOV	47.3° x 47.3°
Overall detector size	16.7 mm x 16.7 mm

Table 4.4.4-1 Basic design characteristics of miniaturized optronic device

If the sensor is used for broadband sources a filter with a bandwidth of less than 50 nm shall be used to restrict the wavelength range, since a chromatic correction cannot be performed efficiently with the optical configuration chosen. The filter layer will be located on the subaperture surface.

Table 4.4.4-2 shows the radiometric performance of the sensor. With a total number of electrons of 6700 e^- it is possible to achieve position interpolation

	Radiometric performance
Source : G0 star, mv = 0	
Irradiance at lens aperture	$5.57 \cdot 10^{-14}$ [W/cm^2]
Lens surface	0.0707 [cm^2]
Power on detector with lens transmission 0.9	$7.572 \cdot 10^{-15}$ [W]
Number of electrons at detector output (1 sec integration time, conversion factor of EEV CCD)	6746 e$^-$

Table 4.4.4-2 Radiometric performance characteristics of miniaturized optronic device

accuracies of 0.1 pixel (1 σ), which leads to a performance in terms of noise equivalent angle (NEA) of NEA = 0.032°. To achieve an accuracy of 1 arcsec (= 0.000277°) with a one second integration time, it is necessary to have an input irradiance at the lens aperture of $1.74 \cdot 10^{-13}$ W at 830 nm.

The size of the overall sensor device is circa 30x30x15mm^3, the mass is well below 50g. Compared to star sensor heads with similar optical and radiometric performances this new sensor represents a dimensional reduction of a factor of circa 28 and a mass reduction of a factor of about 10. This type of device has therefore an excellent potential for applications in space and other areas requiring miniaturized optical sensors.

A patent application for this type of sensor device has been filed [9.25].

4.4.5 Optical System for Tracking Sensor/Receiver Combinations

This example shall illustrate the possibility of combining different optical performance characteristics within one hybrid optical element. The optical element which shall be described is part of a miniaturized tracking sensor/receiver combination. Such a combined sensor can be used for reception of signals and simultaneous detection of transmitter position within the sensor field-of-view, in order to derive a control signal for a beam

stabilizer. Figure 4.4.5-1 shows the principles of the sensor. It consists of the tracking sensor optics with a hybrid optical element, the tracking detector and the receiver with its optics.
The tracking detector has a central hole and the receiver is located on-axis behind the tracking detector. A second optical element - the receiver optics - is used to focus the incoming light onto the receiver. The tracking detector and the receiver with its optics is assembled in one solid substrate (optical glass, fused silica or zerodur), which allows for highly stable and temperature insensitive performance.

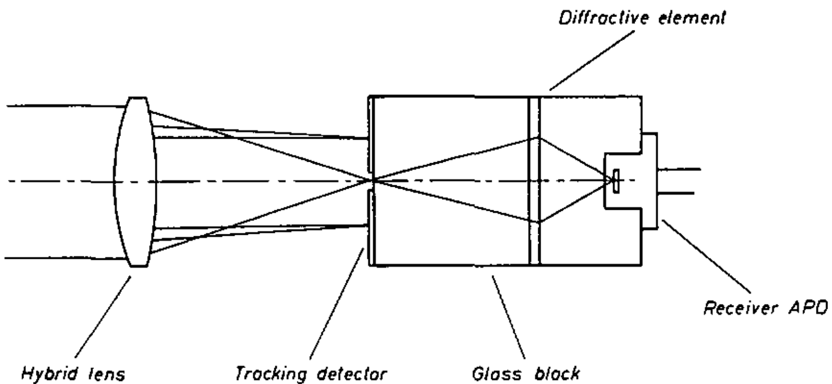

Fig. 4.4.5-1 Overall configuration of tracking sensor / receiver combination

The tracking sensor optics consists of a number of lenses and a diffractive optical element (a hybrid system) which includes chromatic correction and generates - in addition to the sharp focus spot - a concentric ring of light around the focus, which impinges on the tracking detector, a 4-quadrant detector (APD or PIN diode) located in the focal plane of the tracking sensor optics. The aperture in the 4-quadrant detector acts as field stop for the subsequent imaging onto the receiver. Either a hybrid or a conventional lens can be used as receiver optics. A wide range of detector sizes can be accommodated by appropriate dimensioning of the receiver optics.

The principles of the tracking scheme are shown in figure 4.4.5-2a to c.

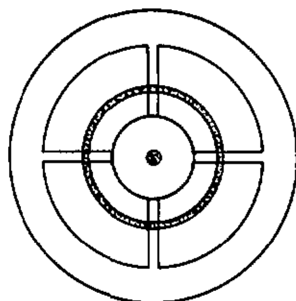

a.

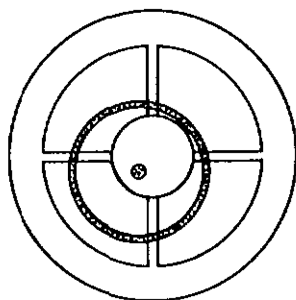

b.

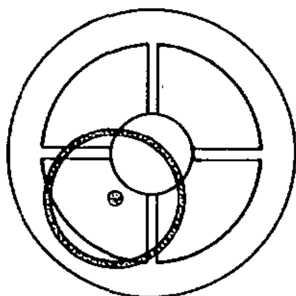

c.

Fig. 4.4.5-2 Tracking sensor operational modes: fine tracking (a), degraded fine tracking (b), coarse tracking (c)

In nominal tracking mode (fine tracking mode) the peak intensity is located centered within the tracking detector central aperture (figure a). Any decentration is detected via shift of the ring pattern (figure b) and a corresponding change of the centroid output of the four quadrant sensor. With stronger mispointing the central spot leaves the central aperture and illuminates one of the four quadrants, giving an indication for the offset direction (coarse tracking mode, figure c).

The ring shaped intensity distribution is generated by combining two optical functions in the hybrid element:

- focusing of the incoming light into the detector plane
- deflection of part of this light into a different elevation angle

Figure 4.4.5-3 shows this in more detail. The outer zone of the hybrid element is modified with a type of ring prism which deflect part of the incoming light and does not disturb the focusing properties of the remaining part of the lens. The energy apportionment is performed via the width of the "prism".

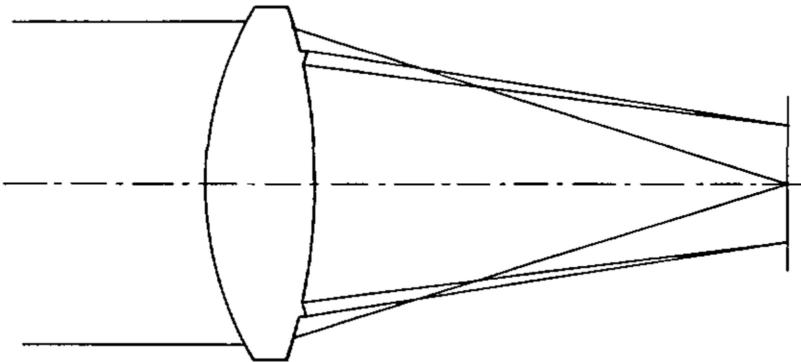

Fig. 4.4.5-3 Design principles of hybrid element for tracking sensor/receiver combination

The basic design approach for the hybrid is similar to the one described in section 4.6.2, it shall therefore not be repeated here.

The advantages of this tracking sensor/receiver combination over the conventional schemes described in the literature are:

- High miniaturization potential

- Insensitive to thermomechanical effects (causing misalignment/drift between tracking sensors and receiver) due to small dimensions and rugged mounting concept

- Reliable operational concept due to two operational modes in one sensor (fine and coarse tracking)

- Optimum energy apportionment, high central intensity peak and only one well defined ring pattern with lower intensity.
  In conventional tracking sensors the image spot is artificially enlarged by defocusing and/or systematic tuning of aberrations, which would lead in the case of a functional combination to an unacceptably high loss in the receive path.

- Easy adaptation of various detector sizes by change of receiver optics data

Such a sensor concept can only be realized by hybrid optical systems using CGOE's for the implementation of the function of the "deflecting ring prism", in particular if the dimensions have to be minimized.

A patent application has been filed for this type of tracking sensor/receiver combination [9.24].

Chapter 5

REQUIREMENTS FOR OPTICS FOR SPACE APPLICATIONS

5.1 General

Hybrid optics designed for applications in space have to comply with a number of requirements, which are derived from basic space specific operational constraints and the environmental loads the hardware is exposed to during launch and in-orbit operation. Of course, mission specific requirements have to be observed in addition to that. Basic operational constraints to be taken into account for the development of space hardware are:

- No possibility for in-orbit servicing
- "Prototype production" without learning curve
- Optimum exploitation of available payload mass

The requirements which are derived from these constraints are:

- High reliability for long lifetimes
- Good reproducibility of manufacturing processes
- Low mass and small dimensions
- Low power consumption (In the case of optics minimization of heater power)

The environmental loads to be taken into account for the design of space optics can be summarized as follows (see also [5.1]):

- Thermal loads
- Mechanical loads (vibration, acceleration, shock)
- Radiation loads (UV, particles, high energy photons, etc)
- Vacuum conditions
- Atomic oxygen (in low earth orbits)
- Micrometeorites

Within this chapter, the basic space specific requirements shall be described briefly and references shall be given to relevant publications on the corresponding fields. The influence of these requirements on space optics

design in general shall be identified and the constraints resulting from it for design/fabrication of hybrid optics for space applications shall be highlighted.

5.2 Lifetime and Reliability

The lifetime of space hardware after successful completion of qualification/acceptance tests has two main phases, the on-ground storage period up to the launch and the operational/non-operational in-orbit lifetime. The duration of on-ground storage is determined by the time span between completion of tests and scheduled launch date and includes usually a provision for unforseen events, like delays due to launcher failures, system integration problems, etc. Depending on the type of project, on-ground storage might be requested for up to five years. Of course, the storage will take place in well controlled environment.

The in-orbit lifetime depends on the type of mission and the orbit selected [5.2]: for a commercial communication satellite in geostationary orbit one aims for 10 years in-orbit lifetime, scientific satellites in low earth orbits might have lifetimes of one to three years depending on the orbital parameters. Interplanetary missions can have mission durations between three to ten years. Space shuttle supported experimental missions stay in orbit sometimes only for a couple of days or weeks.

Space hardware has to be designed such, that it fulfils its specified performance requirements over the entire lifetime, without the possibility of servicing during operation in orbit. This means that the design concept has to be kept inherently insensitive to technological problems by incorporation of sufficient margins, by selection of well characterized and appropriate materials, by minimization of interfaces, and by application of only highly reproducible and controllable manufacturing processes (see section 5.3).

The reliability of a system defines its probability to survive for the specified lifetime. The term "survive" is defined usually by unambiguous failure criteria, which are project specific. Deterministic effects must not be considered for calculation of the reliability figure. Guidelines for spacecraft reliability prediction are given in [5.3]. The definition of reliability and the methods for their calculation originate from assessment of electronic systems, which involve components with large production quantities. The transposition of the approach to optical systems is not possible without adaptation to the specifics

of the technology involved. An attempt for transposition of the established reliability calculation approach to optical systems is presented in [5.4].

Reliability figures are usually not quoted for optical systems in isolation, but as part of a higher integrated system, e.g. for an attitude control sensor involving optics, structure, thermal control, software and electronics. Reliability figures for such equipment are in the range of 0.99 for ten years operational lifetime in orbit.

The design of hybrid optics and the definition of manufacturing processes involved shall be oriented on a target reliability figure of better 0.99 for 5 years on-ground storage and 10 years operational in-orbit lifetime in the geostationary orbit, taking into consideration the environmental loads defined in section 5.4. That implies that only materials with well known long-term behaviour are used.

5.3 Reproducibility of Manufacturing Processes

Space hardware is manufactured in rather small production quantities, compared to other commercial products, and is always tailored to specific applications. The qualification/acceptance tests at the end of the manufacturing/assembly phase are the final (sometimes the only) opportunity to identify design and/or manufacturing flaws. Once such weakness was found, it must be possible to identify its cause by tracing back the manufacturing and design documentation. Prerequisite for success of such approach is, that only reproducible processes were involved in the fabrication. Reproducible means in this context that the same operation carried out in the same conditions on an identical material must lead to the same results.

For this reason, if a new technology product, like hybrid optics, is proposed for application in space it is necessary to evaluate all manufacturing processes involved with respect to their reproducibility, with the aim to assess its potential for later-on space qualification. Manufacturing processes which are already established for other products and well characterized by statistics gained with high production quantities are usually promising candidates.

5.4 Environmental Loads

5.4.1 Thermal Environment

Optical systems for space applications have to be designed such that they can withstand the thermal environment on ground and in space. These environments are completely different in terms of heat transfer mechanisms: on ground heat transfer takes place by convection, radiation, and conduction, in space heat transfer results only from radiation and conduction. The temperatures of a satellite in orbit are determined by the balance between absorbed radiation from sun, earth or other celestial bodies and the heat radiated against the deep space background. Optical equipment at the outside of the satellite facing deep space can reach extremely low temperatures since it is in radiative exchange with the 5 K space background, facing the sun it is heated up with 1.35 kW/m^2 and can reach, depending on its surface properties, several hundred °C. In both situations, strong temperature differences can develop between exposed and shadowed areas and the low heat conductivity of optical glasses can lead to high temperature gradients within optical elements, which result in performance degradations. It is the task of the satellite thermal control system to balance the temperatures and to equalize temperature gradients as far as possible. However, it cannot be avoided that certain components are exposed to larger temperature ranges which they have to survive without damage. For instance, complex optical sensors located on outer satellite walls might have to cope with temperature ranges of -20°C to +40°C for operational and -30°C to +50°C for non-operational conditions [5.5], with qualification temperatures which are usually 10°C higher/lower. For some applications, the entire optical system has to be cooled even further down to reduce detector noise, e.g. some optical systems in the SOHO mission are cooled to -80°C. A comparison between the requirements of several space projects and the temperature ranges usually specified for high performance commercial or military optics (DIN or MIL standards) showed that the temperature requirements for severe environments are comparable. Therefore the following temperature range specification shall serve as a guideline for the technological evaluation of hybrid optics:

- Non-operational temperature range
  DIN 58 390,2 type 14.5: -55°C to +70°C
- Operational temperature range
  DIN 58 390,2 type 14.3: -25°C to +70°C

However, the individual materials used for the system shall be capable of withstanding the temperature limits given as guidelines in the relevant ESA document [5.6], namely -100°C to +100°C.

5.4.2 Mechanical Loads

Space hardware is exposed to significant mechanical loads only during ground handling (assembly, integration, test, transport), during launch, and, in the case of shuttle retrievable systems, during reentry. The latter is not relevant for the operational performance, only overall integrity shall not be endangered when exposed to these loads.
During operational in-orbit life time no significant permanent vibration loads exist. Therefore, with respect to equipment performance, launch loads are always considered as the driving design case. Several types of launch loads can be distinguished:

- Steady state acceleration
- Low frequency vibrations
- Random vibrations
- Acoustic noise
- Shock

General quantitative specifications can only be given for the adapter acting as interface between the launch vehicle and the spacecraft (for ARIANE see [5.7], for STS see [5.8]). The vibration loads individual optical equipment might be exposed to depend strongly on the structural design of the entire spacecraft and can be significantly higher as specified for the adapter ring. However, as initially stated, these loads are imposed on the equipment only for a relative short period during launch: for ARIANE 44LP the third stage cut-off takes place ca. 18 min. after ignition, the period with high acceleration/vibration levels ends with 2nd/3rd stage separation after 5 min 40 sec., for STS the vibration intensive launch period ends with main engines cut-off after ca.8 min 45 sec.

The vibration load specification for various space optics equipment was compared with the mechanical loads proposed for test of optical instruments by the DIN standard [5.9]. In particular, in view of the moderate number of load cycles applicable for space hardware it was found that for the case of severe environment DIN states quite comparable values. The DIN standard

does not cover the acoustic noise loads. However, this is considered to be of minor importance for individual optical components of moderate size. The evaluation of hybrid optics for space application shall be therefore oriented on the requirements of DIN 58390, however, these requirements are certainly not critical due to the moderate size of the optical components under consideration and their resulting high eigenfrequencies.

Another type of mechanical load which cannot be underestimated with regard to optical systems are the loads due to cleaning processes which are sometimes necessary in order to remove contaminants. The optical elements shall be tolerant against certain types of cleaning operations e.g. wiping with a soft cotton swab. The requirements of the MfL standards ([5.10], [5.11]) with regard to cleaning aspects (severe abrasion, moderate abrasion) are certainly not fully applicable on space optics, but are of some help for evaluation purposes.

5.4.3 Radiation Loads

5.4.3.1 General

The radiation environment in space shall be classified here in two types, firstly the UV radiation with wavelength between 300 nm and 115 nm and, secondly, the high energy radiation consisting of particles and higher energy photons.

A comprehensive overview about the different types of radiation in space is given by Adams and Holmes-Siedle [5.12] and Stassinopoulos [5.13]. Basic publications describing the interaction of radiation with glass have been made by Jahn ([5.14], [5.15]). Malitson [5.16], Griscom [5.17] and Levy [5.18] gave overviews about radiation damage mechanisms in optical material. Space radiation related problems have been treated by a number of publications, a selection is given in references [5.19] to [5.33].

Within the following sections the two basic radiation types shall be discussed briefly, main damage mechanisms/degradation effects shall be described, and some guidelines shall be established for the evaluation of hybrid optics with respect to radiation sensitivity.

5.4.3.2 UV Radiation

The sun is the dominant source for UV radiation within the wavelength range between 300 nm to 115 nm. The corresponding energies are between 4.1 eV and 10.8 eV, well within the absorption band of most of the optical materials. This type of radiation produces a free electron-hole pair which is trapped at latent defect positions, forming a colour centre. Colour centres absorb light in the blue end of the visible spectral range, the glass becomes brownish. The effect is known as solarization and is described in more detail by Jahn ([5.14], [5.15]), Becker [5.1] and Griscom [5.17]. Measurement results on UV irradiated samples have been published, besides others, by Nicoletta [5.19] and Setta [5.27]: Nicoletta reported on solarization effects on various types of fused silica, Setta presented test results on cerium doped and normal glasses: some of the cerium doped glasses showed good resistance to UV, however, not all of them were found to be as stable as the undoped versions. This might be due to the fact that the cerium doping was developed for stabilization in the gamma/X-ray range and that it is not optimized for the UV: cerium doped glasses are slightly yellowish and, consequently, their absorptivity for UV is increased.

Another UV induced damage effect is stress build-up, which was reported by Ooka [5.28] for binary borate glasses. This effect is not confined to this glass type but can be assumed to be common to most of the optical materials (see also [5.17]).

Optical coatings like antireflection coatings and interference filters can exhibit also strong degradation effects, however, such effects are dependent on the individual element design.

Besides glasses, optical cements can show also strong degradation effects due to UV irradiation. Measurements performed on cemented plane plates within a currently running ESA contract show effects like strong discoloration, disintegration of cement layer or cracks in glass induced by cement shrinkage [5.34]. Of all materials tested, silicones seem to have the best resistivity to UV, however their adherence to glass is not very good and they are very soft, which makes them not ideally suited as optical cement for high performance applications.

Therefore, to reduce the risk for potential damage, optical elements on-board a spacecraft should be shielded against UV radiation as much as

possible. If this is not possible, due to mission constraints, only materials with high UV resistivity can be used, such as fused silica of highest purity, sapphire, certain cerium stabilized glasses and normal glasses with high lead contents. The glass types shall be in any case UV tested, since their properties are to some extent melt dependent. Guidelines for UV testing of spacecraft materials are published in [5.35]. The measured degradation characteristics can subsequently be taken into account for the system design. The possibility of shielding low resistivity materials by highly resistant front elements can be also taken into consideration. If shielding against UV is not possible, the use of optical cements must be completely avoided for high performance optical systems.

For the purposes of technological evaluation of hybrid optics a UV radiation test with the selected materials according to the guidelines established in [5.35] is recommended.

5.4.3.3 Highly Energetic Radiation

The high energy radiation in space consists of the following radiation types (see also [5.12], [5.36]):

Trapped radiation

Trapped radiation consists of charged particles, mainly electrons up to 7 MeV and protons which are trapped by the earth's magnetic field in the van Allen belts. For electrons two flux maxima exist at distances of 8920 km resp. 28670 km from earth's centre, for protons only one maximum exists at a distance of 10830 km [5.12].

Quiet sun radiation

Quiet sun radiation - apart from visible and near UV radiation - consists of extreme UV to soft X-rays from 200 nm to 4 nm wavelength, which is composed of a weak continuum and numerous emission lines [5.36].

Solar flare radiation

Solar flare radiation is a transient type of radiation depending on solar activity, which has a mean cycle of 11 years, varying between 7 and 17 years. The following effects can be observed:

- Increase of soft X-ray level (λ = 2 to 0.1 nm) by two to three orders of magnitude.
- Hard X-ray bursts below λ = 0.1 nm
- Strong gamma radiation with lines at 0.5 MeV and 2.2 MeV
- Protons and α-particles (100:15), in the range of 100 MeV to 10 GeV
- Electrons
- Heavy particles

Cosmic rays

The main constituents of cosmic ray radiation are electrons, protons and gamma photons with energies from 1 MeV to 1 GeV. All elements up to Uranium are represented but Z = 30 is the highest Z with a significant population.

Low energy plasma

The low energy plasma consists of protons and electrons up to 100 keV.

These primary radiation sources can cause secondary radiation like Bremsstrahlung, if electrons are slowed down inside the spacecraft material, or secondary protons and neutrons, if high-energy protons are impacting the material.

The high energy radiation environment in space varies strongly depending on the epoch of the launch and the orbital position of the spacecraft. Model calculations taking into account the various particle types, energies, orbits, epoch lead to the following figures on 4π total dose absorbed radiation which can be expected for a low earth orbit (LEO), respectively a geostationary orbit (GEO) spacecraft (data from [5.12]):

- LEO: 1 - 2 krad (Si)/year with 4 mm Al equivalent shielding
- GEO: 15 - 20 krad (Si)/year with 4 mm Al equivalent shielding

The higher figures apply for the case of one large solar flare, the lower figures assume no flare.

Interaction with the above mentioned radiation types with optical materials can cause various types of radiation damage (see also [5.14], [5.15], [5.16], [5.17], [5.18]).
The basic damage mechanisms are radiolysis by ionization, displacement damage and electron rearrangement [5.17]. All these mechanisms lead to local structure defects, and - depending on received total dose and radiation type - this is manifested as follows:

- Transmission degradation (solarization)
- Refractive index change
- Dielectric breakdown
- Stress build-up
- Radioluminescence

The dominating effect is certainly solarization, which is due to development of colour centres ([5.14], [5.15], [5.18]). This effect is observed for higher received doses also in fused silica if the material has impurities ([5.21], [5.25], [5.16]). The addition of polyvalent cations (like cerium, arsenic, antimony, lead) stabilizes the glass since these ions act as electron acceptors ([5.14], [5.15]). Doping additions of 1% to 2% are sufficient to achieve an effective stabilization [5.23]. A number of publications report on recovery from radiation damage: it was observed that unstabilized flint glasses with high lead contents show recovery after 4 to 12 hrs, stabilized glasses showed even faster recovery intervals ([5.25], [5.16]).

Refractive index changes were reported for total doses of 1 Mrad Co60 or electron doses of about $6{\cdot}10^{13}$ to 10^{15} e/cm^2 [5.16]. Index changes of up to $2{\cdot}10^{-4}$ were observed, the cerium doped versions showed higher changes than the non-doped versions. Electron irradiation caused stronger effects than gamma rays. The changes were higher in crown glasses than in flint types which are more resistant due to their higher lead contents. The indices for shorter wavelength in the blue and in the UV region showed larger variations than the indices at longer wavelength. The measurements reported by Malitson were confirmed by the results of other investigations [5.30].

A further effect which is observed for electron irradiation with higher doses/dose rates is dielectric breakdown: charges are accumulated in the

glass and the sudden discharge is often accompanied by mechanical breakdown in the glass structure (Lichtenberg figures) ([5.16], [5.31]). This type of damage does not depend on glass stabilization.

Stress build-up is also identified in several publications as degradation mechanism ([5.31], [5.32], [5.17]).

Radioluminescence and scintillation effects in irradiated optical materials do not directly represent a damage of the material itself but a disturbing effect which can lead to increase of noise on detectors or to misinterpretation of measurements. Therefore it was included in the list of damage effects. Measurement results on natural quartz have been presented in [5.18], test results on quartz, glasses and sapphire were published in [5.25]. The measurements were made for electron irradiation of 2.5 Mev with dose rates of $5 \cdot 10^2$ to $5 \cdot 10^5$ rad/sec. For quartz, a luminescence line was detected at ca 185 nm, for BK7G14 at 420 nm and for sapphire at 250 nm and 696 nm, the latter was due to material impurities.

Other optical materials, like cements show similar degradation effects due to radiation. Additionally, embrittlement of the material can lead to delamination. However, only few test results are published [5.33]. More extensive studies are performed on this subject in the frame of a currently running ESA contract [5.34]. The irradiation was performed with a Co60 source up to total doses of 200 krad. The transmission losses observed were not by far as high as for UV irradiation, which is due to the small material thickness and the source type used.

Particle irradiation and high energy photons cannot be shielded as efficient as UV radiation. For the design of space optics it is therefore necessary to determine in each case the total dose to be expected during the mission together with the dominant type of radiation and to define the most appropriate design configuration based upon that.
Preferably cerium stabilized glasses should be used for space optics and other insensitive materials, like highest grade fused silica or sapphire. If non-stabilized glass types must be used sufficient shielding by other glass elements or by mounting material should be provided. Implementation of front windows made of less sensitive materials (e.g. high purity fused silica, sapphire) can be considered in critical cases to avoid unacceptable degradation effects. For precision optics the use of optical cements must be avoided in exposed areas completely.

For purposes of technological evaluation a Co60 irradiation to a 4π total dose of 200 krad(Si) and a proton irradiation can be recommended. The Co60 irradiation dose simulates the conditions for a 10 years lifetime with 4 mm Al shielding in geostationary orbit.

5.4.4 Vacuum Conditions

Space hardware has to withstand a wide range of pressure conditions which comprise ambient pressure on ground, the depressurization phase during launch, and ultrahigh vacuum during its in-orbit lifetime. The ultrahigh vacuum in orbit is usually the design driver for space hardware, since various effects can degrade seriously the hardware performance ([5.37], [5.1]).
For the design of optical systems following vacuum effects have to be taken into account:

- Depressurization effects
- Change of refractive index/dispersion of the environment
- Change of heat transport mechanisms
- Outgassing effects
- Condensation effects
- Structural changes/reorientations in materials

The first point concerns the launch phase which represents the transition from ambient pressure to high vacuum conditions as characterized by launcher specific depressurization profiles. The depressurization from ambient conditions to high vacuum takes place usually in less than 8 minutes [5.7]. This implies very high gas flow rates. To avoid damage on optical systems in this phase, venting holes must be implemented in the mechanical mounts with sufficient dimensions to avoid high pressure build-up.
The holes shall be covered by porous filter plates (ceramic or metal), as contamination barriers.

Another effect concerns the optical properties of vacuum. Refractive indices and dispersions of optical materials are defined usually with respect to air (see [5.38]): the index for air is set to 1 and the dispersion is defined correspondingly. For high performance optics the difference between the index of air and vacuum and the resulting dispersion difference must be taken into account for the design of refractive space optics. Use of

air-to-vacuum compensation systems for on-ground operations might be necessary in critical cases.

The difference in heat transfer mechanisms has been discussed already in chapter 5.4.1.

Material outgassing in vacuum can cause two types of effects, first change of material properties of the outgassing material and, secondly, contamination of other surfaces by the outgassing products. To avoid such effects it is mandatory to use only materials with low outgassing rates. Guidelines for material selection are given in [5.39], an outgassing test procedure is defined in [5.40]. According to that, for optical devices and in their vicinity only materials with outgassing rates of $< 0.1\%$ recovered mass loss (RML) and $< 0.01\%$ collected volatile condensed material (CVCM) are acceptable (for the definition of terms, see [5.40]. For critical applications - optical systems designed for UV for instance - it is necessary to establish a contamination budget, which makes allocations for acceptable amounts contaminants collected during on-ground operations and in-orbit lifetime. Guidelines for material selection and test are given in [5.39] and [5.40].

Another vacuum effect is the change of material properties due to decomposition, sublimation and outgassing. This effect is not restricted to organic materials, but is also observed for metal alloys having compounds with lower vapour pressure. In particular for metallic mirror coatings or antireflection coatings this effect should be considered for material selection. Again, guidelines are given in [5.39].

The technology and material selection for hybrid optics shall reflect the above mentioned constraints. In particular the required low outgassing rates suggest to avoid the use of organic materials for hybrid optics as far as possible.

5.4.5 Atomic Oxygen

On early space shuttle flights (F3,5,8) two phenomena have been observed: material erosion on outer spacecraft materials and luminescence effects on exposed surfaces. The effects were caused by atomic oxygen, one of the most important atmospheric constituent in low earth orbits (150 km to 600 km). The reactivity of the atoms in connection with the high spacecraft velocities

lead to equivalent energies of the impacting atoms of 5 eV. The number of atoms collected during in-orbit lifetime depend on orbital parameters, solar activity and orientation of the exposed surface with respect to the velocity vector. Mathematical models have been established which were adapted to the results of exposure experiments made on a number of space shuttle flights. The results are given in terms of atomic oxygen fluences (number of atoms per square cm per observation time interval), which can be converted to a material dependent abrasion. Results for optical materials are published in a number of papers (see [5.41] to [5.46]).
Typical recession figures reported from space shuttle flights for Kapton foil after 40 hrs exposure in 225 km altitude were 12 μm with a fluence of $3.375 \cdot 10^9$ atoms/$cm^2 \cdot h$.
On lens coatings with hard outer layers atomic oxygen seems to have no significant effect. On mirror surfaces the effects are also negligible as long as the protective coatings are intact and not damaged by micrometeorites. In case of damage, oxidative undercutting will corrode the mirror metal, in particular sensitive metals like silver.

Since the effects on appropriately coated glass surfaces seem to be negligible, in particular for higher orbits, the effects of atomic oxygen on hybrid optics can be ignored for the purposes of technological evaluation.

5.4.6 Micrometeorites

Micrometeorites exist in interplanetary space in random distribution and as particle streams. A description of the micrometeorite distribution is given by Levadou [5.47], which takes into account both random distribution and meteorite streams. The sizes of the particles range from few μm to several tenth of millimetres and their velocity can be in the range of 11 to 72 km/sec with an average value of 20 km/sec. The average density of the particles is assumed to be 0.5 g/cm^3. A larger micrometeorite can definitely destroy an optical component completely, smaller particles can cause cratering which leads to an increased straylight level. In low earth orbit such damage can lead, on mirrors, to strong degradation due to atomic oxygen. It is possible to predict the degradation due to micrometeorites and space debris by a computer model taking into account the particle distribution in space and the orbital parameters. The predicted degradation shall be taken into account for dimensioning of the optical system.

Chapter 6

MANUFACTURING OF HYBRID OPTICAL ELEMENTS

6.1 Review of Hybrid Optics Manufacturing Technologies

6.1.1 General

The manufacturing technologies for diffractive optical elements (DOE's) including hybrid optics were already shortlisted in section 3.3.3, itemizing criteria for their classification. Purpose of this chapter is to go more into the details of the manufacturing technologies discussing materials and processes, in order to establish a sound basis for the selection of a technology qualifiable for space applications, with respect to the criteria established in chapter 5.

In manufacturing hybrid optics one has to combine conventional optical manufacturing methods with special technologies used for fabrication of the diffractive component. The review presented here will concentrate on the DOE fabrication technologies and the aspects related to the combination of the diffractive component with the conventional one. The methods of conventional optics manufacturing technologies are assumed to be well known and shall be therefore not discussed here in more detail.

The DOE's, which are used for the fabrication of hybrid optics are without exception computer generated optical elements (CGOE's). This is due to the fact that only CGOE's provide sufficient design flexibility to be attractive for larger scale industrialization and transfer into space qualifiable technology. Having designed a hybrid element, the diffractive component has to be converted from a mathematical formulation into a physical structure. The first part of this chapter, before discussion of materials and processes technology, will be therefore devoted to the process of DOE pattern generation and transfer.

6.1.2 Methods of DOE Pattern Generation and Transfer

As result of the optical design both components of the hybrid element are defined by a mathematical formula, or, in special cases, by means of discrete

data points. The processing steps necessary to convert the data for the diffractive component into a physical structure are shown in figure 6.1.2-1. First, the data have to be processed in an appropriate way by methods like coding, quantization or application of special limiter functions (see section 3.3.3). The resulting data describe either directly the DOE effective structure or - in case of multilevel structures - the patterns of the individual masks. Usually the data are provided in form of an ASCII file. To transform this file in a form suitable for the particular output device used, processing of the data with a conversion program is usually necessary. This program is always output device specific and performs an optimization of the writing path, the adequate quantization of continuously shaped geometrical features, and the implementation of control data.

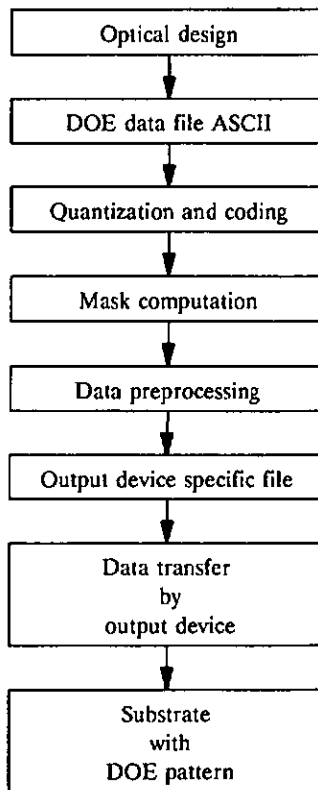

Fig. 6.1.2-1 DOE data processing steps and pattern transfer

Examples for the required conversion procedures for the case of an electron beam writer are given by Buczek and Teijido [3.15], Arnold [6.1], Hawley and Gallagher [6.2] and Logue [6.3]. The final data file is then sent to the output device which transfers it onto the data carrying medium in form of a two-dimensional pattern, with intensity levels of 0 and 1 or with intensity modulation.

Based upon the data transfer mechanism one can distinguish four basic types of output devices: conventional drawing devices, optical devices, electron beam writers and devices using a machining process. Besides other features, all of them can be characterized by the achievable space-bandwidth-product (SBWP). Table 6.1.2-1 gives an overview about the various output device types and some of their characteristics.

All of the devices are in principle used for binary recording, some of them have also intensity modulation capability, as indicated.
The drawing devices operate with non-photosensitive carrier material, which are highly dimensionally stable like special paper types or plastic foils. The geometrical forms are either plotted with a pen or written, by a laser printing process for instance. Due to the relatively coarse feature size a photographic reduction is required in most of the cases. The reduced pattern is then used for reproduction. This reproduction can be made either directly on photoresist deposited on the final DOE substrate or on an intermediate mask, sensitized by an appropriate photographic medium, depending on the light source used for the process.
The process of pattern transfer using drawing devices is shown in figure 6.1.2-2. Optical output devices perform the pattern transfer by writing on a photosensitive substrate. Three basic optical device types are mentioned in table 6.1.2-1, which are fundamentally different in their concept: photo plotters write with light sources/source outputs, which are mounted on an x/y-stage and move over a stationary substrate. Other types have the substrate fixed on a drum and the source head is moved in only one dimension. The minimum achievable feature size is relatively coarse and a photographic reduction is usually required involving similar processing steps as described above for drawing devices (see also figure 6.1.2-2). Other types of photoplotters for smaller format substrates use galvanometer scanners as deflection devices.
The substrate types used are photographic film, photoplates or photoresist coated mask material for higher resolution devices.

Device Type	Device Characteristics		
	Minimum Feature Size [μm]	SBWP	Notes
Drawing Devices			
- Pen/electrostatic-plotter	20	$1.6 \cdot 10^9$	2,4,6
- Printer	80	$9.7 \cdot 10^6$	2,3,7
Optical Devices			
- Photo plotter	10	$1.0 \cdot 10^1$	1,2,4
- Laser beam writer	0.5	$6.5 \cdot 10^1$	1,3
- Cathode Ray Tube (CRT) writer	10	$6.5 \cdot 10^6$	1,2,3
Electron beam writer	0.025	$2.58 \cdot 10^{13}$	3
Machining devices	1	$7.0 \cdot 10^1$	4,5,8

Notes:
1. Device has intensity modulation capability
2. Photographic reduction process required
3. X/Y addressing
4. Vector addressing
5. Only rotationally symmetric structures, 300mm diameter in example.
6. A0 format
7. A4 format
8. Surface quality dependent on mechanical stability, structure generation by pointwise machining

Table 6.1.2-1 Output device characteristics

Laser beam writers operate with diffraction limited beam focusing optics in the blue wavelength range and achieve beam spot sizes in the submicron range. Due to the small working distance, the substrates are usually mounted on an x-y-stage for scanning. Laser beam writers have, next to electron beam writers, the smallest feature size and the highest SBWP. The substrates used in connection with laser beam writers can be either directly the DOE substrate coated with photoresist, or a mask substrate. The mask substrates are chromium coated glass or fused silica plates with photoresist as photosensitive top layer. DOE substrates are photosensitized by photoresist coating as well. Due to the high definition, a photographic reduction is usually not required. However, it is sometimes performed if the pattern

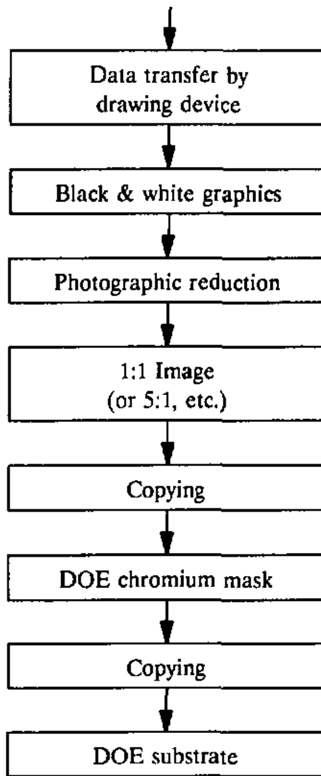

Fig. 6.1.2-2 DOE pattern transfer with drawing devices

transfer onto the final substrate is done with a mask process using step-repeaters. Figure 6.1.2-3 illustrates the pattern transfer process with the laser beam writer.

Cathode ray tube writers are early precursors of electron beam writers and were used for generation of photomasks for integrated circuit production [6.4]. The substrate for exposure is either fixed on the faceplate of the cathode ray tube or the pattern is imaged by an optical relay system onto the substrate. Similar substrate types are used as for photo plotters. The electron beam writer uses an electron beam for pattern generation. Since the beam can only be deflected over a limited scanfield of about 1 to 2 mm square, the substrate has to be translated on an x/y-stage for generation of larger patterns. The motion is interferometrically controlled to minimize alignment errors. More detailed descriptions of pattern generation processes with

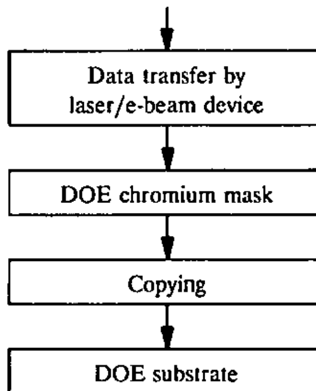

Fig. 6.1.2-3 DOE pattern transfer with laser beam writer or electron beam writer

electron beam writers are published by Buczek and Teijido [3.15] and other authors. Electron beam writers have the highest SBWP. The substrates used are chromium masks coated with special e-beam resist or are resist coated DOE substrates. Pattern reduction is of course not required for production of most of the optical devices. However, if step-repeaters are used in the production process a reduction can take place. The process flow is similar to that shown in figure 6.1.2-3.

Another possibility of DOE data transfer is the use of a numerically controlled turning lathe. This is of course restricted to rotationally symmetric elements with relatively coarse structures for infrared applications. It is easily possible to manufacture elements on curved substrates by this means. This is the only method, which directly results in a three-dimensional structure, all other output devices produce two-dimensional structures (if the single step process is excluded), which have to be transferred into a three dimensional structure by further processing steps. However, the diffractive structure is generated here in pointwise contact with a tool and this requires extreme stability of tool and machining equipment for the entire machining operation, to end up with good results. This is an inherent disadvantage of this method and therefore results are not fully comparable with the quality obtained using the other methods.

For certain applications, special output devices have been reported in literature: for recording of rotational symmetric structures for instance a beam deflector using a rotating prisms was proposed [6.5].

The output from the pattern generation and transfer process is one of the following items:

- Masks
  Chromium on glass or fused silica
- DOE Substrates with photoresist mask
- Machined DOE's

From these starting points, multilevel DOE's can be fabricated cost efficiently either by multiple mask processes or by machining a negative master CGOE and replication of its structure.
Direct writing on CGOE substrates is certainly possible, but far too expensive. Furthermore, it does not give a significant advantage compared to the other processes.

6.1.3 Material Selection and Processing

A list of the materials and processes used for DOE production was provided in section 3.3.3 serving as basis for a technological classification. Based upon that, and the guidelines for material selection for space optics provided in chapter 5, suitable materials and processes for the fabrication of space qualifiable hybrid optics shall be selected.
The identification of suitable materials and processes will be oriented on the following requirements:

- Long term stability of optical and mechanical properties (lifetime/reliability)
- Good thermal stability
- Resistivity to cleaning operations
- Stability against damage due to ionizing radiation
- Low outgassing rates
- Good resistivity against atomic oxygen for LEO applications

For the fabrication of transmissive hybrid optics, this leads to a preference for the following materials:

- Optical glasses
  - Cerium stabilized glasses
  - Glasses with high lead content
- Dielectrics/Semiconductors
  - Fused silica
  - Sapphire
  - Silicon
  - Germanium
  - Titanium oxide
  - Magnesium oxide
  - Silicon nitride
  - Gallium arsenide
  - Diamond

The hybrid element design presented in section 4.4.2 for instance was based on the use of an optical glass (LaFN21), which is available in a cerium doped version. However, this list is not exhaustive and there may be other materials well suited for space applications. It is in any case recommended to perform an evaluation testing in order to verify technological compatibility.

For hybrid optics incorporating reflective components the following materials can be used:

- Metals
  - Aluminium
  - Copper
  - Beryllium
  - Gold
- Optical glasses with reflective coatings
- Dielectrics/semiconductors with reflective coatings

The organic materials listed in table 3.3.3-1 are considered less suitable for the envisaged applications in space, mainly due to high outgassing rates and their limited long term stability. However, some of the materials can be considered as potential candidates and a more detailed evaluation testing

should be performed. These are some types of photoresist, if treated with dedicated hardening processes (e.g. high temperature hardbake, UV hardening) and photopolymers like DMP 128, which seem to have good stability to ionizing radiation. Test results for DMP128 were published by Golden [3.37] and Ingwall et al. ([3.22], [3.38]).

The processing methods which can be used for impregnation of the DOE effective structure are all based upon mask processes, except the method of machining, as mentioned already in the previous chapter.

For mask processing, the DOE substrate is coated with photoresist, the DOE pattern is transferred from the master mask onto the photoresist by projection or contact copying, and the substrate is developed. A photoresist pattern remains on the substrate with openings which define the effective structure geometry. This is the starting situation for all mask dependent processes for DOE pattern impregnation. The following methods can be used now to generate the effective DOE structure, either in a single step as bilevel structure or as multilevel structure using several mask processes:

- Etching
  - Dry etching
  - Wet etching
- Deposition
  - Galvanic processes
  - High vacuum deposition processes
- Ion exchange
- Ion implantation

The characteristics of these processing technologies shall now be briefly outlined.

Etching processes impregnate the DOE effective structure into the substrate surface through the openings in the photoresist layer on top of the substrate. Substrate material is removed.

<u>Dry etching</u>

Dry etching techniques make use of etchants like photochemically excited gasses (laser assisted gas etching, photon etching), neutral gasses (gas phase etching), plasma, ion beams or electron beams [6.4]. Most of these etching

processes are based on chemical reactions, which take place at higher temperatures, gas phase etching for instance between 800°C to 1100°C. Ion beams allow for physical and/or chemical etch processes: which type dominates depends on the pressure conditions during the process, the composition of residual gasses and the type of process gas. Ion beam processes allow for anisotropic etching, the other processes run predominantly isotropic. Dry etching is frequently used for fabrication of DOE's for various operational wavelength ranges (see [6.1], [3.39], [3.17]).

Wet etching

The etchants in wet etching processes are acids, alkalis or other chemicals which react with the substrate material resulting in material removal. Wet etching processes are isotropic. Hasman reports about fabrication of DOE's in GaAs using a wet etching technique [3.41].

Deposition techniques create the effective structure on top of the DOE substrate surface. Substrate and effective structure must not consist necessarily of the same material. Such techniques are for instance:

Galvanic processes

Galvanic processes are mainly used in connection with conductive substrates. However, it is also possible to process non-metallic substrates if a conductive surface layer is deposited on top. The effective structure is generated by electrochemical material deposition at the points which are not insulated by the photoresist layer. The process is useful for fabrication of reflective DOE's and production of elements for the infrared range on silicon, germanium, and other conductive materials.

High vacuum deposition processes

The effective structure is created in this case by deposition of evaporated or sputtered material on the DOE substrate in high vacuum. The technologies are similar to those used for fabrication of thin film coatings: thermal evaporation, evaporation by electron bombardment, sputtering, etc. Since the entire substrate surface is coated one has to use a lift-off technique for resist stripping. To allow for stripping agent attack, it is necessary to avoid coating of the sidewalls in the resist openings. This requires tuning of the

process for directional selectivity (anisotropy). Jahns reported about fabrication of Fresnel lenses using this technique. Silicon oxide was deposited on a fused silica substrate and an array of 10 x 10 elements with eight phase levels was produced [3.28]. In contrast to galvanic processes this technology is of course independent of substrate conductivity.

Ion exchange processes are restricted to optical glasses and the fabrication of transmissive elements. The processes are based upon the exchange of sodium ions against ions of higher polarizability. The ion exchange causes an increase of the refractive index at the affected areas, which is used to impregnate the effective structure into the substrate material. Doremus gives a detailed overview about various techniques for ion exchange [3.30]. The ions used for exchange are for instance cesium, rubidium, potassium, silver, thallium, lithium, copper or lead. The exchange is performed usually by contact of the glass with a salt melt, the temperatures are between 150°C and 400°C, depending on the materials, in any case below the glass transformation points. The diffusion can be accelerated by electric field assistance, field strength between 3 V/mm and 150 V/mm have been reported. The achievable refractive index changes depend also strongly on the type of glass used: the highest changes have been reported for the glass TiF6. With silver nitrate at 300°C index changes of up to 0.22 have been generated within some minutes [6.6].
The geometries of the structures generated by ion exchange are not well defined since the process is basically a diffusion process which runs isotropically from a certain depth on. The situation can be improved to some extent by electric field assistance. The DOE's fabricated by ion exchange have an effective structure which is buried in the substrate material. Consequently, it is rather insensitive to mechanical damage.
Ion exchange processes are well characterized since they are used extensively in the field of integrated optics for fabrication of complex waveguide structures ([6.7], [6.8], [6.9], [6.10]). Yatagai has reported about the fabrication of a DOE with ion exchange [3.29].

Ion implantation is a technology derived from semiconductor manufacturing processes. It can be used only for the production of transmissive elements since it results in a buried structure. However, it is not restricted to glass, infrared materials can also be processed with this method. Ions are implanted into the material introducing a refractive index change. A wide range of materials can be used. The technique is described in detail in the literature concerning semiconductor fabrication technologies.

Table 6.1.3-1 links the various materials which were listed initially as promising candidates for space applications with suitable processing techniques (see also table 3.3.3-3).

Material type	Substrate processing					
	Etching		Deposition		Ion exchange	Ion implantation
	Wet	Dry	Galvanic	Vacuum		
Optical glasses		X		X	X	X
Dielectrics/Semiconductors						
Fused silica		X		X		X
Sapphire		X		X		X
Silicon	X	X				X
Germanium	X	X				X
Titanium oxide	X	X				
Magnesium oxide	X	X				
Silicon nitride	X	X				
Gallium arsenide	X	X				
Diamond		X				
Metals						
Aluminium	X	X	X			
Copper	X	X	X			
Beryllium	X	X	X			
Gold		X	X			
Reflective coated glasses		X				
Reflective coated dielectrics/semiconductors		X				

Table 6.1.3-1 Processing technologies for space hybrid optics materials

For fabrication of the hybrid element described in section 4.4.2 as well as for other precision elements in glass a dry etching process with an ion beam is preferred to other methods due to following reasons:

- Ion beam etching can be tuned to be a pure physical process which does not modify the glass properties due to chemical attack
- The heat load during etching can be kept low to avoid tension build-up due to excessive temperature loads
- The process is highly direction sensitive and results in high edge definition
- The process can be fine tuned in terms of etching rate to minimize depth errors
- The process parameters can be easily monitored during etching, thus giving reliable and reproducible results

Besides aspects of functional performance, the dominating requirement for the selection or definition of the manufacturing process is its reproducibility. This requirement is certainly fulfilled by ion beam etching, since this technology is well characterized due to its extensive application in semiconductor industry. The required processing plants including auxiliary equipment are commercially available and are sufficiently supported to have good industrial development perspectives.

This technology fulfils therefore the requirements on manufacturing processes for space optics listed in section 5.3, and a DOE will be manufactured as an example using this technology (see section 6.2). The next section will be devoted to a more detailed description of the manufacturing process for hybrid optics by means of ion beam etching.

6.1.4 Ion Beam Etching

6.1.4.1 Process Description

This section shall describe the characteristics of the ion source/etching plant and the overall process which was developed for the DOE manufacturing.

The broad beam source which was used in the process was a Kaufmann source. This source type was developed by H.R.Kaufmann end of the 1950's in the frame of a NASA space development programme for electrical propulsion systems [6.11]. Such sources generate ions by electron bombardment of a process medium and use DC electrostatic acceleration to accelerate the ions in the direction of a target outside the ionization chamber. Due to this configuration the ion generation process is kept independent and undisturbed from the etching processes on the target material.

Figure 6.1.4.1-1 shows the configuration of the source. The process gas is introduced in the back of the source chamber and is ionized by energetic electrons generated by the cathode filament. A magnetic field parallel to the source axis forces the electrons into twisted paths and no anode current flows unless an electron is deflected by collision with a gas molecule towards the anode at the chamber wall. The ions which are approaching the orifice of the source chamber are extracted and accelerated by the accelerator grid which is at a high negative potential with relation to the extractor.

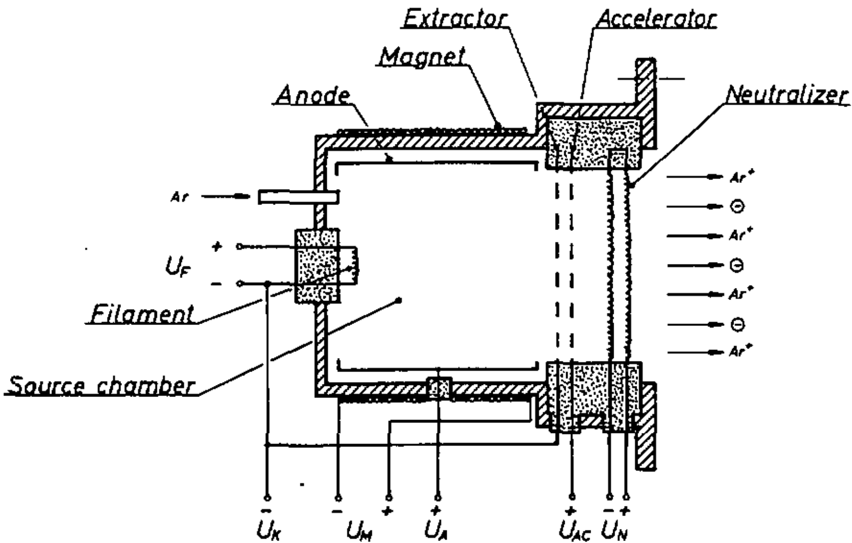

Fig. 6.1.4.1-1 Principles of the ion beam source (Kaufmann type)

This accelerator grid consists of a plate with a dense hole pattern over the entire surface. The accelerator grid material is shielded from direct particle impact by a screen with identical hole positions, which is at the cathode potential. This configuration produces a well collimated ion beam with low non-uniformity and allows for highly directional, anisotropic etching processes. A filament in front of the source aperture neutralizes the ion beam by electron injection, and the result is a plasma consisting mainly of ions and electrons. The neutralized ion beam is hitting the target with a beam power P [W] of:

$$P\,[W] = I \cdot U \tag{103}$$

U [V] is the acceleration voltage and I [A] the overall beam current. The maximum achievable beam current results from the Langmuir-Schottky-Child equation and is:

$$I\,[A] = \frac{4}{9} \cdot \epsilon_0 \cdot \sqrt{2\,\frac{Q_i}{m_i}} \cdot \left(\frac{U^{3/2}}{d^2}\right) \cdot A \tag{104}$$

ϵ_0 is the dielectric constant of the vacuum, Q_i the ion charge, m_i the ion mass, U the acceleration voltage, A the source area, and d the distance between shield and accelerator grid (see [6.12]). Replacing ion charge and ion mass by atomic mass and relative charge results, after having introduced numeric values for the constants used, in an equation for the current density J [A/m^2] of the ion source:

$$J\,[A/m^2] = 5.45 \cdot 10^{-8} \cdot \sqrt{\frac{z}{m_a}} \cdot \frac{U^{\frac{3}{2}}}{d^2} \tag{105}$$

A numeric example may give an impression of the current densities theoretically achievable, taking argon as processing gas:

Atomic mass of argon	m_a = 39.95
Relative charge	z = 1
Accelerator voltagc	U = 1000 [V]
Shield-accelerator distance	d = 0.003 [m]

With these assumptions the current density is:

$$J = 30.297\ [A/m^2]$$

Taking a beam diameter of 100 mm, the overall current is:

$$I = 0.238\ [A]$$

With the accelerator voltage of 1000 V this results in a total beam power of

$$P = 0.238 \cdot 1000 = 238\ [W]$$

According to Kaufmann, these theoretical figures are never achieved in reality, and he quotes that the maximum achievable values are about 20% to 50% of the theoretical limits.

In figure 6.1.4.1-2 is presented a schematic of the ion beam etching system as it was used for the experimental work. Figure 6.1.4.1-3 shows the equipment, a MILLATRON IV System (Commonwealth Scientific Corporation), in the actual configuration equipped with auxiliary cooling systems and control instrumentation.

The ion beam is injected from the source (visible on the right side of the vaccum chamber) into a cylindrical vacuum chamber in the direction of the sample. The sample is mounted in a special holder on a stage, which can rotate and perform in addition lateral motions to average beam non-uniformities if larger samples are etched. Stage and sample holder are cooled during etching in order to keep the sample temperature within reasonable limits (see also section 6.1.4.2). The angle of the stage with respect to the beam direction can be adjusted, since the etch rate achieved depends also on the ion beam incidence angle on the target. The optimum incidence angle with respect to the normal on the target surface is approximately 30° for glasses [6.13]. The beam current is measured with a probe placed close to the sample. This probe consists of a metallic plate with defined area, which is mounted insulated from the chamber metal. It is connected to cathode potential via an ammeter. The ion beam current density can be calculated from the measured current and the known probe area. Since the etching depth depends on the time integral of the beam power it is recommended to register the ion current time integral (i.e.deposited charge in Coulomb) on a plotter and to control the process via

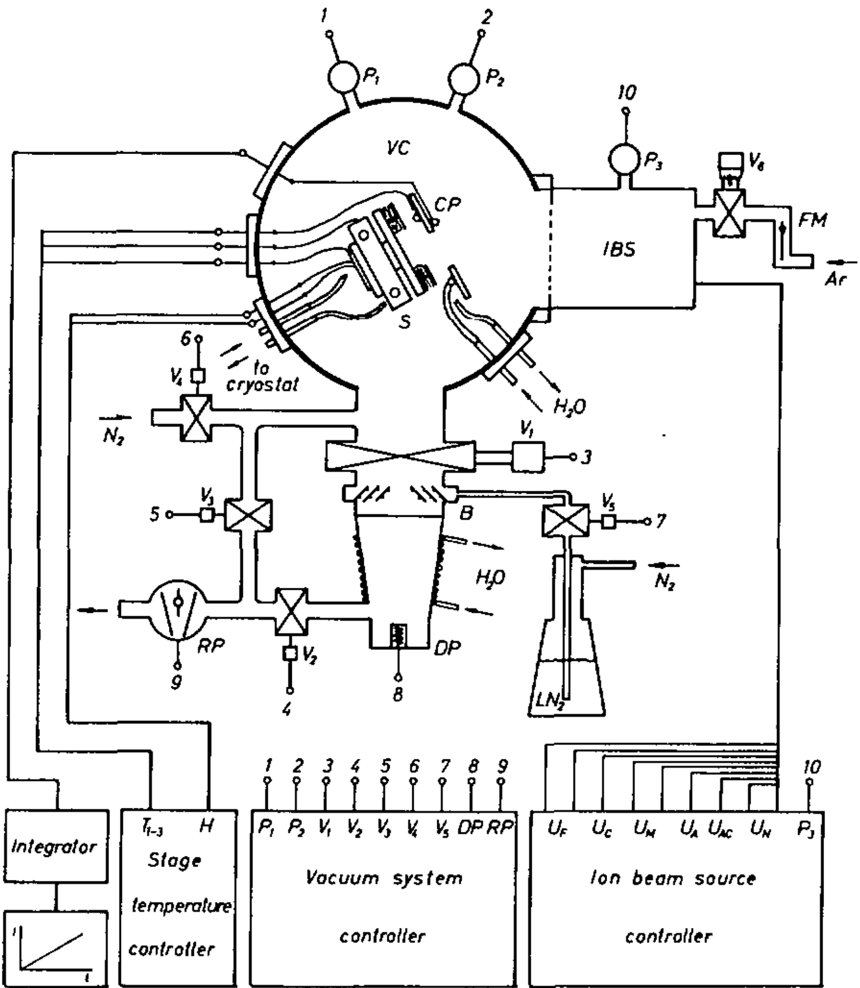

VC	Vacuum Chamber	H	Heater supply
S	Stage	$T_{1\text{-}3}$	Thermocouples
IBS	Ion beam source	$P_{1/2}$	Coarse/Fine vacuum gauge
FM	Flow meter	P_3	Ion source pressure gauge
BC	Cooled baffle	$V_{1\text{-}5}$	Vacuum system valves
DP	Diffusion pump	V_6	Argon pressure regulator valve
RP	Rotary pump	V_{xx}	Ion beam source supply voltages

Fig. 6.1.4.1-2 Schematic of ion beam etching system

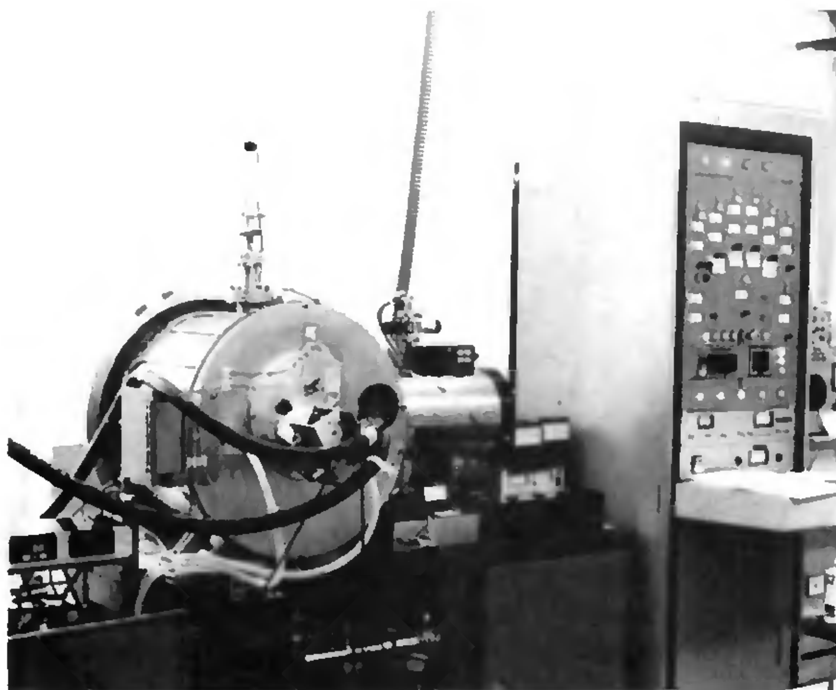

Fig. 6.1.4.1-3 Ion beam etching system used for DOE etching (MILLATRON IV Commonwealth Scientific Corporation)

the integral value while keeping the accelerator voltage constant.
In the process described here argon is used as the process gas. Since argon is an inert gas, the etching of the sample is a purely physical process due to ion impact on the target surface. However, on the path between source orifice and target the electrons in the plasma can collide with residual gas molecules and can cause their ionization.

The ionization can result in highly reactive products like atomic oxygen or nitrogen, which also cause chemical etching of the target (reactive ion beam etching, RIE, makes use of this by using process gasses like CF_4, O_2, CCl_4 for instance, or additions of reactive gasses to an inert process gas). Chemical etch reactions disturb the anisotropy of the process and can cause changes in substrate surface material structure leading to deterioration of surface optical properties.

To minimize similar disturbances caused by residual gasses the chamber pressure before start of etching has to be as low as possible, at least in the range of 10^{-5} mbar. During etching the chamber pressure shall be kept at about 10^{-4} mbar. The pressure inside the ion source is of course higher and depends - via the thermodynamics of the ionization process - also on the electrical parameters, like filament current, cathode voltage, etc. The gas inlet valve must allow for very fine adjustments of low gas flows. If this is the case an active flow regulation is not required.

The vacuum system shall be dimensioned such that it can cope with the process gas and the large number of etching products which can be volatile and non-volatile. Regular cleaning of the chamber from etch products is recommended to achieve good high vacuum and reproducible sample cleanliness.

The vacuum chamber walls shall be equipped with a heating system to support material degassing during evacuation and a water cooling system to keep the chamber walls cool during etching. If a good starting vacuum is established, the etching process is controlled typically with the following operational parameters:

- Type of process gas
- Process gas parameters
  - Pressure in ion source
  - Flow rate
- Ion source electrical parameters
  - Cathode filament current
  - Cathode voltage
  - Accelerator voltage
  - Magnet current
- Geometry factors

The preadjustment of these parameters in experimental runs using test samples is required prior to start of the actual DOE fabrication. The determination of the etch parameters and the associated etch rates is discussed in section 6.1.4.3.

Figure 6.1.4.1-4 shows a flow chart of a typical etch process.

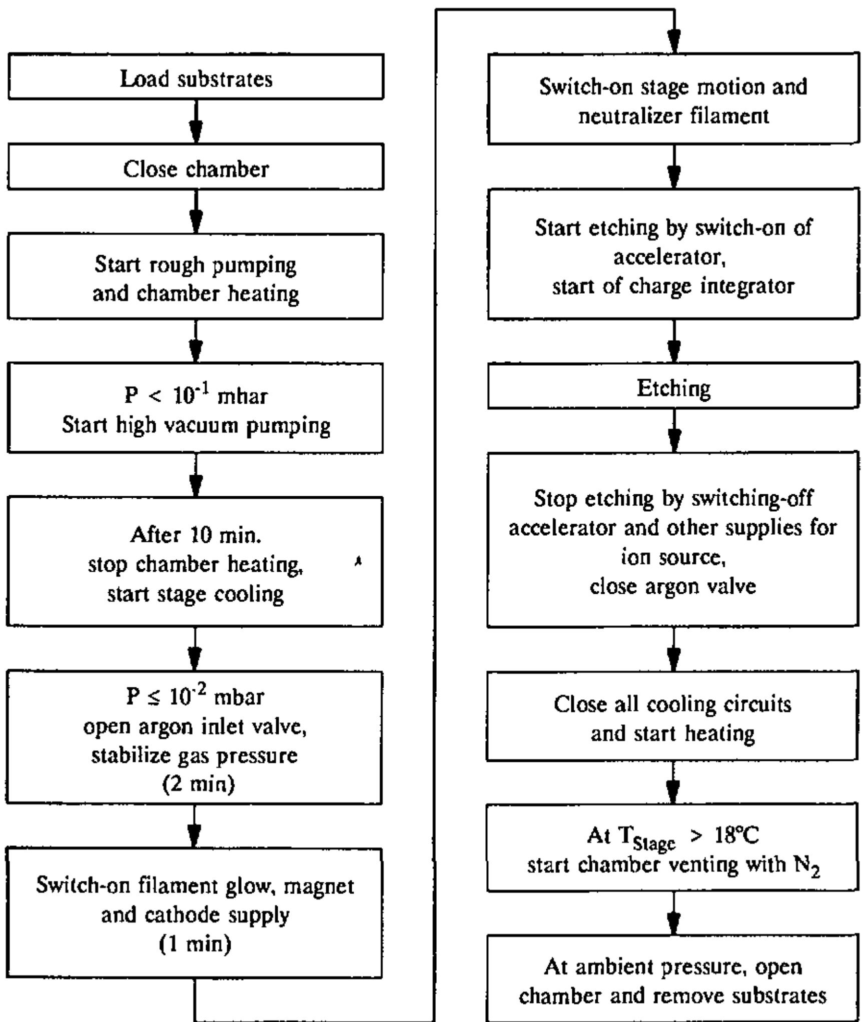

Fig. 6.1.4.1-4 Ion beam etching process flow chart

6.1.4.2 Process Thermal Control

The theoretical beam power density for argon ion beams, assuming a grid-accelerator distance of 3 mm and an accelerator voltage of 1000 V results in beam power densities in the order of 30 kW/m^2. Taking into

account that the values achieved in reality are only about 20% to 50% of that, the power density at the sample is still in the order of 6 to 15 solar constants.
Such power densities lead to strong temperature increase of the sample during etching, depending on etch times, several hundred degrees °C are possible. This can cause material tension and other degradations in the optical material, moreover, the photoresist mask starts melting and looses its pattern definition.
Figure 6.1.4.2-1a to c shall illustrate this: (a) shows a test pattern in photoresist after 5 min. etch time. The structure is well defined and no degradation is visible. (b) shows the same type of structure, but after 20 min. etch time. The resist started melting already. Both photographs show test pattern with 250 lines/mm which are part of a larger test plate. The magnification is 400x. Figure (c) shows the same type of test plate after ca 60 min. etch time (25x magnification): the resist is here strongly degraded and partly carbonized, it cannot be removed any more with usual stripping agents.

This highlights the necessity for an efficient thermal control of the sample during etching and the experimental investigations done on this field and the results obtained shall be reported in the following.
There are basically two strategies to keep the sample temperature low during etching: one is to work in intermittent operation, the other is to implement a suitable active and/or passive thermal control system for stage and sample. In any case, the ion beam diameter should be kept as small as possible to cover the area to be etched, but large enough to avoid edge sputtering effects.
The intermittent operation with beam switch-off has the disadvantages that the beam is frequently operated in the instable initial phase after switch-on and that the total processing time is more than doubled since the cool down time must be longer than the etch time (exponential law!). In addition, the sample is subjected to strong thermal cycling which is normally not desired for precision optics. To avoid the disadvantages of the unstable period after switch-on, it is possible to install a shutter for sample protection and to operate the source in continuous mode, switching the beam on and off with the shutter. However, this cannot solve the other problems mentioned above.

It was therefore decided to concentrate on the development of a thermal control system consisting of an active cooling system and efficient thermal insulation/shielding.

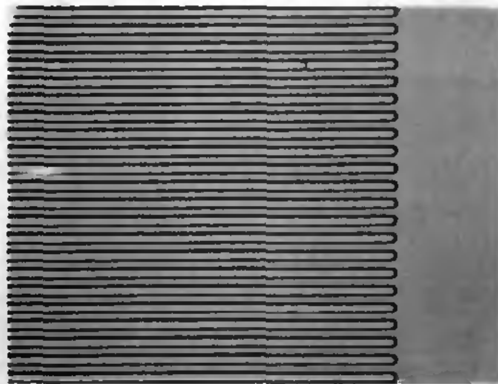

(a)

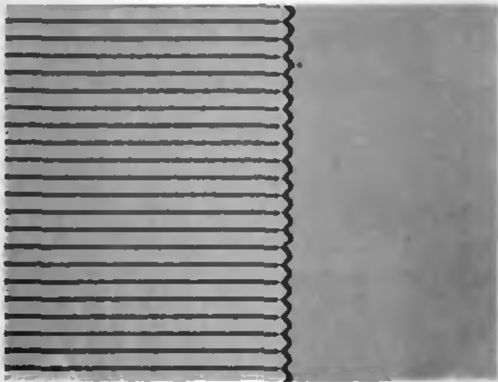

(b)

(c)

Fig. 6.1.4.2-1 Degradation effects of photoresist pattern by overheating during ion beam etching (see text)

Figure 6.1.4.2-2 shows the configuration of the stage with the sample used for the first experiment. This configuration represents the worst case condition in terms of sample thermal control and was the starting point for the thermal control design iterations. A glass plate (LaFN21 coated with photoresist) was held on the stage cold plate by an aluminium plate, which was fixed with four steel screws. No contact medium was used at the interface between glass plate and cold plate. Thermocouples were fixed at the positions indicated at the drawing.
The ion beam operational conditions for all tests reported here in this connection were as follows:

▪ Accelerator voltage	900 V
▪ Ion beam current density	approx. 2.93 A/m^2
▪ Beam power	20.7 W
▪ Beam diameter	100 mm
▪ Chamber pressure	ca. $8 \cdot 10^{-4}$ mbar

For all tests the stage was tilted by 30° w.r.t the beam incidence direction.The temperatures were measured at various points using copper-copper/nickel thermocouples (0.05 mm diam. each), with teflon insulation, connected to an external thermometer via a high vacuum thermocouple feedthrough. The instrument was electrically compensated and had a selector switch for up to 8 thermocouples. The measurement accuracy of the instrument was 0.1% with an error for thermocouple linearization of <0.2°C. The thermocouples were fixed such that errors due to α/ϵ differences with the base material to be measured were minimized.

A first run was made in the above described basic configuration and figure 6.1.4.2-3 shows the temperatures at various points for different operating conditions: after evacuation of the chamber the neutralizer filaments were switched on first (without ion beam) in order to determine the influence of their radiation. The filaments dissipate ca. 54 W. This power caused, within 32 min., a temperature increase of 3°C at the glass sample surface located at a distance of ca. 30 cm. The influence of the neutralizer on the overall thermal control can be therefore considered negligible.
After a cool down period the ion beam was switched on, first with a low magnetic field and after 8 minutes with the nominal one. The temperature increase of the glass plate is clearly visible. The beam was again switched off for a longer cool down period. After a further switch-on with nominal beam conditions the temperature at the glass plate increased by 36°C within

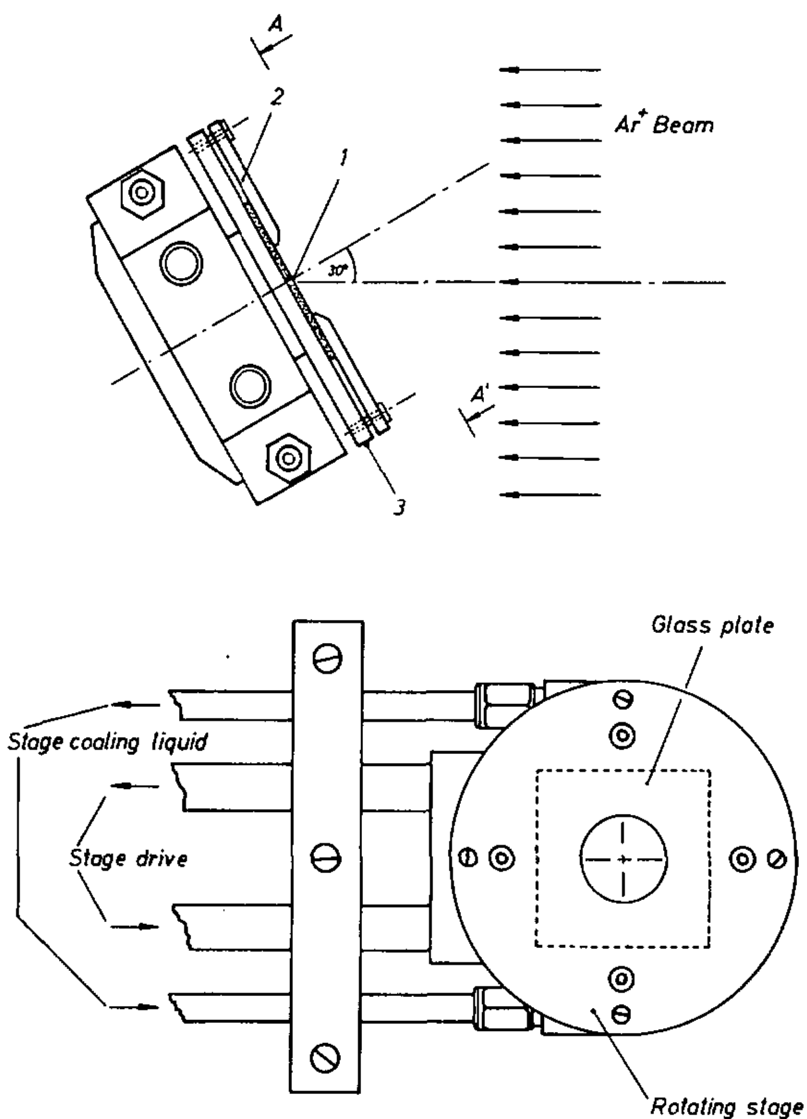

Location of temperature sensors:
1 Glass surface
2 Glass plate holder
3 Stage cold plate

Fig. 6.1.4.2-2 Basic stage configuration (configuration 1)

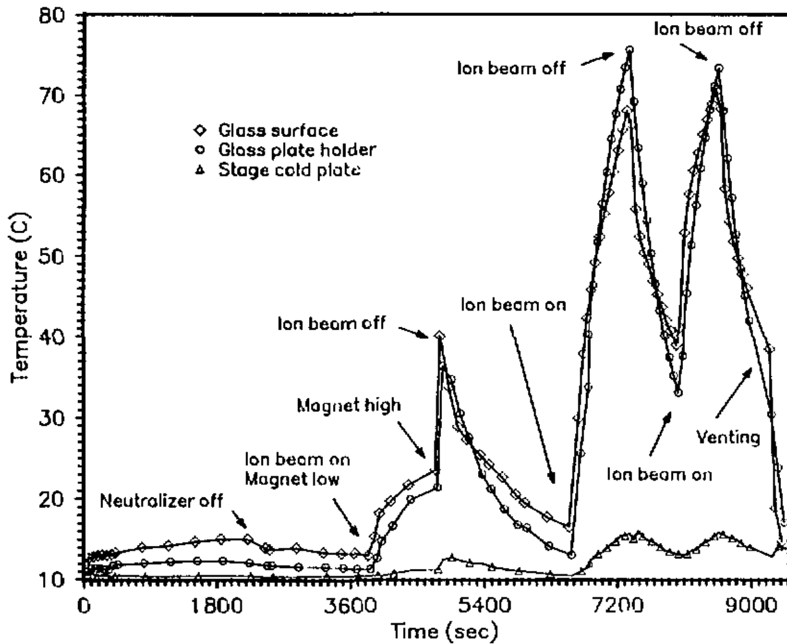

Fig. 6.1.4.2-3 Process temperatures for configuration 1 (Basic stage configuration)

13 min., the temperature of the aluminium holder was raised from 18°C to 67°C within the same time. The stage cold plate temperature was only marginally affected by this increase, resulting from the bad conductive coupling (no interface filler).

After this first measurement the configuration was changed to the one indicated in figure 6.1.4.2-4. The aluminium plate holder was replaced by a copper plate which fully surrounded the glass plate and was in direct contact with the stage cold plate. The coupling between the glass plate and stage cold plate and copper plate to stage cold plate was improved by using an interface filler. A thin aluminium plate (0.5 mm) was fixed in front of the copper plate at a distance of ca. 10 mm by four teflon stands to provide good thermal insulation. A small superinsulation blanket (30 layers aluminized Kapton foil with Dacron spacers) was placed between the copper plate and the aluminium top to minimize radiative exchange. The stage cold plate was cooled with water, as before.

Figure 6.1.4.2-5 shows the temperature profiles measured with this configuration. The temperature increase of the glass plate was now only

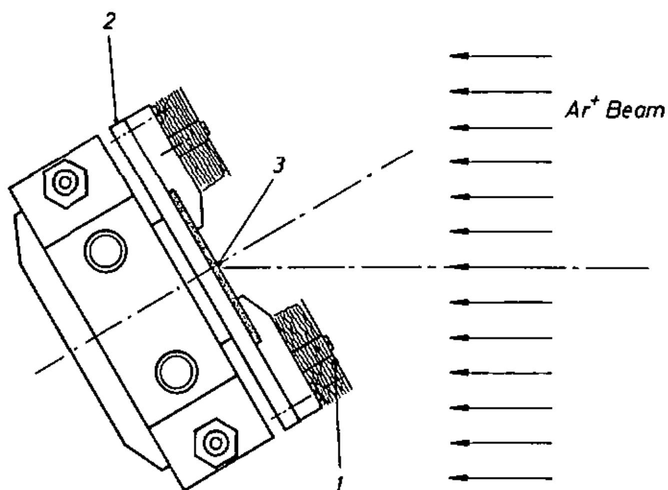

Temperature sensor locations:
1 Aluminium cover plate
2 Stage
3 Glass surface

Fig. 6.1.4.2-4 Stage configuration 2

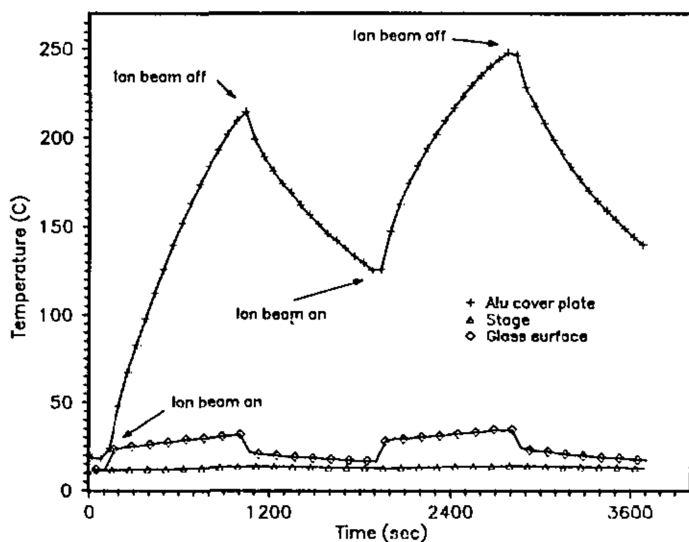

Fig. 6.1.4.2-5 Process temperatures for configuration 2

20°C within 14 min., resulting in a final temperature of 31.5°C. The aluminium plate in front reached a temperature of 214°C within the same time. The effect of the interface filler was determined in a further test run which was performed without filler. The temperature increase of the glass plate in this case was ca 50°C within the same etch time. Since the thermal design had to cope with etching times of more than 60 minutes, a further iteration was required. In figure 6.1.4.2-6 is presented a schematic of this configuration. The same stage configuration was used, but a water cooled copper plate was put in front of the stage, leaving an opening for the ion beam large enough for etching of a sample of 22 mm diameter.

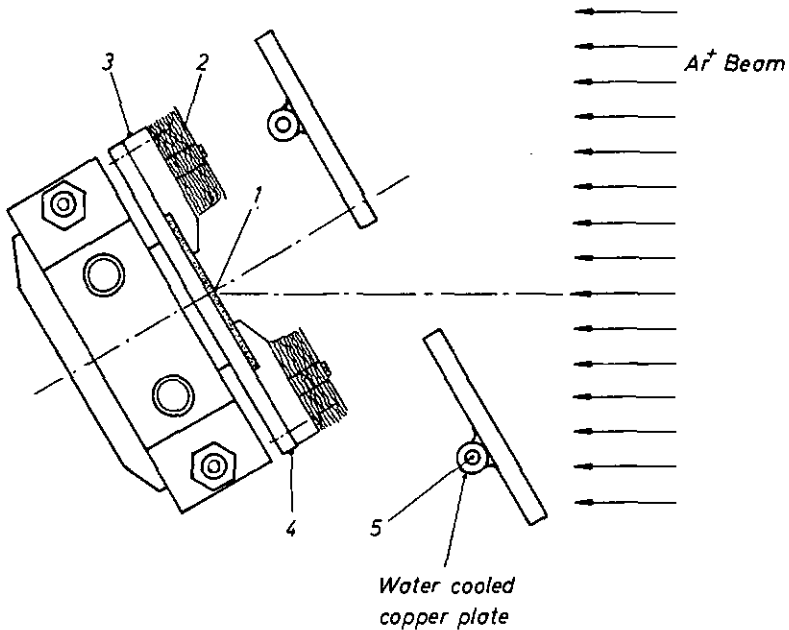

Temperature sensor locations:
1 Glass surface
2 Aluminium cover plate
3 Glass plate holder
4 Stage
5 Cooling water

Fig. 6.1.4.2-6 Stage configuration 3

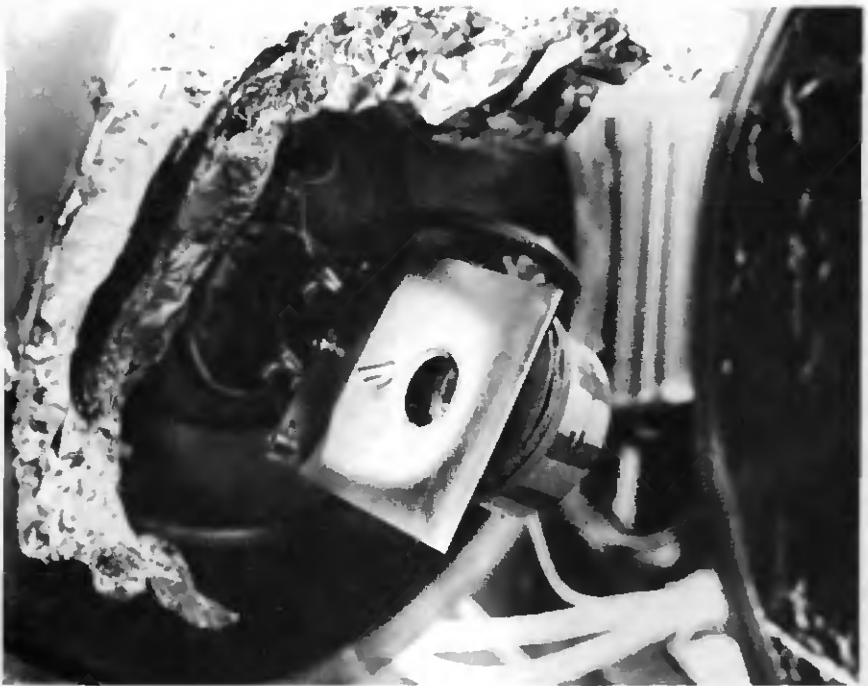

Fig. 6.1.4.2-7 Stage with cooled thermal shield (configuration 3)

Figure 6.1.4.2-7 shows the stage with the sample holder which is mounted with various motion mechanisms at the vaccum chamber door. The water cooled copper plate is visible in front of the stage. Its chromium plating is already eroded by ion beam attack. The small cylinder close to the opening is the beam current probe, which is mounted on the copper plate with an insulated feedtrough. Behind the copper plate the multilayer insulation package can be seen, which is protected with a thin aluminium shield. This insulation is fixed on the sample holder, a gold plated copper plate which is hold the glass sample to be etched in good contact with the cold stage plate. The aluminium foil is used for protection of the cables and the water supply fittings.

To achieve lower temperatures at the stage, the water cooling was replaced by a cryostat cooling circuit which allowed the stage to reach temperatures of - 15°C. To avoid condensation on the sample surface and other cold areas,

a dedicated electrical heater was implemented to accelerate warming-up of the stage prior to venting/exposure to ambient air after opening of the chamber.

Figure 6.1.4.2-8 shows the results achieved with this concept. For an etching time of more than 80 min. the glass sample temperature did not increase beyond 27°C from a starting temperature of 19°C. The temperature increase of the aluminium cover plate was also kept at a moderate level with a maximum of about 85°C. This configuration was considered suitable to keep the thermal loads of the glass samples sufficiently small and it was used therefore for the fabrication of the diffractive elements, as described within the following sections.

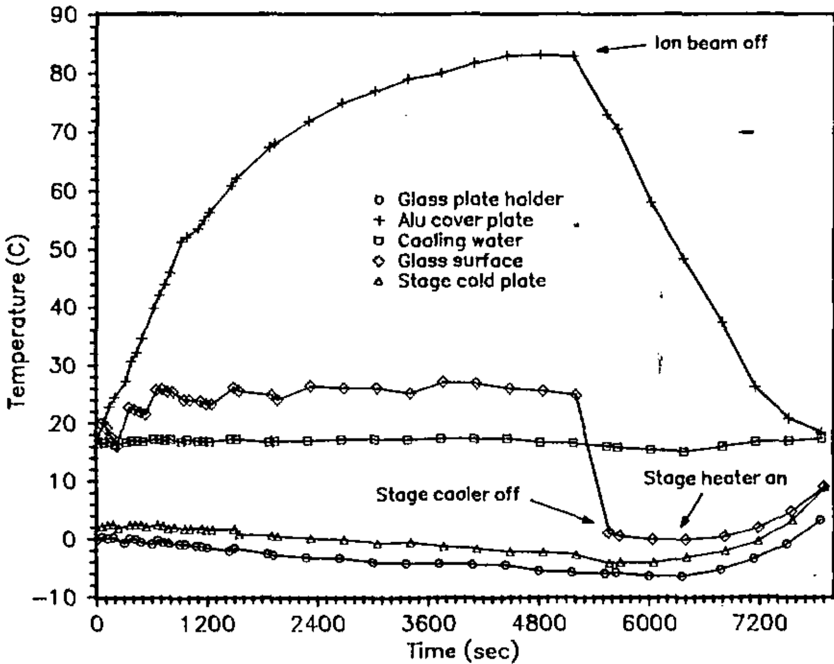

Fig. 6.1.4.2-8 Process temperatures for configuration 3

6.1.4.3 Etch Rates of Optical Materials

Ion beam material etch rates depend on the following factors:

- Material properties
- Acceleration voltage
- Type of process gas
- Influence of residual/reactive gasses
- Angle of incidence and chamber geometries

The dominating factor is of course the acceleration voltage and the type of process gas used because this defines the ion beam current density at the target. With the number of influencing factors it is necessary to determine the material specific etch rates in the particular etching plant used, and this was also done in this case with following operating conditions:

- Process gas: Argon
- Initial chamber pressure: $3.5 \cdot 10^{-5}$ mbar
- Ion beam current density: 0.29 mA/cm^2

Most of the etch tests have been carried out with the glass LaFN21 from Schott, which was selected for the manufacturing of the hybrid optical element described in section 4.4.2.

Figure 6.1.4.3-1 shows the dependence of the etch depth with time for this glass. The dispersion of some of the results is due to the fact that some early test runs were not controlled by integration of the ion beam current. However, based upon these results the etch depth can be assumed to be linearly dependent on the etching time.

In addition to the detailed investigations on LaFN21, 19 other optical materials have been tested. The material selection included seven cerium doped glasses and their undoped counterparts. For each material type two samples were etched in different batches and the etch depths were measured at 10 points minimum per sample. From these results an average etch rate was calculated, which takes into account the batch variation.

The time integral of the current density for all these test runs was 534 $\pm$1.2 Coulomb/cm^2. The accuracy of the integrator (AMEL Model 721) was quoted to be $\pm$0.5%. This leads to an overall accuracy for the charge

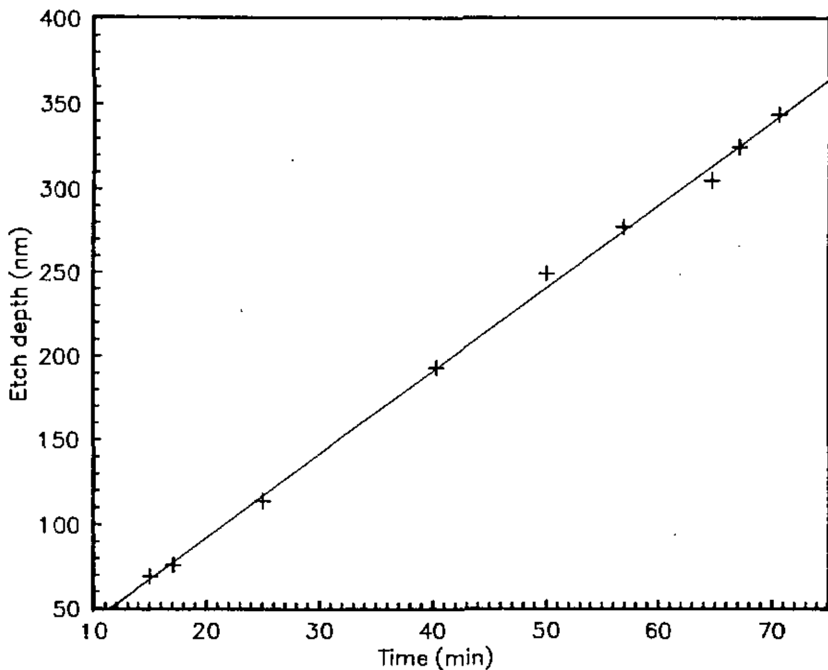

Fig. 6.1.4.3-1 Etch time vs. etch depth for LaFN21

measurements of ±3.9 Coulomb/cm^2 p-v or ±2.9 Coulomb/cm^2 rss. For the depth measurements an Alphastep 200 (Tencor) was used, the technical data of which are provided in section 7.2.1.

Figure 6.1.4.3-2 shows the dependence of the etch rate on the Knoop hardness as an example. It gives an indication that the etch rates are linked to also to other material characteristics, like micro hardness for instance.

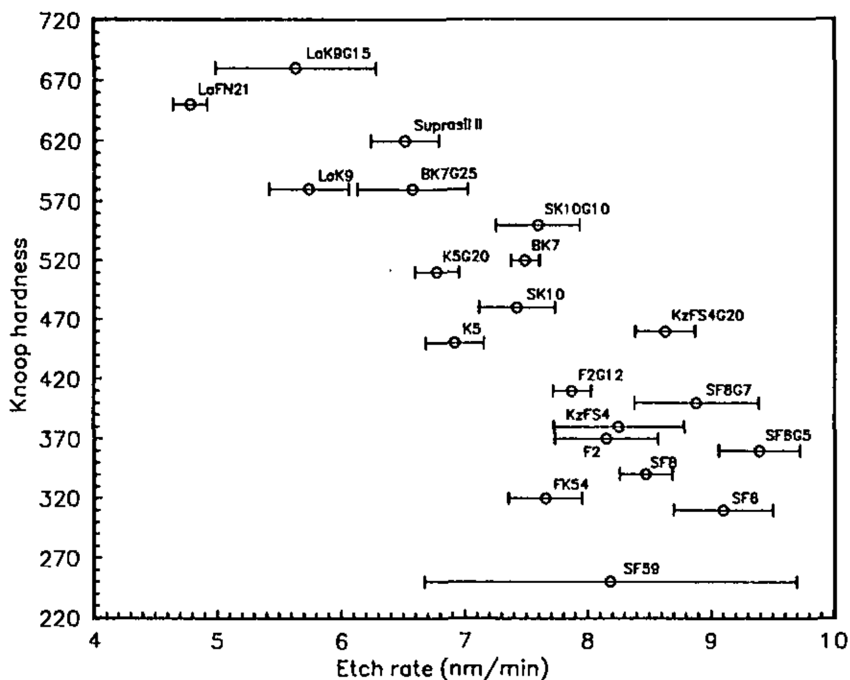

Fig. 6.1.4.3-2 Etch rates of optical materials vs Knoop hardness

6.2 Description of Hybrid Optics Manufacturing Process

6.2.1 General

This section is devoted to the description of the manufacturing process of a hybrid achromat, the design of which was described in section 4.4.2. It was the intention to prove thereby the validity of the design approach and to demonstrate the technological feasibility of its manufacture. Furthermore, it was the aim of this undertaking to study the processes involved and to identify critical aspects as early as possible.
Section 6.2.2 describes all steps from transformation of the design data to the final multilevel DOE. Since it was decided to split the hybrid into a DOE on a plane plate and a plano-convex lens it was necessary to develop an assembly procedure accurate enough to meet the demanding alignment tolerances between the DOE and the lens optical axis. The alignment tools and the assembly process for DOE and lens are described in section 6.2.3.

6.2.2 DOE Manufacturing Process

The diffractive element described in section 4.4.2 as part of a hybrid was designed as multilevel element with eight digitization levels, three masks were therefore required for manufacturing (mask numbers 1, 2 and 3). The masks were fabricated with an electron beam writer as positive chromium masks. In preparation for that the mask patterns which were defined by data files specifying ring pitch and width had to be transposed into a two dimensional ring pattern. This was done by processing with a special CAD system for electronic circuit design (CALMA) which provides output files suitable for the electron beam preprocessor (see section 6.1.2). In addition to the diffractive pattern as central feature of the mask design several other motifs had to be incorporated, which served technological control purposes: etch depth test marks, alignment marks and a ring for centering control. These motifs were directly created at the CAD workstation and linked with the files defining the diffraction pattern. The alignment marks represented references for adjustment of the masks with respect to the etched patterns and the centering control ring served as a reference for the DOE/lens centering operation during the cementing. These patterns had to stay on the DOE substrate throughout the entire process and were represented in form of an aluminium pattern. Consequently, a dedicated mask had to be designed for the aluminium etching process (mask number 0).

As mentioned already in section 4.2.2. the split of the hybrid into a plano convex lens and a DOE on a plane plate with subsequent cementing of the two, was motivated by the necessity of using existing tools as far as possible. This was also the reason of defining the format of 50 mm x 50 mm for the DOE substrate. This format is a standard substrate size for photolithographic processes and is supported by a wide range of handling devices, vacuum chucks, plate holders and other auxiliary equipment.

The lay-outs for all four masks are shown in figures 6.2.2.-1 to 4. On the drawings the square substrate shape is indicated, however, the masks blanks were round with a 3 inch diameter. The masks are designed for use with positive photoresist, i.e. the openings in the chromium represent openings in the photoresist layer, once exposed via the mask and developed. The photoresist used in the photolithographic process was AZ 1470 (Hoechst). Figure 6.2.2-5 shows the combination of all four mask patterns as they will appear on the finally etched DOE substrate.

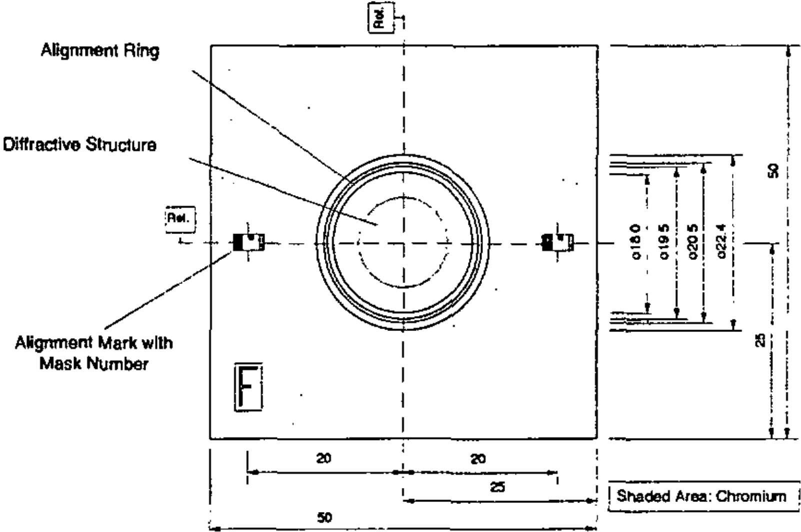

Fig. 6.2.2-1 Mask layout - Level 0 -

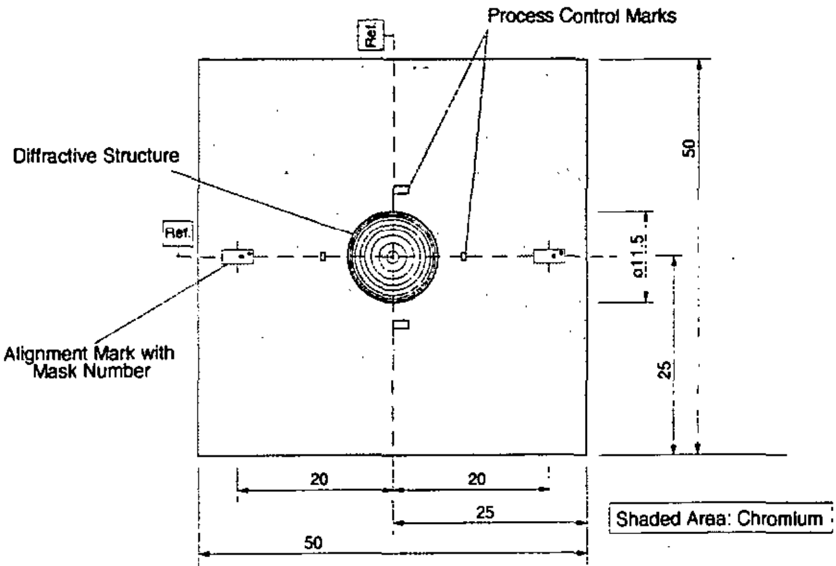

Fig. 6.2.2-2 Mask layout - Level 1 -

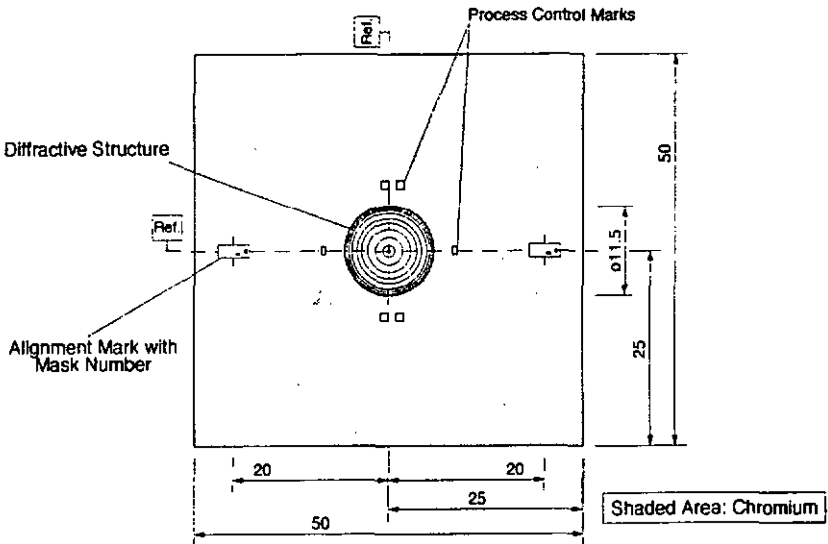

Fig. 6.2.2-3 Mask layout - Level 2 -

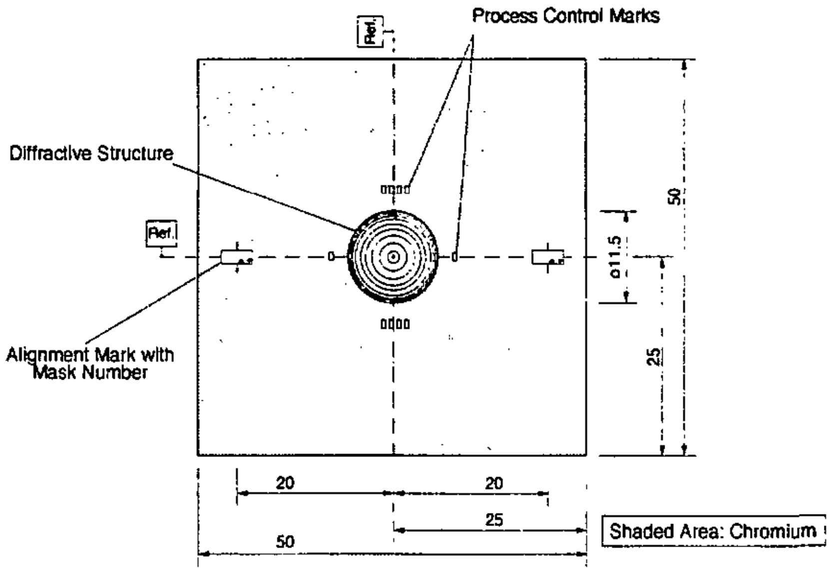

Fig. 6.2.2-4 Mask layout - Level 3 -

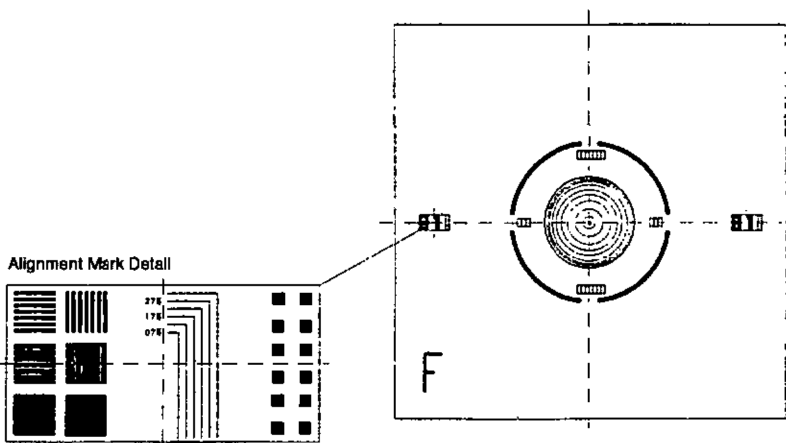

Fig. 6.2.2-5 Etch pattern on final DOE (combined masks)

The processing steps for fabrication of the DOE are shown in figure 6.2.2.-6. It does not seem to be necessary to discuss the individual steps in detail, only some particulars of the process should be mentioned: due to the fact that the substrate material is a special optical glass, the standard cleaning procedures for semiconductor materials cannot be used, since they involve aggressive chemicals like hot sulphuric acid or hydrogen peroxide. All glass cleaning operations during the process described here were performed exclusively with acetone, isopropanol and demineralized water in MOS quality (cleanliness class 0). To avoid excessive thermal stress of the glass substrates the hardbake, after photoresist deposition, was performed in several temperature steps with slow cool down. The thermal control during ion beam etching required use of an interface filler for improvement of the conductive coupling between the substrate and the heat sink (see section 6.1.4.2). To avoid contamination of the process chemicals, careful substrate cleaning was required to completely remove the filler, using at least three solvent baths. The long ion beam etching times lead to partial carbonization of the photoresist on the substrate. After stripping, a further cleaning process by oxidizing plasma was necessary to remove resist residues completely.

The ion beam etching process was controlled via the integral of the beam current and the etch parameters were calibrated for each run. The etch parameters varied slightly from batch to batch, but a typical set for the individual levels was:

▪ Process gas	Argon
▪ Starting chamber pressure	$\leq 3.5 \cdot 10^{-5}$ mbar
▪ Accelerator voltage	900 - 1000 V
▪ Ion beam current density	0.28 mA/cm^2 to 0.37 mA/cm^2
▪ Etch times	
- Mask 1	ca. 1100 sec
- Mask 2	ca. 2200 sec
- Mask 3	ca. 4400 sec

Overall, 3 batches (15 pieces) with the final masks have been fabricated to characterize the process and all steps involved sufficiently well to be able to establish reliable and reproducible manufacturing processes with the required documentation.

The alignment of the masks 1 to 3 was performed with respect to the outer aluminium alignment marks on the substrate and the symmetry of the ring

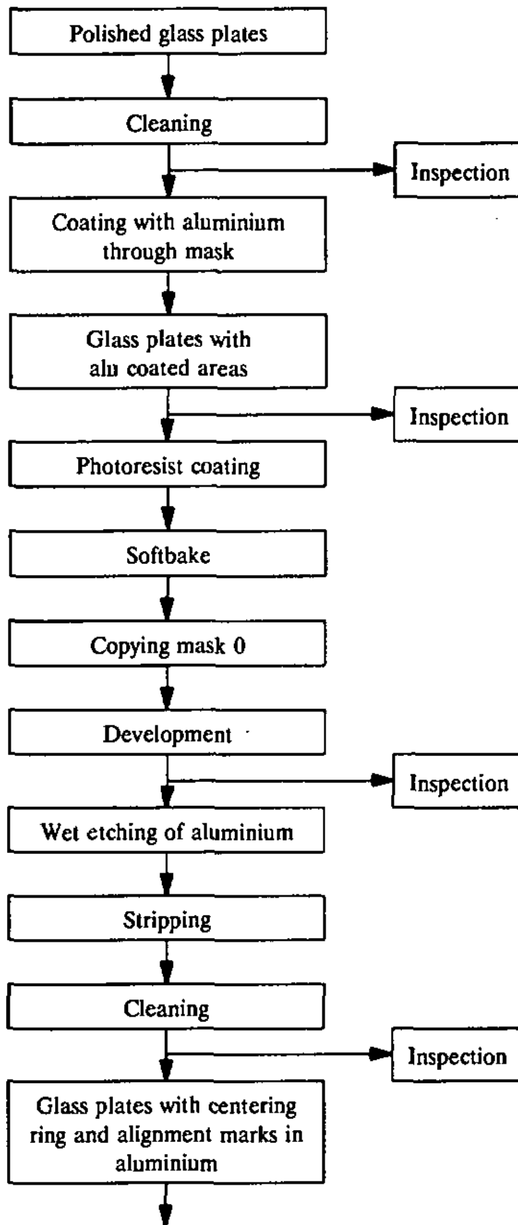

Fig. 6.2.2-6 DOE manufacturing flow chart

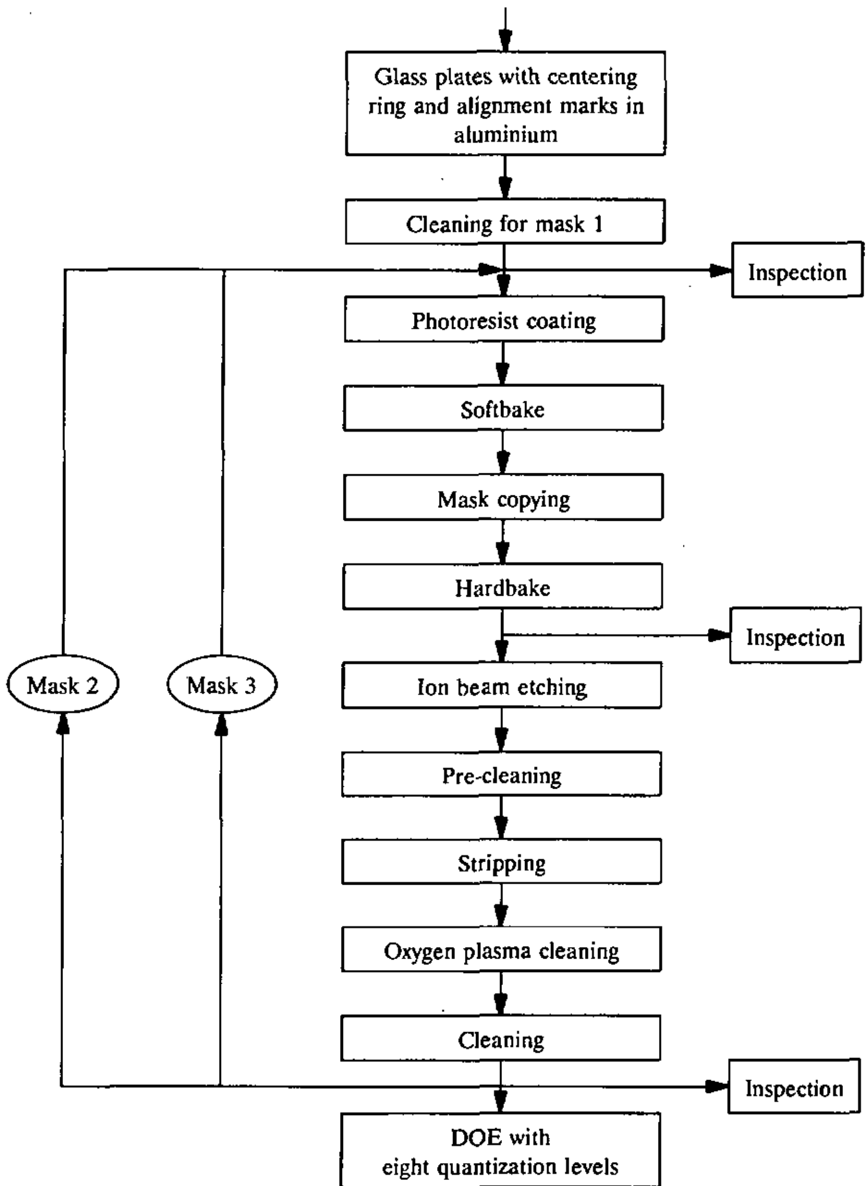

Fig. 6.2.2-6 (cont'd.) DOE manufacturing flow chart

structure. The mask aligner used for this operation gave an alignment accuracy of better than 1 μm. The resist exposure was performed in contact with the mask. It was important to keep the temperatures constant throughout the entire process, to avoid dimensional changes due to temperature differences between substrate and mask. Misalignments between the new mask and the features already on the substrate cause disturbances in DOE symmetry.

Figure 6.2.2-7 shows an example for a slight misalignment between two masks and the corresponding profiles in x- and y-direction. In x-direction (a) the profile has eight clearly defined steps, whereas in y-direction (b) a peak is visible in one of the steps.

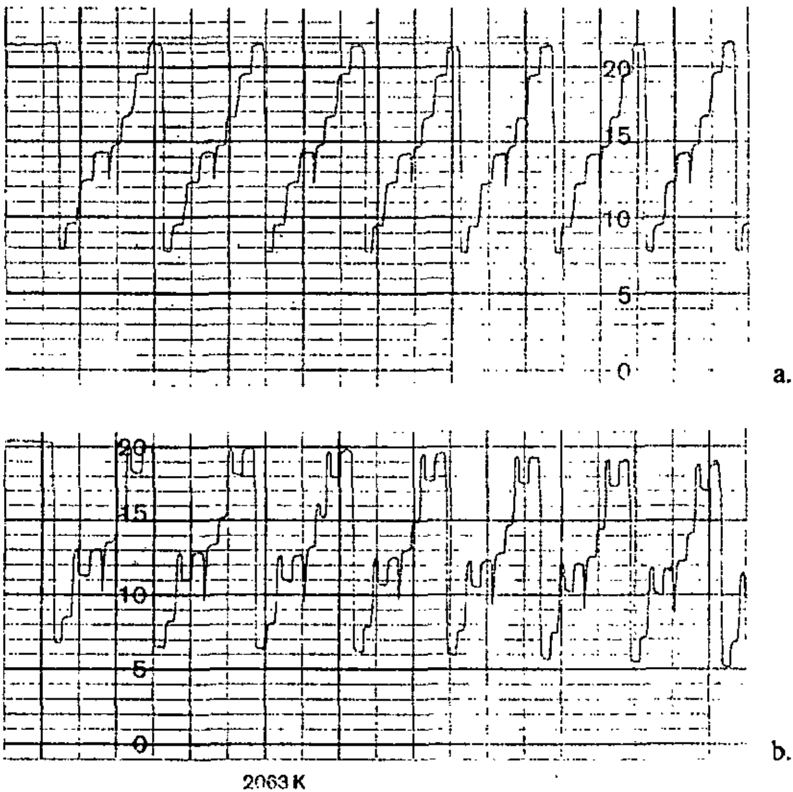

Fig. 6.2.2-7 Mask misalignment effects: x-direction (a), y-direction (b)

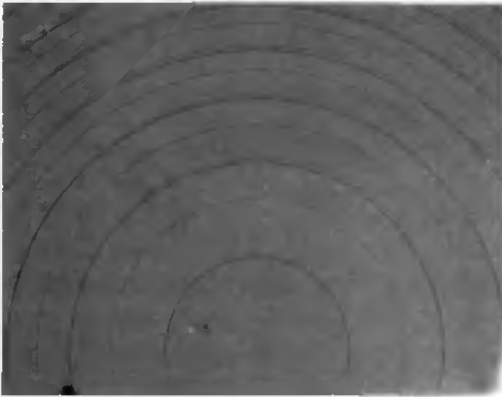

Fig. 6.2.2-8 Mask misalignment effect on DOE structure

Figure 6.2.2-8 shows a photograph of a misaligned DOE structure. This type of misalignment causes astigmatism in the final hybrid lens.

As indicated in the process flow charts, inspection and control steps were implemented at various points: the optical quality of the substrates in terms of flatness and surface defects was measured at the beginning of the process and at the end, prior to assembly. Interferometric measurements showed a surface flatness which was always better than $\lambda/10$ p-v over the inner test area of 25 mm diameter. After processing this has not changed significantly. The surface defects were found to be compliant with the specifications. After completion of the photoresist mask on the substrate an optical inspection was performed to be able to correlate the final etching results with the start conditions, in terms of contamination for instance.
After etching and complete stripping the surface quality was inspected to identify potential degradations or surface flaws due to the etching process.

Etch depth measurements were performed with three different instruments:

- Talystep (Rank, Taylor & Hobson)
- Alphastep 200 (Tencor)
- Laser Stylus RM 600 (Rodenstock)

Figures 6.2.2-9a to c shows examples of DOE etch depth measurements performed with these instruments on different samples.

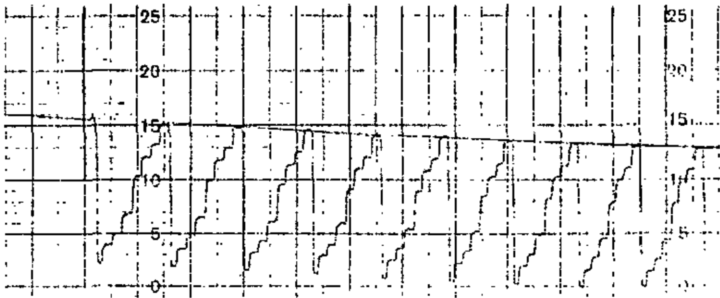

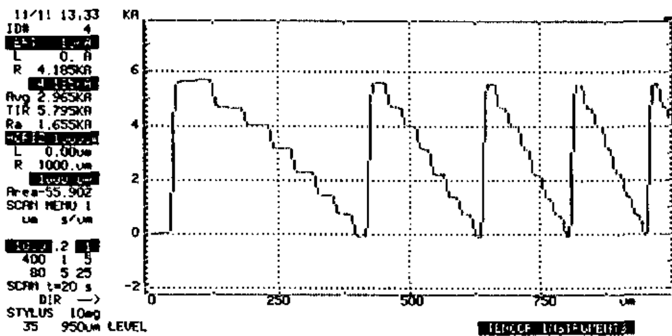

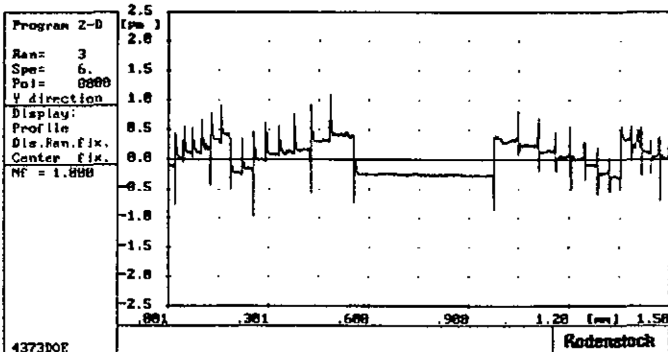

Fig. 6.2.2-9 Etch depth measurements performed with Talystep (a), Alphastep 200 (b) and Laser Stylus (c)

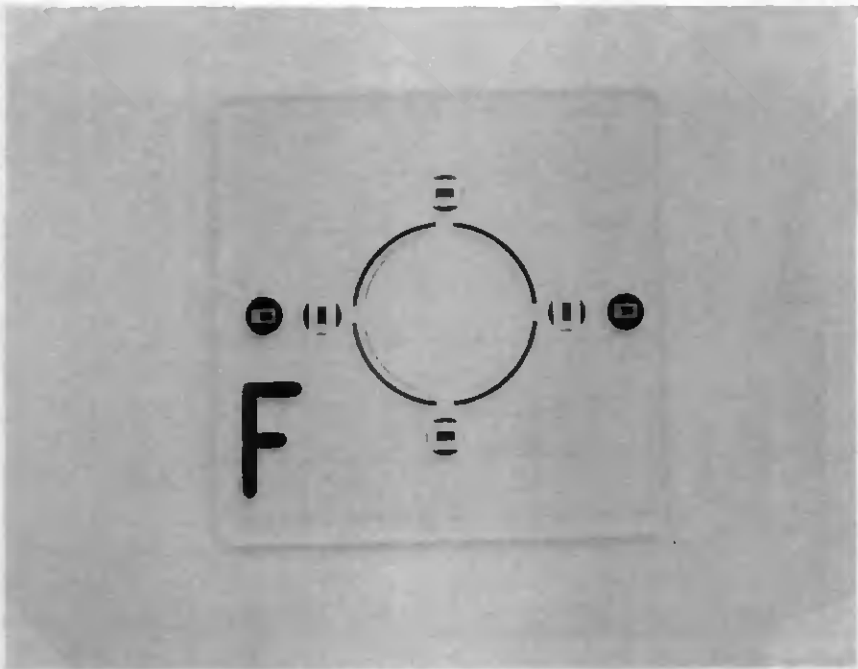

Fig. 6.2.2-10 Etched DOE in centre of glass substrate with alignment marks (substrate size 50 mm x 50 mm, DOE diameter 12.5 mm)

Figure 6.2.2-10 shows a photograph of the final DOE on the substrate with all alignment marks. The DOE is in the centre of the glass plate inside the aluminium centering ring. The two outer pattern on left and right side of the DOE serve for mask prealignment and contain some fiducial marks for the mask processing. The F mark facilitates the orientation of the plate during the process (back and frontside). The DOE will be cut out of the substrate later on during the hybrid assembly process.

Figure 6.2.2-11 shows a microphotograph of part of the diffractive structure close to its centre. The photograph was taken with a differential interference contrast microscope with incident light. The periodicity of the structure is clearly visible: the brighter lines indicate the π-phaseshift steps, whereas the 2π-steps are located between the wider separated lines, barely visible in some areas.

Fig. 6.2.2-11 Microphotograph of DOE structure (differential interference contrast, incident light)

Figure 6.2.2-12a and b shows the etch profile inspected with a scanning electron microscope (SEM). The eight digitization levels are clearly visible in (a), the fine lines running across the structure are marks of the profilometer diamond tips. The quantization levels requiring longer etch times (over 1 hour) suffer from edge degradation due to secondary sputtering effects. An enlarged detail of one of these edges is shown in (b). Such structures contribute to the straylight caused by the DOE. However, these effects can be improved by further process optimization (change of beam incident angle, for instance).

After manufacturing of the components, during handling and integration it might be necessary to clean the DOE's of contaminants. A number of cleaning operations were performed during/after the manufacturing process, and it was found that the same methods can be used as for other types of high precision optics designed for low straylight levels. For cleaning of contaminants deposited deeply inside the etched grooves cotton swabs sufficiently wet with solvents were successfully used without damaging the structure.

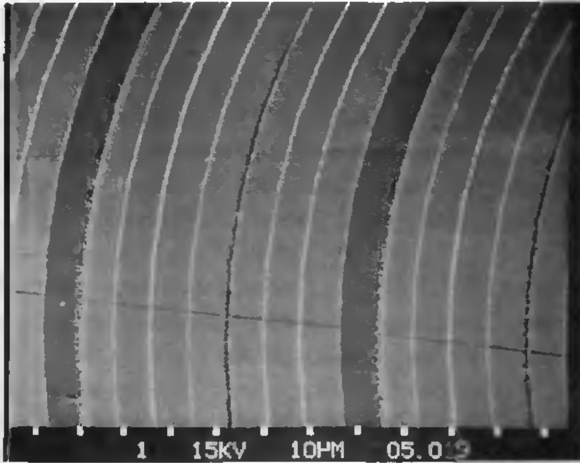

(a)

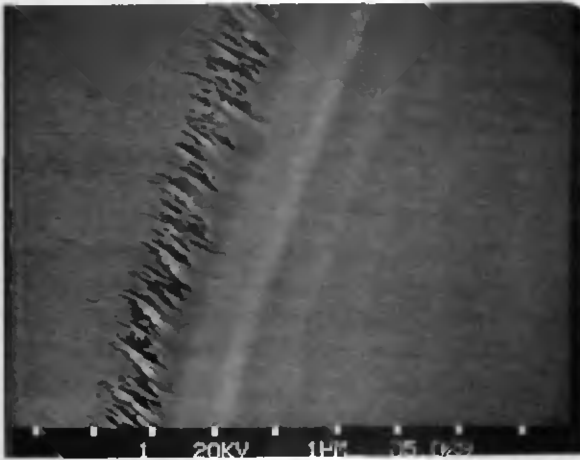

(b)

Fig. 6.2.2-12 SEM photograph of an eight level DOE in glass: overview with lower magnification (a), details at phase step with long etch time (b)

6.2.3 Assembly of DOE and Lens

Due to the fact that the DOE was fabricated separately from the lens both components had to be assembled after fabrication by cementing. Prior to assembly the DOE had to be cut out of the substrate. This was performed with a diamond crown drill in a special drill jig. The diameter of the cut-out disk was 22 mm, the DOE motif was centered within ± 0.1 mm. After edge chamfering and cleaning the DOE's were ready for assembly.

During assembly the DOE had to be centered with respect to the lens optical axis and the cement layer between both components had to be adjusted for uniform thickness over the entire contact area. In this context, some definitions shall be recalled which are important for the understanding of the centering method applied. For centering of a spherical lens the lens optical axis has to be brought in coincidence with the reference axis, within the limits defined by the optical design. The optical axis of a spherical lens is defined by the line connecting the two centres of curvatures. The definition of the reference axis depends on the type of lens and the mounting technique used. A number of examples are given in DIN 3140, part 7 [4.1]. The centering of lenses and the measurement of decentration in optical systems is treated in detail in the publications of Hofmann [6.14] and Schuch [6.15]. For the plano convex lens taken in this example, the reference axis shall be defined by the surface normal on the plane defined by the intersection curve of the edge cylinder with the convex optical surface, as shown in figure 6.2.3-1a. The angle κ_1 between this reference axis and the optical axis defines the centering error for the lens component. This lens has to be assembled with the DOE, which has the form of a plano-aspheric lens.

The definition of centration for aspheric lenses is different from the spherical case since aspherics are in general not point symmetric (DIN 3140,7 does not apply for this case). In the present case of a rotationally-symmetric asphere (represented by the DOE effective structure), the rotation axis of the asphere is the symmetry axis. This axis, which represents also the optical axis of the surface shall coincide in the well centered case with the surface normal on the plane side. The rotation axis of the edge cylinder is this case usually in coincidence with the surface normal as shown in figure 6.2.3-1b on the left side. The centering error of the DOE is defined therefore by the angle κ_2 between the symmetry axis of the asphere and the surface normal on the plano side of the substrate, and the lateral decentration Δy of the DOE with respect to the rotation axis of the edge cylinder.

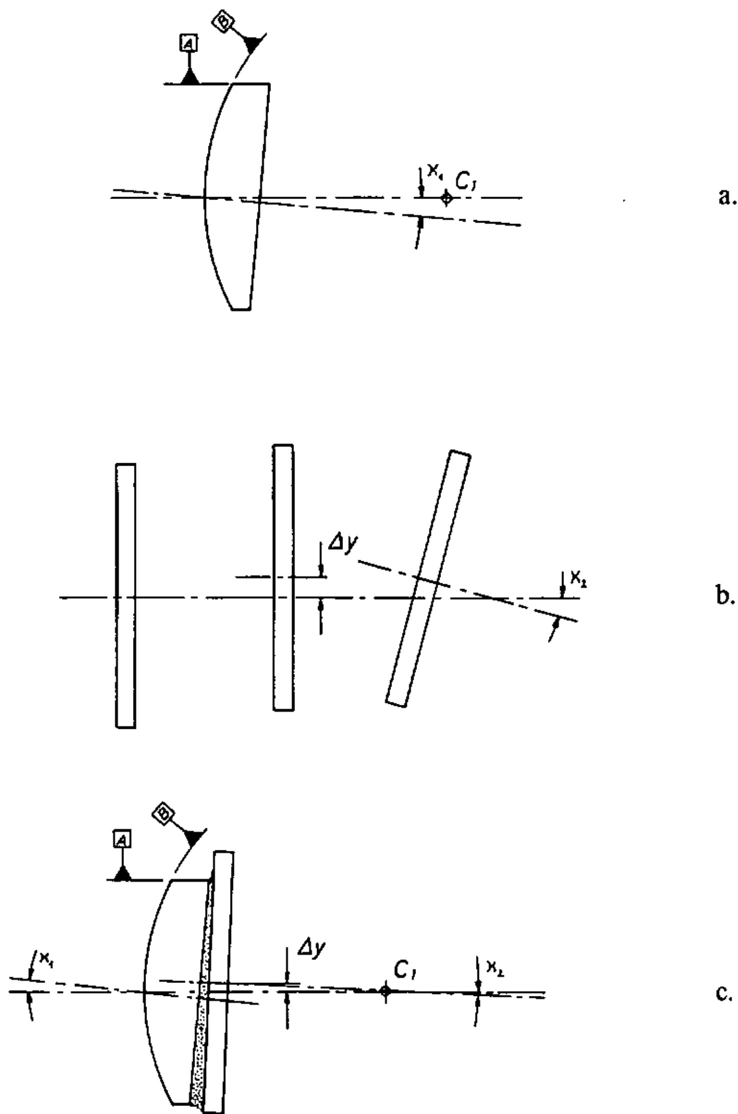

Fig. 6.2.3-1 Centering of lenses and DOE's: centering of plano-convex lens (a), centering of DOE (b), centering of hybrid lens (c)

For assembly of the hybrid, the optical axes of both components have to be brought in coincidence with the reference axis, which shall be in this case the one defined for the lens. Figure 6.2.3-1c shows the assembled hybrid with the optical axes of the components and the reference axis.

The worst case centering error shall be defined in this case by the sum of the two surface tilt angles and the lateral decentration of the aspheric surface. According to the optical design, the sum of the tilt angles can be up to 1 arcmin and the lateral decentration 5 µm. However, it was decided to keep the errors as small as possible in order to eliminate their influence on the overall performance.

A special centering device was required for the centering/cementing operation. The principles of this equipment are shown in figure 6.2.3-2.

The core of this device is a highly precise spindle with a hollow axis and an interchangeable centering bell. All reference parts on spindle and bells are ground and eccentricity/axial wobble of the ring edge on the bell was better than 1 µm. The surface normal in the centre of the plane defined by the turning ring edge represents the reference axis of the centering device. Its direction is transferred to a visual reference in the following way: a collimator is positioned on one side of the spindle and an autocollimator on the other, both in adjustable mounts. A plane reference mirror with polished back side is placed with its mirror surface on the ring edge of the centering bell. The autocollimator axes are adjusted in autocollimation with the mirror surface. The direction of the reference axis is transferred by this means to the autocollimator. The reference mirror is removed and the collimator graticule becomes visible in the autocollimator. The collimator axes are then adjusted with respect to the autocollimator reference, thus transferring the reference to the collimator. The centering device is now aligned and ready for operation.

Figure 6.2.3-3 shows the centering equipment which was designed and built within this project for assembly of hybrid optical elements.

The assembly of the hybrid starts with centered fixation of the lens on the centering bell: the lens is put with its convex side onto the ring edge of the bell along with a drop of molten wax. The spindle drive is switched on and the plano side of the lens is then adjusted in autocollimation until the image in the autocollimator is stationary. If this is the case, the drive is switched off,

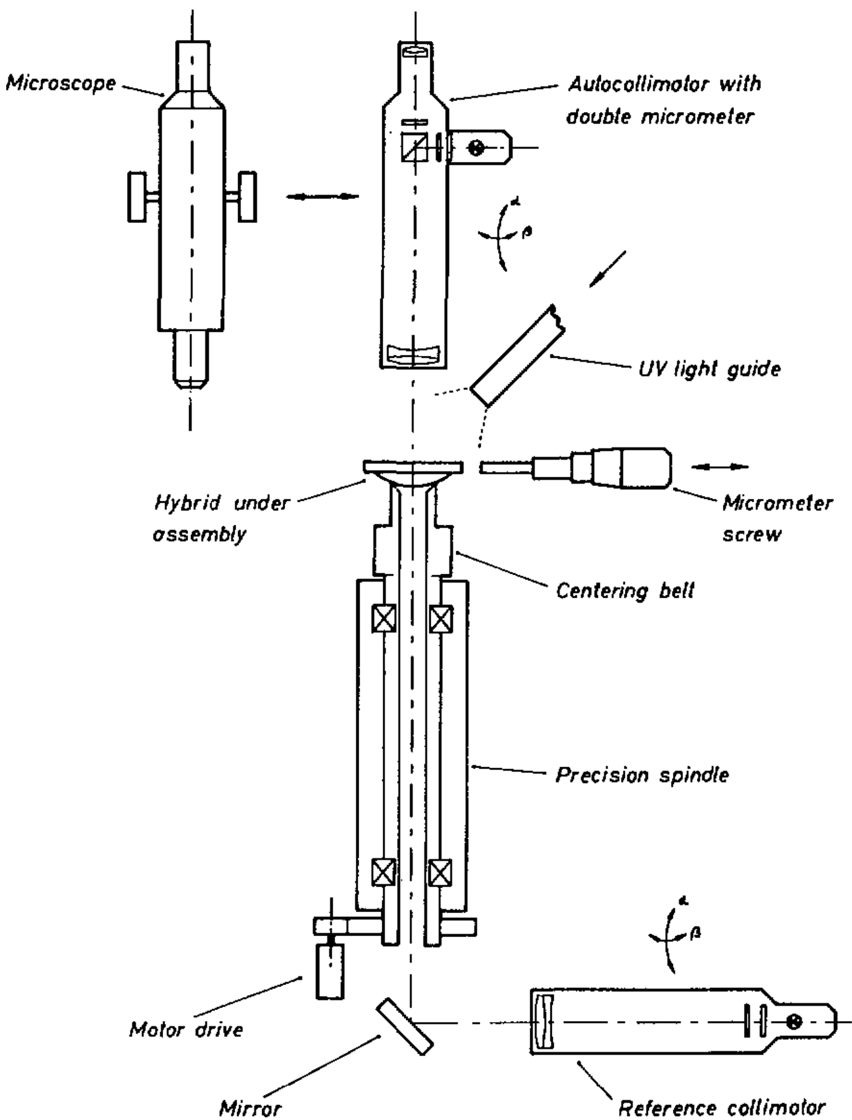

Fig. 6.2.3-2 Principles of the centering device for hybrid optical elements

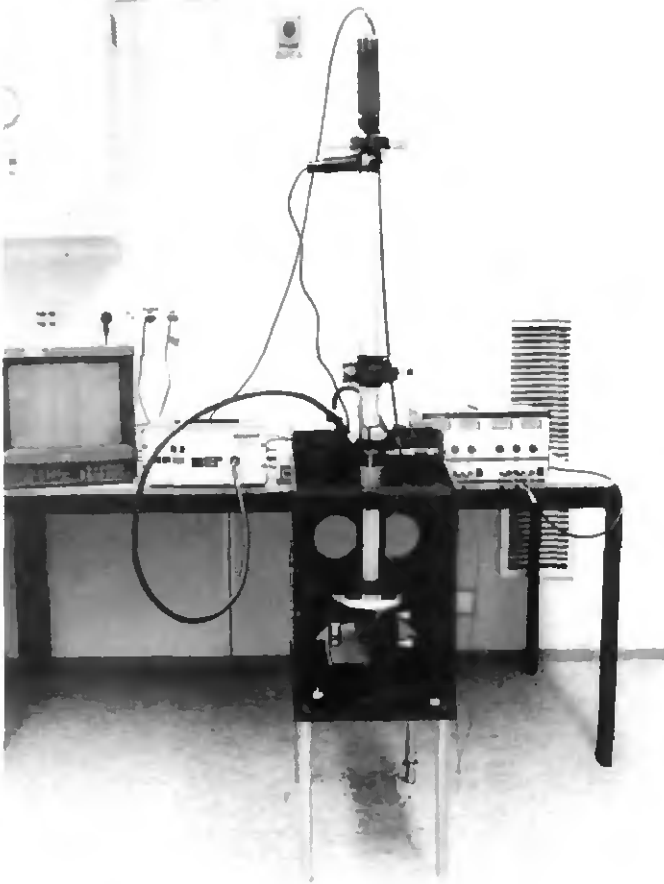

Fig. 6.2.3-3 Centering and cementing equipment for hybrid optics

the wax is allowed to cool in order to fix the lens position. The autocollimator is then replaced by a microscope and the collimator illumination is switched on.

A drop of UV curing cement is applied to the plane lens side and the DOE is pressed on the cement with slightly rotating motions to eliminate air inclusions in the cement layer. The motor drive is switched on again and the centering ring on the DOE is observed with the microscope. The DOE can be laterally adjusted by pushing it gently with a differential micrometer screw

Fig. 6.2.3-4 UV curing of hybrid after centering

while the motion of the centering ring with respect to crosshairs in the microscope eyepiece is observed. Alternatively the image of the collimator crosshairs can be taken as references. The DOE adjustment is perfect if the ring does not move laterally any more and the image seems motionless. If this is the case and the thickness of the cement layer is in tolerance, the cement can be cured by illumination with UV from the attached UV light guide, as shown in figure 6.2.3-4.

After curing the hybrid can be removed from the centering bell by heating up the wax. Afterwards, the hybrids can be cleaned and are ready for mounting.

The centering accuracies which can be achieved with this centering device depend on various factors:

- Lens radius
- Diameter of ring edge on centering bell
- Spindle accuracy, i.e. ring edge at centering bell
  - axial wobble
  - eccentricity (lateral)
- Autocollimator accuracy
- Microscope magnification

In addition, the ability of the technician performing the centering operation is of course of great importance. No detailed calculations shall be reported here on this subject, only a brief assessment shall be presented, which gives an indication of the centering quality achievable with the device: the radius of curvature of the convex lens surface is 17.678 mm, the diameter of the ring edge at the centering bell was 13 mm. The ring edge had a measured eccentricity of < 0.5 μm, the axial wobble was ca. 0.06 μm (measured with plane mirror and autocollimator). The autocollimator had a focal length of 500 mm and was equipped with a dual micrometer eyepiece. The micrometer drum was divided in 5 μm intervals, allowing for 2.5 μm estimates. With the given focal length this corresponds to an angular readout of 2 arcsec. In autocollimation 1 arcsec tilt of the reference mirror can be detected. The microscope magnification of 200 allowed eccentric motions of ca 2 μm to be identified.

This allows for the actually produced samples to achieve centering accuracies of ca. 9 arcsec for the plano convex lens, ca. 1 arcsec for DOE tilt angle and ca. 2 μm for lateral decentering.

The cemented hybrids were mounted for characterization in specially designed lens holders (figure 6.2.3-5). The lens is self-centering in the holder, being pressed by a retainer ring against a ring edge. The groove with the O-ring which is pushing the lens is lined-up coaxially with the ring edge in the other part of the holder, within the tolerances of the thread. The centering of the hybrid within this holder with respect to the outer cylinder

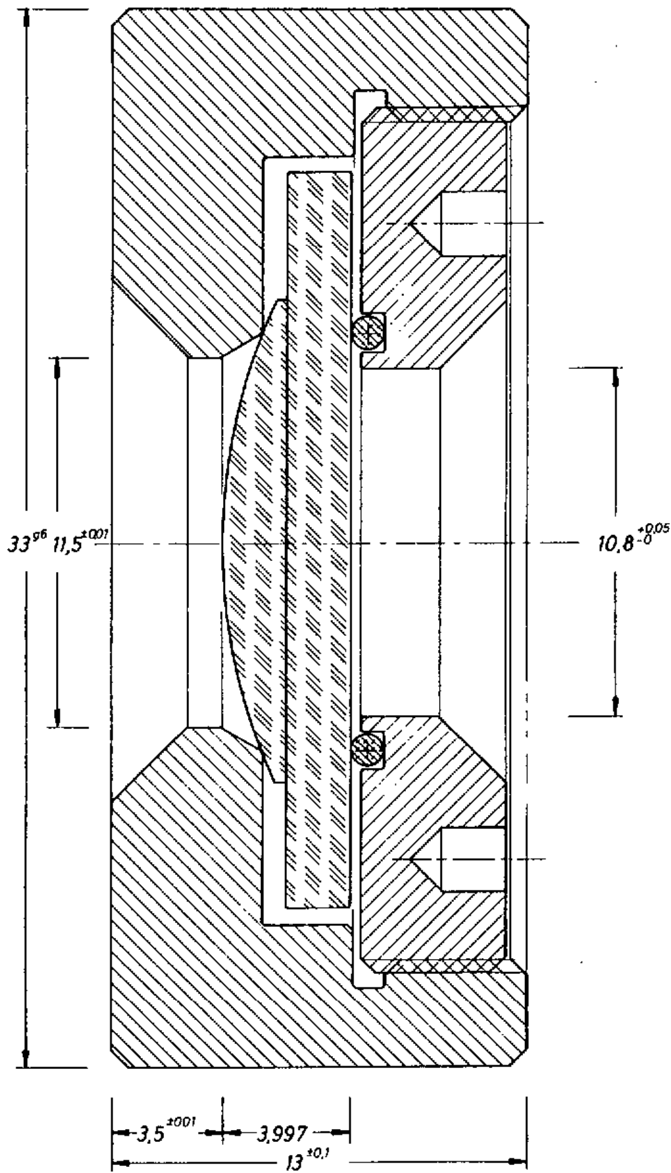

Fig. 6.2.3-5 Hybrid lens in reference lens mount

of the mount is better than 1.7 arcmin. The front surface of the mount serves as a precise reference to the lens vertex. The dimensions of the holders were controlled individually and documented in measurement reports as input for some of the verification tests. Figure 6.2.3-6 shows the reference lens mount with a hybrid lens in front.

Fig. 6.2.3-6 Hybrid lens and reference lens mount

Chapter 7

HYBRID OPTICAL ELEMENT PERFORMANCE VERIFICATION

7.1 Description of Verification Approach

It was the aim of the verification activities to check whether the actual performance of the hybrid optical elements complies with the predicted performance figures (see section 4.4.2) and to perform a technological evaluation with respect to the general requirements on space optics outlined in chapter 5.
The first part, the experimental verification, comprises following three elements:

1. Initial characterisation of basic components, i.e. lenses and DOE substrates
2. DOE manufacturing tests
3. Characterization of the assembled hybrid lenses

The individual tests performed within these groups are listed in table 7.1-1. The test activities shown there can be condensed to the following set of basic measurements:

- Visual/microscopic inspections
- Image quality assessments
- Etch profile measurements
- Interferometric tests
- Spherical/chromatic aberration measurements
- Relative spectral transmission measurements
- Focal length measurements
- Diffraction efficiency/pattern measurements

For some of these tests dedicated test equipment was developed and this equipment shall be briefly described within the following section, together with the definition of the test methods used. Section 7.3 is devoted to the presentation of test results, their interpretation and the comparison with the theoretical predictions. Finally, the results of the hybrid optics technology evaluation with respect to the general space optics requirements will be presented and discussed.

Test element	Etch test samples	Plane plates	Lens	OOE etch step			Hybrid
				1st	2nd	3rd	
Initial characterization							
Visual inspection	X	X	X				
Surface flatness		X					
Rel.spectral transmission		X					
Manufacturing tests							
Visual inspection				X	X	X	X
Etch profile	X			X	X	X	
Optical performance tests							
Diffraction efficiency				X	X	X	
Diffraction pattern						X	X
Focal length			X			X	X
Chromatic focus shift			X				X
Chromatic aberrations			X				X
Wavefront errors			X				X
Image quality			X				X

Table 7.1-1 Elements of the hybrid optics verification programme

7.2 Test Methods and Equipment

7.2.1 General Description

The test methods used for the verification activities were as far as possible derived from established test methods which are known to give results which are traceable to existing standards. In some cases it was necessary to develop some dedicated test equipment and descriptions are provided in section 7.2.2. The performance of this equipment was verified prior to use and appropriate calibrations were performed.
The following description of test methods reflects the outline given in the previous chapter.

Visual/microscopic inspection
Visual and/or microscopic inspections were performed as part of the initial characterization of the hybrid basic components in order to determine their compliance with the specifications of the manufacturing documents. For these tests a stereo zoom microscope was used in dark field transmission mode with magnifications between 6.4x to 256x (WILD M3Z). Surface defects on the test specimen were compared to a test plate with standard defects according to DIN 3140. Inspections of the DOE substrates were performed throughout the whole DOE etching process in order to verify the quality of the pattern in terms of alignment, defects or residual photoresist. For this purpose a microscope with higher magnification (up to 400x) in bright field reflective mode was used.

Image quality assessments
The image quality of the hybrids was visually assessed by imaging test targets. The target used for this purpose was a high resolution test target with 30 groups of gratings from 1 lp/mm to 625 lp/mm, i.e. 0.8 μm minimum linewidth (Heidenhain target 31a). The tests were performed with monochromatic illumination and white light and a comparison with simple lenses and achromats was made. In addition, the Airy spot was photographically recorded for some of the components at different illumination wavelengths.

Etch profile measurements
The geometric shape of the diffracting pattern on the DOE was determined by etch profile measurements. Two different methods were used, a contacting method and an optical, non-contacting method: the principle of the contacting method is to scan the surface with a small diamond tip and to gain the profile information from tip deflection. The equipment used was a Talystep (Rank,Taylor&Hobson) and an Alphastep 200 (Tencor). The characteristic data concerning depth and lateral resolution of both instruments are:

- Talystep

– Depth resolution	10 μm range:	0.4 μm
	0.05 μm range:	0.002 μm
– Accuracy for step size	2 μm:	± 0.05 μm
	0.5 μm:	± 0.01 μm
	320 Å:	± 50 Å

- Alphastep 200

– Depth resolution	160 μm range:	0.005 μm
	16 μm range:	0.0005 μm
– Lateral resolution for diamond tip radius 12.5 μm:		0.040 μm

A disadvantage of a contacting test method is of course that the pattern can be disturbed by a very fine line scribed by the diamond tip. This potential disadvantage is avoided by optical measurement methods, with a laser profilometer for instance. A single axis Laser Stylus (Rodenstock RM600) was used to perform optical profile measurements. This device measures the profile by scanning a diffraction limited laser light spot over the sample surface and measuring the refocussing distance required to compensate for profile depth changes. The characteristic data of this instrument are:

- Laser stylus (Rodenstock RM600)

– Sensor head		
• Depth resolution	± 300 μm range:	200 nm
	± 30 μm range:	20 nm
	± 3 μm range:	2 nm
• Linearity	<0.3%	
– Scanning system accuracy for 60 mm scan length	Depth error:	<0.2 μm

The errors of the scanning system are significantly reduced at smaller scan length. A disadvantage of this equipment is that the slowest commandable scan speed is still too high for measurement of steep edges: the measurements are disturbed by overshooting signals. However, this seems not to be a principal problem, it can be solved by appropriate data processing (filtering) without influencing the results.

Interferometric tests

Interferometric tests were executed at various points during the manufacturing process and as final performance test: the surface shape of the basic components, i.e. the lenses and DOE substrates, was measured interferometrically before and during manufacturing in order to identify any process related surface shape changes. The interferometer used was a Fizeau type (ZYGO Mk IV) with plane reference plates and reference objectives for spherical waves. The accuracy of the instrument is dominated by the quality of the reference surfaces: the plane reference had a quality of 0.028λ p-v and

0.005λ rms (λ = 632.8 nm), respectively, for 100 mm diameter, the spherical reference (f/1.5) was 0.057λ p-v and 0.009λ rms, respectively. The overall system accuracy for absolute testing of flats is quoted to be $\lambda/50$ p-v. Some plane plates were also measured with a similar interferometer of the same type, making use of a commercial software package for fringe evaluation (WYKO WISP). The accuracy of the reference plate used was better $\lambda/20$ p-v for 100 mm diameter, the system accuracy can be considered comparable to that of the above mentioned ZYGO MkIV. The measurements of final performance of the hybrids were not possible with the same type of interferometer, since the interference pattern was severely disturbed by parasitic interferences between the plane side of the lens and the reference flat, due to the long coherence length of the source (HeNe laser). Therefore, another interferometer (Twyman-Green type) with a partially coherent source was built-up. The interferometer was white light compensated and it was possible to work with a halogen source or a mercury-cadmium lamp. The characteristics of this interferometer will be described in some more detail in one of the following sections.

Chromatic aberration measurements

An important performance feature of hybrid optics is the chromatic aberration performance. Chromatic aberrations can be in principle measured interferometrically, like monochromatic types of aberrations by using several wavelengths consecutively, keeping the same basic adjustment of the lens. However, it was decided to design as an alternative test equipment for chromatic aberrations, which is based on the Hartmann method [7.1]. It will be described in more detail in section 7.2.2.2. This method is used in connection with a position sensitive detector operated with a modulated light source for spot position measurements.

The measurement accuracy achievable with this test concept is in principle sufficient to obtain reliable results for the envisaged tests: simulations in the frame of an ESA contract have shown that measurement accuracies of better than $\lambda/50$ rms for a 100 mm diameter wavefront can be realized [7.2].

Focal length measurements

The focal length as a first order optical parameter is measured on the lenses, the DOE's and on the final hybrid lenses. It is measured on a goniometer with a special test set jig which allows also for back focal length and distortion measurements. The test method is described in more detail in section 7.2.2.4. The overall measurement accuracy achieved with this instrument is better than 0.5%.

Diffraction efficiency/pattern measurements

The diffraction efficiency and the diffraction pattern were measured for the DOE's, for the hybrids only the diffraction pattern shape was determined. Due to the strong aberrations which are introduced by the DOE, the diffraction efficiency had to be measured in a slightly unconventional way by comparing the normalized measured encircled energy with the theoretically predicted encircled energy. For determination of the diffraction pattern, two different test methods were required due to the different spot sizes of the DOE's and the hybrids. For the DOE's the focal plane was scanned by a pinhole, the diffraction pattern of the hybrid was measurable by a solid state camera with video analyzer. Both test methods are described in more detail in section 7.2.2.3.

7.2.2 Special Test Equipment

7.2.2.1 Twyman-Green Interferometer

A Twyman-Green interferometer with partially coherent sources was built up to test the wavefront quality of the hybrid and to support the chromatic aberration measurements. The principles of the interferometer are illustrated in figure 7.2.2.1-1, figure 7.2.2.1-2 shows a photograph of the instrument. A sandwich table on a vibration isolated stand was used as basis. The interferometer has two light sources, which can be alternatively used: a mercury lamp and a halogen source. The instrument concept complies with the requirements for adjustment of two beam interferometers formulated by Slevogt [7.3]:

1. Equal optical path length in both arms
2. Coincidence of the images of the aperture stops
3. Coincidence of the images of the field stops

The light source used is imaged with a condenser into the aperture stop of the interferometer, a field lens at the aperture stop images the field stop to infinity. The collimator lens has two functions: imaging of the field stop onto the mirror planes and collimation of the light emerging from the interferometer aperture stop (Köhler illumination path). The test beam diameter was limited by an aperture at the collimator to ca. 20 mm diameter. A compensator plate was placed in the reference beam to compensate for the beam splitter plate optical thickness. The lens under test was mounted

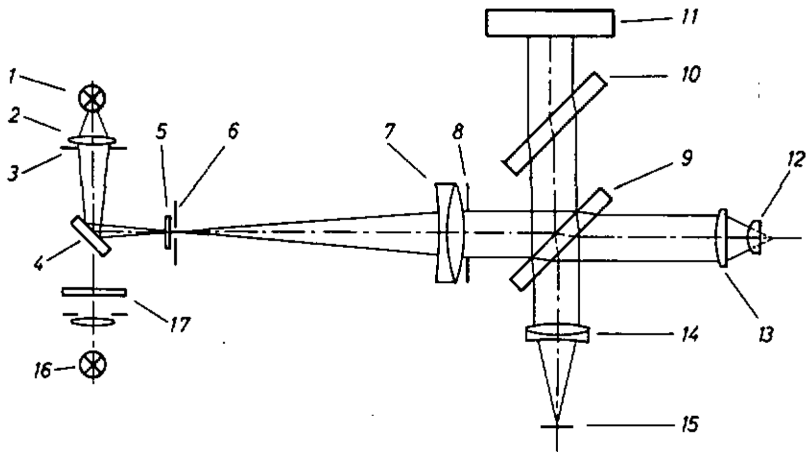

1	Spectral lamp	9	Beam splitter
2	Condenser	10	Compensator plate
3	Field stop	11	Reference mirror
4	Mirror	12	Spherical mirror
5	Field lens	13	Hybrid lens under test
6	Aperture stop	14	Imaging lens
7	Collimator lens	15	CCD camera

Fig. 7.2.2.1-1 Twyman-Green interferometer for testing of hybrid lenses

on a 5 axis adjustable mount, a convex mirror was placed with its centre at the focus of the lens. A plane mirror is used as reference in the other arm of the interferometer. The mirrors, the beam splitter and the compensator plate were mounted in adjustable mounts.
Interference filters or colour glasses were inserted in front of the light sources to limit the spectral bandwidth. To tune the optical path length in both arms the interferometer was also adjusted for white light fringes. The interference pattern is observed with a magnifier in the plane of the mirrors, a telescope serves for adjustment of the pupils. The visual observation path can be replaced by a CCD camera connected to a computer for fringe pattern analysis. For data acquisition and analysis a commercial software package was used (WYKO WISP).

The instrumental accuracy can be derived from the quality of the components used in the instrument. The collimator lens was an achromat

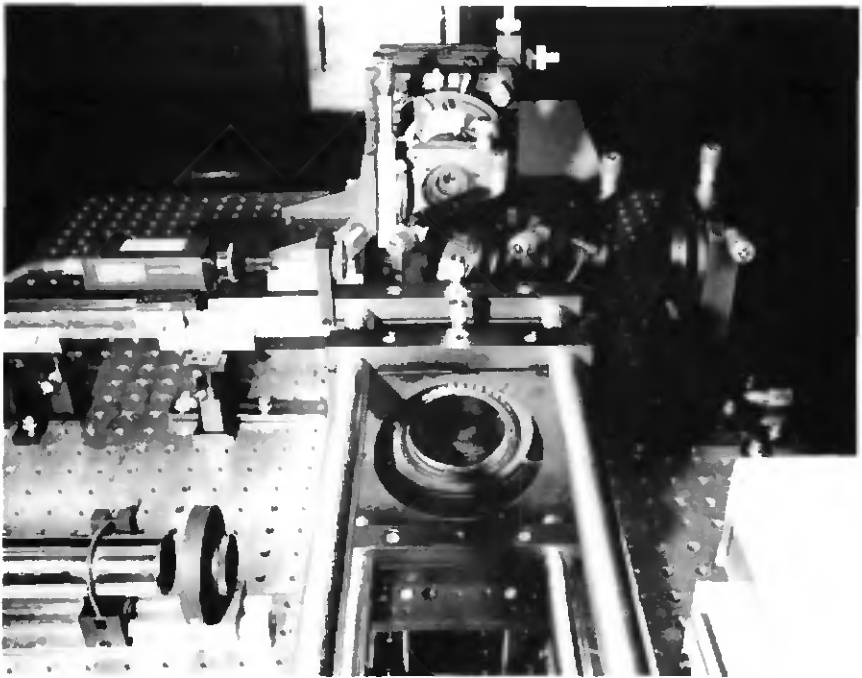

Fig. 7.2.2.1-2 Tywman-Green interferometer: view from collimator to beamsplitter and test sample, left side TV camera, right side reference flat

with a focal length of 400 mm, and an f-number which was reduced to f/20. The quality of this lens was interferometrically measured and found to be better than $\lambda/15$ p-v and $\lambda/100$ rms, respectively (λ = 632.8 nm), for a test diameter of 25 mm.

Table 7.2.2.1-1 shows the wavefront errors induced by the interferometer components and derives a value for the accuracy of the instrument based upon rss summation. According to the table the interferometer has an overall accuracy of $\lambda/33$ rms for a 25 mm beam diameter. For the actually used diameter (12 mm) the accuracy is in the range of $\lambda/50$ rms.

Element	Induced wavefront error (λ rms)
Plane mirror	0.007
Beam splitter	0.02
Compensator plate	0.013
Convex reference mirror	0.014
Collimator	0.01
Total RSS (25 mm diameter)	0.030

Table 7.2.2.1-1 Twyman-Green interferometer accuracy (λ = 632.8 nm)

7.2.2.2 Hartmann Test Setup

The principle of the Hartmann test method is to sample a wavefront at well defined positions with small subapertures and to determine the ray positions in a recording plane, as shown in figure 7.2.2.2-1.

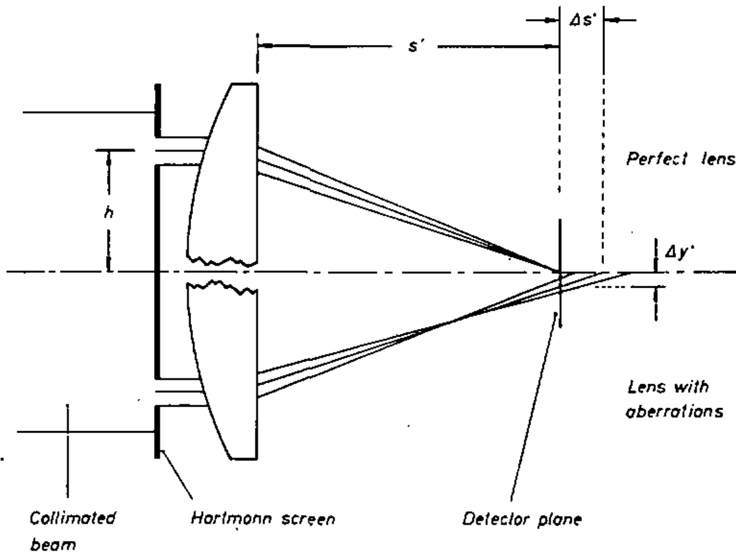

Fig. 7.2.2.2-1 Principles of the Hartmann test method

From the ray position in the recording plane and the distance between sampling plane and recording plane, one can calculate the directions of individual "rays". Using this principle the imaging quality of optical components can be determined if a wavefront of good quality is used for illumination of the component. The upper part of the figure shows the situation for a perfect lens, the lower side shows an aberrated lens under test. From the ray directions one can determine different types of ray aberrations and can compute also wavefront shapes. If several wavelengths are used, chromatic aberrations can be measured. The theory of Hartmann test methods is well described in literature [7.1] and shall not be repeated here. The Hartmann test method has been known since the beginning of this century when it was mainly used for test of astronomical telescopes. At this stage photoplates have been used to detect the ray positions in the recording plane, which made the test inconvenient to use because it was not possible to make "real time" measurements.
It became attractive again today due to the possibilities offered by the use of modern position sensitive detector devices in connection with computer controlled data acquisition and processing. The ray position in the recording plane can be measured directly and fast aperture sampling makes it possible to achieve a short measurement/data evaluation time. According to the results of an ESA contract on this subject the accuracies which can be achieved are comparable to interferometric test methods [7.2]. Therefore, the Hartmann test principle can be considered today again as a valuable alternative to interferometric methods.

The principles of the Hartmann test equipment developed in the frame of this work are illustrated in figure 7.2.2.2-2. It consists of the sensor head with its electronics including the holder for the test sample and a collimator unit. Figure 7.2.2.2-3 shows the sensor unit, figure 7.2.2.2-4 the collimator.
The collimator unit was conceived to be used also for the other tests to be performed (diffraction efficiency/pattern). It consists of a collimator lens with a pinhole in its focal plane, interchangeable light sources - a HeNe laser with 2 mW output power and a 100 W mercury arc lamp -, and a chopper for light source modulation. The collimator lens is an apochromatic system with a built-in iris diaphragm (f = 600 mm, 1:10 to 1:128). It was characterized interferometrically with the ZYGO Mk IV. The wavefront error at full aperture (60 mm diam.) is 1.686λ p-v or 0.314λ rms, respectively. At the actually used aperture of ca 12 mm diameter, the wavefront error is 0.051λ p-v or 0.011λ rms, respectively. This quality can be considered reasonably good for the envisaged application.

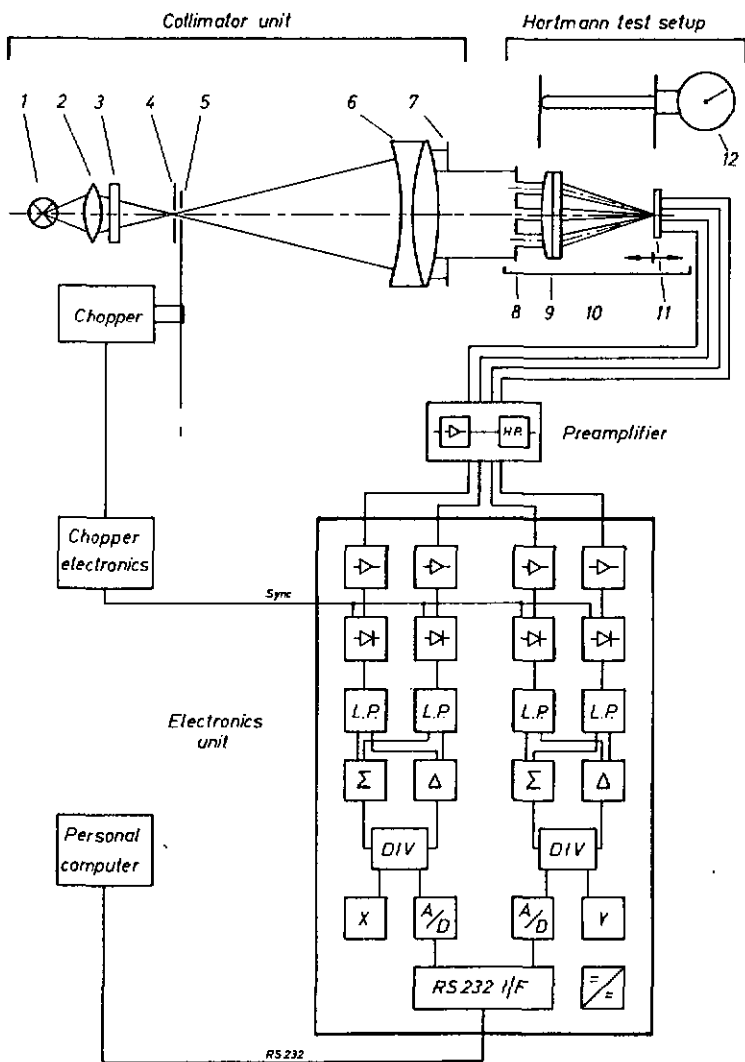

1	Light source	7	Collimator aperture
2	Condenser	8	Hartmann screen
3	Interference filter	9	Lens under test
4	Diaphragm	10	Focusing stage
5	Chopper wheel	11	Position sensitive detector
6	Collimator lens		

Fig. 7.2.2.2-2 Hartmann sensor head with electronics unit

Fig. 7.2.2.2-3 Hartmann test setup for hybrid lens testing

The objective is mounted in a rigid holder together with an adjustable pinhole in the focal plane.
The pinhole size depends on the light source used: for the HeNe laser the pinhole acts as a spatial filter illuminated via a microscope objective, and its size is 20 µm. If the mercury lamp was used, a larger diaphragm of 1 mm diameter had to be taken due to energetic reasons.The arc of this lamp was focused with an high aperture quartz condenser on the pinhole.
The mercury lamp was used in connection with two interference filters (see table 7.2.2.2-1).

Wavelength [nm]	Transmission [%]	Halfwidth [nm]
546 ± 1%	40	11.5
436 ± 1%	35	11.5

Table 7.2.2.2-1 Characteristics of interference filters used for Hartmann tests

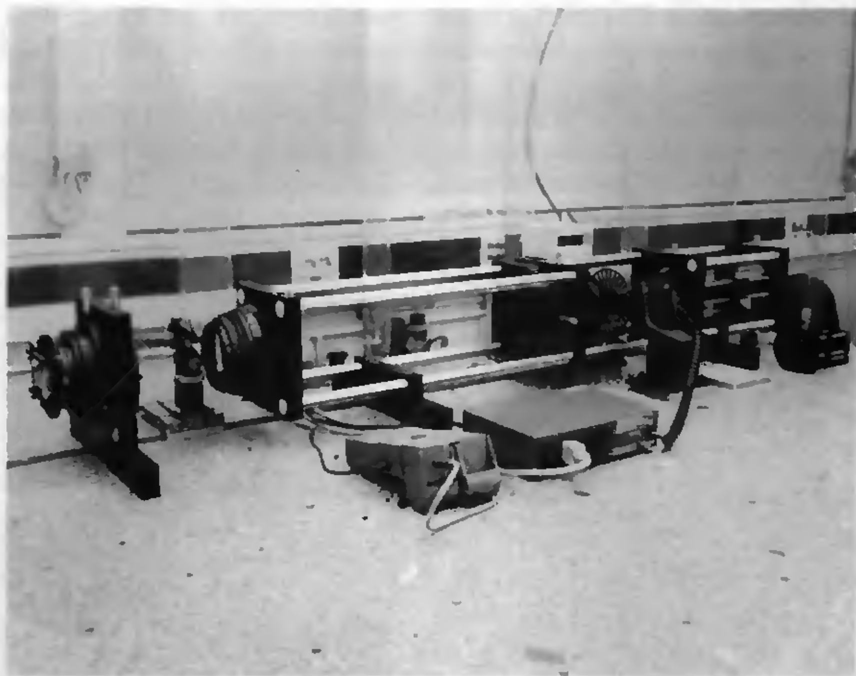

Fig. 7.2.2.2-4 Collimator unit

The chopper disc is placed in front of the pinhole and modulates the light emerging from it. The focusing of the collimator was performed by axial adjustment of the pinhole, the focusing status was tested by a lateral shearing interferometry at 632.8 nm. The shearing plate used was better than $\lambda/20$ p-v per side. The collimator was adjusted with this interferometer for interference contrast in both azimuth. Due to the apochromatic correction of the lens only minor differences are expected for the other wavelengths. The beam was restricted to ca. 20 mm diameter by the built-in iris diaphragm. The Hartmann sensor with the lens holder was placed in the collimated light beam in front of the collimator. A position sensitive detector was used for detection of the intensity centroid of the light spot.
The sensor was built on the basis of a test jig which was initially designed only for measurement of focal length and distortion (see section 7.2.2.3) and some compromises had to be made therefore concerning its ease-of-operation (however, it was not the intention to design an automated test system). This test jig consists of a baseplate with a fixed holder for the

element under test and the Hartmann screen in front of it, and an adjustable holder (z-axis for focusing) for the position sensitive detector. The Hartmann screen was interchangeable with good centering accuracy. Each screen had three apertures, one on axis and the other two placed symmetrically above and below it. The distance off axis was different for each screen. Figure 7.2.2.2-5 shows all the configurations used in one drawing. The aperture diameter was 1 mm, only one aperture was used per measurement.

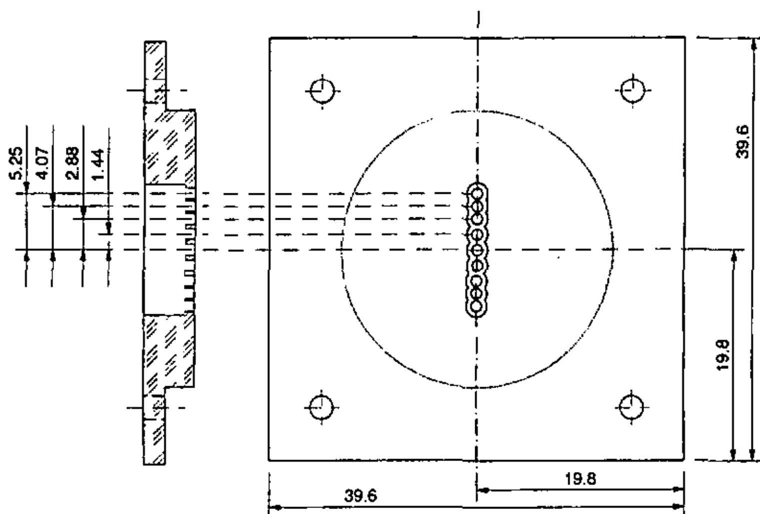

Fig. 7.2.2.2-5 Aperture positions in the Hartmann test screens

The detector used was a SiTek PSD 2L4 with 4 mm x 4 mm area without cover glass, mounted in a dedicated housing, which was inserted and fixed in the adjustable holder. The position and orientation of the detector surface in the holder was determined by optical measurements to an accuracy of ±4 μm. The distancc between the PSD and the reference surfaces of test specimen (front lens vertex) was measured with a dial gauge to ±5 μm accuracy. The detector system was designed for light input power levels between 1 nW and 500 nW (850 nm). The PSD was operated in AC mode to keep drift influences and disturbances due to ambient light as low as possible. It was connected to the electronics unit via a preamplifier with high-pass filter. The electronics unit incorporated the main amplifiers for four signal channels (four quadrants) followed by precision rectifiers and low-pass filters tuned to the chopper frequency. After summation and normalization the x- and y-signals were digitized by an 11 bit A/D converter. The digitized position signals were sent to a personal computer for

subsequent processing via an RS232 interface card. In addition, the coarse position of the light spot on the detector surface was indicated at the electronics box front panel by two LED displays for X and Y.

A dedicated software package was developed within the frame of this work and installed on the processing computer to handle the incoming data stream and to perform the evaluation: the position of the light spot on the detector was graphically displayed on the monitor in real time, which was quite convenient for adjustment purposes. By command, a data acquisition cycle could be started with a selectable number of samples (for the measurements reported later always 1000 samples were taken).

The light spot positions in sensor coordinates were calculated using a calibration polynomial, and mean value/standard deviation for this position was calculated, displayed and written in a data file.
The calibration of the detector was performed in the original mount. For this purpose a light spot was scanned over the detector surface in steps of 0.1 mm and the actual light spot position was registered together with the PSD output. The data set acquired in this way was used for computation of the calibration polynomial, which was then implemented in the data processing software. For the detector used a ninth order calibration polynomial gave the best results.
The calibration curve is shown in figure 7.2.2.2-6 together with the errors due to the polynomial fit. The mean deviation from the real values was ±1.1 μm over the entire detector height, with a maximum deviation of +2.8 μm. This is in the same order as the digitization error which is ±0.5 bit, corresponding to 1 μm. The calibration was performed at a power level of 60 nW (850nm) with a spot diameter of approximately 460 μm. The calibration curve was found to be very insensitive to input power changes. The errors of the test setup can be classified in systematic and random errors and an error budget is presented in table 7.2.2.2-2, which takes also into account the misalignment effects during through focus measurements.

The Hartmann test measurements were performed in the following way:
the lens to be measured was mounted in the lens holder and aligned with an autocollimator in its orientation w.r.t the collimated test beam. The Hartmann sensor was adjusted approximately to the theoretical focus position of the lens under test. The first Hartmann screen was inserted and the position of the light spot was measured by sampling over 1000 readings, and the results stored.

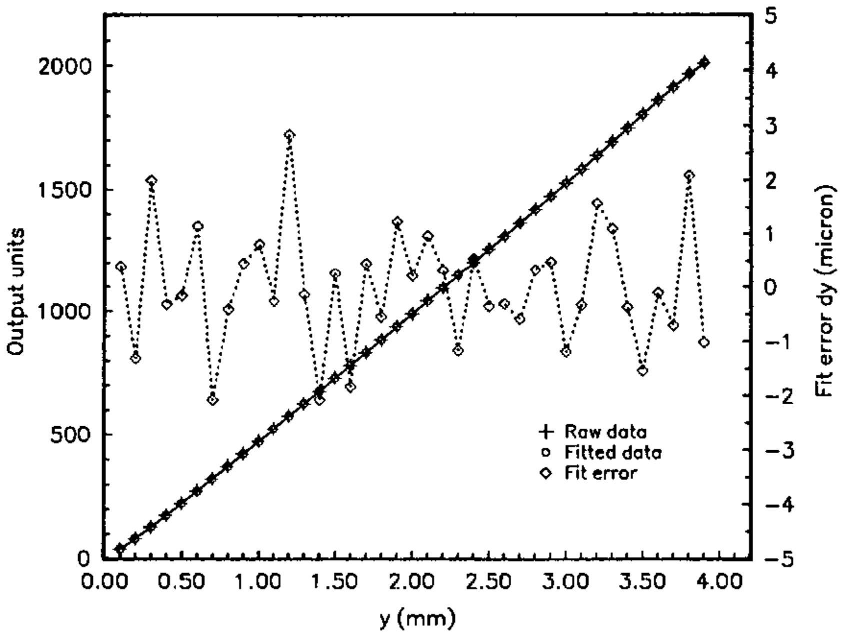

Fig. 7.2.2.2-6 Hartmann sensor calibration curve (SITEK PSD)

The data were referenced always to the screen central aperture position representing the optical axis, in order to eliminate offset errors. The next screen was inserted and the measurement was performed as before. After completion of the measurements at the first focus position, the detector was axially moved to the next position and the measurements were repeated as described before. The through-focus measurements were usually performed at four to five positions. Subsequently, the measurements were repeated for another wavelength.

The directions of the ray bundles emerging from the subapertures in the Hartmann screen can be calculated based upon the acquired data. Ray aberrations can be computed based upon that. In this case the calculated rays were presented on a plot for different incidence heights and wavelength, for comparison with the theory.

Error type	Error [μm]
Random Errors	
Digitization error	± 1
Calibration error (position)	± 1
Detector Noise (P = 450 nW)	± 10
Reference errors	
Translation stage (focus)	± 3
Screen position	± 5
RSS	± 11.7
Systematic errors	
Calibration polynomial	± 1.1
Calibration misalignment	± 2
Reference offset	± 5
Sum	± 8.1
Total RSS	± 14.2
Sum	± 19.8

Table 7.2.2.2-2 Error budget for Hartmann sensor for through-focus measurements (1σ/axis)

7.2.2.3 Diffraction Efficiency/Pattern Test Equipment

The functional block diagram of the test equipment used for measurement of the diffraction efficiency is shown in figure 7.2.2.3-1. The test setup consists of the collimator unit described in the previous section (see figure 7.2.2.2-4), an adjustable sample holder and the detection unit. The mercury lamp in the illumination part of the collimator unit was replaced by a halogen source in order to cover a wider wavelength range. The detection unit is mounted on a two-axis linear translation stage which can be aligned in a guide rail in the direction of the collimator optical axis. This allows the detection unit to be positioned at variable, well defined distances from the sample. The measurement principle for the diffraction efficiency is adapted to the special attributes of the samples to be measured: the DOE designed for the hybrid lens had to correct for the lens aberrations and is consequently not well corrected on its own. The spherical aberrations of the

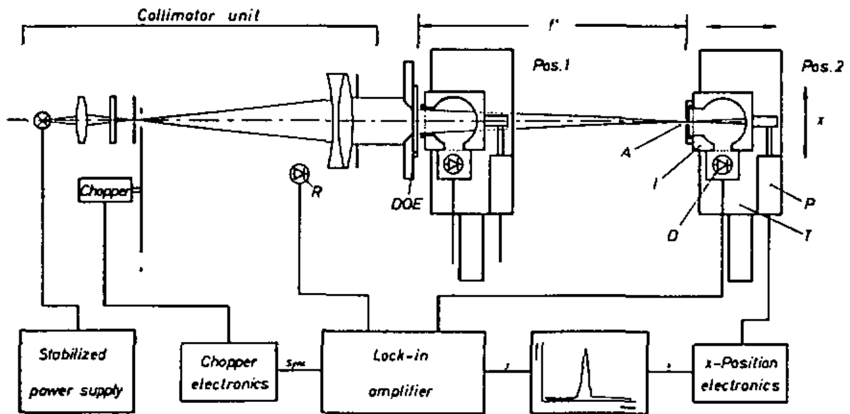

DOE	DOE under test	P	X-position sensor
A	Test aperture	T	Translation stage
I	Integrating sphere	R	Reference detector
D	Detector (Si PIN Diode)		

Fig. 7.2.2.3-1 Diffraction efficiency test setup

marginal rays are 10.7λ, in the zone 3.2λ. Consequently, the 100% energy diameter at the image plane is much larger than for a well corrected element; for this element the diameter of the image spot is 7.49 mm at the theoretical focus position. The other problem is common to all on-axis DOE's and results from the fact that the diffracted light is always superimposed with undiffracted light. This influences the test results in particular for large focus patches.
The test method chosen has to compromise on these problems and the following approach was taken: The total transmitted light flux was measured directly behind the sample using a detector system with an entrance aperture larger than the DOE area. In figure 7.2.2.3-2 this detector system is shown at its measurement position. After this first measurement the unit was shifted with its entrance aperture to the focus position and the light flux was measured with different aperture diameters. The values taken were normalized with the total flux measured directly at the DOE. These values were compared with encircled energy simulation results for the same diameters and serve as indication for the diffraction efficiency.

The detector unit used for the measurement consisted of an integrating sphere with a large area PIN diode, which made the detector insensitive to variations of incidence beam geometries. The photodiode was connected directly to a preamplifier with switchable gain. The output was then fed into a lock-in amplifier which was synchronized with the chopper of the collimator unit. The intensity values were read from the amplifier display. The overall intensity was controlled by a reference detector. However, since a highly stabilized power supply was used for the halogen lamp no significant fluctuations were registered after a burn-in time of ca. 15 min.

Item	Diameter [mm]
Sphere aperture	12.7
Aperture 1	7.50
Aperture 2	6.39
Aperture 3	3.098
Aperture 4	1.492

Table 7.2.2.3-1 Aperture diameters for diffraction efficiency measurements

The entrance aperture of the sphere was interchangeable, the various aperture diameters used are listed in table 7.2.2.3-1. The measurements were performed with the halogen lamp and the laser source. The data of the interference filters used with the halogen lamp are described in table 7.2.2.3-2. The overall error for the diffraction efficiency measurements can be quoted to be ca. ±2%.

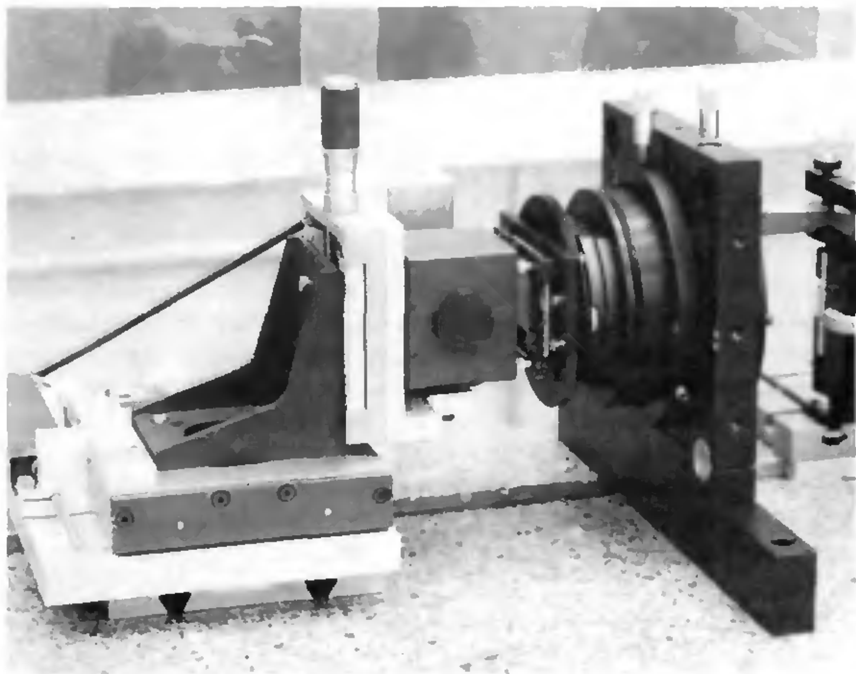

Fig. 7.2.2.3-2 Detector system for diffraction efficiency measurements (measurement of total integrated light flux behind DOE)

Wavelength [nm]	Transmission [%]	Halfwidth [nm]
546 ± 1%	40	11.5
589 ± 1%	40	11.5
633 ± 1%	40	11.5
650 ± 1%	35	11.5
656 ± 1%	35	11.5

Table 7.2.2.3-2 Interference filters used for diffraction efficiency measurements

The diffraction pattern was measured for the DOE's and the hybrids. Some experiments were made in determining the diffraction pattern with a solid state camera (Sony XC77CE) together with a video analyzer (Colorado Video Model 321). The camera had a pixel size of 11 μm x 11 μm and a resolution of 756H/581V with a 8.6 mm x 6.6 mm sensitive area size. However, the Airy disk diameter of the hybrid was too small compared to the camera pixel size to provide sufficient resolution at

the best focus position. On the other hand, the diffraction pattern of the DOE alone was too large for complete detection. An intermediate imaging was not envisaged, since it could potentially disturb the pattern to be measured.

Another test method was therefore chosen making use of the equipment developed for the efficiency measurements.

The detector unit of this equipment was mounted on a two axis translation stage, which had one axis for the height adjustment in y-direction and a second for lateral motions in x-direction. The y-axis was coupled to a linear precision potentiometer for position measurement. A pin hole with a diameter of 0.1 mm ±0.005 mm was mounted on the integrating sphere aperture. This pinhole was used to scan the diffraction pattern of the DOE. The table position was measured electrically with the potentiometer and the intensity data were taken from the lock-in amplifier. The pattern was registered with an x-y-recorder. The position resolution provided by these means is better 0.04 mm, the overall accuracy in terms of intensity and position is ca. ±2%.

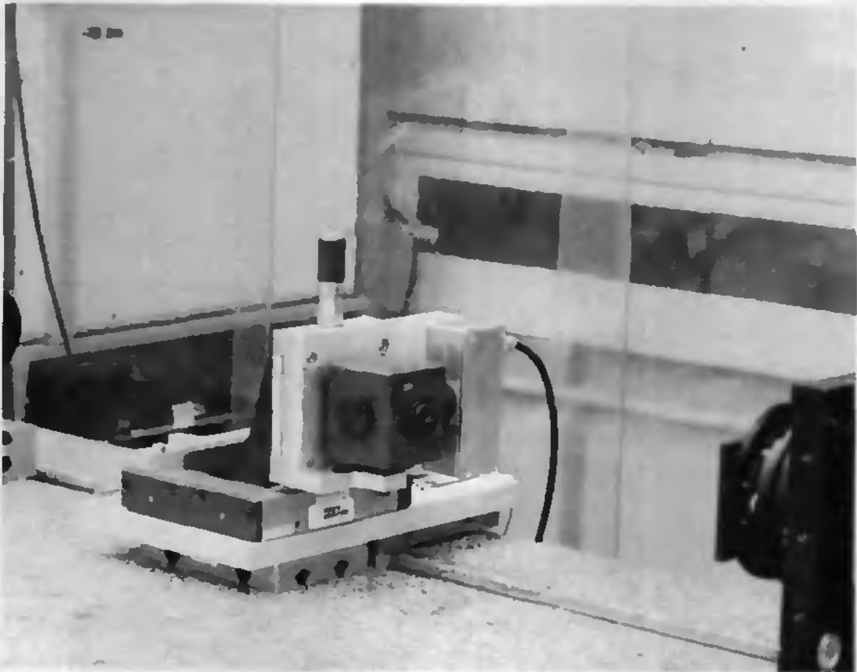

Fig. 7.2.2.3-3 Detector system for diffraction pattern scanning with pin hole

Figure 7.2.2.3-3 shows the detector head with a pinhole for diffraction pattern scanning. In addition to these measurements, the diffraction patterns were also analyzed visually with a microscope.

7.2.2.4 Focal Length Test Setup

The focal length of the optical elements,i.e. lenses, DOE's and hybrids, were measured with a goniometer: a graticule with a well known structure is placed in the focal plane of the test specimen, as shown in figure 7.2.2.4-1.

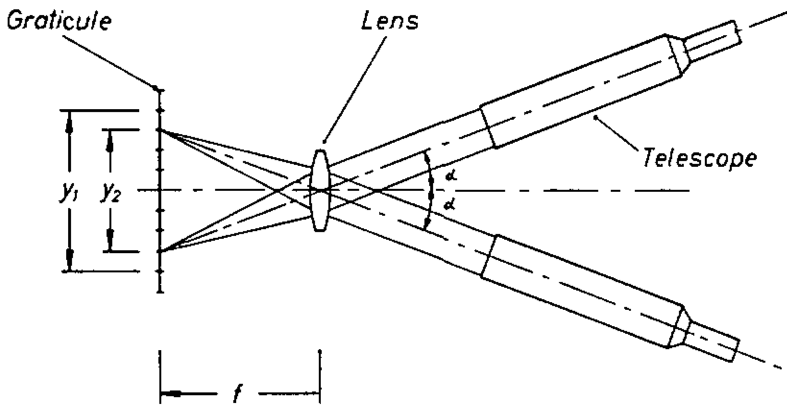

Fig. 7.2.2.4-1 Principle of focal length measurements

The test specimen is placed in the goniometer axis and the angular size of the test structure is measured by aiming with the telescope at different object heights and reading the corresponding angles from the goniometer system. The paraxial focal length f_0 can be defined via the image height y_0 and the angle α_0 as (see figure 7.2.2.4-1)

$$f_0 = \frac{-y_0}{\tan\alpha_0} \tag{106}$$

assuming small apertures and the angle α_0 approaching zero. The paraxial focal length is a definite system constant. An effective focal length can be defined in the same way for other angles α according to

$$f = \frac{-y}{\tan\alpha} \quad (107)$$

The effective focal length is a function of the field angle and is usually defined with respect to the actual application of the instrument. The field dependence of the effective focal length results in image distortion, manifested by field dependence of image size. The distortion in percent is therefore defined as the difference between the theoretical image height and the measured image height, normalized by the theoretical height, and multiplied by 100:

$$D\ [\%] = \frac{y-y_0}{y_0} \cdot 100 \quad (108)$$

The measurement result for the image height depends on the focal length value used for calculation. If the paraxial focal length is used the distortion shall be called paraxial distortion, if a mean focal length value is taken the distortion can be reduced to the photometric distortion.

The test jig (figure 7.2.2.4-2) used for the focal length measurements was designed to be usable also for the Hartmann tests described already in section 7.2.2.2. In this test jig the test specimen is placed into a fixed holder which is mounted on an optical bench. A graticule (Heidenhain Okularmikrometer No.12) is mounted in an adjustable holder which had a focusing range of 15 mm and a coarse adjustment range up to 120 mm. Focal length measurements of up to 250 mm were possible by interchanging the base plate. The maximum test specimen diameter is 33 mm. The graticule is illuminated from the back with a halogen fibre light source with interference filters. The same set of filters was used as mentioned in the previous section. The distance between the graticule and the lens under test is measurable via reference points with a dial gauge to an accuracy of ±0.005 mm. This allows also for easy determination of the back focal length. Figure 7.2.2.4-3 shows the test jig on the goniometer. The optical bench of the test jig is fixed on the table of the goniometer (Möller-Wedel Goniometer II) with the test specimen principal plane in line with the goniometer turning axis. The angular read out of the goniometer provides an accuracy of 1 arcsec. Taking into account the precision of the graticule, an overall measurement accuracy of ±0.25% can be achieved. The test setup was used for determination of paraxial focal length and distortion. A computer programme was developed for data acquisition and evaluation of the results.

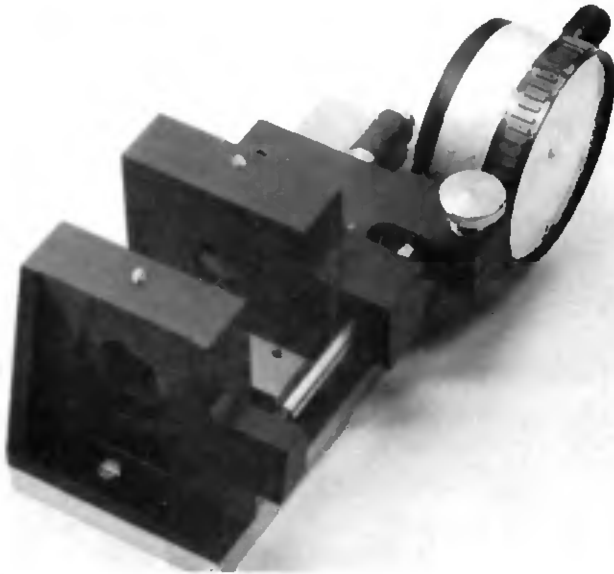

Fig. 7.2.2.4-2 Focal length test jig

In addition, the chromatic focus shift was determined, by measuring the differences in back focal length for the various wavelengths used: for a given wavelength the lens was focused visually for maximum edge contrast on the graticule and the corresponding back focal length was measured. The focusing was controlled by observation with the goniometer telescope. After measurement for all the wavelengths used, the differences to the nominal wavelength position were computed.

Whereas the accuracy of the focal length test method is largely independent of focusing errors, this is not the case for the back focal length measurements, since it is based on visual focusing on the target graticule. For the f-number of the hybrids under test the focusing error is ca. ± 4.5 μm for the control wavelength, according to the Rayleigh criterium. Together with the dial gauge accuracy this results in an rss error of ± 6.7 μm. Systematic errors can be in the order of 10 μm.

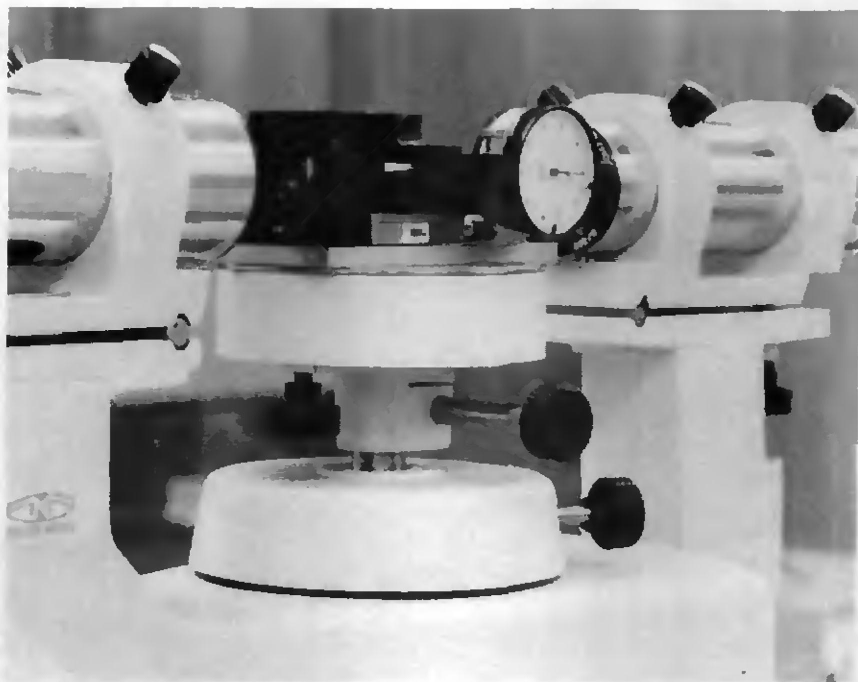

Fig. 7.2.2.4-3 Focal length test jig on goniometer

7.3 Verification Results

7.3.1 General Test Results

The results of various tests and/or inspections which have been performed during the manufacturing phase shall be summarized here. Typical manufacturing tests are etch depth measurements and microscopic inspections.
Figure 7.3.1-1 shows etch profile measurements made after the individual etching processes. The measurements were performed with the Talystep. Figure 7.3.1-2 shows a DOE etch profile with the finally adjusted etching depth, measured with the Alphastep 200.

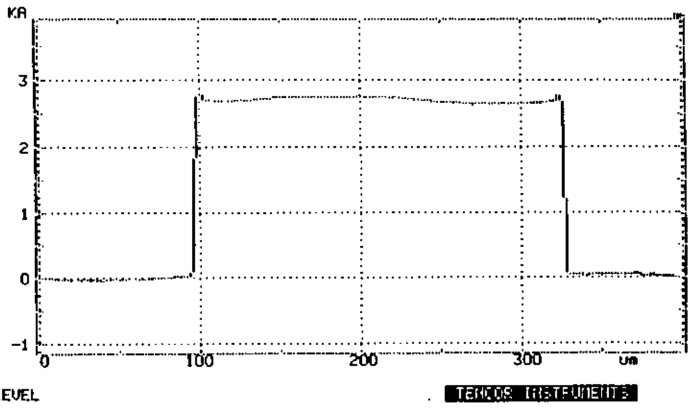

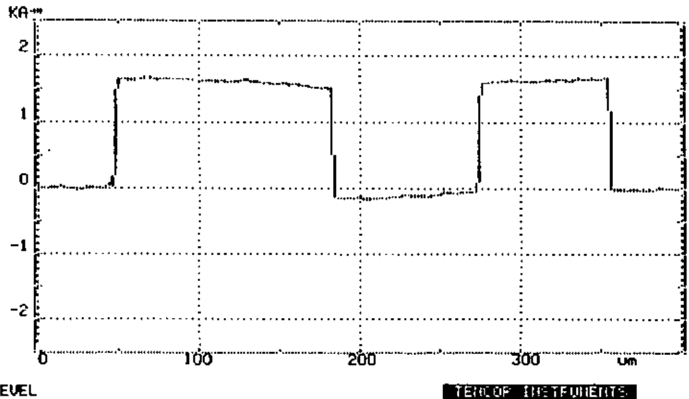

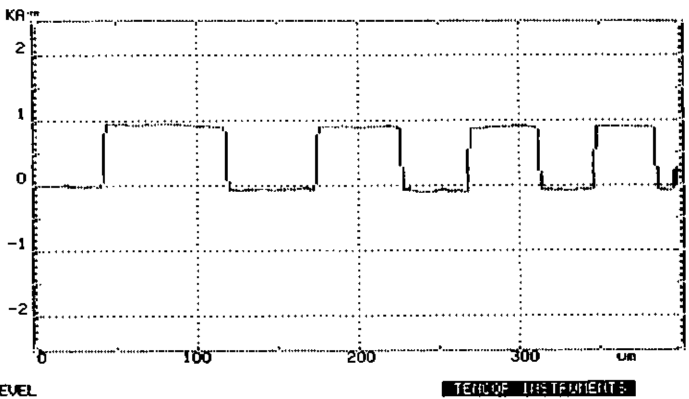

Fig. 7.3.1-1 Etch profiles for mask level 1 (a), level 2 (b) and level 3 (c)

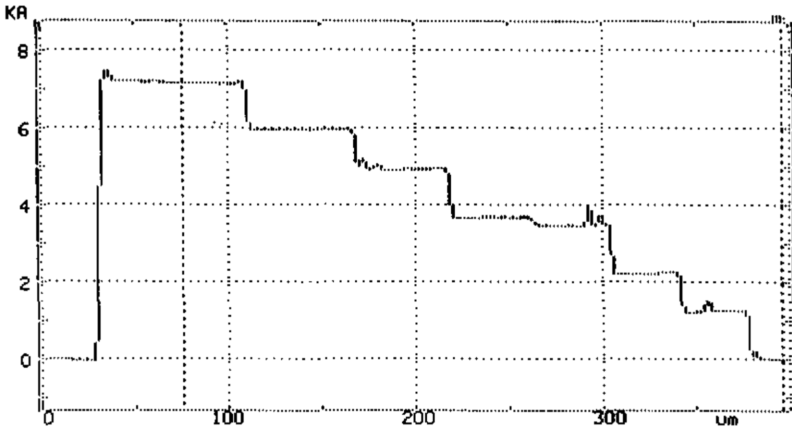

Fig. 7.3.1-2 Etch profile of DOE after final etching step

Microscopic inspections have been also part of the routine tests required to identify surface defects or misalignments. Some photographs of the etched samples have been already shown in section 6.2.2.

Image quality assessments were performed with the hybrid elements, as described in the previous chapter. Some of the results can be presented in the following figures: figure 7.3.1-3 shows photographs which are taken with the hybrid HY9 and a high resolution test plate (Heidenhain target 31a) as object (see also section 7.2.1). The largest bar in the square has a width of 50 µm. In (a) the test plate is shown for monochromatic illumination (550 nm), (b) shows the same plate in white light, with higher magnification. The same test plate was observed with the plano-convex lens element of the hybrid (figure 7.3.1-4). Again, (a) shows the monochromatic illumination, (b) the white light case.
The imaging performance of the hybrid is clearly superior the single lens: the strong spherical and chromatic aberrations of the lens are fully corrected in the hybrid. The resolution of the hybrid in the white light case is well above 156 lp/mm, whereas the resolution of the lens is rather limited to not more than 100 lp/mm.

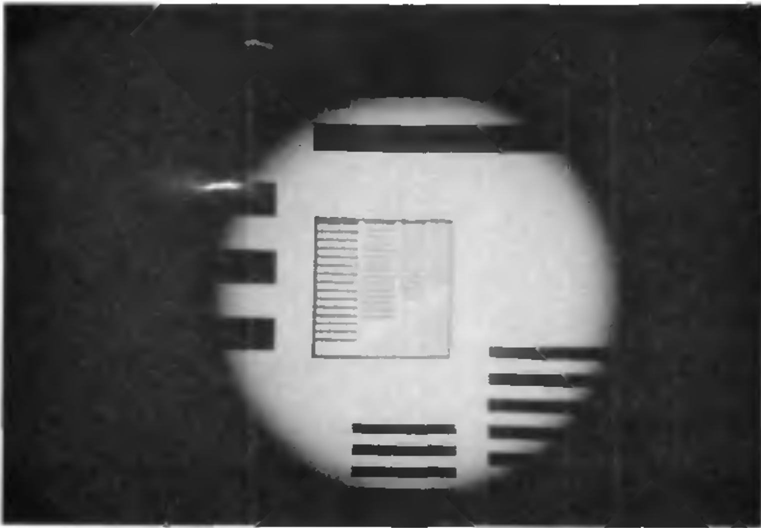

(a)

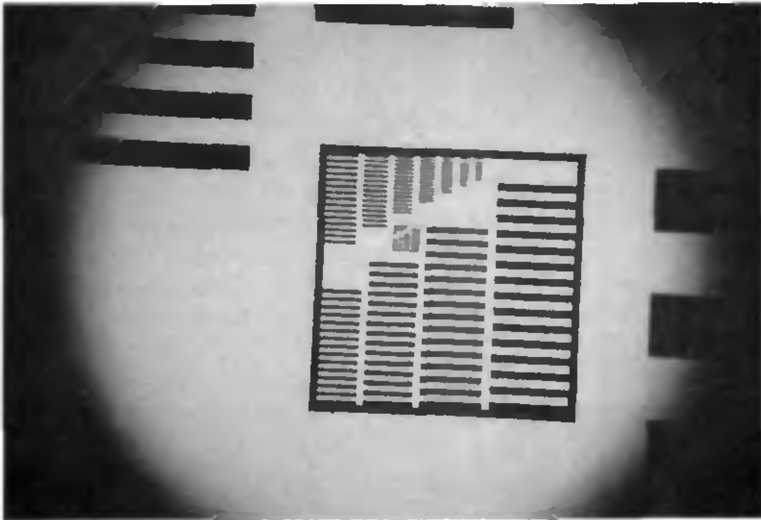

(b)

Fig. 7.3.1-3 Test pattern photographs with hybrid lens HY9 in different magnifications: (a) monochromatic illumination (550 nm), (b) white light

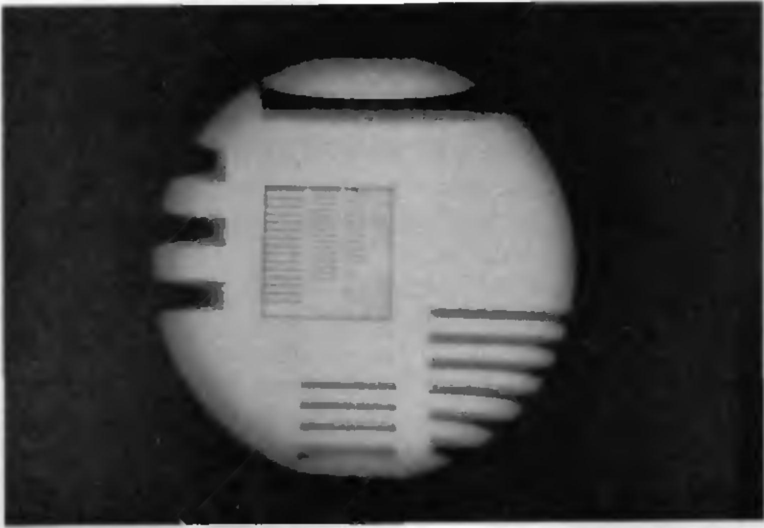

(a)

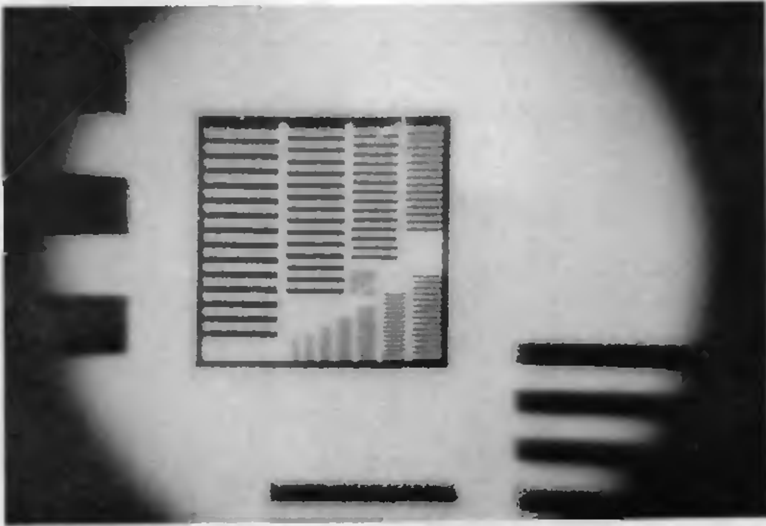

(b)

Fig. 7.3.1-4 Test pattern photographs with plano-convex lens component: (a) monochromatic illumination (550 nm), (b) white light

7.3.2 Diffraction Efficiency/Pattern

The diffraction efficiency has been measured for 9 DOE's manufactured in two different batches (out of 15 pieces in total, manufactured in three batches) with the method described in section 7.2.2.3. The test results at the design wavelength of 632.8 nm are shown in figure 7.3.2-1, for two different sampling apertures, 1.49 mm and 7.49 mm diameter. The spot diagram calculation has shown that 100% of the incident flux should be confined within a circle of 7.498 mm at the design wavelength (n.b.: this calculation is purely based on geometric ray tracing and does not include diffraction effects). The theoretically expected diffraction efficiency for an eight level element is 94.96% (see section 3.3.4). The theoretical diffraction efficiency target values for both aperture diameters are indicated in the graph. The variation of the efficiency within the measured batches is 5.2%, which is comparable with the etch depth variation within the batches of 10% (see also figure 4.3-2). This depth variation is due to a slight variation of etch parameters during fabrication.

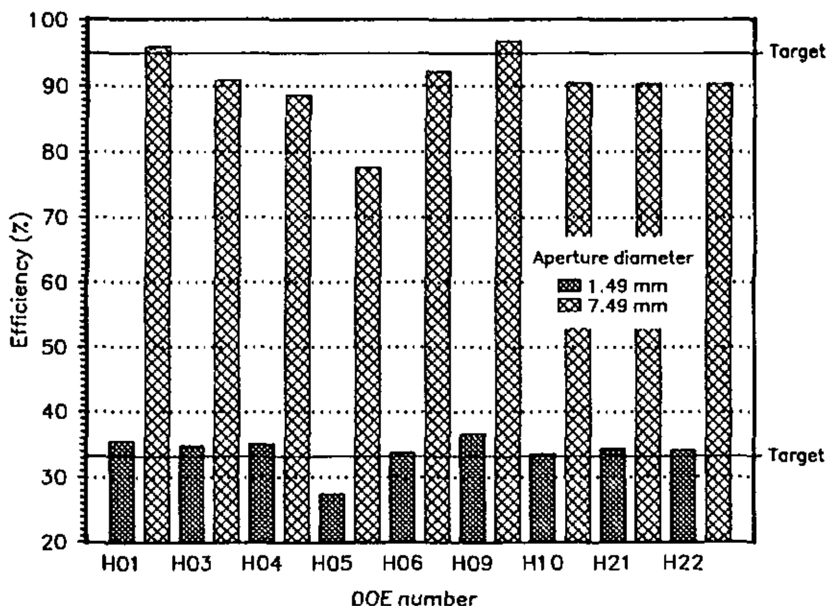

Fig. 7.3.2-1 Measured DOE diffraction efficiencies (λ = 632,8 nm)

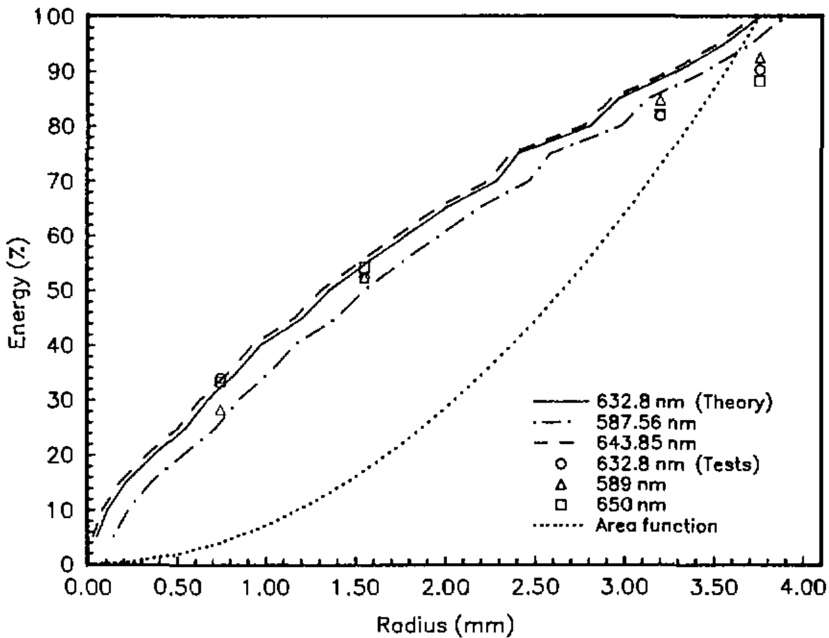

Fig. 7.3.2-2 DOE encircled energy: test results and theoretical predictions

Figure 7.3.2-2 shows the results of encircled energy computations based upon spot diagram calculations for five wavelengths and the measured results for a representative DOE in comparison. Due to the large aberrations of the DOE it is justified to perform the analysis here on a purely geometrical approach. The test area is increase as function of the sampling aperture radius is indicated by a dotted line. Based upon these results one can state that the theoretically predicted diffraction efficiencies were reached, within the limits of measurement uncertainties.

The diffraction pattern for the DOE's was measured by linear scan with a pinhole, as described in section 7.2.2.3. Figure 7.3.2-3 shows a scan for DOE number H21. The wavelength was 632.8 nm, a laser was used. The pinhole diameter was 0.1 mm. The scan length is 30 mm, 1 mm at the plotter corresponds to 0.0787 mm in the image.

Two scans with different lock-in amplifier sensitivities were performed: the first scan with a sensitivity of 10 mV, corresponding to 40 μV at the lock-in input per 1 mm at the plotter, the second with a sensitivity of 20 μV, corresponding to 0.08 μV at the lock-in input per 1 mm at the plotter. Therefore, the intensity scaling factor between the two scans is 500.

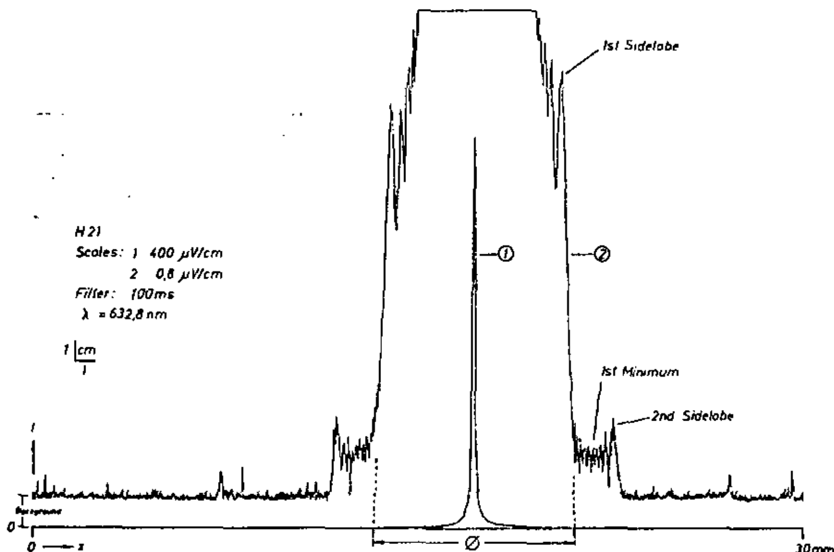

Fig. 7.3.2-3 Scan through DOE focus spot (element H21)

In the figure presented for H21 (figure 7.3.2-3), the first minimum has an intensity level of 0.026% of the maximum peak intensity, the second sidelobe has an intensity of 0.04% only (background levels are subtracted). The average value for the first minima - over all nine DOE's measured - was 0.02% ±0.009%.
The average values are for the first sidelobe maxima 0.23% ±0.01%, for the second sidelobe maxima 0.04% ±0.015% of the maximum peak intensity measured.

This can be considered negligible, the 100% encircled energy diameter was therefore defined as shown in the figure: for element H21 the diameter this diameter is 7.831 mm, no correction is made for the size of the scanning aperture (0.1 mm diameter).

In figure 7.3.2-4 a compilation of the results of the diffraction pattern measurements is presented. For all nine samples the intensity levels measured in the diffraction pattern are given (absolute units in logarithmic scale): the first column for each data set gives always the central peak

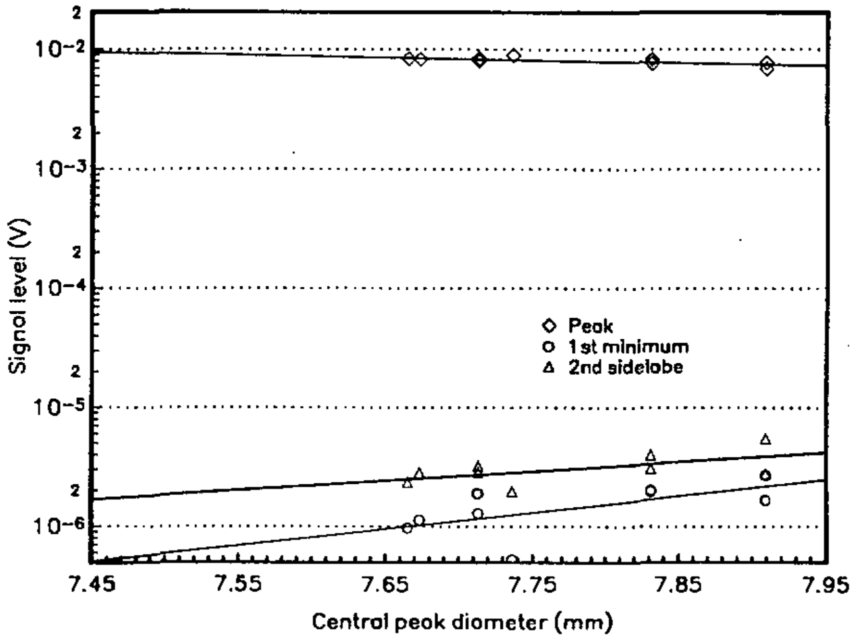

Fig. 7.3.2-4 Diffraction pattern intensity distribution

intensity, the second gives the first sidelobe, the third the following first minimum and the fourth column represents the second, lower sidelobe. In case of asymmetries in the sidelobes, always the higher value was taken into account.

Figure 7.3.2-5 shows for all samples the dependence of the intensities in the peak, the first minimum and the second sidelobe from the measured central peak diameter. The results are given in absolute intensity units in a logarithmic scale. With increasing central peak diameters, the peak intensity is reduced and more flux is shifted into the sidelobes of the diffraction pattern, which is in conformance with the theory.

The measured central peak diameters are between 2.23% to 5.48% larger than the theoretical predictions made by spot diagram computations (see above). However, this is considered tolerable and can be explained by the finite size of the scanning aperture (0.1 mm diameter), additional diffraction effects and measurement errors.

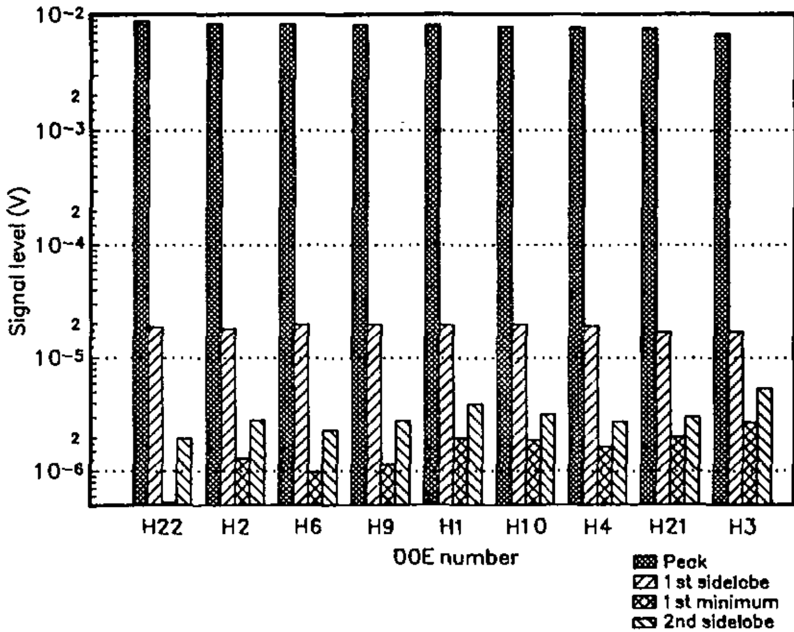

Fig. 7.3.2-5 Diffraction pattern peak diameters vs signal levels in peak, first minimum & second sidelobe

After evaluation of the test results it seems that the analysis of the diffraction pattern of DOE's is an interesting possibility for the determination of the diffraction efficiency by analysis of pattern shape and computation of the integral value.

The diffraction pattern of the hybrid lenses was characterized also visually by microscopic observations, as described in section 7.2.2.3.
Figure 7.3.2-6 shows photograph of the Airy spots of a hybrid lens close to the best focus position. (a) shows the spot as found with white light illumination, (b) for green light at 550 nm. In this photo is slightly visible the effect of angular discretization which is due to the mask generation process: a three fold geometry appears to be in the diffraction pattern. Photograph (c) shows the same lens with stronger defocusing.

(a)

(b)

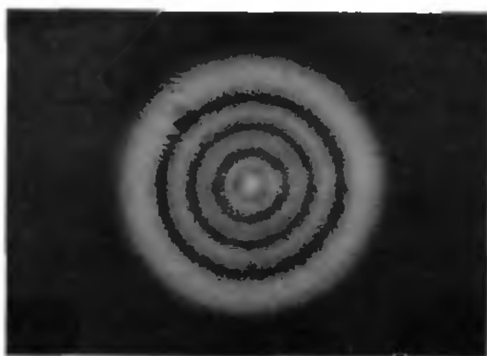

(c)

Fig. 7.3.2-6 Airy spot photographs of hybrid lenses (HY6): (a) white light (close to focus), (b) green light (550 nm, close to focus), (c) green light (defocused)

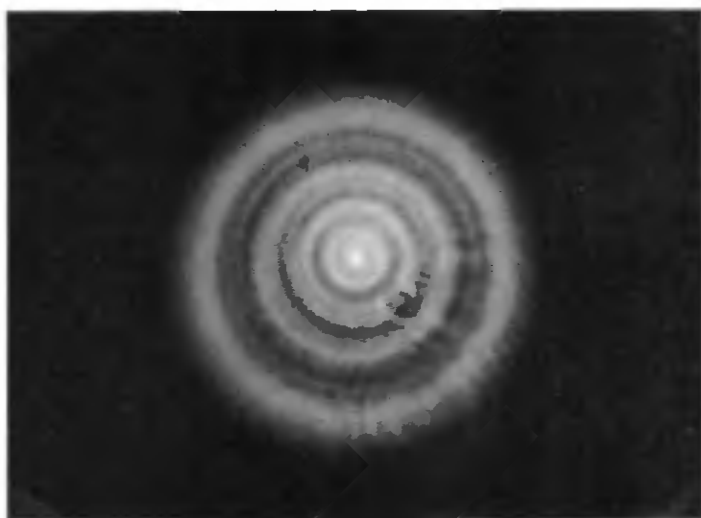

(a)

(b)

Fig. 7.3.2-7 Airy spot photographs in white light and defocused conditions: (a) cemented achromat 1:2.3, (b) hybrid HY6 1:1.8

Figure 7.3.2-7 shows a defocused spot in white light for a cemented achromat with an f-number of 1:2.3 (a) and the same for the hybrid lens HY6 with the f-number of 1:1.8 (b). The achromat shows strongly coloured fringes with pronounced structure, whereas the spot of the hybrid lens is chromatically much more balanced and is not as conspicuously structured as the achromat spot image. This confirms visually the good chromatic correction achieved with the hybrid achromat design.

In figure 7.3.2-8 is presented the performance of the hybrid achromat at higher field angles, again in white light: as predicted by the theory, the lens exhibits in the field some coma, the coma figure shown here was found at about 5°.

Fig. 7.3.2-8 Coma figure of hybrid lens (HY6) in white light (ca. 5° off-axis)

7.3.3 Focal Length

The focal lengths of DOE's, lenses and combined hybrids were measured with the goniometer as outlined in section 7.2.2.4. Table 7.3.3-1 shows theoretically predicted focal length for these elements for the five design wavelength.

Wavelength [nm]	Focal length [mm]		
	DOE	Lens	Hybrid
546.07	267.2208	22.3094	20.7503
587.56	248.3523	22.4215	20.7316
632.8	230.5979	22.5207	20.7002
643.85	226.6414	22.5421	20.6889
656.27	222.3502	22.5649	20.6752

Table 7.3.3-1 Theoretical focal lengths for DOE, lens and hybrid

The focal length of the hybrids, f, is deduced from the component focal length f_1, f_2 as follows

$$\frac{1}{f} = \frac{1}{f_1} + \frac{1}{f_2} - \frac{e_1}{f_1 \cdot f_2} \qquad (109)$$

with e_1 being the distance between the component principal points, which is in this case 2.2405 mm, including the 10 µm cement layer between the components.

The measured focal length for the DOE's and lenses are shown in table 7.3.3.-2. The measurement errors have been determined to be ±3 mm rms for the DOE's and ±0.05 mm rms for the lenses. The values for the DOE's are always longer than theoretically predicted, which is mainly due to systematic errors in the angular measurements caused by the strong aberrations of the elements. The focal lengths of the lenses correspond to the theoretical prediction, taking into account the accuracy of the test equipment.

Element number	Focal Length [mm]				
	546nm	589nm	633nm	650nm	656nm
H1		263.694	248.320	238.53	
H2		263.672	247.142	239.536	
H3		264.626	247.553	240.269	
H4		262.848	250.409		242.206
H5		263.349	249.370		240.844
H6		262.895	263.422		256.967
H9		263.070			
H10		265.051	266.636		
H21		263.949	246.985	237.246	
H22		266.630	247.087	238.401	
Lens 1	22.324	22.356	22.486	22.468	22.483
Lens 2	22.319	22.386	22.476	22.547	22.477
Average	22.322	22.371	22.481	22.508	22.480

Table 7.3.3-2 Measured focal lengths for DOE's and lenses

The lenses were assembled with the DOE's, and the hybrid numbers correspond to the DOE nomenclature. Table 7.3.3-3 shows the focal lengths measurement results for the hybrids, an achromat and a biconvex lens. The measurement errors are again ±0.05 mm.

Table 7.3.3-4 compares the measured focal length of the hybrids (for some wavelengths) with the focal length calculated from the individual element measurements using equation (109) and the e_1 value which corresponds to the theoretical glass thicknesses and the 10 μm cement layer, e_1 = 2.240535 mm. The differences in percent are quoted between the measured hybrid focal length and the focal length calculated from component measurements, as described above. The last column shows the differences between measured focal length of the hybrids and the theoretical values given in table 7.3.3-1.

Element number	Focal length [mm]				
	546nm	589nm	633nm	650nm	656nm
HY00	20.839	20.826	20.824	20.790	20.773
HY1	20.800	20.812	20.817	20.789	20.750
HY2	20.777	20.802	20.788	20.767	20.766
HY3	20.792	20.844	20.816	20.797	20.766
HY6	20.816	20.837	20.805	20.810	20.829
HY9	20.792	20.797	20.807	20.779	20.807
HY10	20.807	20.814	20.815	20.795	20.824
HY21	20.805	20.850	20.781	20.815	20.799
HY22	20.853	20.774	20.767	20.763	20.729
HY23	20.798	20.824	20.787	20.755	20.766
Achromat	20.674	20.679	20.702	20.650	20.644
Biconvex lens	21.152	21.233	21.260	21.282	21.284

Table 7.3.3-3 Measured focal lengths for hybrids, achromat and biconvex lens in comparison (see text)

Element	λ[nm]	Focal length [mm]		Delta f [%]	
		Meas.	Calc.	Meas-Calc	Meas-Theory
HY1	589	20.812	20.784	0.13	0.36
	633	20.817	20.787	0.14	0.55
	650	20.789	20.746	0.21	
HY2	589	20.802	20.784	0.09	0.31
	633	20.788	20.779	0.04	0.41
	650	20.767	20.752	0.07	
HY3	589	20.844	20.789	0.26	0.51
	633	20.816	20.782	0.16	0.55
	650	20.797	20.757	0.19	
HY6	589	20.837	20.780	0.27	0.48
	633	20.805	20.877	-0.35	0.49
HY9	589	20.797	20.781	0.08	0.28
HY10	589	20.814	20.792	0.11	0.37
	633	20.815	20.895	-0.38	0.54
HY21	589	20.850	20.786	0.31	0.54
	633	20.781	20.778	0.01	0.38
	650	20.815	20.736	0.38	
HY22	589	20.774	20.801	-0.13	0.17
	633	20.767	20.779	-0.06	0.31
	650	20.763	20.744	0.09	

Table 7.3.3-4 Measured and calculated focal lengths for the hybrids elements

The table shows that the measured focal lengths were always slightly longer than the theoretical predictions: however, the largest deviation from the theoretical value is only 0.55%, the smallest 0.17%. The differences between the measured hybrid focal length and the calculated ones are very small and are partly due to the assumption of a constant cement thickness of 10 μm, which is certainly not valid for all samples. An additional systematic error

Design wavelength [nm]	Focal length [mm]		Difference Theory-Measrmt. [%]	Measurement wavelength [nm]
	Theory	Measurement[1,2]		
546.07	20.7503	20.808 ±0.022	-0.28	546
587.56	20.7316	20.818 ±0.022	-0.42	589
632.80	20.7002	20.801 ±0.018	-0.49	633
643.85	20.6889			
656.27	20.6752	20.781 ±0.031	-0.52	656

Notes: 1. Average values for 10 hybrid achromats
2. Measurement accuracy better 0.05 mm

Table 7.3.3-5 Summary results of focal length measurements

was likely to be caused by the polynomial fit used for the measurement data evaluation. Table 7.3.3-5 summarizes the results of the measurements.The mean focal lengths per test wavelength are calculated from the measurement results of 10 hybrids (see table 7.7.7-3) and compared with the design results (see table 7.3.3-1): the maximum difference between the measured mean focal length and the theory is only 0.52%. Taking also into account the measurement uncertainty, this is in excellent agreement with the theory and fully confirms the design approach chosen.
Another measurement performed within this test series was the determination of the chromatic focus differences. The measurements were performed for all hybrids listed above, for the lens component alone, for a biconvex lens, and a conventional achromat. The data for the biconvex lens and the achromat are:

- Biconvex lens
  - Focal length at 633 nm — 20.26 mm (nominal)
  - f-number — 1:0.95
  - Glass — BK7

- Achromat
  - Focal length at 633 nm — 20.71 mm (nominal)
  - f-number — 1:2.3
  - Glass — SSK51, SF56

Figure 7.3.3-1 shows the chromatic focus shift dz' with reference to the nominal position at 633 nm, measured for five wavelengths per element. In addition, the theoretical data for the hybrid and the lens component are shown. The data of hybrid HY21 are representative for the results obtained from the other elements. The data displayed in the figure are uncorrected. A linear regression was chosen to show the tendencies, however, it is clear that this does not fully represent the reality of the glass dispersion function. The chromatic correction achieved for the hybrid is clearly demonstrated and in that its characteristics are similar to that of the achromat. The overcorrection in comparison with the theoretical data is due to the longer focal length of the DOE's (see table 7.3.3-3).

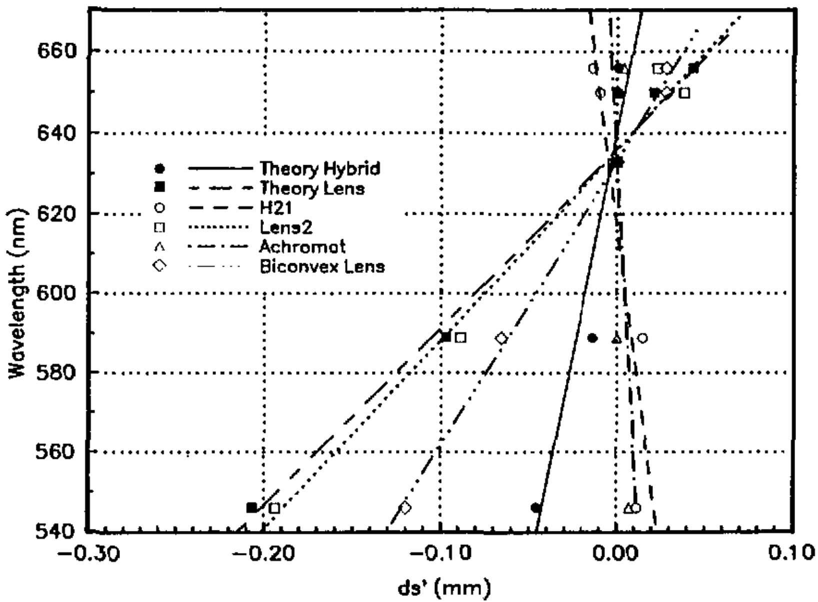

Fig. 7.3.3-1 Chromatic focus shifts for hybrid lens, single lens and achromat: theoretical predictions and measured results

Figure 7.3.3-2 shows the data measured with the other hybrids. Again, the measured points are just fitted by linear regression. The results for ten elements have a maximum spread of 10 μm which is well inside the measurement accuracy for this type of test (see section 7.2.2.4). These results also the theory of hybrid chromatic correction.

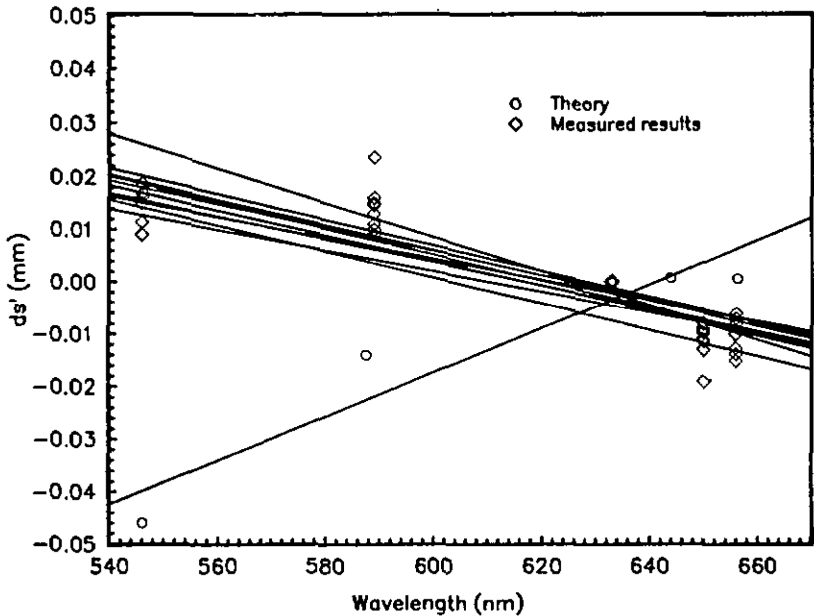

Fig. 7.3.3-2 Variation of chromatic focus shift measurement results of hybrid lenses and comparison with theory

7.3.4 Chromatic Aberrations

The chromatic aberrations of the hybrids were measured with the Hartmann test method, as described in one of the previous sections. The measurements were performed at three wavelengths, 546.07 nm, 632.8 nm and 435.8 nm. Five through-focus positions were measured in increments of 0.2 mm. For each position and wavelength, four incidence heights, each positive and negative, were measured, in addition the reference aperture in the centre of the screen. The beam positions measured at the other incidence heights were referenced to this centre position. The data set obtained in this way for each incidence height, each wavelength and the set of through-focus positions defines the coordinates of the light beams in image space. The beams are defined by the connections of the respective data points by a straight lines.

Figure 7.3.4-1a to c shows the test results for hybrid HY00 for the three wavelengths mentioned. Figure 7.3.4-2a to c shows the results for lens 2. The scales are the same for delta y' and delta s', for the lens only a shift of the delta s' scale was required. The incidence heights of the beams are in both cases the same and indicated in the plots. Similar results can be shown for the other hybrids.

The uncorrected lens shows strong spherical aberrations and a large "circle-of-least-confusion", the diameter of the focus patch is minimum at 632.8 nm with 0.9 mm, the maximum at 435.8 nm is 1.2 mm. The hybrid shows a much better corrected spherical aberration. The diameter of the focus patch diameter was measured to be 0.04 mm for 632.8 nm and 546.07 nm, only for 435.8 nm it seems to be larger. However, this wavelength was not taken into account for the chromatic correction. In any case, the comparison between the two elements shows that the chromatic aberrations were significantly improved.

The theoretically predicted spot sizes for the hybrid and the lens are significantly smaller than the measured results, but this was to be expected from an analysis of the measurement accuracy provided in section 7.2.2.2. The accuracy of the test setup - with the given signal levels - is dominated by detector noise and other errors due to Hartmann screen positioning.

Most of these errors can only be eliminated by a highly automated test setup, the development of which was far beyond the objectives of this work. However, the results show that the basic chromatic correction approach was valid and, moreover, that the Hartmann test concept implemented using modern sensor technology has an interesting potential as a diagnostic tool for measurement of ray aberrations. The accuracy of the measurements, for the light input power levels used, can be quoted to be for the laser line ± 11.7 µm rms error, for the other wavelengths ± 20.9 µm rms error, the systematic errors for both cases being ca. ± 8.1 µm. This leads to values of ± 14.2 µm rss and ± 22.4 µm rss for the laser and the other wavelengths, respectively .

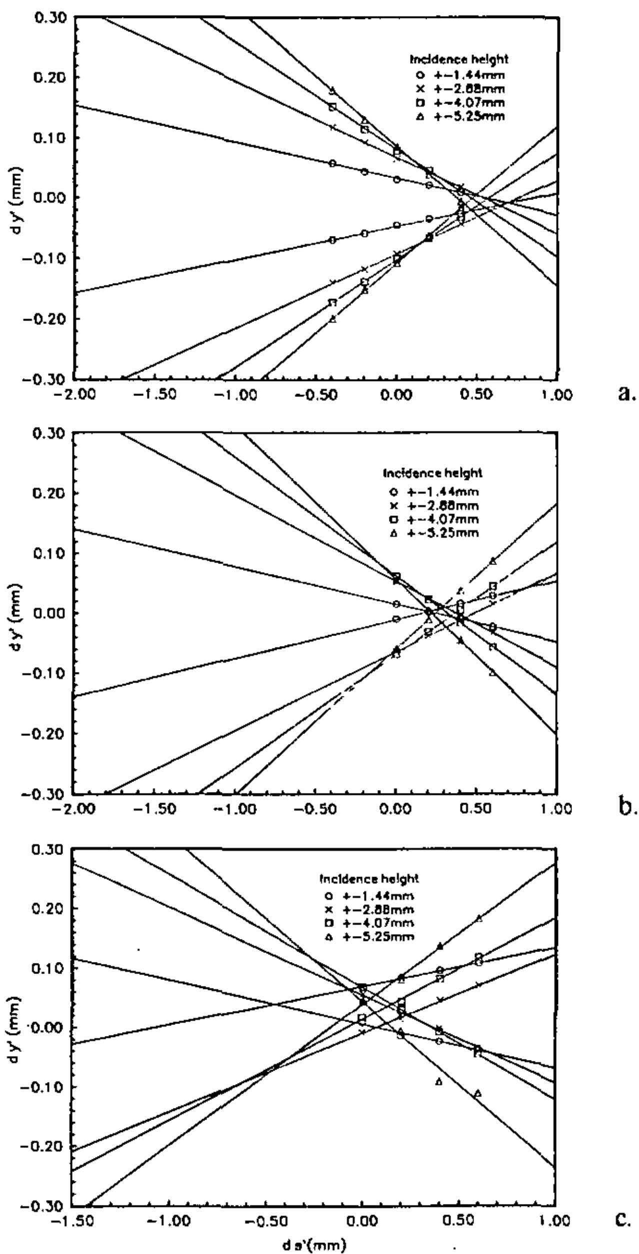

Fig. 7.3.4-1 Through-focus Hartmann test results (hybrid HY00) for 632.8 nm (a), 546.07 nm (b), and 435.8 nm (c)

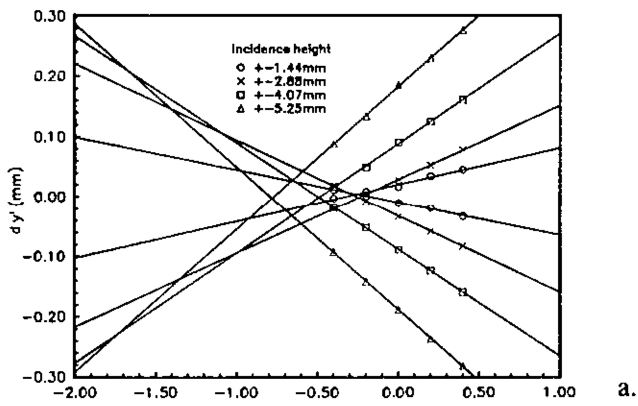

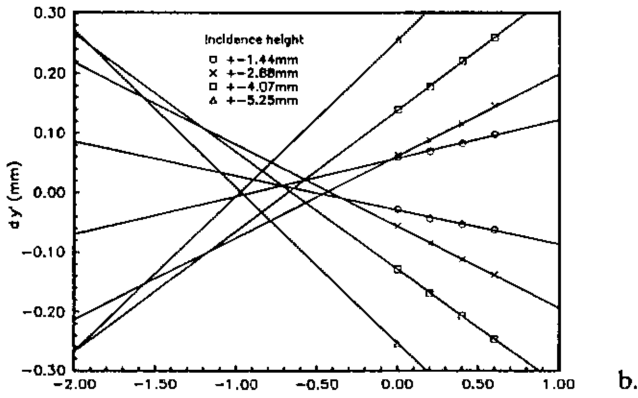

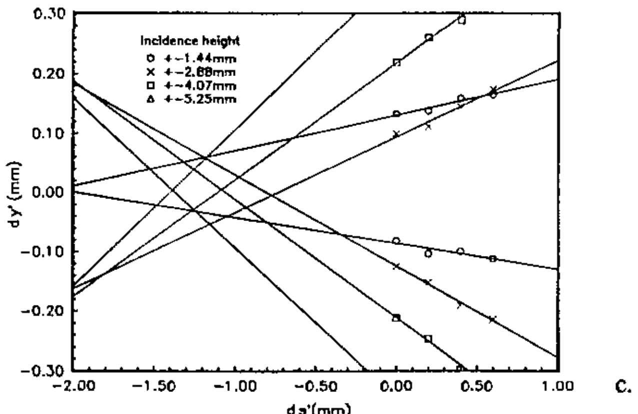

Fig. 7.3.4-2 Through-focus Hartmann test results for plano-convex lens for 632.8 nm (a), 546.07 nm (b), and 435.8 nm (c)

7.3.5 Wavefront Quality

The wavefront quality of the hybrids was tested with a Twyman-Green interferometer at a wavelength of λ = 643.8 nm using a mercury-cadmium lamp. The reasons for this approach and the design details for the interferometer are given in section 7.2.2.1.

Figure 7.3.5-1 (a) shows the interferogram of the plano-convex lens component of the hybrid alone, (b) shows the result for the hybrid HY6, as a typical example. The overall wavefront error of the lens is circa 25λ, which is in accordance with the theoretical predictions. The evaluation of the interferogram of the hybrid lens gave the results shown in figure 7.3.5-2: the wavefront quality of the hybrid was measured to be 0.19λ p-v or 0.032λ rms. This is in excellent agreement with the theoretically predicted wavefront errors of 0.172λ p-v for this wavelength (see figure 4.4.2-1). The dominant residual error is due to coma caused by DOE misalignment. Again, the design approach chosen for hybrid optics is confirmed with these results.

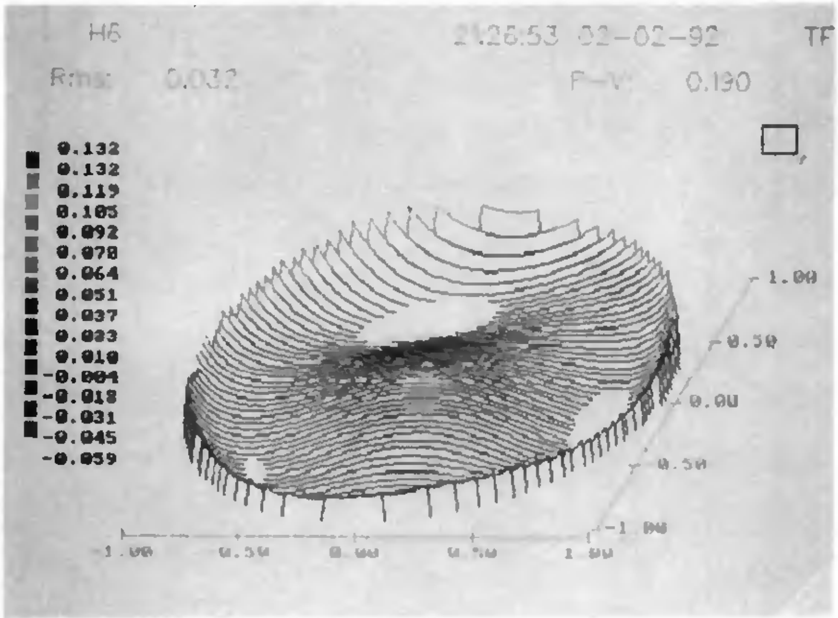

Fig. 7.3.5-2 Wavefront error map of hybrid lens HY6 at λ = 643.8 nm

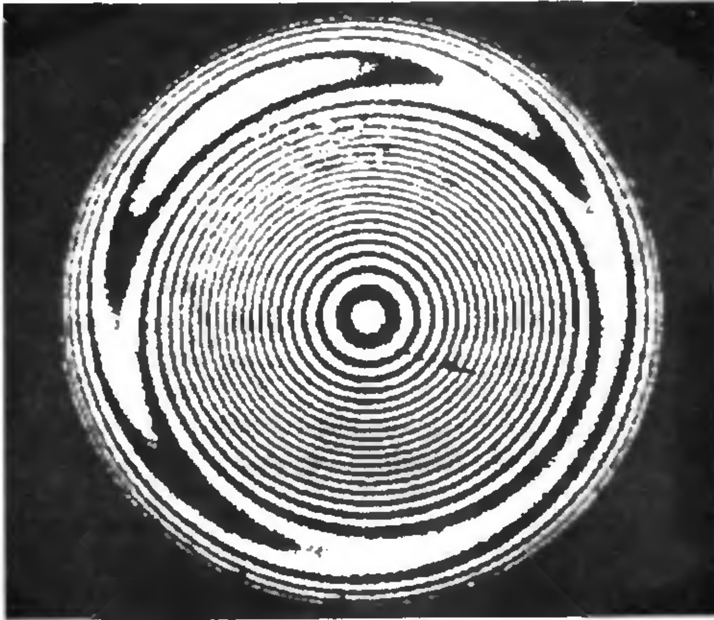
(a)

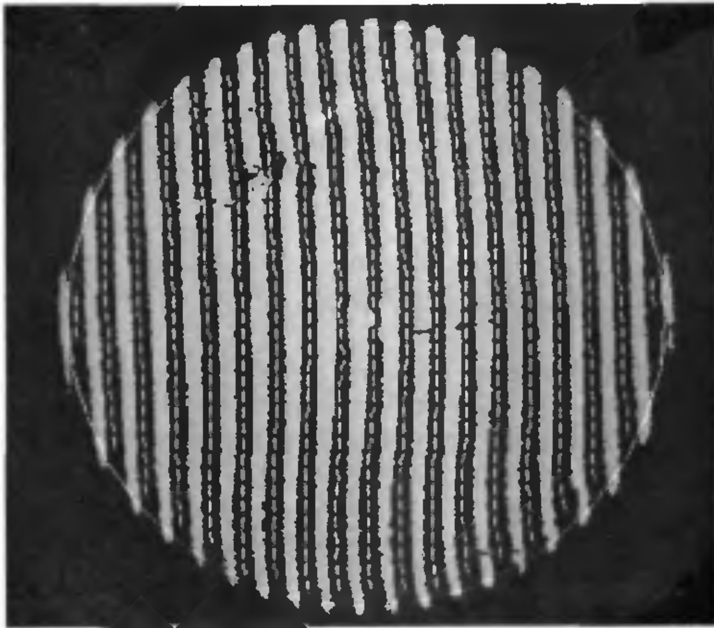
(b)

Fig. 7.3.5-1 Interferograms of plano-convex lens (a) and hybrid lens HY6 (b)

7.4 Technological Evaluation

The evaluation of a technological process shall give evidence about its suitability for space applications. The evaluation of hybrid optics technology shall be performed here with respect to the requirements for space optics as defined in chapter 5.

Lifetime and Reliability

The possible lifetime of hybrid optics is in principle not much different from the lifetime of other space optics, since the same materials can be used. However, due to design simplifications possible with hybrid optics the margins to be taken into account for performance degradation per element can allow for the prediction of longer lifetimes for hybrid optics than for conventional systems. The reliability of hybrids - if the definitions of [5.4] are adopted - is superior to that of conventional optics, since the number of elements and interfaces is reduced for hybrid optics compared to conventional systems of the same performance. A quantification of both aspects, lifetime prediction and reliability depends strongly on the system design: for a simple optical system, an achromat, a reliability assessment was presented in [5.4], which came to the result that the reliability figure of the hybrid is by 0.01 higher than for a conventional achromat. This might look negligible, but it can add up in more complex designs to significant improvements over conventional systems. For both aspects, lifetime and reliability, a hybrid optical system can be qualified for space applications, moreover, it offers some advantages compared to conventional optics.

Reproducibility of Manufacturing Processes

The manufacturing processes taken for hybrid optics are derived from the high volume production processes used in semiconductor industry and are very well characterized and known to be reliable. It is noteworthy that the variation of optical performance characteristics, within this batch of hybrid elements from the first ever pilot production run, is very small. The selection of ion beam etching technology was a prerequisite for this, since the process is well controllable due to its time function and it is based on a purely physical mechanism that avoids any chemical reactions, which depend for their action on the optical materials being processed. Based upon this, the manufacturing processes required for the production of hybrid systems can

be classified as highly reproducible and well characterized, and can be therefore qualified for space applications.

Environmental Loads

The resistance of hybrids to thermal loads is potentially better than that of conventional systems because of the possibility to perform achromatization with one single material only, instead of at least two for the conventional systems: matching of expansion coefficients and selection of appropriate optical cements is not required for this technology. For the thermal compensation of infrared systems hybrid optics offers significant advantages compared to conventional optics (see section 4.4.3).

As far as resistance to mechanical loads is concerned, there is no difference between hybrid optics and conventional optical systems on the component level. However, on system level, aspects like mass and dimensions have to be taken into account for design dimensioning, and the use of more lightweight and smaller systems can help to increase the resonance frequencies and to keep the mechanical loads lower.
In view of the ionizing radiation loads to be expected in space, it was shown that hybrid optics can be manufactured with a wide range of radiation resistant glasses including fused silica: etch rates for a representative selection of optical glasses, their cerium doped versions and fused silica have been successfully determined (see 6.1.4.3). The fact that hybrid achromats do not require the use of optical cements since they consist of one glass component only makes them inherently insensitive against the strong degradation of optical cements due to UV radiation.
For some applications requiring high UV radiation tolerance this is a decisive advantage of hybrid optics over conventional systems. From this point of view, the resistance of hybrid optics to space radiation loads offers sufficient margins also for long term missions.

Material outgassing in vacuum does not represent a problem for hybrid optics since in the technology elaborated within the frame of this work no organic components or other constituents are involved, which could contribute to degradation of the environment due to outgassing products. With respect to space environmental loads like atomic oxygen or micrometeorite impact, hybrid optics has comparable properties as

conventional optics: certain design rules have to be observed for both technologies to come to a flight-worthy equipment design.

The evaluation of the technological aspects of hybrid optics, including the material selection, has shown that no severe problems exist which could prohibit the use of this technology for the fabrication of space hardware. On the contrary, a number of interesting advantages of this technology have been shown compared to conventional optical systems in particular in the field of reliability, tolerance to certain types of ionizing radiation and the behaviour under thermal loads. As a result of this evaluation it can be stated that the technology of hybrid optics, as developed within the frame of this work, is qualifiable for space applications.

Chapter 8

THE TECHNICAL POTENTIAL OF HYBRID OPTICS

The assessment of the technological potential of hybrid optics in general and in particular for applications in space shall be discussed being guided by two basic questions:

1. Is the technology useful to improve existing products in terms of technical performance, production cost and production time?

2. Is it possible to develop new products on a competitive basis using this technology?

The first question concerns the relation between the well established conventional optics and hybrid optics, or diffractive optics in general, with all their facets. During the previous chapters several technical features have been highlighted which indicate that implementation of hybrid optics can improve the technical performance of conventional optical design concepts, for instance:

- **Chromatic correction with single material.**
  DOE special dispersion properties can be used for the design of hybrid achromats consisting of one material only.

- **Improvement of transmission properties.**
  Hybrid achromats can be made thinner than conventional achromats, which can lead to considerably higher transmission for UV and IR optics.

- **IR optics thermal compensation.**
  The use of silicon hybrids provides thermally compensated IR systems without further design complications.

- **Design flexibility.**
  Hybrid optics can be designed (and manufactured!) in almost any effective structure shape, including non-rotationally symmetric aspherics, which provides all degrees of freedom for design optimization.

- **Reduction of optical element numbers.**
  The possibility of combining several optical element functions into one single element can lead to a reduction of element numbers and consequently to a simplification of optical systems.

A number of further examples can certainly be found by in-depth review of existing designs which will support the statement that hybrid optics can be beneficially implemented in existing products, resulting in technical improvement and cost saving solutions. This is also evident from the large number of research activities running in this field world-wide, which affect not only the "Hi-Tech" sector, but also clearly the consumer oriented high-quantity market. For space applications there is a pronounced trend to use this type of optical technology in particular in the field of earth observations. Typical usage is within such instruments as imaging spectrometers, radiometers or limb sounders. This enables the demanding performance specifications of new generation optical payloads to be met and also enables compliance at the same time with the operational/design constraints which limit mass and dimensions. It will be mandatory in future to implement this new type of optical technology.
However, it is also clear that hybrid optics will not replace the well established conventional optics technology in future, neither for ground nor for space applications, but it will complement it. From the experience gained in dealing with hybrid optics for quite a while, the second question is maybe the more interesting one, and an answer to it can be given to some extent by referring to the results of this work:

Two patent applications for new products using hybrid optics were filed and two others in the field of space system design were stimulated as a direct consequence of the carrying-out of this project.

The main motivation for dealing with hybrid optics is clearly the large creative potential offered by this technology: it is not the question only of being able to design complex aspheres, it is the possibility to design optical/optoelectronic systems without the restrictions imposed by conventional optics concerning geometrical configurations and manageable dimensions. This will be in future the prime motivation for investing in hybrid and diffractive optics.

The design and production of hybrid optics on an industrial scale requires a multidisciplinary approach to be taken: optical components are manufactured

here with technologies derived from VLSI production. To be successful in the field of hybrid optics/optronics requires therefore to combine the know-how of both disciplines - VLSI and optical technology - and to initiate dedicated development activities in this field. Taking this approach, hybrid optics will become an important technology for development of innovative products covering a wide range of applications on ground and in space.

Chapter 9

APPLICATION OF HYBRID OPTICS IN SPACE

The discussion of the technological potential of hybrid optics has emphasized the possibilities of this technology for the development of new system concepts, which can be of special interest for applications in space. A review of existing optical space instrumentation and the systems under development supplemented these aspects and led to identification of the following areas of application for hybrid/diffractive optics in space:

- Displays for manned space missions
  - Head-up displays for transport system avionics ([9.1], [9.2], [9.3])
  - Helmet displays for EVA ([9.4], [9.5], [9.27])
  - Front panel displays [9.6]
  - General display purposes ([9.30], [9.31])

- Image data processing
  - SAR image processing ([9.28], [9.29])

- Spectroscopic applications (scientific instrumentation, earth observation payloads)
  - Imaging spectrometer [9.7]
  - Stellar spectrometer [9.8]
  - Analytic spectrometry for environmental monitoring

- Spectral filtering
  - Wavelength multiplexing/demultiplexing ([9.9], [9.19])
  - Spectral isolation [9.9]
  - Narrow bandpass filtering [9.5]

- Beam shaping
  - Laser beam far field shaping ([9.10], [9.11], [9.12])
  - Coherent power combining ([9.13], [9.14])

- Imaging applications
  - Infrared systems ([9.15], [9.17])
  - Ultraviolet systems [3.49]
  - Phase plates and corrector elements ([9.16], [9.17])

  - Fiber couplers ([9.18], [9.21])
  - Micro-optical components [9.28]

- Signal processing [9.20]

- Planar optics

- Integrated optoelectronics
  - Amacronics: layered structures of micro-DOE's, detectors and processing electronics for parallel image data acquisition and processing ([9.23], [9.25])
  - Smart sensors: satellite attitude control sensors, rendez-vous docking sensors, general control sensors ([9.22], [9.24])

- Monolithic optoelectronic systems [9.26]

Further areas of applications are listed in the various publications (see for instance [9.32], [9.33], [9.34], [9.35]). Some of these have already been studied successfully in the frame of ESA contracts, e.g. imaging spectrometry, laser diode far field shaping, wavelength multiplexer, laser diode mode spectrometer, others are in the status of conceptual consideration for future ESA programmes.

This list clearly shows that hybrid/diffractive optics have excellent potential as well as ample flexibility for use in a wide range of space technology applications.

Chapter 10

SUMMARY AND CONCLUSIONS

It was the intention of this research activity to investigate the potential of hybrid optics for applications in space, to establish fundamental design tools and to define and test manufacturing processes which are qualifiable for the fabrication of such optics. Figure 10-1 summarizes the results and highlights the areas treated within the project. The figure reflects the structure of the work programme which was initially established (see figure 2-1).

The theoretical studies identified the need for a classification scheme of the DOE component of hybrid optics. This was necessary to identify and characterize the basic types of DOE's that were feasible for use in hybrid systems. It also allowed the technological and manufacturing aspects to be taken into account and examined in detail. This approach was found to be invaluable in making a choice of DOE type, material used and manufacturing process, especially given the severe constraints of space qualifiability.

A review of various design methods for DOE's was performed and one method, the High Refractive Index (HRI) model, was identified as being an excellent tool for the design of DOE's and complete hybrid optical systems, since it can be implemented in principle in any commercial lens design software. Various software packages were extensively tested for their compatibility with this model and one program (ACCOS V) was identified to give the best results in terms of hybrid element modelling and performance optimization. The computation results obtained in this way describe the DOE component as a thin, two-dimensional element. A dedicated program was developed to transform the DOE design into a three-dimensional structure by optical path length quantization and computation of associated mask sets, for manufacturing of multilevel binary structures.

The potential of this design approach was demonstrated successfully with several examples: two hybrid achromat designs and two more complex optical systems, which formed part of optoelectronic components, were presented.

The basic requirements for optics in space applications were recalled and candidate materials and manufacturing technologies were identified, which can comply with these requirements.

Theoretical Studies	Sample Manufacturing	Performance Verification
▪ Review of DOE/hybrid technology ▪ DOE classification ▪ Hybrid optics design – Theory – Design/optimization tools – Quantization and mask generation programme ▪ Design examples ▪ Definition of space qualifiable manufacturing processes	▪ Multilevel ion beam etching process – Thermal control – Etch rates for 19 glass types – Process characterization ▪ Centering techniques ▪ Experimental Verification of Manufacturing Process	▪ Development of verification methods and associated equipment ▪ Test results ▪ Confirmation of design approach and theoretical predictions

Table 10-1 Summary of project results

Ion beam etching technology was selected to have the best potential for processing optical glasses.

As part of the experimental activities concerning sample manufacturing, the ion beam etching process was characterized in detail and optimized for the optical materials used in terms of reproducibility and processing time. Etch rates were determined for 19 different optical glasses (normal and cerium doped versions) and fused silica, as a representative selection for potential space optical glass materials. It was shown that all these glasses can easily be processed with good and reproducible results, which is a prerequisite for the consideration of hybrid optics for space applications.
One of the design examples, a hybrid achromat for the visible wavelength range (f-number 1:1.8), was manufactured with ion beam etching in a three-mask process, resulting in an eight level quantized element.

The third group of activities carried out in the frame of this project included the optical performance verification of the elements fabricated. These elements were characterized in various optical tests, in order to compare their performance with the theory. For these tests a number of dedicated test systems were developed.
The results of the verification activities on the hybrid elements showed good agreement with the theoretical predictions: the diffraction efficiency of the diffractive component was consistently about 90% (compared to a theoretical value of 94.6%), and the chromatic aberration correction was successful, resulting in differences of the chromatic focus shifts from theory of smaller than 0.5%. The wavefront aberrations of the elements were smaller than 0.19λ p-v for the full aperture, measured at the second design wavelength, which is in full agreement with the theory.
These results fully confirm the validity of the chosen design approach and the efficiency of the production procedures developed.
The evaluation of hybrid optics technology with regard to the space specific environmental loads has shown that hybrid optics is well suited for applications in space and offers, in several areas, clear advantages over conventional systems, e.g. mass, dimensions and in some cases optical performance superior to that achievable with conventional systems. The possibilities of this technology for the design of more complex optoelectronic systems was demonstrated with two design examples, which showed the inherent design flexibility of computer generated optical elements in combination with conventional optics and electronic detector components.

The results of this work have realized and confirmed the initially stated theses on hybrid optics technology and its potential for space optical system development as well as for on-ground applications. Furthermore, it was shown that the application of VLSI production technologies to the fabrication of optical systems leads to a wide range of new possibilities in optics design, promoting the development of novel optical and optoelectronic systems.

During the execution of the research activities and in evaluation of their results a number of areas were identified which would justify some follow-on activities in this field:

- One of the most important topics concerns the development of methods for cost efficient fabrication of DOE's on curved substrates. This is one prerequisite for the perfect correction of field-dependent aberrations.

- Another area is the derivation of a better definition for the diffraction efficiency of on-axis DOE's, including the refinement of the presently used test approaches.

- The Hartmann test method used here for some of the optical tests showed quite interesting results for diagnosis of optical system aberrations. This test method seems to be a promising alternative to the established interferometric tests, since it provides an analytical tool for identification of different error types including the case of polychromatic illumination. The development of such test equipment for high performance applications could result in a valuable complement to the range of existing high performance optical test equipment.

- The design of miniaturized optronic sensor devices is a further area of high interest in particular in view of space applications. This will require most likely a larger scale industrial research activity. However, some aspects concerning the methods of array optics optimization are certainly also of scientific interest, in particular for the development of fast optimization strategies using parallel processing.

ACKNOWLEDGEMENTS

I wish to express my thanks to

Prof.Dr.R.Dändliker, the director of this thesis, for his excellent encouragement and the fruitful discussions we had during the execution of this work on the various aspects of diffractive optics.

Dr.H.Buczek, who strongly promoted the idea for this research project and provided all necessary support during its realization, combining his strong personal commitment with an efficient organizational approach.

Prof.Dr.K.Biedermann, Institute of Optical Research, Royal Institute of Technology Stockholm, for his interest in this project and the valuable suggestions he made for this work.

Prof.Dr.N.deRooij, who made it possible to benefit from the professional infrastructure of the IMT semiconductor research laboratories and agreed to review the results of this work as member of the jury.

The research project on hybrid optics and the preparation of this thesis was supported by the European Space Agency and I gratefully acknowledge this assistance. I am specially indebted to Dr.K.-H.David who always generously supported my research activities on this field and made it possible to establish the required optical test instrumentation at ESTEC. I would like to thank also Dr.A.Menardi and Dr.H.Lutz for their encouragement during the execution of this work.

The fabrication of the hybrid optical elements was performed in cooperation with the Centre Suisse d'Electronique et de Microtechnique (CSEM) in Neuchâtel and I wish to thank the management of CSEM for this support and the excellent assistance which was provided by the scientific and technical staff. In particular I would like to thank J.M.Mayor, Dr.P.Regnault, Dr.I.Kjelberg, J.M.Teijido, F.Droz, and F.Ess from the Optical Systems Department, headed by Dr.H.Buczek.

I would also like to thank Dr.H.P.Herzig and K.Weible from the Institut de Microtechnique (IMT), Université de Neuchâtel, for their contributions to this project.

Part of the activities was supported by the Foundation Suisse pour la Recherche en Microtechnique (FSRM) within the frame of a project in the field of diffractive optics conducted at IMT Neuchâtel.

The efficient and helpful support of industry during the execution of this work in solving various problems was very much appreciated and I would like to thank here the companies FISBA OPTIK AG St.Gallen, CARL ZEISS Oberkochen/Jena and LEICA AG Heerbrugg for their contributions.

During the verification tests of the hybrid elements at ESTEC I have experienced great assistance by the XA technical staff and I would like to mention here in particular the work performed by S.Hughes and M.Martin in the development of the electronic test equipment and by L.Moretti who was assisting in developing data evaluation software.
I especially want to thank my colleague D.Doyle who cooperated in the development of optical test equipment and who patiently assisted during many time consuming test series. I am also greatly indebted to him for the editorial work and the proofreading he performed during the finalization of this thesis.
Here, I would like to thank also Dr.A.Popescu for his help during the first edition of this work.
I would like to thank also Dr.L.Adams who reviewed the chapter on environmental loads in space and contributed valuable suggestions.
I would like to mention here gratefully also the support I have experienced from D.Ruiz-Estopinan early in this project and the important suggestions made by P.Blattner during the finalization of this report.
For the thermal control design of the ion beam etching process I have received valuable information from Dr.P.Poinas.
I would like to thank also Miss A.van der Geest for the photographs she took of the optical test equipment in the XA optics laboratory.
Furthermore, I am grateful for the excellent support I have received during the execution of this work from the mechanical workshop at ESTEC headed by J.Postema.

Finally, I would like to thank my wife Anke and our son Hauke-Thomas: without their great understanding, their help and their endless patience over the last years this work would have not been possible.

REFERENCES

Chapter 3

3.1 A.Sommerfeld: Vorlesungen über theoretische Physik, Band V: Optik Akademische Verlagsgesellschaft Geest&Portig Leipzig (1964)

3.2 G.Kirchhoff: Berl.Ber. 1882, p.641

3.3 G.Kirchhoff: Ann.Physik u. Chemie (2) Bd.18 p.663 (1883)

3.4 M.v.Laue: Eine quantitative Prüfung der Theorie für die Interferenzerscheinungen bei Röntgenstrahlen Sitz.Ber.Bayer.Akad.Wiss. 8.6./6.7 (1912)

3.5 W.L.Bragg: The diffraction of short electromagnetic waves by a crystal Proc.Camb.Phil.Soc. 17 p.43 (1912)

3.6 M.Born,E.Wolf: Principles of Optics Pergamon Press New York (1964)

3.7 C.B.Burckhardt: Diffraction of a plane wave at a sinuisoidally stratified dielectric grating; JOSA 56 p.1502 (1966)

3.8 E.Wolf: Opt.Comm.1 p.153 (1969)

3.9 H.Kogelnik: Coupled wave theory for thick hologram gratings Bell Syst.Tech.J. 48 p.2909 (1969)

3.10 E.Evans: Opt.Comm.2 p.317 (1970)

3.11 R.Magnusson, T.K.Gaylord: Diffraction regimes of transmission gratings JOSA 68,6 p.809 (1978)

3.12 R.Magnusson, T.K.Gaylord: Diffraction efficiencies of thin phase gratings with arbitrary grating shape; JOSA 68,6 p.806 (1978)

3.13 B.R.Brown,A.W.Lohmann: Complex spatial filtering with binary masks Appl.Opt. 5,6 p.967 (1966)

3.14 W.H.Lee: Computer-generated holograms: Techniques and applications Prog.Opt. XVI (1978)

3.15 H.Buczek, J.M.Teijido: Application of electron beam lithography at CSEM for fabricating computer-generated holograms; Proc. SPIE 884 p.46 (1988)

3.16 J.J.Burch: Proc.IEEE 55 p.599 (1967)

3.17 G.J.Swanson,W.B.Veldkamp: Diffractive optical elements for use in infrared systems; Opt.Eng. 28,6 p.605 (1989)

3.18 H.Buczek: Design and manufacture of holographic optical elements (HOE) for use in systems with diode laser sources; SPIE 1212, p.297 (1990)

3.19 M.L.Rizzi: Replication techniques: Different procedures for recording 2D, 3D images and transmission holographic optics; CISE Milano Italy

3.20 K.Biedermann: Holographic recording materials in: Topics in Applied Physics Vol.20, H.M.Smith (Edt.)
Springer Verlag Berlin, Heidelberg, New York (1977)

3.21 T.A.Shankoff: Phase holograms in dichromated gelatin
Appl.Opt.7 p.2101 (1968)

3.22 R.T.Ingwall, H.L.Fielding: Hologram recording with a new photopolymer system; Opt.Eng. 24,5 p.808 (1985)

3.23 S.Lelievre, J.J.A.Couture: Dichromated polyvinyl alkohol films used as a novel polarization real time holographic recording material
Appl.Opt.29,29 p.4384 (1990)

3.24 R.Changkakoti, S.V.Pappu: Methylene blue sensitized dichromated gelatin holograms: a study of their storage life and reprocessibility
Appl.Opt.28,2 p.340 (1989)

3.25 T.Kubota, T.Ose, M.Sasaki, K.Honda: Hologram formation with red light in methylene blue sensitized dichromated gelatin; Appl.Opt.15,2 p.556 (1976)

3.26 S.Hart, G.Mendes, K.Bazargan, S.Xu: Deep-red holography using a junction laser and silver-halide holographic emulsion
Opt.Let.13 p.955 (11 Nov 1988)

3.27 CSEM: Holographic optics; ESTEC Contract No. 7817/88/NL/PB(SC) (1989)

3.28 J.Jahns,S.J.Walker: Two-dimensional array of diffractive microlenses fabricated by thin film deposition; Appl.Opt.29,7 p.931 (1990)

3.29 T.Yatagai, R.Sugawara, H.Hashizume, M.Seki: Phase-only computer generated hologram produced by an ion-exchange technique
Opt.Let.13 p.952 (11 Nov 88)

3.30 R.H.Doremus: Ion exchange in glass I/II
McGraw Hill, New York (1962); Dekker, New York (1969)

3.31 O.Salminen, T.Keinonen: On absorption and refractive index modulations of dichromated gelatin gratings; Opt.Acta 29,4 p.531 (1982)

3.32 G.M.Naik et al.: Dichromated gelatin holograms: an investigation of their environmental stability; Appl.Opt. 29,35 p.5292 (1990)

3.33 J.P.Golden et al.: Resistance of holograms made in dichromated gelatin emulsion to fission neutron damage; Appl.Opt. 29,29 p.4343 (1990)

3.34 J.J.Clair,C.I.Abitol: Recent advances in phase profiles generation
Prog.Opt. XVI (1978)

3.35 D.Schreier: Synthetische Holographie
Physik Verlag, Weinheim (1984)

3.36 R.T.Ingwall, A.Stuck, W.T.Vetterling: Diffraction properties of holograms recorded in DMP-128; SPIE Vol.615 p.81 (1986)

3.37 J.P.Golden, G.P.Summers, W.H.Carter: Resistance of holograms made in Polaroid DMP128 photopolymer to ionizing radiation damage
Opt.Let. 13, p.949 (11 Nov 88)

3.38 R.T.Ingwall, M.Troll: Mechanism of hologram formation in DMP-128 photopolymer; Opt.Eng.28,6 p.586 (1989)

3.39 G.J.Swanson, W.B.Veldkamp: Binary lenses for use at 10.6 micrometers
Opt.Eng. 24,5 p.791 (1985)

3.40 M.Kato, S.Maeda, F.Yamagashi, H.Ikeda, T.Inagaki: Wavelength independent grating lens system; Appl.Opt.28,4 p.682 (1989)

3.41 E.Hasman et al.:Efficient multilevel phase holograms for CO2 lasers
Opt.letters 16,6 p.423 (1991)

3.42 E.Menzel,W.Mirande,I.Weingärtner: Fourier-Optik und Holographie
Springer Wien New York (1973)

3.43 U.Tietze,Ch.Schenk: Halbleiter Schaltungstechnik
Springer Verlag Berlin Heidelberg New York (1980)

3.44 H.A.Macleod: Thin-film optical filters
Adam Hilger Ltd, Bristol (1986)

3.45 W.C.Sweatt: Describing holographic optical elements as lenses
JOSA 67,6 p.803 (1977)

3.46 W.A.Kleinhans: Aberrations of curved zone plates and Fresnel lenses
Appl.Opt. 16 p.1701-1704 (1977)

3.47 D.A.Buralli,G.M.Morris: Design of a wide field diffractive landscape lens
Appl.Opt.28,18 p.3950 (1989)

3.48 T.Stone, N.George: Wavelength performance of holographic optical elements;
Appl.Opt. 24,22 p.3797 (1985)

3.49 T.Stone, N.George: Hybrid diffractive-refractive lenses and achromats
Appl.Opt. 27,14 p.2960 (1988)

3.50 H.Kogelnik: Reconstructing response and efficiency of hologram gratings
Proc.Symp.Modern Optics, p.605 (1967)

3.51 H.Kogelnik: Bell Syst.Tech.J. 44, p.2451 (1965)

3.52 H.Chang, N.George: Holographic dielectric grating: theory and practice
Appl.Opt.9 p.713 (1970)

3.53 E.J.Saccocio: Application of the dynamical theory of X-ray diffraction to
holography; J.Appl.Phys.38 p.3994 (1967)

3.54 R.Alferness: Analysis of optical propagation in thick holographic gratings
Appl.Phys.7 p.29 (1975)

3.55 R.Alferness: Analysis of propagation at the second-order Bragg angle of a
thick holographic grating; JOSA 66 p.353 (1976)

3.56 R.Alferness: Optical propagation in holographic gratings
PhD Thesis, Univ. Michigan, Ann Arbor (1976)

3.57 P.P.Silvester, R.L.Ferrari: Finite elements for electrical engineers
Cambridge University Press, Cambridge (1983)

3.58 H.R.Schwarz: Methode der finiten Elemente
B.G.Teubner, Stuttgart (1984)

3.59 T.W.Stone: Holographic optical elements
Ph.D.Thesis University of Rochester (1986)

3.60 F.G.Kaspar: Diffraction by thick, periodically stratified gratings with complex dielectric constant; JOSA 63, p.63 (1973)

3.61 R.Magnusson, T.K.Gaylord: Analysis of multiwave diffraction of thick gratings JOSA 67, p.1165 (1977)

3.62 T.Stone, N.George: Bandwidth of holographic optical elements JOSA Opt.Lett. 7,9 p.445 (1982)

3.63 M.G.Moharam,T.K.Gaylord: Rigorous coupled-wave analysis of planar-grating diffraction; JOSA 71 p.811 (1978)

3.64 M.G.Moharam,T.K.Gaylord: Rigorous coupled-wave analysis of grating diffraction-E-mode polarization and losses; JOSA 73 p.451 (1983)

3.65 M.G.Moharam,T.K.Gaylord: Three-dimensional vector coupled-wave analysis of planar-grating diffraction; JOSA 73 p.1105 (1983)

3.66 R.Magnusson,T.K.Gaylord: Equivalence of multiwave coupled-wave theory and modal theory for periodic-media diffraction; JOSA 68 p.1777 (1978)

3.67 R.Alferness: Equivalence of the thin-grating decomposition and coupled-wave analysis of thick holographic gratings; Opt.Comm. 15 p.209 (1975)

3.68 J.N.Latta: Appl.Opt.10 p.2698 (1971)

3.69 J.L.Latta: Analysis of multiple hologram optical elements with low dispersion and low aberrations; Appl.Opt. 11,8 p.1686 (1972)

3.70 W.T.Welford: A vector raytracing equation for hologram lenses of arbitrary shape; Opt.Comm. 14,3 p.322 (1975)

3.71 H.P.Herzig: Holographic optical scanning elements PhD Thesis, Université de Neuchâtel (1987)

3.72 G.Dausmann, H.Buczek, D.Basler: Holografisch optische Elemente Tutorial DGaO Tagung Interlaken (1990)

3.73 W.C.Sweatt:Mathematical equivalence between a holographic optical element and an ultra high index lens; JOSA 69, 3 p.486 (1979)

3.74 J.Flügge: Leitfaden der geometrischen Optik und des Optikrechnens Vandenhoeck & Ruprecht, Göttingen (1956)

3.75 H.Haferkorn,W.Richter: Synthese optischer Systeme Deutscher Verlag der Wissenschaften, Berlin (1984)

3.76 R.Kingslake: Lens design fundamentals
Academic Press Inc., London (1978)

3.77 W.T.Welford: Aberrations of optical systems
Adam Hilger, Bristol Philadelphia (1986)

3.78 M.Berek: Grundlagen der praktischen Optik
de Gruyter, Berlin (1970)

3.79 S.J.Bennett: Achromatic combinations of hologram optical elements
Appl.Opt.15,2 p.542 (1976)

3.80 I.Weingärtner, K.J.Rosenbruch: Correction of two- and three-element
holographic imaging systems; Optica Acta 29,4 p.519 (1982)

3.81 D.Faklis, G.M.Morris: Broadband imaging with holographic lenses
Opt.Eng. 28,6 p.592 (1989)

3.82 C.Hoffmann: Die optische Abbildung
Akademische Verlagsgesellschaft Geest&Portig, Leipzig (1980)

3.83 R.E.Stephens: Selection of glasses for three-color achromats
JOSA 49,4 p.398 (1959)

3.84 M.Herzberger: Colour correction of optical systems and a new dispersion
formula; Opt.Acta 6 p.197 (1959)

3.85 N.v.d.Lessing: Selection of optical glasses in apochromats
JOSA 47,10 p.955 (1957)

3.86 T.M.McHugh, H.A.Levenstein: An overview of binary optics at the
Perkin-Elmer Corporation; Proc. SPIE 884 p.100 (1988)

3.87 R.G.Eguchi, E.A.Maunders, I.K.Naik: Fabrication of low-loss waveguides in
BK7 by ion exchange; Northop Research and Technology Centre,
One Research Park, Palos Verdes Peninsula, California 90274

3.88 M.Oikawa, K.Iga, M.Morinaga, T.Usui, T.Chiba: Distributed-index
formation process in a planar microlens; Appl.Opt. 23,11 p.1787 (1984)

3.89 W.H.Zacharasien: The atomic arrangement in glass
J.Am.Chem.Soc.54 p.3841 (1932)

3.90 R.H.Katyl: Compensating optical systems. Part 1: Broadband holographic
reconstruction; Appl.Opt.11,5 p.1241 (1972)

3.91 R.H.Katyl: Compensating optical systems. Part 2: Generation of holograms with broadband light; Appl.Opt.11,5 p.1248 (1972)

3.92 R.H.Katyl: Compensating optical systems. Part 3: Achromatic Fourier transformation; Appl.Opt.11,5 p.1255 (1972)

3.93 R.C.Fairchild, J.R.Fienup: Computer-originated aspheric holographic optical elements; Opt.Eng.21,1 p.133 (1982)

3.94 W.Veldkamp: Method of fabricating high efficient binary planar optical elements; US Patent Application SN-852587

3.95 S.M.Arnold: Electron-beam generated holographic optical element research Honeywell Corp. Techn. Centre, Bloomington, Minnesota 55420

3.96 C.C.Guest et al.: Design of computer generated holograms for electron beam fabriaction by means of a computer-aided design system; SPIE 884 p.33 (1988)

3.97 J.N.Cederquist et al.: CGH fabrication techniques and facilities SPIE 884 p.40 (1988)

3.98 G.Lippmann: C.R.Acad.Sci.Paris 112 p.274 (1891)

Chapter 4

4.1 DIN 3140: Zeichnungsangaben für Optikeinzelteile (Mai 1978)

4.2 H.P.Herzig: Diffraction efficiency simulation program

4.3 M.W.Farn, J.W.Goodman: Effects of VLSI fabrication errors on kinoform efficiency; Proc. SPIE 1211 p.125 (1990)

Chapter 5

5.1 R.A.Becker: Optical material problems of interplanetary space Appl.Opt. 6,5 p.955 (1967)

5.2 P.Sagirow: Satellitendynamik Bibliographisches Institut, Mannheim Wien Zürich (1970)

5.3 ESA-PSS-01-30: Reliability assurance of ESA spacecraft and associated equipment

5.4 R.H.Czichy: Reliability prediction for optical systems
ESA internal working paper (1991)

5.5 Dornier System: ROSAT System specification

5.6 ESA-PSS-01-704: A thermal cycling test for the screening of space materials and processes

5.7 Arianespace: Ariane 4 Users Manual, Issue 1 (1983)

5.8 NASA JSC: Space shuttle payload structural / mechanical interfaces and requirements; JSC 20052, Vol.8

5.9 DIN 58390: Umweltprüfung von optischen Geräten

5.10 MIL-C-675C: Coating of glass optical elements.

5.11 MIL-O-13830A: Optical components for fire control instruments.

5.12 L.Adams,A.Holmes-Siedle: The radiation design handbook ESA-PSS-01-609

5.13 E.G.Stassinopoulos: The geostationary radiation environment
J.Spacecraft 17,2 p.145 (1980)

5.14 W.Jahn: Die Einwirkung von radioaktiver Strahlung auf Glas
Glastechn.Berichte 31,2 p.41 (1958)

5.15 W.Jahn: Untersuchungen über den Verlauf von Durchlässigkeitskurven röntgen-und gammabestrahlter Gläser; Zeiss Mitteilungen 1,6 p.199 (1958)

5.16 I.H.Malitson: Radiation damage in optical glass; Meeting Standards & Metrology Div. (1968)

5.17 D.L.Griscom: Nature of defects and defect generation in optical glasses
SPIE 541 p.38 (1985)

5.18 P.W.Levy: Overview of nuclear radiation damage processes: phenomenological features of radiation damage in crystals and glasses;
SPIE 541 p.2 (1985)

5.19 C.A.Nicoletta, A.G.Eubanks: Effect of simulated radiation on selected optical materials; Appl.Opt.11,6 p.1365 (1972)

5.20 P.N.Grillot, W.J.Rosenberg: Proton radiation damage in optical filter glass Appl.Opt.28,20 p.4473 (1989)

5.21 K.P.Semenov, A.A.Fotchenkov: Effectiveness of the action of various forms of radiation on quartz; Sov.Phys.Crystallogr. 22,3 p.326 (1977)

5.22 S.F.Pellicori et al.: Radiation induced transmission loss in optical materials Appl.Opt.18,15 p.2618 (1979)

5.23 B.McGrath et al.: Effects of nuclear radiation on the optical properties of cerium-doped glass; Nucl.Instr.Methods 135 p.93 (1976)

5.24 M.J.Treadaway et al.: Radiation coloration and bleaching of glass IEEE Trans.Nucl.Sc.NS-23,6 p.1820 (1976)

5.25 M.J.Treadaway et al.: Luminescence and absorption of electron-irradiated common optical glasses, sapphire and quartz IEEE Trans.Nucl.Sc.NS-22,6 p.2253 (1975)

5.26 R.T.Williams: Nature of defects and defect generation in optical crystals SPIE 541 p.25 (1985)

5.27 J.J.Setta et al.: Effects of UV solarization on the transmission of cerium-doped optical glasses; SPIE 970 p.179 (1988)

5.28 K.Ooka, T.Kishi: Stress build-up in binary borate glasses by UV radiation J.Ceram.Assoc.Japan 74,12 p.363 (1966)

5.29 S.S.Mitra et al.: Optical absorption characteristics of neutron irradiated heavy metal fluoride glasses; Appl.Opt.26,20 p.4443 (1987)

5.30 Schott Glaswerke Mainz: Der Einfluss energiereicher Strahlung auf die Brechzahl und die Homogenität optischer Gläser; Technische Notiz 1975

5.31 E.Raedlein: Simulation der Wechselwirkung von Weltraumstrahlung mit Glas und Glaskeramik; Dissertation TU Clausthal (1991)

5.32 P.L.Higby et al.: Radiation effects on the physical properties of low-expansion-coefficient glasses and ceramics J.Amer.Ceram.Soc.71,9 p.796 (1988)

5.33 M.T.Shetter,V.J.Abreu: Radiation effects on the transmission of various optical glasses and epoxies; Appl.Opt.18,8 p.1132 (1979)

5.34 Leica AG: Cementing/mounting technologies for high performance optics ESA Contract 8719/90/NL/DG (1992)

5.35 ESA-PSS-01-706: The particle and ultraviolett (UV) radiation testing of space materials

5.36 H.Schäffler, H.Elsässer: Physik der Sterne und der Sonne
Bibliographisches Institut Mannheim (1974)

5.37 H. Göhre: Einfluss des Vakuums auf Materialien und Geräte
Raumfahrtlehrgang Aachen Oktober 1964

5.38 Schott Katalog Optisches Glas 3111d IX/80

5.39 ESA-PSS-07: Guidelines for space material selection

5.40 ESA-PSS-01-702: A thermal vacuum test for the screening of space materials

5.41 J.J.Park et al.: Effects of atomic oxygen on paint and optical coatings
Meeting preprint (1984)

5.42 W.K.Stuckey et al.: Effects on optical and metallic surfaces
AIAA meeting, Oct.1983

5.43 A.F.Whitacker: LEO atomic oxygen effects on spacecraft materials
Meeting preprint (1984)

5.44 L.Leger: Oxygen atom reaction with shuttle materials at orbital altitudes
Meeting preprint (1984)

5.45 D.A.Gulino: Atomic oxygen durability of impact damaged solar reflectors
J.Spacecraft 25,1 p.39 (1988)

5.46 H.K.A.Kan: Space environment effects on spacecraft surface materials
SPIE 541 p.164 (1985)

5.47 F.Levadou: Micrometeorid hazard erosion on ECS
ESTEC working paper no. 1443

Chapter 6

6.1 S.M.Arnold: Electron beam fabrication of computer generated holograms
Opt.Eng. 24,5 p.803 (1985)

6.2 R.W.Hawley, N.C.Gallagher: Efficient electron beam pattern data format for the production of binary computer generated hologram
Appl.Opt.29,2 p.216 (1990)

6.3 J.Logue: Fabrication of binary optics using electron beam lithography SPIE 884 p.95 (1988)

6.4 W.M.Moreau: Semiconductor lithography Plenum Press, New York and London (1989)

6.5 C.I.Abitol, J.J.Clair: Opt.Acta 2 p.145 (1975)

6.6 J.L.Coutaz, P.C.Jaussaud: High index gradient in glass by ion exchange Appl.Opt. 21,6 p.1063 (1982)

6.7 K.Forrest, S.J.Pagano, W.Viehmann: Channel waveguides in glass via silver-sodium field-assisted ion exchange IEEE J.of Lightw.Techn. LT-4,2 p.140 (1986)

6.8 R.L.Morgan, G.F.Lehnigk: Characteristics of planar optical waveguides fabricated by sodium-silver ion-exchange; US Army Missile Command, Redstone Arsenal, Alabama Techn. Report RD-RE-86-4 (1986)

6.9 R.V.Ramaswamy, S.I.Najafi: Planar, buried, ion-exchanged glass waveguides: diffusion characteristics; IEEE J.Quan. Elec. QE-22,6 p.883 (1986)

6.10 T.Suhara, K.Kobayashi, H.Nishihara, J.Koyama: Gradient-index Fresnel lenses for integrated optics

6.11 H.R.Kaufmann: An ion rocket with an electron-bombardment ion source NASA Techn. note D 585 (January 1961)

6.12 H.Loeb, J.Freisinger: Ionenraketen F.Vieweg & Sohn, Braunschweig (1967)

6.13 S.M.Rossnagel et al.: Handbook of plasma processing technology Noyes Publications, Park Ridge New Jersey (1990)

6.14 Ch.Hofmann: Definition und Messung der Dezentrierung sphaerischer Einzellinsen; Exp.Techn.Phys. 9,4 p.145 (1961)

6.15 K.Schuch: Methoden zur Messung der Zentrierung optischer Systeme Optik 16,10/11 p.652 (1959)

Chapter 7

7.1 D.Malacara: Optical shop testing Wiley and Sons, New York (1978)

7.2 LEICA Heerbrugg: Optical antenna test equipment
ESA contract no. 1273/90/NL/PB (1991)

7.3 H.Slevogt: Zur geometrischen Optik der Zweistrahlinterferometer
Optik 11,8 p.366 (1954)

Chapter 9

9.1 W.S.Colburn, R.C.Fairchild: Design study for a low-distorsion holographic HUD Radar and Optics Division, Env.Res.Inst. of Michigan (Jan.1982)

9.2 J.C.Perrin: Wide angle distorsion free holographic head-up display
SPIE Vol.600 p.178 (1985)

9.3 R.L.Fisher: Design methods for a holographic head-up display curved combiner
Opt.Eng. 28,6 p.616 (1989)

9.4 Y.Amitai et al.: Holographic elements with high efficiency and low aberrations for helmet displays; Appl.Opt.28,15 p.3405 (1989)

9.5 J.R.Magarinos, D.J.Coleman: Holographic mirrors; Opt.Eng. 24,5 p.769 (1985)

9.6 P.del Vo et al.: Holographic head-up display for the automotive industry
CISE Milano Italy

9.7 LEICA, CSEM: Breadboard for medium resolution imaging spectrometer
ESA Contract no. 8700/89/NL/PB(SC) (1989)

9.8 M.C.E.Huber et al.: Imaging extreme ultraviolet spectrometer employing a single toroidal diffraction grating: the initial evaluation; Appl.Opt. 27,16 p.3503 (1988)

9.9 Pilkington PPE: Study of spectral isolation methods for laser diode intersatellite communications link; ESA Contract No. 6772/86/NL/PB(SC) (1988)

9.10 CSEM: Laser beam far field shaping; ESA Contract no. 7725/88/NL/DG (1990)

9.11 H.P.Herzig,R.Daendliker,J.M.Teijido: Beam shaping for high power laser diode array by holographic optical elements; Proc.Int.Conf.Hologr.Syst. (1989)

9.12 D.Yap et al.: Fabrication of miniature lenses and mirrors for InGaAsP/InP lasers Proc.SPIE 898 p.18 (1988)

9.13 J.R.Leger et al.: Astigmatic wavefront correction of a gain-guided laser diode array using anamorphic diffractive microlenses; Proc.SPIE 884 p.82 (1988)

9.14 J.R.Leger et al.: Coherent addition of AlGaAs lasers using micro lenses and diffraction coupling; Appl.Phys.Lett.52,21 p.1771 (1988)

9.15 G.J.Swanson, W.B.Veldkamp: Infrared applications of diffractive optical elements; Proc.SPIE 883 p.155 (1988)

9.16 H.Chen, Q.Shan: Using holographically generated corrector plates to fabricate low f/No. HOE objectives and collimators; Appl.Opt.27,16 p.3542 (1988)

9.17 C.Abitol, J.J.Clair, L.H.Torres: Optical synthesis of different wavefronts by kinoform principle and fabrication of a Schmidt plate SPIE Proc Instr.Astron.II p.223 (1974)

9.18 J.M.Finlan et al.: Miniature holographic optical elements created using hybrid holograms; Proc. SPIE 884 p.120 (1988)

9.19 Y.Hori et al.: Fabrication of a focusing grating mirror by electron beam lithography; Appl.Opt.29,17 p.2522 (1990)

9.20 M.R.Feldman, C.G.Guest: Interconnect density capabilities of computer generated holograms for optical interconnection of very large scale integrated circuits; Appl.Opt.28,15 p.3134 (1989)

9.21 S.Kawakami,O.Ogawa: Light beam redistribution using computer generated phase plates; J. Lightwave Techn. 7,9 p.1412 (1989)

9.22 T.Shiono et al.: Reflection micro-Fresnel lenses and their use in an integrated focus sensor; Appl.Opt. 28/15 p.3434 (1989)

9.23 W.Veldkamp: Binary optics and its applications; SPIE OE Reports 67 (1989)

9.24 R.H.Czichy: Miniaturised optical tracking sensor/receiver combination ESA/PAT/274 (1992)

9.25 R.H.Czichy: Microooptronic device ESA/PAT/288 (1992)

9.26 R.H.Czichy,M.Wittig: Equipment for transmission and reception of modulated laser radiation; ESA paper XA91/229/RC (3.10.91)

9.27 H.Nishihara: Efficiency of holographic wave-front converter
Appl.Opt.21,11 p.1995 (1982)

9.28 C.W.Gill: Holographic correction of aberrations in optical systems employing synthetic apertures; Thesis, Air Force Institute of Technology
AFIT/GNE/ENP/87M-3 (1987)

9.29 D.A.Jacobs: Correcting aberrated wavefronts from synthetic apertures holographically; Thesis, Air Force Inst. of Technol., Ohio (1986)

9.30 M.M.McDonell: Holographic terrain displays; SPIE Vol.120 p.163 (1977)

9.31 J.A.LaRussa, A.T.Gill: The holographic pancake window
SPIE 162 p.120 (1978)

9.32 D.H.Close: Holographic optical elements
SPIE 69 Laser systems (1975)

9.33 H.J.Caulfield: Computer holograms: a critical review
SPIE 532 p.101 (1985)

9.34 W. Lee: Recent developments in computer-generated holograms
SPIE Vol.215 p.52 (1980)

9.35 J.A.Cox: Overview of diffractive optics at Honeywell
Proc.SPIE 884 p.127 (1988)